PLASMA/NEUTRAL GAS TRANSPORT IN DIVERTORS AND LIMITERS

by

Paul Joseph Gierszewski

B.A.Sc., University of Toronto
(June 1978)

Submitted in Partial Fulfillment
of the Requirements for the Degree of
Doctor of Science
at the
Massachusetts Institute of Technology
September 1983

Signature of Author _____
Department of Nuclear Engineering, September 8, 1983

Certified by _____
Borivoje B. Mikic, Thesis Supervisor

Accepted by _____
A. F. Henry, Chairman, Departmental Committee on Graduate Students

PLASMA/NEUTRAL GAS TRANSPORT IN DIVERTORS AND LIMITERS

by

Paul Joseph Gierszewski

Submitted to the Department of Nuclear Engineering
on September 8, 1983 in partial fulfillment of the
requirements for the Degree of Doctor of Science
in Nuclear Engineering

ABSTRACT

The engineering design of the divertor and first wall region of fusion reactors requires accurate knowledge of the energies and particle fluxes striking these surfaces. Simple calculations indicate that $\sim$ 10 MW/m^2 heat fluxes and $\sim$1 cm/yr erosion rates are possible, but there remain fundamental physics questions that bear directly on the engineering design. The purpose of this study was to treat hydrogen plasma and neutral gas transport in divertors and pumped limiters in sufficient detail to answer some of the questions as to the actual conditions that will be expected in fusion reactors.

This was accomplished in four parts: (1) a review of relevant atomic processes to establish the dominant interactions and their data base; (2) a steady-state coupled 0–D model of the plasma core, scrape-off layer and divertor exhaust to determine gross modes of operation and edge conditions; (3) a 1–D kinetic transport model to investigate the case of collisionless divertor exhaust, including non-Maxwellian ions and neutral atoms, highly collisional electrons, and a self-consistent electric field; and (4) a 3–D Monte Carlo treatment of neutral transport to correctly account for geometric effects.

The edge model was applied to comparing particle and energy flows in INTOR and ALCATOR–DCT with a single–null poloidal divertor, toroidal pumped limiter or advanced bundle divertor. All options yielded reasonable edge conditions. The poloidal divertor and pumped limiter were sensitive to uncertainties in cross-field diffusion coefficient and core particle confinement – small variations could trigger transition from a "hot" to a "cold" edge. The bundle divertor naturally operated in a cold, high recycling condition because of the difficult return path for neutrals, and so is insensitive to the same variables. The high neutral density may also eliminate the need for high–vacuum pumps.

The expected range of applicability of the kinetic model is to divertor plasmas with temperatures above roughly 50 eV – a condition that is plausible, yet is not adequately addressed with currently available collisional fluid models. The results include the characterization of a family of solutions with an electrostatic potential peak in the divertor region, as opposed to a monotonically decreasing potential profile.

The neutral transport model utilizes a simple geometry that allows fast evaluation of complex 3–D systems, as long as interactions with plasma, other neutrals, or walls produce an approximately isotropic flux. It has been applied to determining geometric effects for the 0–D edge model, and to neutral transport calculations in advanced bundle divertors.

Thesis Supervisors:

Borivoje B. Mikic, Professor of Mechanical Engineering, M.I.T.

Richard Morse, Professor of Nuclear Engineering, University of Arizona

Tien-Fang Yang, Senior Staff Scientist, Plasma Fusion Center, M.I.T.

Thesis Reader:

Lawrence M. Lidsky, Professor of Nuclear Engineering, M.I.T.

ACKNOWLEDGEMENTS

It is a pleasure to acknowledge the many people who made time in their work to help me in mine. Prof. Bora Mikic was a constant source of support and optimism in his dual role as advisor and housemaster. Prof. Dick Morse of the University of Arizona shared his physical and numerical insight on collisionless plasmas and made Chapter 5 possible. Dr. Ted Yang and his divertor efforts inspired this thesis and provided constant calibration as to what was or was not important. Prof. Larry Lidsky agreed to be my thesis reader because he expected to learn something, he said, but I am nonetheless grateful since he accepted responsibility on short notice. Prof. Neil Todreas first encouraged my interest in fusion engineering and gave me the opportunity to explore it. And I will always remember Prof. Louis Scatturo, who was willing to take a chance on a stranger and so brought me here for graduate school.

With the friends I have made here, I leave M.I.T. with much more than just a doctorate. Daniel Bankson was my roommate for the first hectic years, and we learned to swim the M.I.T. current of courses and qualifiers together. I am also grateful to Steve Piet for his technical comments, for sharing his public speaking skills and for the fine standard he set me in his Sc.D. thesis; to Alan Wan, Randy Erickson and Walt Strohmayer, the special kind of people you can always rely on to lend a hand or an ear; to Anna Kotsopoulos, for her EMACS and TEX consulting; to Pat McKenty, my friendly competition; and to Warren Krueger, an officemate and a gentleman, who put up with me through the final stages of this thesis.

I am grateful to my parents for many things, but this project rests in no small way on their early encouragement of my reading and learning, which sparked my curiosity and imagination and led me to this goal.

Finally, I wish to thank my friend and my wife, Sue Gierszewski, who endured these thesis years with patience and good humor. Much of the typing and figures are her work, and I'm quite sure she would have done the research too, if I had let her.

My stay at M.I.T. was financially supported by a Canadian government N.S.E.R.C. scholarship, by the U.S. Department of Energy, and by the Nuclear Engineering Department.

TABLE OF CONTENTS

LIST OF TABLES

LIST OF FIGURES

"...And hast thou slain the Jabberwock?
Come to my arms, my beamish boy!
Calloo, Callay, Oh frabjous day!",
he chortled in his joy.

Lewis Carroll, Jabberwocky

PLASMA/NEUTRAL GAS TRANSPORT IN DIVERTORS AND LIMITERS

1.0 Introduction

Steady-state operation of a fusion reactor requires a method to remove impurities and helium ash from the main reactor chamber. Furthermore, it is desirable to protect the first wall from energetic plasma particles, and to shield the plasma from wall-generated impurities. The method must also be able to handle the high particle and energy fluxes that accompany any interaction of the reactor with the plasma. This problem is becoming an increasingly more important aspect of the technology as attention shifts to TFTR, JET, JT-60 and other long-pulse, tritium-burning experiments.

For tokamaks and similar toroidal machines, the primary candidates are the bundle divertor, the poloidal divertor and the pumped limiter [1.1]. These are shown schematically in Figure 1.1. The bundle divertor draws a localized bundle of flux from the plasma periphery and pulls it through the toroidal field coils into a separate chamber. Here the plasma is neutralized against a target and the resultant neutral gas is pumped through vacuum ducts opening onto the chamber. In the poloidal divertor, the magnetic field (and plasma) are pulled into one or two divertor chambers extending symmetrically around the reactor, and also neutralized and pumped away. The mechanical divertor or pumped limiter consists of a mechanical "scoop", a structure that intersects the plasma and ballistically collects and directs plasma and gas down into the pumping ducts.

Similar concepts can be used on other types of devices, although the details will differ. Mirrors, stellarators and torsatrons have magnetic field configurations that have natural divertor regions where the magnetic field leaves the vessel [1.2,1.3]. Inertial confinement systems are pulsed and might not have magnetic fields, but will still require frequent pumping to control conditions in the reactor chamber.

The physics of the "scrape-off" region between the confined plasma volume and the divertor, as well as the divertor region itself, is not yet well understood. Besides the usual complications of plasma particles in a magnetic field, these are regions of strong gradients in density and temperature between the 10 keV plasma and the 0.02 eV reactor vessel. Recycling hydrogen, helium and impurities produce a "cloud" of neutral or partially

charged particles. The hot plasma particles will travel through this region and strike the first wall and divertor neutralizer target. Simple scaling calculations show that the resultant energy and particle fluxes can deposit $\sim$10 MW/m^2 and erode most materials at rates of $\sim$ 1 cm/year.

The engineering design of the divertor region subject to these conditions is very difficult. While comparable fluxes have been handled successfully for short times or over small areas, there is as yet little accumulated experience for large areas exposed under steady-state conditions (Table 1.1). Even if the heat flux can be handled, the high erosion implies both short life for the target, as well as a large source of impurities that can find their way back to the main plasma and quench it. Several innovative approaches have been proposed to alleviate the engineering problems, such as pellet [1.29], liquid [1.30] or gaseous targets [1.31].

However, at this point there remain fundamental physics questions that bear directly on the engineering design. For example, what is extent of the interaction between incoming plasma and recycling impurities or hydrogen? There is experimental evidence that the plasma can effectively plug the divertor throat [1.27]. This automatically reduces the number of divertor-generated impurities returning to the plasma. Furthermore, it increases the neutral gas density in the divertor and makes the vacuum pumps more effective. If the neutral gas density is large enough, the incoming plasma could be cooled such that the actual heat flux to the divertor chamber and target is carried by radiation and by particles with energies below the sputtering threshold (typically 10 - 300 eV).

The purpose of the present study is to treat the plasma particle and neutral gas interaction that occur in divertors and limiters in sufficient detail to answer some of the questions as to the actual heat flux, particle flux, pressure and pumping that can be expected in fusion reactor exhaust systems. In all cases, the emphasis is on self-consistent solutions of hydrogen and electron behavior, since these carry the bulk of the mass and energy flows. The movement of impurities is certainly important, but since these occur in small concentrations (e.g. $He/DT \approx$ 5%), it is assumed that impurity modelling can reasonably and easily be performed assuming background hydrogen and electron profiles obtained from calculations such as described here.

In the next chapter, divertor experiments and modelling efforts are briefly summarized.

In Chapter 3, the relevant atomic processes are reviewed and correlations established for the more important ones. In the next three chapters, three issues in particle and energy transport are addressed, issues that have not yet been fully explored. In Chapter 4, a global edge model is developed, based on a coupled 0-D description, to provide fast and self-consistent estimates of edge parameters under a wide range of conditions and divertor configurations. In Chapter 5, some consequences of collisionless divertor plasmas are considered, in contrast to the usual fluid assumption. In Chapter 6, a 3-D Monte Carlo neutral transport model is developed to allow accurate treatment of geometry, particularly in bundle divertors. The results are summarized, with recommendations for future work, in the final chapter.

1.1 References

[1.1] "U.S. FED - INTOR, U.S. contributions to the INTOR Phase 2A Workshop, critical issues", Vol. I, USA FED - INTOR/82-1, October 1982.

[1.2] D.Marty, E.Maschke, J.Touche and C.Gordon, Nucl. Fus., 12, 1972, 367.

[1.3] O.Motojima, A.Iiyoshi, K.Uo, "Divertor experiments in the Heliotron-D Device", Nucl.Fus., 15, 1975, 985.

[1.4] B.Schweiger, Power, 121(2), Feb 1977, S1.

[1.5] B.Schweiger, Power, 122(2), Feb 1978, S1.

[1.6] F.Olds, Power Eng., 82(2), Feb 1978, 42.

[1.7] "CANDU 600 station design", Atomic Energy of Canada Ltd., Report PP-28, May 1976.

[1.8] "Hutchinson Island Plant Unit 1, preliminary safety analysis report", Florida Power and Light Co., Vol.1, Table 1.1.

[1.9] "Millstone Nuclear Power Station Unit 1, final safety analysis report", Vol.1, 1968, I-5.2.

[1.10] "CRBR Plant preliminary safety analysis report", Vol. 4, Project Management Corp., 1976, 4.4-4.

[1.11] "Fort St. Vrain Nuclear Generating Station Unit 1, preliminary safety analysis report", NRC Docket - 50267-8, Sept 1966.

[1.12] "Liquid rocket engine nozzles: space vehicle design criteria (chemical propulsion)", NASA SP-8120, July 1976.

[1.13] G.Sutton, "Rocket propulsion elements", 3rd ed., Wiley & Sons, New York.

[1.14] A.Canfield et al, "Space shuttle nozzle review", AIAA 78-951.

[1.15] J.Paterson, G.Koehler and R.Wells, "The design of multi-megawatt actively cooled beam dumps for the neutral beam engineering test facility", 9th Symp. on the Eng. Problems of Fusion Research, Chicago, October 1981, p.1666.

[1.16] J.Easoz and M.Nahemow, "Testing of water-cooled cathodes on the Westinghouse High Surface Heat Flux Test Facility", 9th Symp. on the Eng. Problems of Fusion Research, Chicago, October 1981, p.1670.

[1.17] Y.Chung, "Designing MFTF thermal absorbers", UCRL-8290, Nov 1979.

[1.18] W.Kugel, H.Eubank, T.Kozub, J.Rossmassler, G.Schilling, A.von Halle and M.Williams, "Initial operation and performance of the PDX neutral beam injection system", PPPL-1867, January 1982.

[1.19] B.Labombard, D.Overskei and B.Lipschultz, Bull.Am.Phys.Soc.,26(7), Sept 1981, 886.

[1.20] W.Gambill, R.Bundy and R.Wansbrough, in "Heat transfer", Chem. Eng. Progress Symp. Series, 57(32),1961.

[1.21] J.Schaefer and J.Jack, "Investigation of forced convection nucleate boiling of water for nozzle cooling at very high heat fluxes", NASA-TN-D-1214, 1962.

[1.22] W.Bauer, W.Gauster and D.Cowgill, "Divertor materials comments", Proc. Divertor Tech. Workshop, April 1980, Plasma Fusion Center M.I.T.

[1.23] M.Ulrickson, "Materials studies related to TFTR limiters and wall armor", PPPL-1719, 1980.

[1.24] "Actively cooled limiters for Doublet III, Annual Report, Oct. 1, 1979 - Sept. 27, 1980", General Atomic, GA-A16181, 3-10.

[1.25] J.R.Easoz et al, "Experimental investigation of heavy-walled, water-cooled molybdenum tubing for divertor applications", WFPS:TME-82-001, Westinghouse, February 1982.

[1.26] D.R.Walz, J.Jurow and E.L.Garwin, "Water cooled beam dumps and collimators for the Stanford linear accelerator", Stanford University, SLAC-PUB-95, March 1965.

[1.27] M.Kielhacker and U.Daybelge, "Divertors and impurity control", Nucl.Fus., 21(11),

1981, 1497.

[1.28] C.Thompson, D.Polk and D.McFarlin, "Heat exchanger concepts for neutral beam calorimeters", 9th Symp. on the Eng. Problems of Fusion Research, Chicago, October 1981, p.1658.

[1.29] J.Hugill, "An arc-resistant target for the divertor of a fusion reactor", J.Nucl.Mat., 87, 1979, 353.

[1.30] B.Badger et al, "UWMAK-II – a conceptual tokamak power reactor design", UWFDM-112, University of Wisconsin, October 1975.

[1.31] F.R.Chang and J.L.Fisher, "A supersonic gas target for a bundle divertor plasma", Nucl. Fus., 22(8), 1982.

Table 1.1 High Heat Flux Experience

Application [Reference]	Heat Flux max/avg (kW/cm^2)	Coolant	Pulse Length (s)	Heated Area (m^2)	Configuration
BOILERS					
600 MWe utility[1.4–1.6]	0.04/0.01	water	steady	4200	Tube banks
NUCLEAR REACTORS					
600 MWe CANDU[1.7]	0.13/	water	steady	6900	Coolant flows
800 MWe PWR[1.8]	0.16/0.05	water	steady	4700	over heated
600 MWe BWR[1.9]	0.10/0.04	water	steady	5800	fuel pins
300 MWe LMFBR[1.10]	0.26/0.11	sodium	steady	720	
300 MWe HTGR[1.11]	0.04/0.01	helium	steady	5900	Channels in graphite
ROCKET NOZZLES					
Mariner[1.12]	/0.04	radiation		0.01	Flared nozzle
Apollo service module[1.12]	/0.02	ablation, radiation	750	10	Nozzle with liner
Saturn V, S-1C booster[1.12]	/0.5	ℓ RP-1 fuel	150	30	Nozzle with tube banks
Saturn V,S-II[1.12]	/0.3	ℓ H_2 fuel	400	8	As above
Shuttle boosters [1.13,1.14]	/1	ablation	120	30	Carbon liner
NEUTRAL BEAMS					
MFTF dump[1.17]	3.5/	water	0.5	0.36	2.1 cm ID x 3.6 m
PDX dump[1.18]	2.5/	water	0.3		
NBETF dump[1.15]	2./1.1	water	0.5	0.2	0.2 x 1. m^2 panel
NB cathodes[1.16]	/1.	water	steady	0.004	Cu swirl flow
LIMITERS					
Alcator-C[1.19]	20/2	inertia	0.06	0.003	Mo ring
ELECTRIC HEATING					
Tube CHF tests[1.20]	/1.0	water	steady	0.003	0.8 cm ID x 0.4 m
	/3.9	water	steady	0.001	0.3 cm ID x 0.3 m
Nozzle CHF tests[1.21]	6.9/	water	steady	0.0006	0.4 cm ID x 0.1 m
	13./	water	steady	0.0002	0.4 cm ID x 0.04 m
BEAM HEATING					
Area tests[1.22]	3.	water	steady	0.002	0.2 cm ID x 0.04 m
Area tests[1.25]	2.1	water	steady	0.002	0.7 cm ID x 0.1 m
Spot tests[1.28]	10.	water	steady	0.00005	Cu,Mo swirl,fins
Spot tests[1.26]	2	water	steady	0.0001	W,Cu,Al
Spot tests[1.23]	17	inertia	0.75	0.0001	Pyrolytic graphite
	8.	inertia	0.25	0.0001	Cu
Spot tests[1.24]	1.	inertia	1.	0.0001	TiC

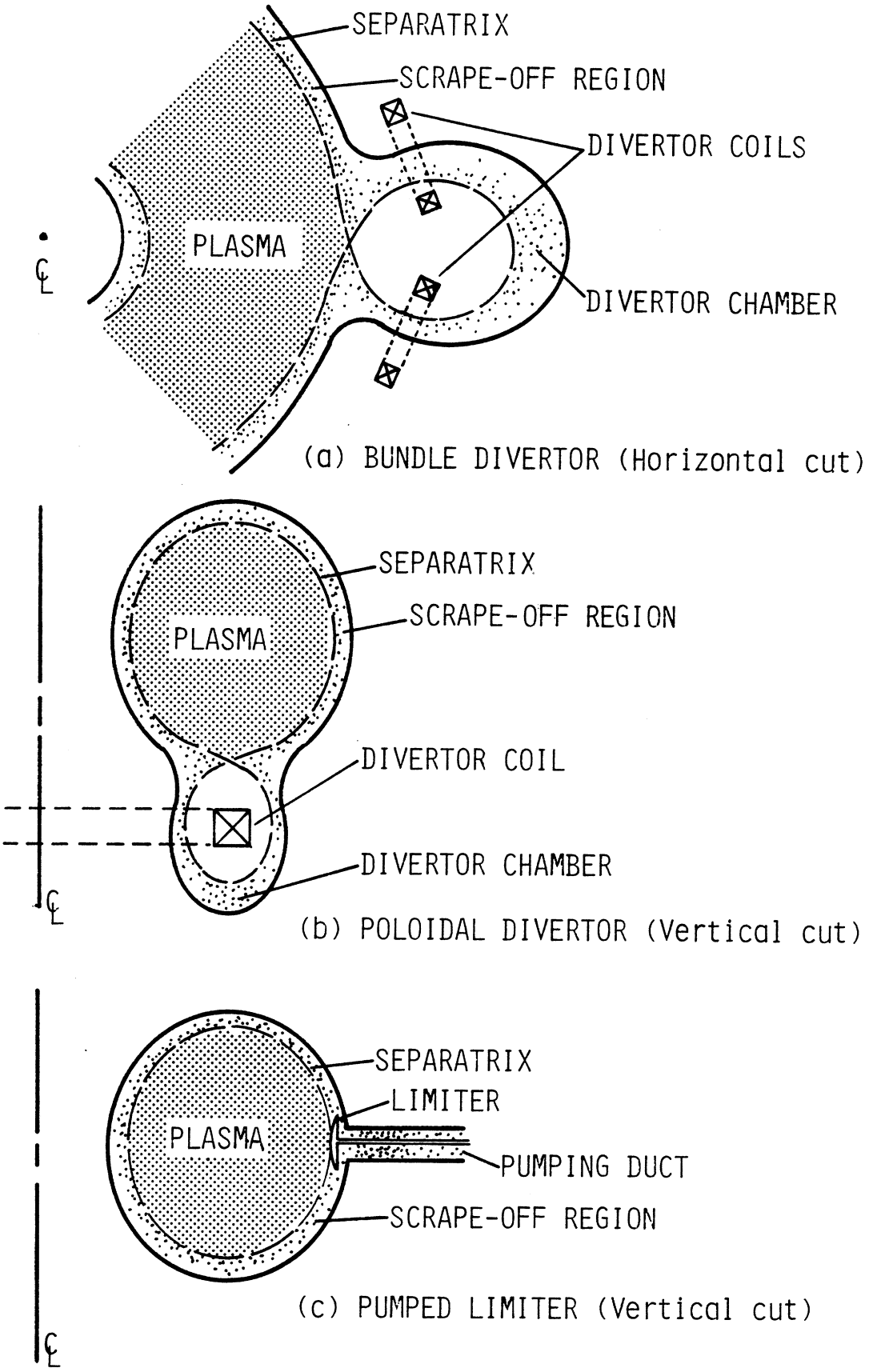

Figure 1.1: Candidate exhaust systems for toroidal machines.

2.0 Divertor Experiments and Theory

In the usual divertor configurations, magnetic field lines on the outer region of a toroidal plasma are channelled into a special chamber. There, helium and impurities can be pumped away. Furthermore, since cross-field transport is much slower than parallel transport, the plasma particle and energy flux to the first wall can be significantly reduced if the diverted or scrape-off region is thick enough. Finally, if neutral impurities from the wall are ionized while passing through the scrape-off region (depending on temperature, density and width), they will also be transported into the divertor. Thus a divertor is in principle able to achieve all three goals of impurity removal, "unloading" of the first wall, and "shielding" of the plasma. The ability of divertors to meet these goals, and the status of the theory, are reviewed here. More detailed discussions are given by Kielhacker and Daybelge [2.12] for experiments, and Harbour [2.13] or Post et al [2.17] for theory.

2.1 Divertor Experiments

The concept of a divertor was first proposed by L.Spitzer in the form of a toroidal divertor for a stellarator [2.1]. Related experiments showed the usefulness of this idea in reducing radiation losses [2.2]. In another early experiment, a poloidal divertor coil was added to the FM-1 Spherator, a toroidal internal ring device at Princeton University [2.3].

Subsequent to the success of these divertors and the growing interest in tokamaks, a number of experiments were designed incorporating poloidal and bundle divertors. Poloidal divertors progressed from the small machines ($\approx$ 50 kA plasma current) DIVA and T-12, to the much larger ($\approx$ 500 kA) PDX, ASDEX and DOUBLET-III, and are currently under construction in JT-60. Bundle divertors were first proposed in Britain and three versions have been tested on DITE ($\approx$ 50 kA Mk1A and B, $\approx$ 120 kA Mk2). Both these and other concepts have been considered or are being considered for other machines, including ISX-B, TEXTOR, ALCATOR-DCT, FED and INTOR.

Typical of experimental experience with these divertors is high particle exhaust efficiency ($\approx$ 100% PDX, ASDEX, DITE Mk2; $\approx$ 30% DIVA, DITE Mk1A) and energy collection efficiency ($\approx$ 50% PDX, DITE Mk1A and Mk2, DIVA; $\approx$ 60% DOUBLET-III; $\approx$ 75% ASDEX) [2.5,2.6,2.12].

In terms of shielding or screening efficiency, divertor experiments have a modest effect on low Z (atomic number) impurities but drop high Z impurity concentrations by an order of magnitude. In DIVA, for example, $Z_{effective}$ was reduced from 6 to 2 and the resulting reduced radiation loss increased the energy confinement time by a factor of 2 to 3 [2.4]. In more recent diverted machines, $Z_{effective} \simeq 1$ and impurity radiation is not so important in the central energy balance [2.12], although radiation can be very important in the plasma edge and divertor [2.25].

Finally, high gas pressures have been observed in front of the divertor plates (ASDEX, PDX), although no actual helium enrichment or depletion has been seen. The high pressure reduces the pumping speeds required to remove the helium and impurities, and possibly protects the divertor plate by radiating some energy [2.12].

Small scale experiments on PLT, MACROTOR, ALCATOR, ISX-B and PDX have shown that particles can be ballistically collected by simple mechanical scoops inserted into the plasma, illustrating the basic physics behind the pumped limiter concept [2.7 – 2.12]. More recent experiments on ISX-B and PDX [2.32] with larger limiters and some pumping ability have shown 40% particle exhaust (ISX-B) and improved energy confinement relative to standard limiters (PDX). The first real test will come soon with the installation of the ALT-1 pumped limiter on TEXTOR [2.32].

2.2 Divertor Theory

Since parallel plasma transport is much faster than cross-field transport, ions that diffuse into the scrape-off layer largely flow along the field lines into the divertor plates where they are neutralized. The characteristic parallel loss time is $\tau_{||} \approx L_{||}/v_{flow}$ where 2 $L_{||}$ is the average length of a field line between divertor plates, and v_{flow} is the ion speed. Generally, $L_{||} \approx q_D \pi R_{major}$, where q_D is a geometric factor and is about 1 for a full poloidal limiter, 2 – 3 for a poloidal divertor or a toroidal limiter, and 10 for a bundle divertor or local pumped limiters. The ion flow velocity is usually based on ambipolar flow of ions and electrons to the divertor plate. Since electrons travel faster than ions at comparable temperatures, more electrons than ions initially strike the divertor plate (assuming it is, as usual, electrically floating). This builds up a negative potential (a sheath potential) in front of the plate which subsequently repels electrons and attracts ions to

achieve an equal or ambipolar flow of each to the divertor plate. Calculations suggest that there is a long presheath region with a small electrostatic field in which ions are accelerated up to a critical velocity of order sonic speed $c_{sonic} \simeq \sqrt{(T_e + T_i)/m_i}$. At this point, within several deBye lengths of the plate, there is appreciable charge separation and the formation of the primary sheath region with an electrostatic potential drop of about $3T_e$, depending on several parameters such as secondary electron emission.

More accurately, particle transport in the scrape-off layer and divertor chamber is modelled as

$$\frac{\partial n}{\partial t} + \nabla \cdot \Gamma = Sources - Sinks \tag{2.1}$$

where

$$\nabla \cdot \Gamma = \nabla_\perp \cdot \Gamma + \nabla_\parallel \cdot \Gamma \simeq -\frac{1}{r}\frac{\partial}{\partial r}\left(rD_\perp \frac{\partial n}{\partial r}\right) + \frac{n}{\tau_\parallel}$$

and n is particle density, Γ is particle flux, and the sources and sinks include atomic reactions such as ionization or charge exchange. In 1-D steady-state, with no sources or sinks, Eqn.(2.1) can be reduced to $n(r) \simeq n(a)e^{(r-a)/\delta}$ where r is the radius, a is the separatrix radius, and $\delta \simeq \sqrt{D_\perp \tau_\parallel}$ is the scrape-off layer thickness. This exponential drop-off behaviour is experimentally observed. A similar equation can be written for energy, and temperature is found to drop exponentially with a roughly comparable scale length. The observed cross-field diffusion $D_\perp$ is much larger than classical Coulomb collisions would suggest, behaving roughly as $0.1 - 10\, D_{Bohm}$ where $D_{Bohm} = T_e/16eB$, with large time fluctuations in density and other properties.

These equations are often used to provide simple boundary conditions to tokamak radial transport calculations [2.14,2.15,2.16]. More detailed models concentrate on the parallel transport along the field lines in the scrape-off layer and divertor chamber and use the radial transport results to provide input boundary conditions. Ref.[2.17] reviews several models relative to poloidal divertors.

For collisional scrape-off layers, fluid models are appropriate. Several 1-D fluid codes are available [2.18] which solve the hydrogen ion and electron conservation equations along the field lines. A detailed 2-D fluid model has also been developed, including e, D^+, T^+ and a Monte Carlo treatment for the neutrals [2.20]. The relative order of the terms in such a detailed fluid model is investigated in Ref.[2.28]. The behaviour of neutral He and DT in a 2-D Monte Carlo poloidal divertor model was also studied [2.26].

On the other hand, if the plasma ions are only weakly collisional in the scrape-off layer, kinetic treatments are more applicable. Early studies have considered drift-kinetic descriptions of the scrape-off plasma [2.27]. More recently, such a description was extended to explain observed asymmetries in power loading to the top/bottom and inner/outer poloidal divertor plates [2.29]. If the plasma is collisionless in the divertor itself (plausible because of the short path length relative to the scrape-off thickness), interaction with the divertor field and recycling neutrals can give rise to significant electric field structure. Simple analytic 1-D models have illustrated this electrostatic potential [2.19,2.22-2.24], and experimental results on the Wisconsin Octupole have shown that there is electric field structure [2.30,2.31].

Overall, the theory is able to explain most experimental results at least qualitatively, with particular models developed to explain specific features in detail. The primary tools are 1-D fluid models generally used to interpret experimental results, and a paired set of 2-D fluid plasma/Monte Carlo neutral transport codes that was originally developed to model INTOR poloidal divertors. However, in spite of the large and growing interest in edge plasmas, there are several areas that have been relatively unexplored. In subsequent chapters, numerical models are developed to study three such issues.

2.3 References

[2.1] L.Spitzer, "A proposed stellarator", AEC Report No. NYO-993 (PM-S-1) 1951 (also "The stellarator concept", Phys. Fluids., 1, 1958, 253).

[2.2] C.Burnett, D.Grove, R.Palladino, T.Stix and K.Wakefield, "The divertor, a device for reducing the impurity level in a stellarator", Paper 359, Proc. 2nd U.N. Int. Conf. on the Peaceful Uses of Atomic Energy, September 1958, Geneva, Switzerland, Vol. 32, Controlled Fusion Devices, p.225.

[2.3] H.Hsuan, M.Okabayashi, S.Ejima, "Measurements of plasma flow velocity into the divertor of the FM-1 spherator by using ion acoustic wave propagation", Nucl. Fus., 15, 1975, 191.

[2.4] M.Nagami et al, "Impurity shielding and sweeping-out by an axisymmetric divertor in DIVA", Nucl. Fus., 18(10), 1978, 134.

[2.5] DIVA Group, "Divertor experiments in DIVA", Nucl. Fus., 15(12), 1978, 1619.

[2.6] D.Goodall, "Energy flux and surface temperature measurements at surfaces in the DITE tokamak", UKAEA, CLM-P472, 1976.

[2.7] J.Schivell, "Method of plasma impurity control without magnetic divertor", Princeton University, PPPL-1342, June 1977.

[2.8] R.Jacobsen, "Preliminary particle scoop limiter measurements in PDX", Princeton University, PPPL-1825, August 1981.

[2.9] S.Talmadge and R.Taylor, "A non-magnetic divertor for tokamaks", UCLA, PPG-476, April 1980.

[2.10] S.Talmadge and R.Taylor, "Pumped limiter experiments on MACROTOR", Paper 9S9, 23rd Annual Meeting of the division of Plasma Physics/American Physical Society, New York, October 1981 (Bull. Am. Phys. Soc., 26(7), 1971, 1057).

[2.11] D.Overskei, "The efficacy of passive limiter pumping of neutral particles", MIT, PFC/JA-80-13, 1980.

[2.12] M.Kielhacker and U.Daybelge, "Divertors and impurity control", Nucl. Fus., 21(11), 1981, 1497.

[2.13] P.J.Harbour, "Divertor problems" in "Plasma physics for thermonuclear fusion reactors", (G.Casini, ed.), Harwood Academic Publishers, England, 1981, 255.

[2.14] M.Gordinier, "The impact of plasma wall interactions on the burn dynamics of tokamak reactors", UWFDM-356, University of Wisconsin-Madison, May 1980.

[2.15] R.N.Byrne et al, "Tokamak reactor codes: MAK0 and MAK1", EPRI ER-1032, March 1979.

[2.16] C.Baker et al, "STARFIRE - A commercial tokamak fusion power plant study", ANL/FPP-80-1, September 1980.

[2.17] D.E.Post, J.Heifetz and M.Petravic, "Models for poloidal divertors", PPPL-1913, July 1982.

[2.18] A.Nicolai and A.T.Mense, "Computer modelling of the bundle divertor, Part 1 Basic Equations", ORNL/TM-6852, May 1979.

[2.19] A.Nicolai, "Numerical simulation of the transport processes in the scrape-off region and the burial chamber of a bundle divertor", Jrnl. Nucl. Mat., 93 & 94 (1980) 231.

[2.20] J.Ogden et al, "One-dimensional transport code modelling of the limiter-divertor region in tokamaks", PPPL-1608, February 1980.

[2.21] D.Heifetz, D.Post, M.Petravic, J.Weisheit and G.Bateman, "Monte-Carlo model of neutral particle transport in diverted plasmas", PPPL-1843, Princeton University (Jrnl. Comp. Phys., 46(2), 1982, 309).

[2.22] G.A.Emmert, "Modelling of bundle divertors", UWFDM-343, University of Wisconsin-Madison, January 1980.

[2.23] G.A.Emmert and A.W.Bailey, "Modelling of bundle divertors - II", UWFDM-365, University of Wisconsin-Madison, July 1980.

[2.24] A.W.Bailey and G.A.Emmert, "A theoretical model for hot plasma flowing to a wall with recycling", UWFDM-473, University of Wisconsin-Madison, May 1982.

[2.25]M.Shimada et al, "Impurity reduction and remote radiative cooling with single-null poloidal divertor in Doublet-III", Nucl. Fus., 22(5), 643 (1982).

[2.26]Y.Seki et al, "Numerical calculations of helium ash enrichment and exhaust by a simple divertor", Nucl. Fus., 20(10), 1213 (1980).

[2.27]F.Hinton and R.Hazeltine, Phys. Fluids, 17, 2236 (1974).

[2.28]C.E.Singer and W.D. Langer, "Axisymmetric tokamak scrape-off transport", PPPL-1920, Princeton University, August 1982.

[2.29]U.Daybelge, "Theory of asymmetric transport in the scrape-off layer of a poloidal divertor", Nucl. Fus., 21(12), 1589 (1981).

[2.30]C.Strawitch and G.Emmert, "Non-ambipolar transport in a magnetic divertor", University of Wisconsin, DOE-ET/53051-3, February 1980.

[2.31]C.Strawitch, "Plasma transport in a simulated magnetic divertor configuration", University of Wisconsin, DOE-ET/53051-20, March 1981.

[2.32]Various papers in "Symposium on energy removal and particle control in toroidal fusion devices", Princeton, July 1983 (to be published in Jrnl. of Nucl. Mat.).

Table 2.1: List of variables

a	Minor radius [m];
B	Magnetic field strength [T];
c_{sonic}	Local speed of sound [m/s];
$D_{\perp}$	Cross-field diffusion coefficient [m^2/s];
D_{Bohm}	Bohm diffusion coefficient, $D_{Bohm} = T_e/16eB$ [m^2/s];
$L_{\|\|}$	Half the average field line length between divertor/limiter plates [m];
m	Particle mass [kg];
n	Density [$1/m^3$];
q_D	Average number of toroidal turns before field line is diverted;
R_{major}	Major radius [m];
T	Temperature [J];
v_{flow}	Bulk flow speed [m/s];
Z	Atomic number;
$Z_{effective}$	Average atomic number;
δ	Scrape-off layer thickness [m];
Γ	Particle flux [$1/m^2$-s];
$\tau_{\|\|}$	Parallel flow time [s];

3.0 Atomic Processes and Data

A variety of atomic processes occur in the plasma/wall interaction region, ranging from interactions between the plasma and gas particles, to sputtering and reflection at the wall. An excellent review is given by McCracken and Stott [3.1]. This chapter concentrates on those processes important to particle and energy transport in the edge, justifies the subsequent choices for the dominant physics, and establishes a reasonably complete set of correlations for use in numerical analysis.

3.1 Plasma/Neutral Gas Interactions

The dominant processes of interest are the collisions occurring in the divertor chamber. In this analysis, impurity transport is neglected and we concentrate on solving hydrogen transport self-consistently since this will provide the background conditions for the much smaller impurity and helium concentrations. We will also not distinguish between deuterium or tritium, but rather use a representative hydrogenic atom with averaged properties.

3.1.1 Ionization, Charge Exchange and Dissociation

The primary species are H^+ and e from the main plasma and scrape-off layer, and H, H^+, H_2^+ and H_2 returning from the divertor target or neutralizer plate. A survey of the literature identified the reactions and corresponding cross-sections sketched in Figures 3.1 to 3.6. Figures 3.1 and 3.2 show ion-neutral collisions including charge exchange, impact ionization, and dissociation. Figures 3.3 and 3.4 show electron-ion interactions. These figures show that other species or excited states such as H^-, $H(2s)$ and H_3^+ can be formed. The subsequent interactions of these other species are indicated in Figures 3.5 and 3.6. Table 3.2 lists the reactions shown, with references. Particularly noteworthy data collections are Refs.[3.41,3.42,3.47,3.48].

In order to simplify subsequent calculations, only the dominant cross-sections are included in the analysis. The likely energy range for the different species is 1 eV to 10 keV, allowing for cold neutrals emitted from the wall up to hot ions escaping directly from the reactor core. Considering the ion-atom interactions (Figure 3.1 and 3.2), neglect, for example, $H^+ + H$ going to $2H^+$ when compared to the corresponding resonant charge exchange reaction. The former only dominates at tens of keV energies. Similarly, note

that the reactions which produce H^-, H(2s) or H_3^+ are less likely than reactions which produce H, H^+, H_2 and H_2^+, so we can neglect these particles. The biggest exception to this latter rule is the reaction $H_2^+ + H_2$ producing H_3^+ which, while the data was not entirely consistent, dominated over the corresponding charge exchange reaction at energies less than about 1 eV. Such low temperatures are not expected in the conditions examined in this study, though they could exist in gas target divertor concepts. Finally, as Figure 3.5 and 3.6 show, the reactions which convert the additional species to the more conventional ones have large cross-sections - often an order-of-magnitude larger than the corresponding conventional reactions. Thus H^-, H(2s) and H_3^+ are less likely to be produced and more likely to be consumed, and so are neglected as major contributors.

Thus, keeping the dominant ionization and charge exchange reactions plus several dissociation processes (for 10 eV $< T_i, T_e <$ 10 keV), the interactions are narrowed down to:

1) $e + H_2 \rightarrow H_2^+ + 2e$ electron impact ionization

2) $e + H_2 \rightarrow 2H + e$ electron impact dissociation

3) $e + H_2 \rightarrow H + H^+ + 2e$ electron impact dissociative ionization

4) $e + H_2^+ \rightarrow H + H^+ + e$ electron impact dissociation

5) $e + H_2^+ \rightarrow 2H$ electron impact dissociative recombination

6) $e + H \rightarrow H^+ + 2e$ electron impact ionization

7) $H_2^+ + H_2 \rightarrow H_2 + H_2^+$ resonant charge exchange

8) $H^+ + H \rightarrow H + H^+$ resonant charge exchange

The dissociation and ionization reactions (1) to (6) may also be caused by thermal energy or by photons. However, since the divertor neutral temperature will probably be below the activation energies (over 4.4 eV), thermal dissociation/ionization is unlikely. The Saha equation for a gas in thermal equilibrium gives this thermally ionized fraction as less than 10^{-3} for a $10^{19}/m^3$, 3 eV gas. And since there will be a high electron density in the divertor and the electron-induced reaction cross-sections are much larger than the photon-induced cross-sections, the electron impact processes are expected to dominate.

For these reactions, the cross-section shape gives a reasonable idea as to the energies involved. Reactions (1) to (4) occur with simultaneous electronic excitation and are governed by the Franck-Condon principle, i.e. the nuclei do not have time to change

nuclear spacing during the excitation so the electronic transition corresponds to a vertical jump between potential curves. Assuming the molecules start off in the ground state at the center of the molecular potential well (Figure 3.7), the energy for each reaction is easily estimated [3.5]. In particular, reaction (1) has a 15.5 eV threshold for H_2, D_2 and T_2 [3.50,3.52], with the product H_2^+ energy comparable to the reactant H_2 energy [3.51]; reaction (2) requires 9 eV for an electron impact reaction and 4.4 eV for thermal dissociation, with the electron impact dissociation energy split roughly evenly at 3 eV/H [3.52]; reaction (3) has a 28 eV threshold from the ground state and an 18 eV threshold from the $n = 2$ state, with the H^+ ion carrying off some fraction of the 15 eV of dissociation energy [3.51]; reaction (4) has a threshold of about 10 eV from lower vibrational states (which are believed to correspond to the bulk of H_2^+ in a plasma) [3.48]; reaction (5) is exothermic; and reaction (6) has an ionization threshold of 13.6 eV for H, D and T [3.52]. The charge exchange processes (7) and (8) are resonant so involve almost no energy transfer.

In order to perform fast calculations, functional fits to the cross-sections were developed. These correlations generally fit the data to within the variation in reported values (30%) where the cross-sections are largest, and have approximately correct scaling to higher and lower energies (unlike polynomial fits). Furthermore, while developed from protium data, the cross-sections are assumed valid for deuterium and tritium on the basis of interaction velocity. This is true for processes with no energy transfer (e.g. resonant charge exchange) where the important cross-section parameter is the interaction velocity since this determines how long the particles remain close [3.49]. It is approximately correct for electron impact processes where interaction energy is important, if the dominant energy source is the electrons [3.49]. In the present problem, we use distribution-averaged electron impact cross-sections and are largely concerned with cold gas and hot electron populations where this assumption is reasonable. References [3.29, 3.30, 3.34 and 3.35] have data on the effect of deuterium versus protium on several cross-sections, and support the above assumptions within the general accuracy of the data.

The correlations developed here are, where the reaction rate σv is in m^3/s and the interaction velocity v is in m/s,

$$(\sigma v)_1 = \frac{(7.57 \times 10^{-8} v)^{20.44}}{1 + (3.50 \times 10^{-7} v)^{18.7} + (3.15 \times 10^{-7} v)^{21.2}} \tag{3.1a}$$

$$(\sigma v)_2 = \frac{(1.78 \times 10^{-7} v)^{30}}{1 + (5.08 \times 10^{-7} v)^{29.6} + (4.60 \times 10^{-7} v)^{36}} \tag{3.1b}$$

$$(\sigma v)_3 = \frac{(3.48 \times 10^{-8} v)^{17}}{1 + (2.58 \times 10^{-7} v)^{14.6} + (2.26 \times 10^{-7} v)^{18.5}} \tag{3.1c}$$

$$(\sigma v)_4 = \frac{(1.69 \times 10^{-7} v)^{33}}{1 + (4.05 \times 10^{-7} v)^{33.6} + (4.10 \times 10^{-7} v)^{33}} \tag{3.1d}$$

$$(\sigma v)_5 = \frac{1.12 \times 10^{-6}}{v^{1.28}} \tag{3.1e}$$

$$(\sigma v)_6 = \frac{(5.32 \times 10^{-9} v)^{8.01} [1 + (4.0 \times 10^{-8} v)^{0.27}]}{1 + (2.6 \times 10^{-7} v)^{8.63}} \tag{3.1f}$$

$$(\sigma v)_7 = \frac{(1.481 \times 10^{-25} v)^{0.71}}{1 + (5.0 \times 10^{-7} v)^{9.5}} \tag{3.1g}$$

$$(\sigma v)_8 = \frac{(2.399 \times 10^{-30} v)^{0.5442}}{1 + (4.28 \times 10^{-7} v)^6} \tag{3.1h}$$

These cross-sections are needed to calculate collision reaction rates

$$n_i n_e \langle \sigma v \rangle = \int \int f_e(\underline{v}_e) f_i(\underline{v}_i) \, |\underline{v}_e - \underline{v}_i| \sigma(|\underline{v}_e - \underline{v}_i|) \, d^3 v_e d^3 v_i \tag{3.2}$$

where $\langle \sigma v \rangle$ is the distribution-averaged reaction rate coefficient. For the case of two interacting 3-D Maxwellian distributions, Eqn.(3.2) becomes

$$\langle \sigma v \rangle = 4\pi \left(\frac{M}{2\pi T} \right)^{3/2} \int_0^\infty v^3 \sigma(v) \, \exp(-\frac{M v^2}{2T}) \, dv \tag{3.3}$$

where

$$\frac{M}{T} = \frac{(m_i/T_i)(m_e/T_e)}{(m_i/T_i) + (m_e/T_e)} = \frac{m_e m_i}{m_e T_i + m_i T_e}$$

For $m_e/T_e \ll m_i/T_i$, this simplifies to

$$\langle \sigma v \rangle \simeq \int_0^\infty \sigma v(v) \left[4\pi \left(\frac{m_e}{2\pi T_e} \right)^{3/2} v^2 \exp(-\frac{1}{2} \frac{m_e v^2}{T_e}) \right] dv \tag{3.4}$$

Alternately, for non-Maxwellian ions we assume $|v_e - v_i| \simeq v_e$ (or $m_e/T_e \ll m_i/T_i$), which is reasonable even at comparable temperatures because of the large mass difference, so Eqn.(3.2) simplifies to

$$\langle \sigma v \rangle = \frac{1}{n_e n_i} \int f_i(v_i)\, d^3 v_i \int f_e(v_e)\, \sigma(v_e)\ v_e\ d^3 v_e \simeq \frac{1}{n_e} \int f_e(v_e) \sigma v(v_e) d^3 v_e$$

which is Eqn.(3.4) again if the electrons are Maxwellian.

After performing the integral at discrete temperatures, the integrated average cross-sections were curve-fitted to obtain, where $\langle \sigma v \rangle$ is in m^3/s and T_e is in eV,

$$\langle \sigma v \rangle_1 = \frac{(6.35 \times 10^{-4} T_e)^6}{1 + (0.146 T_e)^{5.15} + (0.078 T_e)^{6.4}} \tag{3.5a}$$

$$\langle \sigma v \rangle_2 = \frac{(0.00202 T_e)^{6.5}}{1 + (0.33 T_e)^{5.9} + (0.166 T_e)^{8.17}} \tag{3.5b}$$

$$\langle \sigma v \rangle_3 = \frac{(0.0006 T_e)^{7.01}}{1 + (0.109 T_e)^{5.5} + (0.056 T_e)^{7.58}} \tag{3.5c}$$

$$\langle \sigma v \rangle_4 = \frac{(0.00181 T_e)^{6.8}}{1 + (0.131 T_e)^{7.05} + (0.170 T_e)^{6.}} \tag{3.5d}$$

$$\langle \sigma v \rangle_5 = \frac{5.689 \times 10^{-14}}{T_e^{0.64}} \tag{3.5e}$$

$$\langle \sigma v \rangle_6 = \frac{(2.94 \times 10^{-5} T_e)^4}{1 + (0.099 T_e)^{3.1} + (0.059 T_e)^{4.25}} \tag{3.5f}$$

The cross-section curves Eqns.(3.1) and (3.5) are shown in Figures 3.8 to 3.14. For comparison, fitted curves to the data are also shown, from Refs.[3.48] and [3.52]. Reference [3.48] gives error estimates of $\pm$ 50%, 30%, 50% and 10%, for the cross-section data of reactions (2) to (5); Ref.[3.52] gives 7% as estimated error for the reaction (6) data.

3.1.2 Recombination

For very cold ($T_e < 5$ eV) ion-neutral gas mixtures, recombination processes can be particularly important. There are five primary mechanisms, each describing the way the energy released by the recombination is carried away [3.61]:

(1) $e + A^+ \rightarrow A^* + h\nu$ collisional-radiative recombination;

(2) $e + A^+ + e \rightarrow A + e$ electron three-body recombination;

(3) $e + A^+ + B \rightarrow A + B$ heavy particle three-body recombination;

(4) $e + (AB)^+ \rightarrow A + B$ dissociative recombination;

(5) $e + A^+ \rightarrow A^{**} \rightarrow A^* + h\nu$ dielectronic recombination.

where A^+ is the initial ion and charge, A^* is an excited state, and $h\nu$ represents photons.

The radiative recombination rate is [3.62],

$$\langle \sigma v \rangle [m^3/s] \simeq \frac{3.61 \times 10^{-19}}{T_e[eV]^{0.754}} \tag{3.6}$$

for $n_e < 10^{20}/\text{m}^3$ and 1 eV $< T_e <$ 6 eV. At lower temperatures, electron density effects become significant. Above 6 eV, there is a scarcity of data, although Ref.[3.71] gives $\langle \sigma v \rangle \simeq 2.7 \times 10^{-19}/T_e^{0.5}$ at much higher temperatures (10 – 150 keV) in reasonable agreement with Eqn.(3.6). However, above several eV, ionization reactions are far more likely anyway.

Representative values for the three-body processes at $n_e \approx 10^{18}/\text{m}^3$ or $n_{H_2} \approx 2 \times 10^{25}/\text{m}^3$ (e.g., 300 K temperature, 0.1 MPa pressure) are around 10^{-7} m^3/s. Under divertor conditions, the electron three-body process should be larger than the heavy particle three-body process, and has a scaling relation given by

$$\langle \sigma v \rangle [m^3/s] \simeq \frac{5.56 \times 10^{-39} n_e[1/m^3]}{T_e[eV]^{4.5}} \tag{3.7}$$

which agrees with data for $T_e <$ 0.3 eV.

The dissociative recombination process and its reaction rate were discussed in the previous section (Section 3.1.1). This is a particularly effective way to handle the recombination energy, as illustrated by the large cross-section.

In dielectronic recombination, the result is a neutral atom with two simultaneously excited electrons. It is often unstable and shortly decays with the emission of a photon. It is not a possible mechanism for hydrogen recombination.

None of these processes are likely at high temperatures. Under plausible low-temperature, high density divertor scenarios ($T_{H+} \approx$ 25 eV, $T_H \approx T_e \approx$ 3 eV, $n_e, n_{H+}, n_H \approx 10^{18}/\text{m}^3$), the dominant recombination processes are dissociative and

collisional-radiative recombination. However, even these processes are not the principle reactions until the plasma gets much colder.

3.1.3 Elastic Scattering

Energy may also be transferred by elastic collisions. Given the five particles being considered (e, H, H^+, H_2 and H_2^+), there are fifteen possible elastic scattering processes. Six of these are between charged particles, six are charged/neutral collisions, and three are between neutrals.

The total, momentum and energy transfer cross-sections are [3.64]

$$\sigma_t = 2\pi \int_0^\pi \sigma \sin\theta \, d\theta \tag{3.8a}$$

$$\sigma_m = 2\pi \int_0^\pi \sigma(1 - \cos\theta) \sin\theta \, d\theta \tag{3.8b}$$

$$\sigma_E = 2\pi \int_0^\pi \sigma \sin^3\theta \, d\theta \tag{3.8c}$$

where θ is the scattering angle in the center-of-mass system. Neutral collisions are often approximated as hard elastic sphere scattering. With diameter d, the cross-sections evaluate to $\sigma_t = \pi d^2$, $\sigma_m = \pi d^2$, and $\sigma_E = 2\pi d^2/3$. For a mixture of particles, $d = (d_1 + d_2)/2$. Since $d_H = 1.0 \times 10^{-10}$ m and $d_{H_2} = 2.74 \times 10^{-10}$ m [3.69], this implies the energy transfer cross-section is $\sigma_E \simeq 2 \times 10^{-20}$ m^2.

The exact differential collision cross-section, $\sigma = \sigma(\theta, E)$, depends on the form of the interaction between the particles. For charged particle collisions, the long-range interaction is the Coulomb potential $V(r) \approx 1/r$; for charged/neutral collisions, it is by an induced dipole (or polarization) mechanism, $V(r) \approx 1/r^4$; and for neutral-neutral collisions, it is the Van der Waals force (instantaneous dipole of one neutral reacting with the induced dipole of the other neutral), $V(r) \approx 1/r^6$.

The Coulomb collision cross-section for a 90° deflection is [3.63],

$$\sigma_m = \frac{e^4 \ln \Lambda}{18\pi (\epsilon_0 T)^2} \tag{3.9}$$

where T is the effective temperature for different interacting particles,

$$T = \frac{m_1 T_2 + m_2 T_1}{m_1 + m_2}$$

and $\ln \Lambda$ is the Coulomb logarithm, which for ions in charge state Z_1 in a plasma with charge state Z_2 and density n_2 is

$$\ln \Lambda \simeq \ln \left[12\pi \left(\frac{(\epsilon_0 T)^3}{n_2 Z_1^2 Z_2^{\frac{1}{2}} e^4} \right)^{0.5} \right]$$

Typical values for $\ln \Lambda$ in a fusion plasma are about 15 - 20. The energy transferred in a 90° deflection is about $\Delta E/E_{initial} \simeq 2m_1 m_2/(m_1 + m_2)^2$, so the energy transfer cross-section is approximately (Figure 3.15)

$$\sigma_E \simeq \frac{e^4 \ln \Lambda}{18\pi \epsilon_0^2 T^2} \frac{4m_1 m_2}{(m_1 + m_2)^2} \tag{3.10}$$

The charged particle/neutral scattering cross-section is underestimated by the hard sphere model. Experiments and more detailed theoretical models yield the results shown in Figure 3.15. The $e + H$ cross-section is from Ref.[3.62], $e + H_2$ from [3.65], $H^+ + H$ from Ref.[3.68], $H^+ + H_2$ from Ref.[3.79], $H_2^+ + H_2$ from Ref.[3.79], $H + H$ from Ref.[3.41], and $H + H_2$ from Ref.[3.41].

3.2 Surface Reactions

The basic reactions between incident particles and a solid surface are absorption, reflection and sputtering. The extent to which any of these happen is a function of surface conditions, and the type and energy of the incoming particles.

3.2.1 Absorption

Condensation occurs when an atom or molecule condenses out of the vapor phase onto a substrate surface composed of like particles. An arbitrarily thick layer can build up if the surface temperature is appropriate for the phase change. For a temperature of 10K, 65% of incident N_2, 68% Ar and 75% CO_2 will stick to their own frozen deposits. For sufficiently low temperatures, almost all particles striking the surface stick. The degree of pumping achieved in this manner, however, is limited by the vapor pressure of the condensing gas.

Physisorption occurs when incident particles are trapped by a Van der Waals surface attraction. Typically only a monolayer can be absorbed this way. It is only likely if the surface is very clean and the particle energy is low compared with the surface binding energy, for example, 1.7 eV for H_2 on molybdenum or tungsten, 1.2 eV on nickel. Particles may also be physically trapped in the surface if their initial kinetic energy or direction carries them deep into the material.

Chemisorption involves chemical bonding of the incident particle with the substrate. Typical binding energies are on the order of several eV. This effect also saturates as the accessible substrate atoms become reacted.

Surface migration occurs when the incident particle, after physisorption or physical penetration of the surface, is able to diffuse away from the surface and into the bulk material. This depends on the gas solubility and diffusion coefficient in the solid. In practice, only the lighter atoms (hydrogen and helium) are able to diffuse to any measurable extent. Furthermore, helium (and the other noble gases) are insoluble in metals.

A common application of absorption is getter pumping where a layer of absorbing material is deposited. For hydrogen, titanium gettering is popular. The sticking coefficients are 0.06 for H_2 at 300 K (0.04 at 78 K) and 0.1 for D_2 (0.2). The surface saturates around $7 - 100 \times 10^{19}$ molecules/m^2 for H_2 and $6 - 11 \times 10^{15}$ molecules/m^2 for D_2 over the same temperature range [3.69].

3.2.2 Reflection and Desorption

Some fraction of the incident particles are immediately reflected from the divertor neutralizer plate. The remainder bury themselves into the surface and diffuse out as neutral hydrogen molecules with energies characteristic of the wall surface temperature or are knocked out by subsequent incident particles or radiation [3.75]. There have been several studies of the number and energy of the backscattered particles, including Refs.[3.56 - 3.60,3.79]. Much of the experimental work is for energies greater than 1 keV and for normal incidence.

The fraction of particles backscattered R_N and fraction of energy backscattered R_E are usually correlated against a reduced incident energy ϵ, where

$$\epsilon = \frac{0.0325 E_0 A}{Z_0 Z_w (Z_0^{0.5} + Z_w^{0.67})(A_0 + A_w)} \tag{3.11}$$

Z and A are the atomic number and mass, subscripts 0 and w refer to the incident particle

and wall material. For H^+ on iron, for example, $\epsilon = 3.91 \times 10^{-4} E_0$[eV]. Tabata et al [3.56] correlated a wide set of experimental conditions and obtained a fairly complicated expression that was accurate to about 25% for R_N and 15% for R_E for D^+ incident particles with $0.001 < \epsilon < 100$. A much simpler set of relations is

$$R_N \simeq -0.10 \ln\left(\frac{7\epsilon}{\epsilon + 7}\right) + 0.20 \tag{3.12a}$$

$$\frac{R_E}{R_N} \simeq -0.0716 \ln\left(\frac{140\epsilon}{\epsilon + 140}\right) + 0.355 \tag{3.12b}$$

These equations are derived from normal incidence data compiled by McCracken and Stott [3.1]. They are very similar to the equations used by Seki et al [3.77] and Heifetz et al [3.78], except that they apply to all materials and are adjusted to go smoothly to zero as the energy becomes large. For incident energies less than the surface binding energy (a few eV), all particles are absorbed and must thermally desorb.

For angles away from normal, R_N increases to unity as θ approaches 90°. This may be roughly accounted for by including an angular dependence

$$R_N \simeq R_{N,90} \frac{\theta}{90°} + R_{N,0}\left(1 - \frac{\theta}{90°}\right) \tag{3.12c}$$

where $R_{N,90} \simeq 1$ and $R_{N,0}$ is given by Eqn.(3.12a).

The average energy of the reflected particles E is simply $\overline{E} = R_E E_0 / R_N$, although the actual energy distribution of backscattered particles has a pronounced peak at an energy lower than $\overline{E}$ followed by a long tail up to E_0 [3.57–3.59]. For example, the peak is at 1.5 keV for 18 keV H^+ on niobium compared with $\overline{E} \approx$ 4.6 keV [3.58]. A very approximate expression for the reflected energy distribution for normally incident particles is [3.76]

$$f(E) = \frac{2E}{(E_p^2 + E^2) \ln\left[1 + (E_0/E_p)^2\right]}; \quad E < E_0 \tag{3.13}$$

where $E_p \approx 0.3 R_E E_0 / R_N$ is the peak energy. No angular variation is included here because of lack of data. However, some data [3.58] is consistent with this general form for the energy distribution at all emergence angles.

The fraction of particles reflected charged (as opposed to reflected neutral) increases roughly linearly with reflected particle energy. For backscattered particle energies of less than 1 keV, over 99% of the reflected particles should be uncharged [3.1,3.58].

3.2.3 Sputtering

A primary source of impurities in fusion reactors (and current experiments) is the sputtering of wall, limiter or divertor material under the bombardment of energetic particles. Much data has been accumulated relating the incident particle characteristics to the resulting sputtering. In general, sputtering yield peaks at low Z incident particle energies of around 1 keV, falling to less than 0.01 sputtered atom per incident particle at energies below (roughly) 100 eV and above 10 keV.

A theoretical model (the Sigmund equation) for sputtering predicts that yield is proportional to the elastic stopping power of the target for a given incident particle, and inversely proportional to the target material surface binding energy. In addition, there is a threshold energy, possibly related to threshold effect in displacing atoms at crystal surfaces and lattice points [3.54]. Beyond these observations, sputtering yield is correlated by a variety of semi-empirical equations. Data tabulations and correlations can be found in Refs.[3.2,3.54]. It should be noted that experimental results and correlations often agree only within a factor of two.

A recent model for the sputtering yield, including mass, energy and angular dependencies and some evaluation of the often inconsistent data, is [3.2]

$$S(E_0,\theta) = S_1(E_0)S_2(\theta) \tag{3.14}$$

where S is the total sputtering yield, E_0 is the incident particle energy and θ is the angle from the surface normal. The energy-dependent sputtering yield term is

$$S_1(\theta) = \frac{C}{U_w} Z_0^{0.75}(Z_w - 1.8)^2\left(\frac{A_0 - 0.8}{A_w}\right)^{1.5} \frac{(E_0 - E_{th})}{(E_0 - E_{th} + 50Z_0^{0.75}Z_w)^2} \tag{3.15a}$$

and the angle-dependent sputtering yield term is

$$S_2(\theta) = \frac{1}{[\cos\theta]^f} \tag{3.15b}$$

where C is a constant, U_w is wall material binding energy (eV), and E_{th} is the sputtering threshold energy

$$E_{th} = \frac{(4A_0 + A_w)^2}{4A_0A_w} U_w$$

and f is

$$f = \frac{1}{(20Z_0)^{0.5}}\left(\frac{A_w}{A_0}\right)^{0.25}(E_0 - 4E_{th})^{0.25}(1 - \frac{\theta}{90°})^{0.5}$$

Typical values for the constants are $C = 400$ (2000 for H only), and U_w = 7.4 for carbon, 3.4 aluminum, 2.9 titanium, 4.3 iron, 7.8 molybdenum and 11.1 tungsten. The angle dependence is recommended for $E_0 \geq 4E_{th}$ and $0° < \theta \leq 89°$; otherwise $S_2(\theta) = 1$ for $E_0 < 4E_{th}$, and $S_2(\theta) = 0$ for $\theta > 89°$ is suggested.

3.3 Radiation

Radiation is an important energy loss mechanism in plasmas. Under fusion plasma conditions, the primary mechanisms for emission of electromagnetic radiation are the interaction of the charged particles with the electric and magnetic fields (cyclotron and bremsstrahlung radiation) and from electron shell transitions (line and recombination radiation).

Bremsstrahlung arises from the collisional deceleration of charged particles, where the photons carry away the lost collision energy. In non-relativistic situations, ion-electron collisions dominate. A reasonable correlation for the radiated power is [3.63]

$$Q_{brem}[W/m^3] = 4.8 \times 10^{-37} z^2 \, n_i \, n_e \, T_e^{0.5} \tag{3.16}$$

where n_i, n_e are 1/m^3; T_e is in keV; $z^2 = \sum n_i z_i^2 / n_e$; $n_e = \sum n_i z_i$; n_i is the ion density and z_i is the charge state of the ion.

Cyclotron radiation is emitted by particles accelerated in a magnetic field, and primarily arises from electrons spiralling along the field lines. The calculation of total radiated power is complex since it involves relativistic effects, and absorption, emission and reflection of the radiation within the plasma and at the vacuum chamber wall. Typical correlations involve a basic emission term for Maxwellian electrons and a correction for a remaining factors [3.63,3.66,3.70],

$$Q_{cycl}[W/m^3] = 6.2 \times 10^{-17} B^2 n_e T_e f_{cycl} \tag{3.17}$$

where n_e and T_e are as above, B is magnetic field in Tesla, and f_{cycl} is a parameter that depends on the optical thickness of the plasma. Most fusion core plasmas are optically

thick, and the radiated power is limited to the blackbody level at the cyclotron harmonics. A typical assumption is $f_{cycl} \approx 1 + 0.05T_e[keV]$. The exact behavior is not critical here since cyclotron radiation is not an important energy loss mechanism in edge plasmas.

Line and recombination radiation is such a significant power loss mechanism under fusion plasma conditions that impurity control is a primary goal for divertor/exhaust systems. Line radiation occurs when excited electrons return to lower energy states. Recombination radiation is similar, but occurs with the capture of a free electron by a plasma ion. In general, impurities in a hot plasma will have a complex distribution of electron states, and the resulting radiation depends on the relative strengths of the processes that populate or depopulate the electron energy levels. Detailed radiated power calculations have been performed for the case of "coronal equilibrium" and "local thermodynamic equilibrium (LTE)", where the time scales for the atomic processes are short compared to other time scales and spatial gradients are small [3.67]. LTE applies more to dense, cold, collision dominated plasmas while coronal equilibrium requires that radiative decay be balanced by electron excitation collisions. Typical values of $Q_{line}/n_i n_e$ and ionic charge state z_i from the coronal equilibrium model are given in Tables 3.3 and 3.4 for a range of atoms from helium to xenon.

If the charge states are not in equilibrium, the radiated power may be much larger (factors of 10 - 100) since the impurities are likely in lower ionization states with a consequent increase in the excitation rates. Coronal equilibrium applies if $n_e\tau_p \gg 10^{18}$ s/m^3 where τ_p is the particle confinement time [3.74,3.81].

Line radiation from excited states of neutral hydrogen can be accounted for with an empirical function that assigns an enhanced value to the ionization energy, the excess being the radiated excitation energy prior to ionization

$$E_{ionization}[eV] = 17.5 + \left(5. + \frac{37.5}{T_e[eV]}\right)\log_{10}\left(\frac{10^{21}}{n_e[1/m^3] + 10^{17}}\right) \qquad (3.18)$$

This expression, slightly modified from Ref.[3.72], is a fit to calculations by McWhirter and Hearn [3.80]. It is primarily valid (30%) for $n_e < 10^{22}$/m^3 and $2 < T_e < 30$ eV, although it provides approximate scaling outside these bounds as long as $E_{ionization} \geq 13.6$ eV.

3.4 References

[3.1] G.McCracken and P.E.Stott, "Plasma-surface interactions in tokamaks", Nucl. Fus., 19,(7), 1979, 889.

[3.2] D.Smith, J.Brooks and D.Post, "A physical sputtering code for fusion applications", 9th Symp. of Eng. Problems of Fusion Research, Chicago, October 1981.

[3.3] M.Venugopalan, "Reactions under plasma conditions", Vol.2, Wiley-Interscience, New York, 1971, p.35.

[3.4] B.Peart and K.Dolder, "Measurements of cross-sections for the production of protons by collisions between electrons and vibrationally de-excited H_3^+ ions", Jrnl. Phys. B: At. Mol. Phys., 8(8), L143 (1975).

[3.5] E.W.McDaniel, "Collision phenomena in ionized gases", Wiley & Sons, New York, 1964.

[3.6] H.Tawara, "Charge transfer of hydrogen beams in gases and vapors", Atom. Data and Nucl. Data Tables, 22(6), 493 (1978).

[3.7] M.F.A. Harrison, "The relevance of atomic processes to magnetic confinement and the concept of a tokamak reactor", p.15, in M.McDowell and A.Ferendeci (eds.), "Atomic and molecular processes in controlled thermonuclear fusion", Plenum Press, New York, 1980.

[3.8] F.J.DeHeer, "Experiments on electron capture and ionization by ions", p.351, in M.McDowell and A.Ferendeci(eds.), "Atomic and molecular processes in controlled thermonuclear fusion", Plenum Press, New York, 1980.

[3.9] H.W.Drawin, "Thermalization and exhaust of helium in a future thermonuclear reactor: partly an atomic physics problem", in M.McDowell and A.Ferendeci (eds.), "Atomic and molecular processes in controlled thermonuclear fusion", Plenum Press, New York, 1980.

[3.10]B.Peart and K.T.Dolder, Jrnl. Phys. B: At. Mol. Phys., 5,1554 (1972).

[3.11]B.Peart and K.T.Dolder, Jrnl. Phys. B: At. Mol. Phys., 6, 2409 (1973).

[3.12]B.Peart and K.T.Dolder, Jrnl. of Phys. B: At. Mol. Phys., 7, 236 (1974).

[3.13]B.Peart and K.T.Dolder, Jrnl. of Phys. B: At. Mol.Phys., 5, 860 (1972).

[3.14]B.Peart and K.T.Dolder, Jrnl. of Phys. B: At. Mol. Phys., 8, 1570 (1975).

[3.15]B.Peart and K.T.Dolder, Jrnl. of Phys. B: At. Mol. Phys., 7(14), 1948 (1974).

[3.16]B.Peart and K.T.Dolder, Jrnl. of Phys. B: At. Mol. Phys., 7(12), 1567 (1974).

[3.17]Y.Band, Jrnl. of Phys. B: At. Mol. Phys., 7(15), 2055 (1974).

[3.18]P.Defrance, W.Claeys, A.Cornet and G.Poulaert, "Electron impact ionization of metastable atomic hydrogen", Jrnl. Phys. B: At. Mol. Phys., 14, 111 (1981).

[3.19]M.B.Shah, J.Geddes and H.B.Gilbody,"Absolute cross-sections for H(2s) formation in electron capture by protons in gases", Jrnl. Phys. B: At. Mol. Phys., 13, 4049 (1980).

[3.20]J.D.Argyros,"Photodissociation of H_2^+: variation with temperature", Jrnl. Phys. B: At. Mol. Phys., 7(15), 2025 (1974).

[3.21]S.Saha, K.K.Datta, D.Basv and A.K.Barua, "Photodissociation of H_2^+ by the $1s\sigma_g = 2p\pi_u$ transition", Jrnl. Phys. B: At. Mol. Phys., 13, 3755 (1980).

[3.22]B.Peart and R.A.Forrest, "Measurement of cross-sections for double-charge transfer in collisions between H^+ and H^- ions", Jrnl. Phys. B: At. Mol. Phys., 12(1), L23 (1979).

[3.23]D.W.Vance and T.L.Bailey, "Inelastic collisions of H_2^+ and N_2^+ ions with hydrogen molecules", Jrnl. Che. Phys., 44(2) 486 (1966).

[3.24]W.L.Fite, R.Stebbings, D.Hummer and R.Brackman, "Ionization and charge transfer in p-H collisions", Phys. Rev., 119(2), 663 (1960).

[3.25]D.G.Hummer et al, "Charge transfer and electron production in $H^- + H$", Phys. Rev., 119(2), 667 (1960).

[3.26]R.Curran, T.M.Donahue and W.H,Kasner, "Charge transfer for protons in H_2^+", Phys. Rev., 114(2), (1959).

[3.27]G.W.McClure, "Charge exchange and dissociation of H^+, H_2^+ and H_3^+ ions incident on H_2 gas", Phys. Rev., 130(5), 1855 (1963).

[3.28]B.Peart, D.S.Walton and K.T.Dolder, "Measurement of the formation of H^+ from H^- ions by electron impact", Jrnl. Phys. B: At. Mol. Phys., 4, 88 (1971).

[3.29]D.Rapp and P.Englander-Golden, "Ionization by electron impact", Jrnl. Che. Phys., 43(5), 1464 (1965).

[3.30]W.Cramer, Jrnl. Che. Phys., 35(3), 836 (1961).

[3.31]B.Peart, R.Grey and K. Dolder, Jrnl. Phys. B: At. Mol. Phys., 9(17), (1976).

[3.32]H.Rosenstocke et al, "Energetics of gaseous ions", Jrnl. of Phys. and Chem. Ref.

Data, Vol.6, Supp. Nbr. 1, 1977.

[3.33]W.Fite, R.Stebbings and R.Brackman, Phys. Rev., 116(2), 356 (1959).

[3.34]W.Fite, T.Brackman and W.Snow, Phys. Rev., 112(4), 1161 (1958).

[3.35]E.Salvotelli, G.Lantschner and W.Mechback, Jrnl. Phys. B: At. Mol. Phys., 2, 772 (1969).

[3.36]R.Stebbings, W.Fite, D.Hummer and R.Brackman, Phys. Rev., 119(6), 1939 (1960).

[3.37]O.Bely and S.Schwartz, Jrnl. Phys. B: At. Mol. Phys., 2, 159 (1969).

[3.38]D.S.Walter, B.Peart and K. Dolder, Jrnl. Phys. B: At. Mol. Phys., 3, L149 (1970).

[3.39]A.Salin, Jrnl. Phys. B: At. Mol. Phys., 2, 631 (1969).

[3.40]C.Latimer, R.Browning and H.Gilbody, Jrnl. Phys. B: At. Mol. Phys., 2, 1655 (1969).

[3.41]C.F.Barnett et al, "Atomic data for controlled fusion research", ORNL-5207, Feb 1977.

[3.42]C.F.Barnett et al, "Atomic data for controlled fusion research", ORNL-5206, Vol. 1, Feb 1977.

[3.43]R.Neynaber and S.Trujillo, Phys. Rev., 167(1), 63 (1968).

[3.44]C.Giese and W.Maier II, Jrnl. Che. Phys., 39(3), 739 (1963).

[3.45]M.Saporoschenko, Jrnl. Che. Phys., 42(8), 2760 (1965).

[3.46]S.Corrigan, Jrnl: Che. Phys., 43(12), 4381 (1965).

[3.47]H.Massey, E.Burhap and H.Gilbody, "Electronic and ionic impact phenomena", 2nd ed., Vol.II, Oxford University Press, London, 1969.

[3.48]E.M.Jones, "Atomic collision processes in plasma physics experiments: analytic expressions for selected cross-sections and Maxwellian rate coefficients", CLM-R 175, UKAEA, September 1977.

[3.49]D.J.Rose and M.Clark Jr., "Plasmas and controlled fusion", M.I.T. Press, Cambridge, 1961.

[3.50]D.Briglia and D.Rapp, "Ionization of H_2^+ by electron impact near threshold", Jrnl. Che. Phys., 42(9), 3201 (1965).

[3.51]D.Rapp, P.Englander-Golden and D.Briglia, "Cross-sections for dissociative ionization of molecules by electron impact", 42(12), 4081 (1965).

[3.52]E.R.Muller, K.Behringer and H.Niedermeyer, "Total radiation losses and energy balance for ohmically heated divertor discharges in ASDEX", Max-Planck-Institut fur

Plasmaphysik, IPP III/74, December 1981.

[3.53]K.Bell et al, "Atomic and molecular data for fusion, Part 1: Recommended cross-sections and rates for electron ionization of light atoms and ions", CLM-R216, UKAEA, December 1981.

[3.54]N.Matsunami et al, "Energy dependence of sputtering yields of monatomic solids", IPPJ-AM-14, Nagoya University, Japan, June 1980.

[3.55]Y.Kaneko et al, "Cross-sections for charge transfer collisions involving hydrogen reactions", IPPJ-AM-15, Nagoya University, Japan, October 1980.

[3.56]T.Tabata et al, "Data on the backscattering coefficients of light ions from solids", IPPJ-AM-18, Nagoya University, Japan, October 1981.

[3.57]S.H.Overbury et al, "Energy and angular distributions of low energy H^+ and D^+ backscattered from polycrystalline carbon", Jrnl. of Nucl. Mat., 93 & 94 (1980) 529.

[3.58]P.Meischner and H.Verbeek, "Energy distribution of charged and neutral hydrogen atoms backscattered from metal surfaces bombarded with 5 to 18 keV protons", Jrnl. of Nucl. Mat., 53 (1974) 276.

[3.59]G.McCracken and N.Freeman, "Backscattering of keV hydrogen ions in solids", J. Phys. B (AMP), 2 (1969) 661.

[3.60]W.Eckstein and H.Verbeek, "Reflection of hydrogen from stainless steel for non-normal incidence", Jrnl. of Nucl. Mat., 93 & 94 (1980) 518.

[3.61]M.Mitchner and C.Kruger, "Partially ionized gases", J.Wiley and Sons, New York (1973).

[3.62]D.R.Bates (ed.), "Atomic and molecular processes", Academic Press, New York (1962).

[3.63]W.Stacey,Jr., "Fusion plasma analysis", J.Wiley and Sons, New York (1981).

[3.64]W.Vincenti and C.Kruger, "Introduction to physical gas dynamics", J.Wiley and Sons, New York (1967).

[3.65]M.Hayashi, "Recommended values of transport cross-sections for elastic collision and total collision cross-section for electrons in atomic and molecular gases", IPPJ-AM-19, Inst. of Plasma Phys., Nagoya Univ., Japan, November 1981.

[3.66]G.Bekefi and A.Barrett, "Electromagnetic vibrations, waves and radiation", MIT Press, Cambridge Massachusetts, (1977).

[3.67]D.Post et al, "Steady-state radiative cooling rates for low-density high-temperature plasmas", PPPL-1352, Princeton University, July 1977.

[3.68]V.Franco and B.Thomas, "Elastic and inelastic scattering of protons by hydrogen atoms", Phys. Rev. A, 4(3), 1971, 945.

[3.69]G.Weissler and R.Carlson (eds.), "Methods of experimental physics: Vol. 14, Vacuum Physics and Technology", Academic Press, New York (1979).

[3.70]R.Byrne et al, "Tokamak reactor codes: MAK0 and MAK1", EPRI ER-1032, March 1979.

[3.71]D.L.Book, "NRL plasma formulary", Naval Research Laboratory, 1978.

[3.72]P.J.Harbour and J.G.Morgan, "Models and codes for the plasma edge region", CLM-R234, Culham Laboratory, December 1982.

[3.73]A.C.Riviere, "Penetration of fast hydrogen atoms into a fusion reactor plasma", Nucl. Fus., 11, 1971, 363.

[3.74]P.Carolan and V.Piotrowicz, "The behaviour of impurities out of coronal equilibrium", CLM-P672, Culham Laboratory, UKAEA, June 1982.

[3.75]A.Koma (ed.), "Desorption and related phenomena relevant to fusion devices", IPPJ-AM-22, Nagoya University, Japan, April 1982.

[3.76]N.Itoh and E.Thomas (eds.), "Surface data for fusion devices", IPPJ-AM-21, Nagoya University, Japan, December 1981.

[3.77]Y.Seki et al, "Numerical calculations of helium ash enrichment and exhaust by a simple divertor", Nucl. Fus., 20,(10), 1980, 1213.

[3.78]D.Heifetz et al, "A Monte Carlo model of neutral particle transport in diverted plasmas", PPPL-1843, Princeton University (Jrnl. Comp. Phys. 46(2), 1982, 309).

[3.79]S.C.Brown, "Basic data of plasma physics", 2nd ed., MIT Press, 1966.

[3.80]R.McWhirter and A.Hearn, "A calculation of the instantaneous population densities of the excited levels of hydrogen-like ions in a plasma", Proc. Phys. Soc., 82 (1963), 641.

[3.81]D.E.Roberts,"Total impurity radiation power losses from steady-state tokamak plasmas", Nucl. Fus., 21(2), 1981, 214.

Table 3.1: List of variables

A	Atomic mass;
B	Magnetic field strength [T];
d	Atomic diameter [m];
e	Electron charge, 1.6×10^{-19} C;
E	Energy [J];
$f(\underline{v})$	Distribution function [s/m^4];
m	Particle mass [kg];
M	Effective particle mass [kg];
n	Density [1/m^3];
Q	Power density [W/m^3];
R_N	Particle reflection coefficient;
R_E	Energy reflection coefficient;
S	Sputtering coefficient;
T	Temperature [J];
U_w	Wall surface binding energy [J];
v	Velocity [m/s];
z	Atomic charge;
Z	Atomic number;
ϵ	Reduced energy;
ϵ_0	Permittivity of free space, 8.854×10^{-12} C/V-m;
σ	Reaction cross-section [m^2];
$\ln \Lambda$	Coulomb logarithm;

Table 3.2: Major reactions and references

$H + H_2 \rightarrow H^+ + H_2 + e$	3.5, 3.6, 3.79
$H + H_2 \rightarrow H(2s, 2p, 3s, 3p, 3d) + H_2$	3.42
$H + H_2 \rightarrow H^- + H_2^+$	3.5, 3.6
$H^+ + H_2 \rightarrow H + H_2^+$	3.5, 3.6, 3.17, 3.26, 3.27, 3.34, 3.79
$H^+ + H_2 \rightarrow H^- + H_2^{2+}$	3.5, 3.6
$H^+ + H_2 \rightarrow H^+ + H_2^+ + e$	3.5
$H^+ + H_2 \rightarrow H(2s) + H_2^+$	3.17, 3.19
$H^+ + H \rightarrow 2H^+ + e$	3.7, 3.8, 3.9, 3.24, 3.34, 3.39, 3.55
$H^+ + H \rightarrow H + H^+$	3.5, 3.7, 3.8, 3.9, 3.24, 3.34, 3.55, 3.79
$H_2^+ + H \rightarrow H_2 + H^+$	3.34
$H_2^+ + H_2 \rightarrow H_2 + H_2^+$	3.5, 3.23, 3.27, 3.34, 3.40, 3.79
$H_2^+ + H_2 \rightarrow H_3^+ + H + 1.9eV$	3.23, 3.42, 3.43, 3.44, 3.45, 3.79
$H_2^+ + H_2 \rightarrow H_2 + H + H^+$	3.5, 3.23, 3.27, 3.79
$e + H \rightarrow H^+ + 2e$	3.5, 3.9, 3.24, 3.48
$e + H \rightarrow H(2s) + e$	3.36
$e + H(2s) \rightarrow H^+ + 2e$	3.18
$e + H_2 \rightarrow H^+ + H + 2e$	3.41, 3.48, 3.79
$e + H_2 \rightarrow 2H^+ + 3e$	3.41, 3.47, 3.48, 3.79
$e + H_2 \rightarrow H^- + H^+ + e$	3.3
$e + H_2 \rightarrow H_2^+ + 2e$	3.5, 3.29, 3.38, 3.48
$e + H_2 \rightarrow 2H + e$	3.41, 3.46, 3.47, 3.48
$e + H_2 \rightarrow H + H(2s, 2p, n = 3, 4) + e$	3.41
$e + H_2^+ \rightarrow H + H^+ + e$	3.10, 3.13, 3.33, 3.41, 3.47, 3.48
$e + H_2^+ \rightarrow H^+ + H^-$	3.14
$e + H_2^+ \rightarrow 2H + e$	3.12, 3.48
$e + H_2^+ \rightarrow 2H^+ + 2e$	3.11, 3.41, 3.48
$H^- + H_2 \rightarrow H^+ + H_2 + 2e$	3.5, 3.6
$H^- + H_2 \rightarrow H + H_2 + e$	3.5, 3.6
$H^+ + H^- \rightarrow H^- + H^+$	3.22
$H^+ + H^- \rightarrow 2H$	3.22, 3.31
$H^+ + H^- \rightarrow H^+ + H + e$	3.31
$H^- + H \rightarrow H + H^-$	3.25, 3.55
$H^- + H \rightarrow 2H + e$	3.25
$H_3^+ + H_2 \rightarrow H(3s) + H_2^+ + H_2$	3.42
$H_3^+ + H_2 \rightarrow H, H_2, H^+, H_2^+, e$	3.27, 3.41
$e + H^- \rightarrow H^+ + 3e$	3.28
$e + H^- \rightarrow H + 2e$	3.28, 3.37, 3.38
$e + H_3^+ \rightarrow 3H$	3.15, 3.41, 3.48
$e + H_3^+ \rightarrow 2H + H^+ + e$	3.4, 3.16, 3.48
$h\nu + H_2^+ \rightarrow dissociates$	3.20, 3.21

Table 3.3: Line radiation rates $Q_{line}/n_i n_e$ [$\times 10^{-35}$ W·m^3] for selected atoms [3.67].

	Helium	Beryllium	Oxygen	Argon	Iron	Molybdenum	Xenon
T(keV)	z = 2	4	8	18	26	42	54
0.001	0.	0.	0.	0.	0.	0.	0.
0.003	4.0	400.	4000.	0.	0.	0.	0.
0.01	55.0	10.	50,000.	100,000.	45,000.	0.	0.
0.03	7.0	300.	20,000.	100,000.	200,000.	600,000.	500,000.
0.1	2.5	70.	360.	14,000.	280,000.	190,000.	800,000.
0.3	2.2	24.	900.	50,000.	50,000.	120,000.	550,000.
1.0	2.9	20.	200.	2600.	44,000.	190,000.	180,000.
3.0	4.6	21.	130.	3300.	4200.	50,000.	130,000.
10.	7.6	32.	150.	1600.	5300.	11,000.	47,000.
30.	13.0	52.	240.	1700.	4300.	13,000.	20,000.

Table 3.4: Average charge state z_i for selected atoms [3.67].

	Helium	Beryllium	Oxygen	Argon	Iron	Molybdenum	Xenon
T(keV)	z = 2	4	8	18	26	42	54
0.001	0.0	0.0	0.0	0.0	0.0	0.0	0.0
0.003	0.72	2.0	0.0	0.0	0.0	0.0	0.0
0.01	1.95	2.0	1.0	3.0	1.0	0.0	0.0
0.03	2.0	3.1	3.0	7.0	5.0	5.0	2.5
0.1	2.0	4.0	5.7	8.0	10.6	12.5	10.0
0.3	2.0	4.0	6.0	13.0	15.8	15.0	17.5
1.0	2.0	4.0	7.6	16.0	20.0	25.0	25.5
3.0	2.0	4.0	8.0	17.3	23.6	32.0	37.0
10.	2.0	4.0	8.0	18.0	25.0	39.0	46.0
30.	2.0	4.0	8.0	18.0	26.0	41.0	52.0

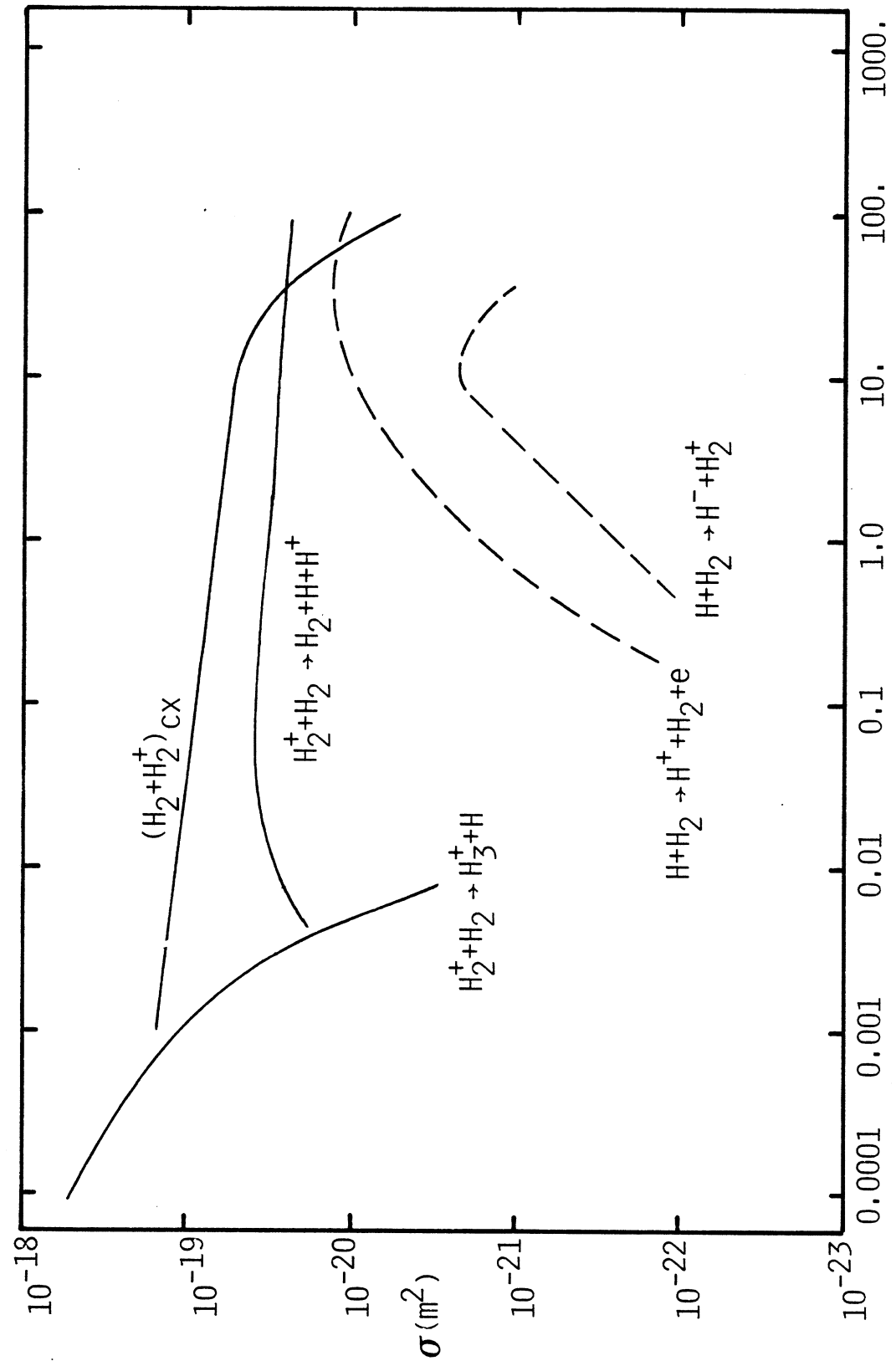

Figure 3.1: Atom-molecule interaction cross-sections.

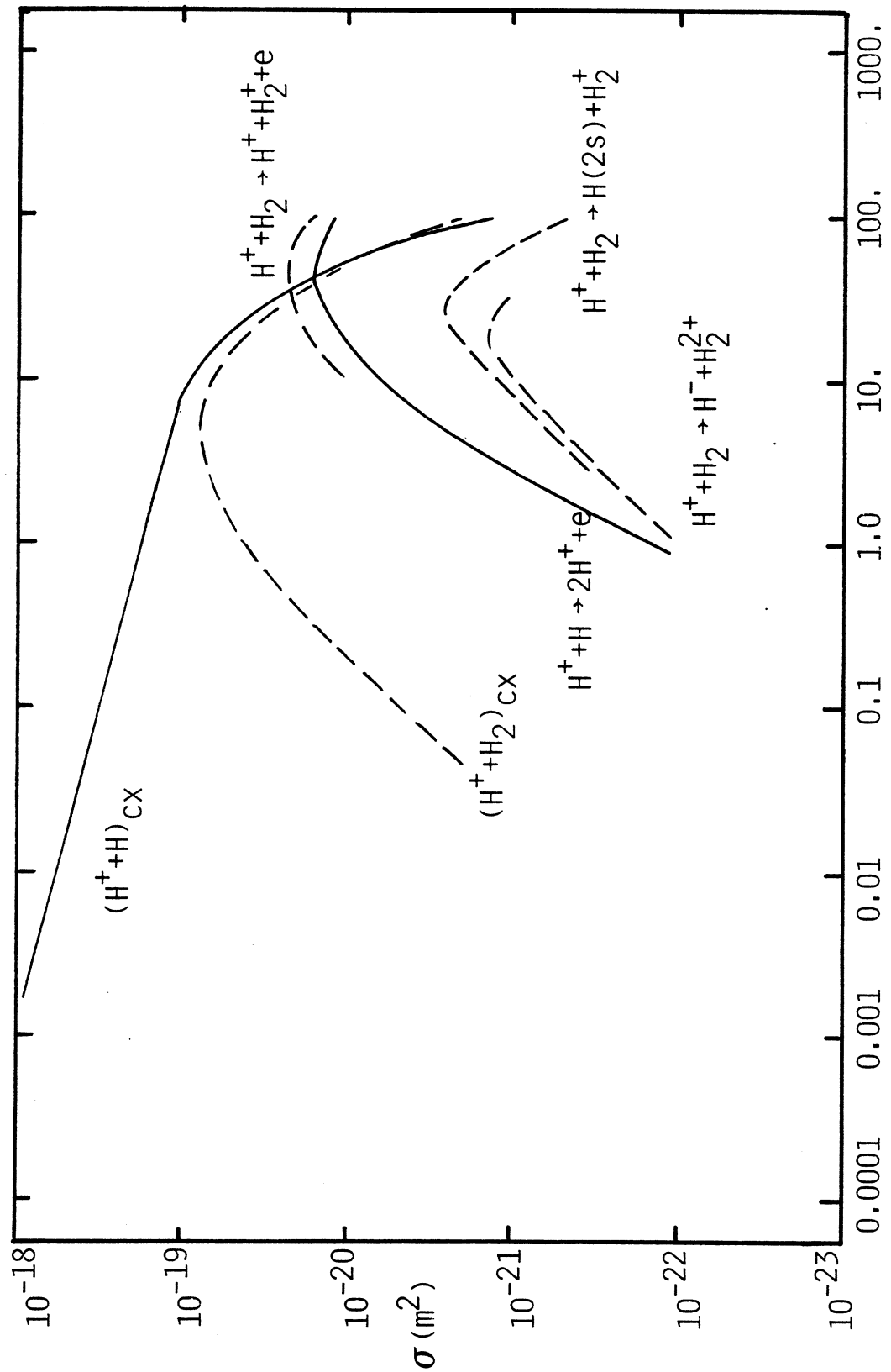

Figure 3.2: Atom-molecule interaction cross-sections.

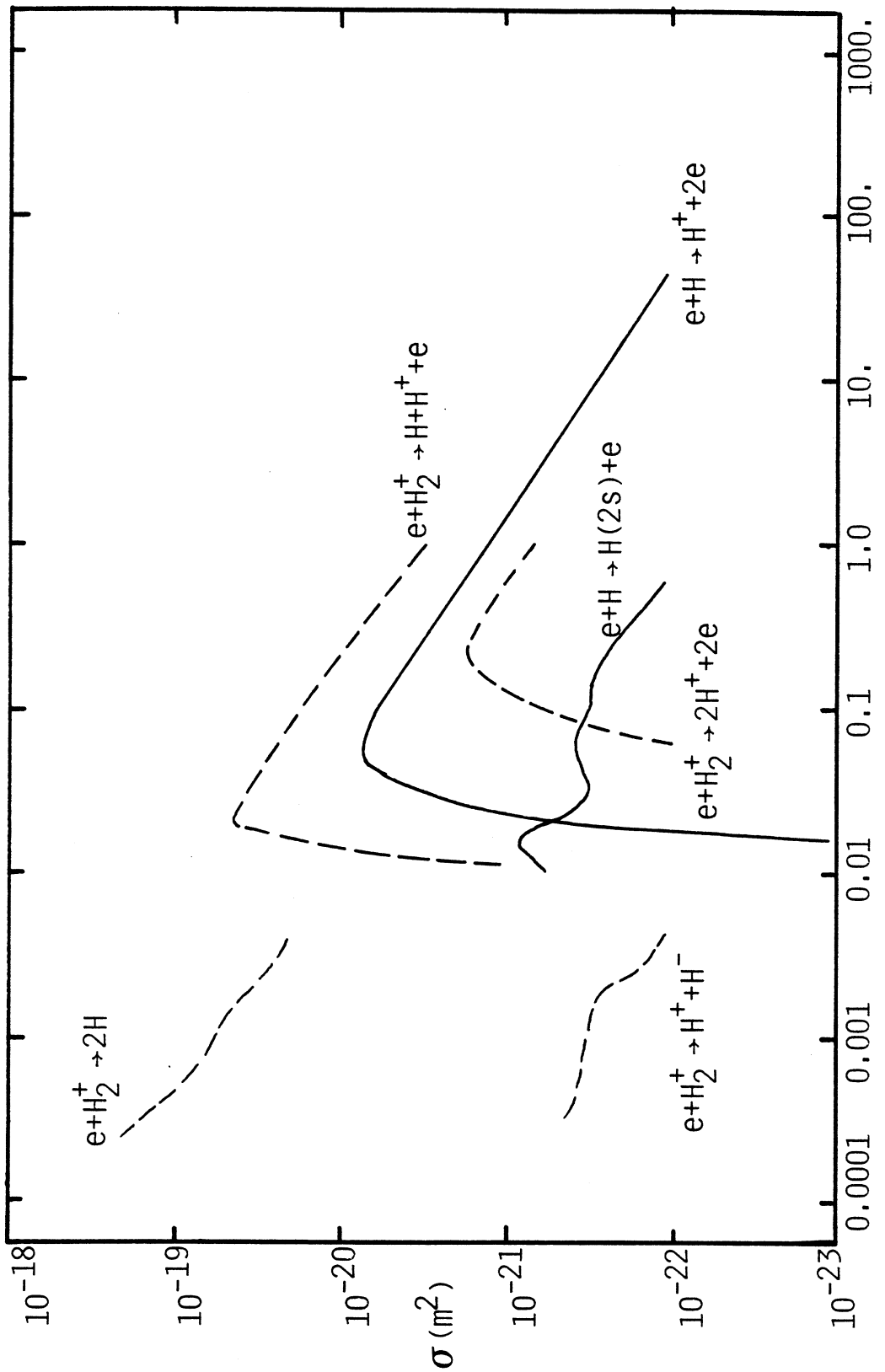

Figure 3.3: Electron impact interaction cross-sections.

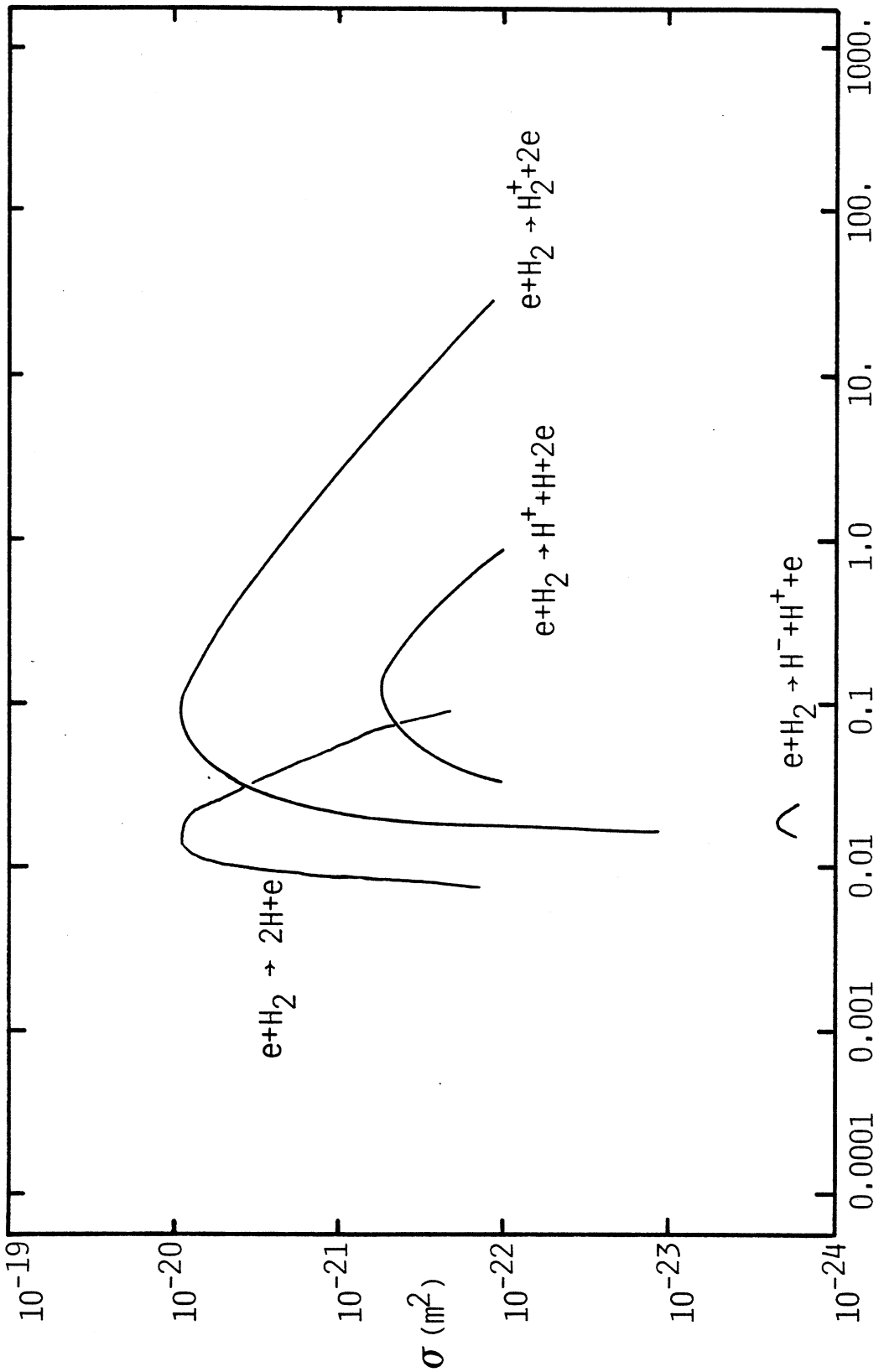

Figure 3.4: Electron impact interaction cross-sections.

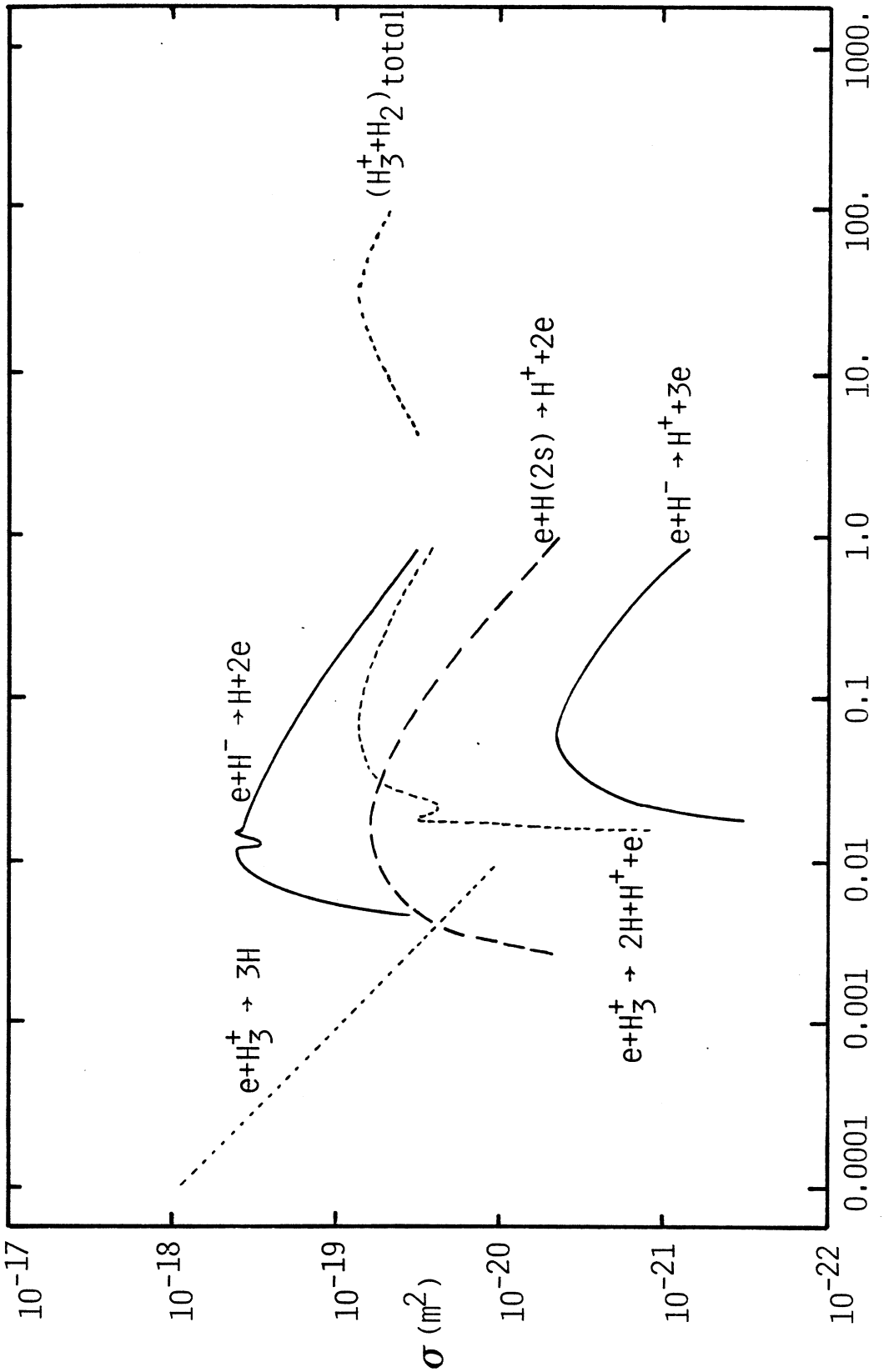

Figure 3.5: H^-, H_3^+, $H(2s)$ interaction cross-sections.

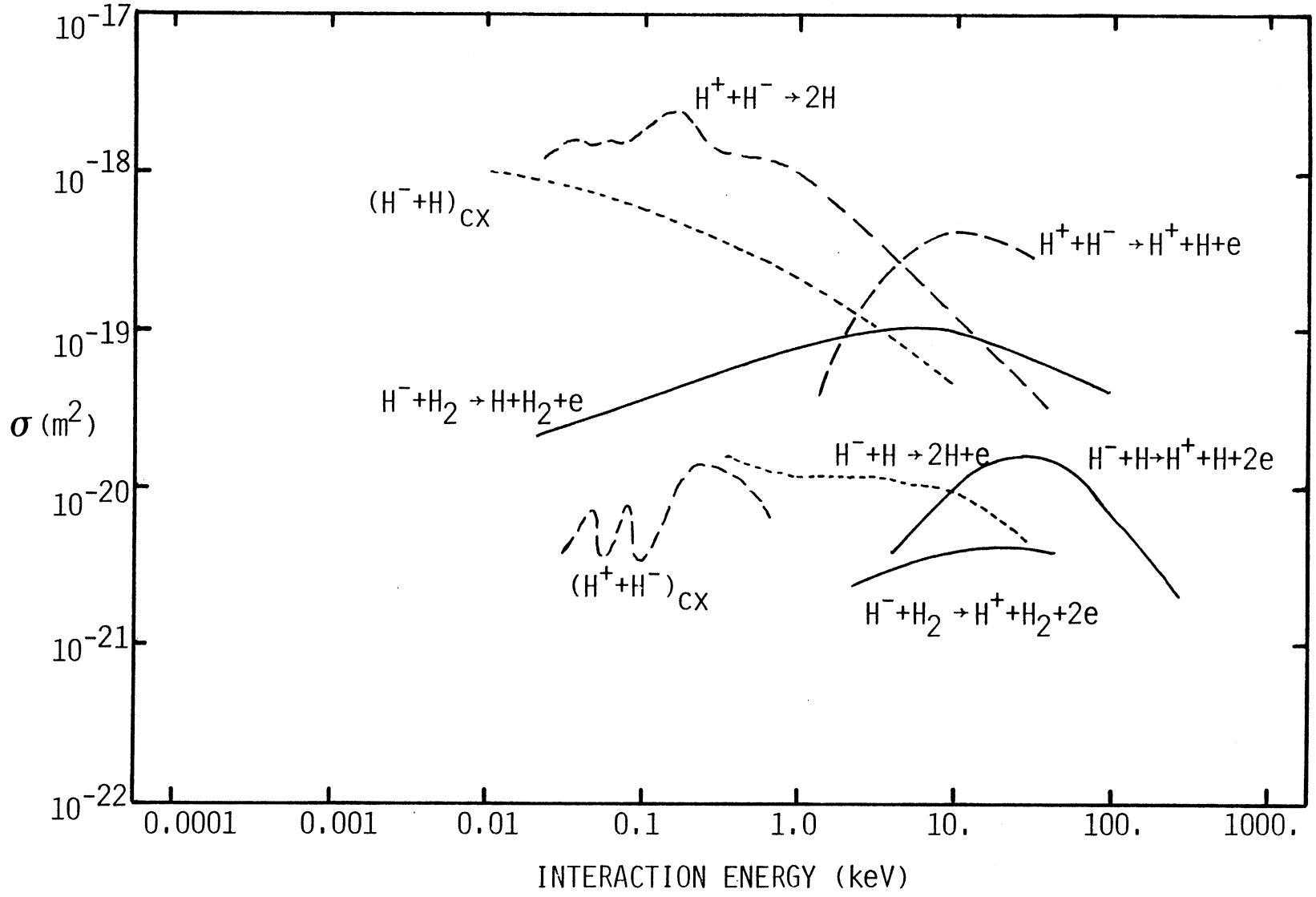

Figure 3.6: H^-, H_3^+, $H(2s)$ interaction cross-sections.

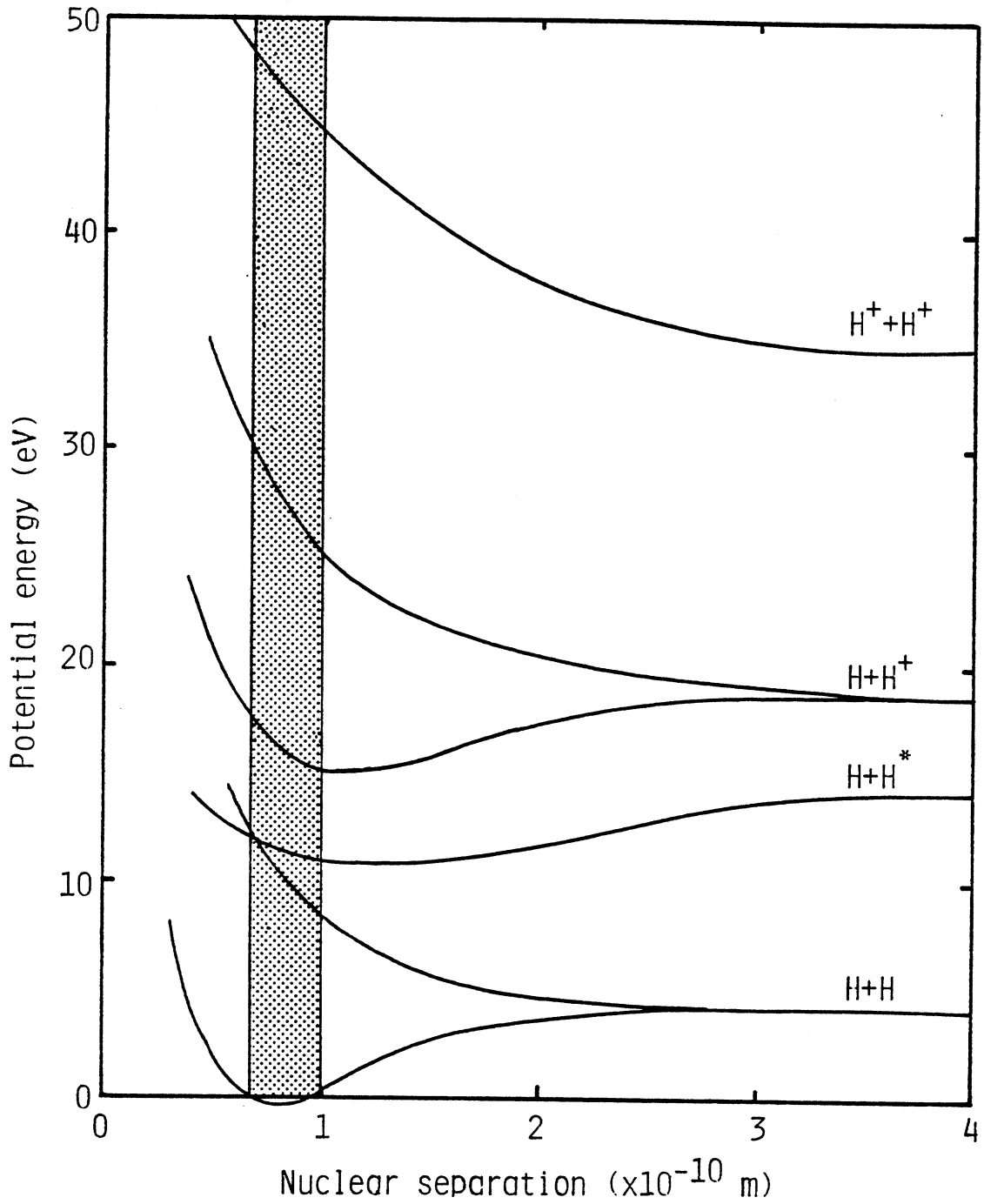

Figure 3.7: Potential energy curves for molecular and atomic hydrogen [3.5]. The shaded region illustrates the electronic transitions possible from the molecular ground state in a Franck-Condon reaction where there is not enough time to change nuclear spacing.

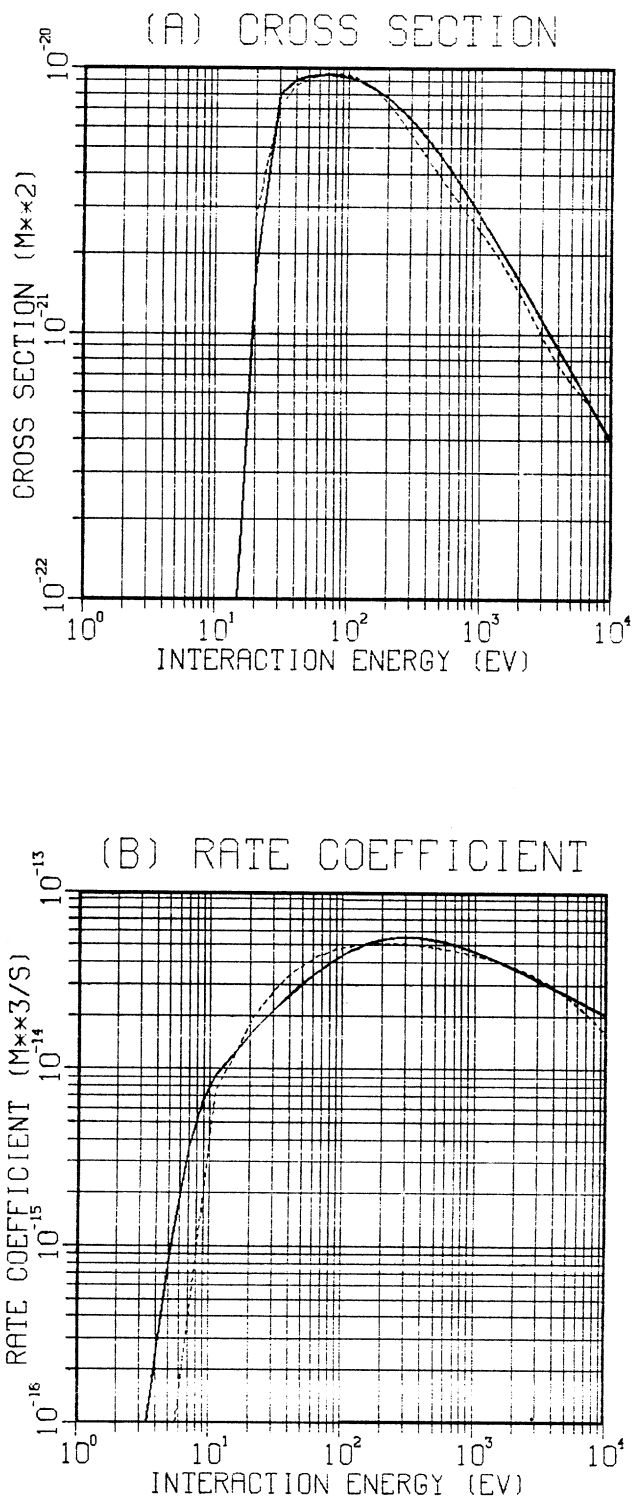

Figure 3.8: Interaction cross-section σ and Maxwellian-electron averaged rate coefficient $\langle \sigma v \rangle$ for $e + H_2 \rightarrow H_2^+ + 2e$. Dashed lines show corresponding curves from Ref.[3.48] for comparison.

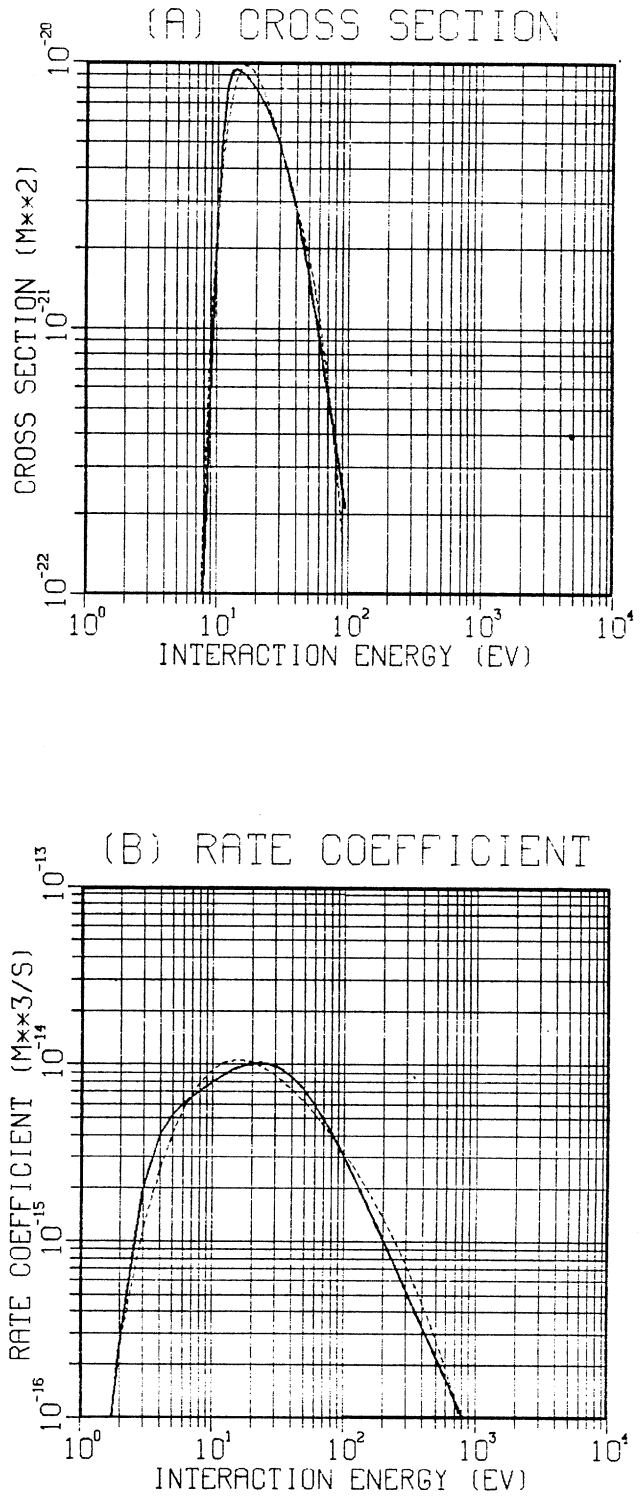

Figure 3.9: Interaction cross-section σ and Maxwellian-electron averaged rate coefficient $\langle \sigma v \rangle$ for $e + H_2 \rightarrow 2H + e$. Dashed lines show corresponding curves from Ref.[3.48] for comparison.

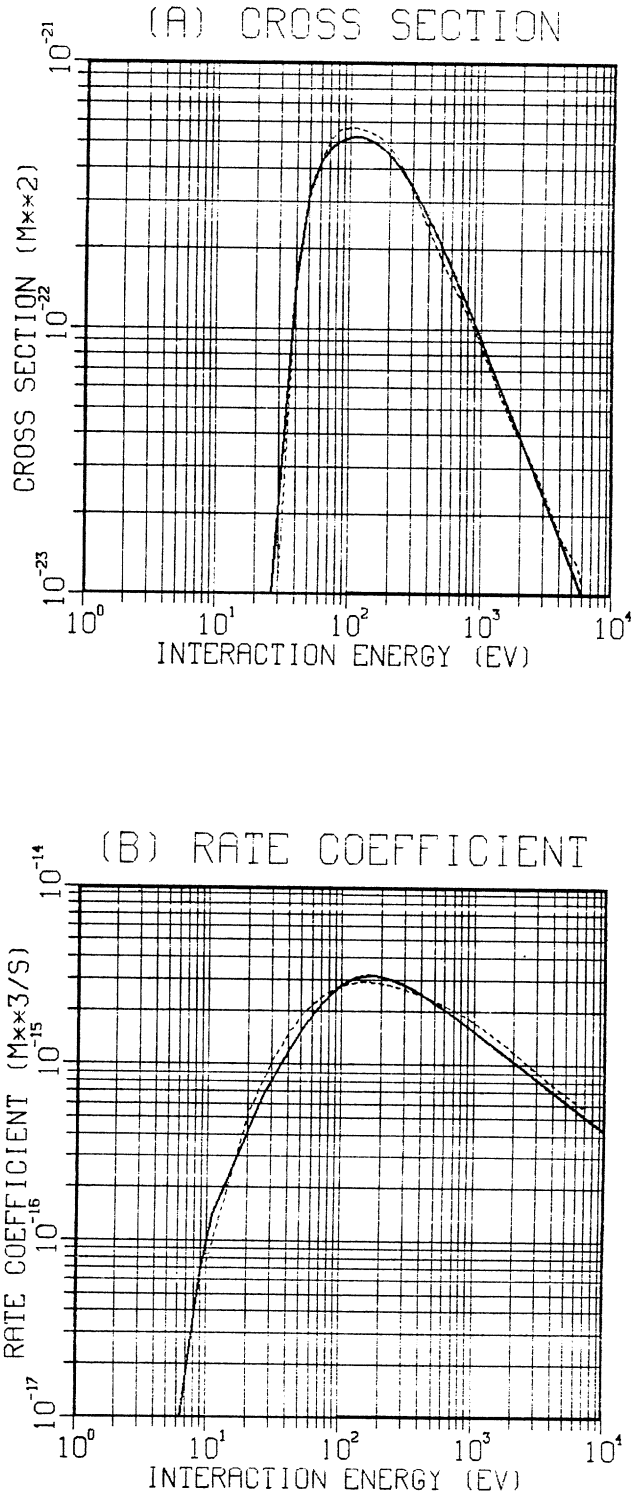

Figure 3.10: Interaction cross-section σ and Maxwellian-electron averaged rate coefficient $\langle \sigma v \rangle$ for $e + H_2 \rightarrow H + H^+ + 2e$. Dashed lines show corresponding curves from Ref.[3.48] for comparison.

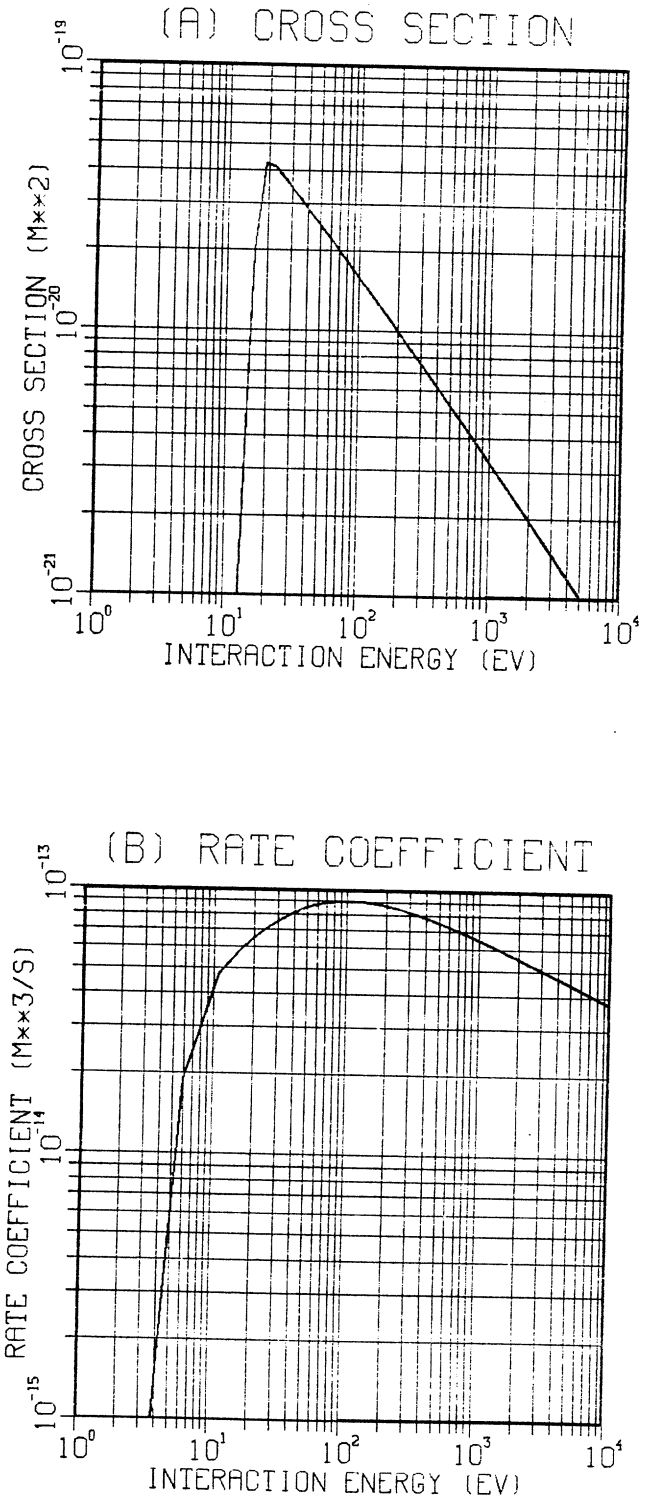

Figure 3.11: Interaction cross-section σ and Maxwellian-electron-averaged rate coefficient $\langle \sigma v \rangle$ for $e + H_2^+ \rightarrow H + H^+ + e$.

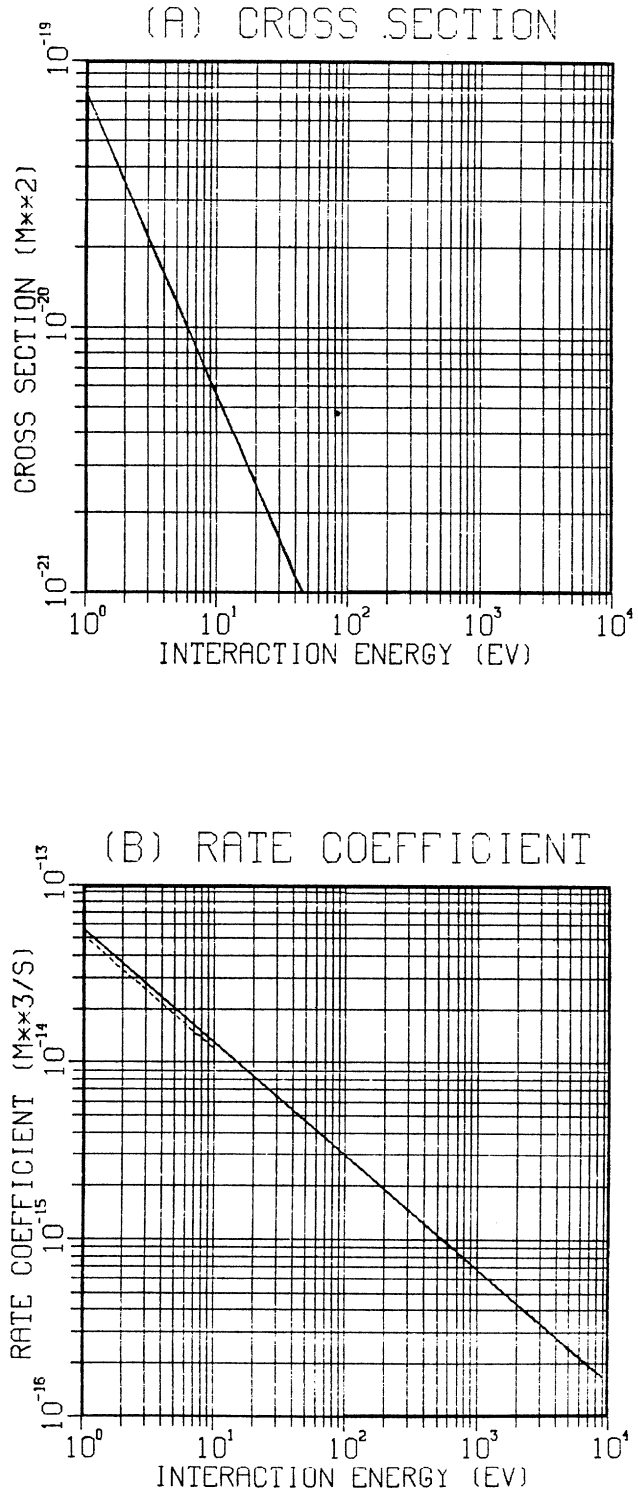

Figure 3.12: Interaction cross-section σ and Maxwellian-electron averaged rate coefficient $\langle \sigma v \rangle$ for $e + H_2^+ \rightarrow 2H$. Dashed lines show corresponding curves from Ref.[3.48] for comparison.

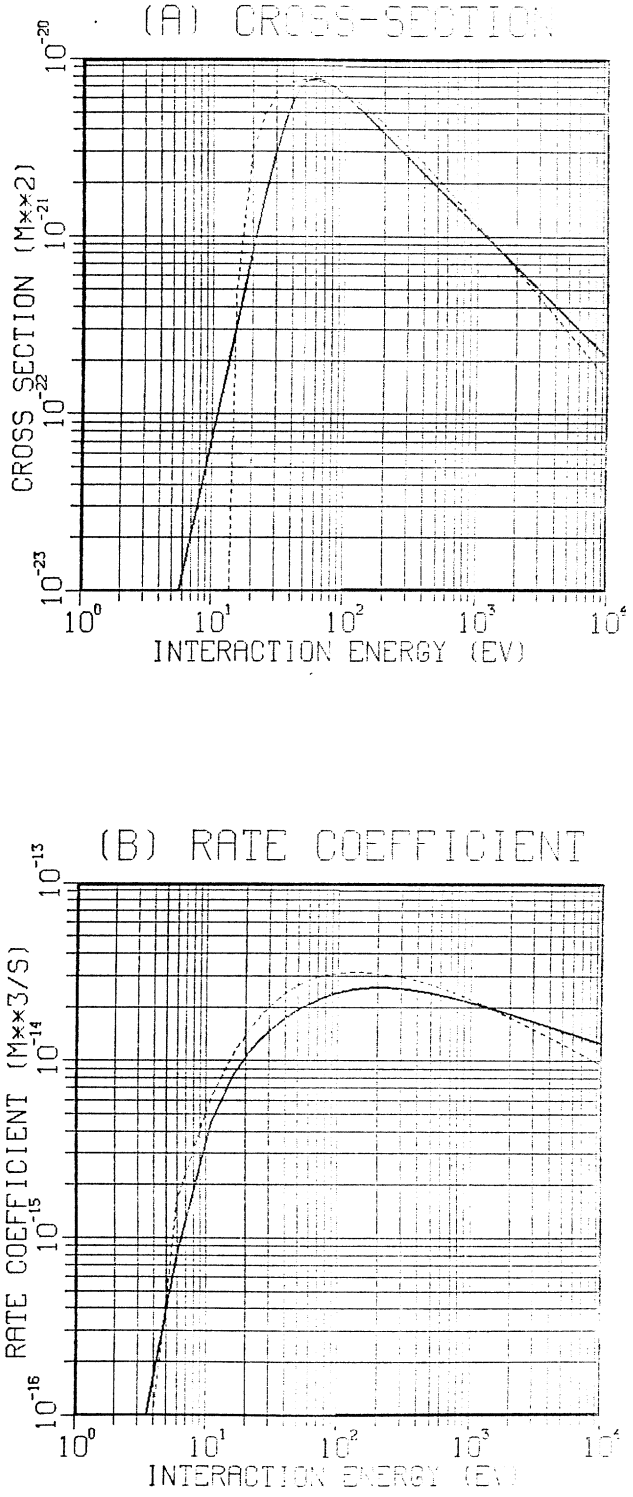

Figure 3.13: Interaction cross-section σ and Maxwellian-electron-averaged rate coefficient $\langle \sigma v \rangle$ for $e + H \rightarrow H^+ + 2e$. Dashed lines show corresponding curves from Refs.[3.73] and [3.53] for comparison.

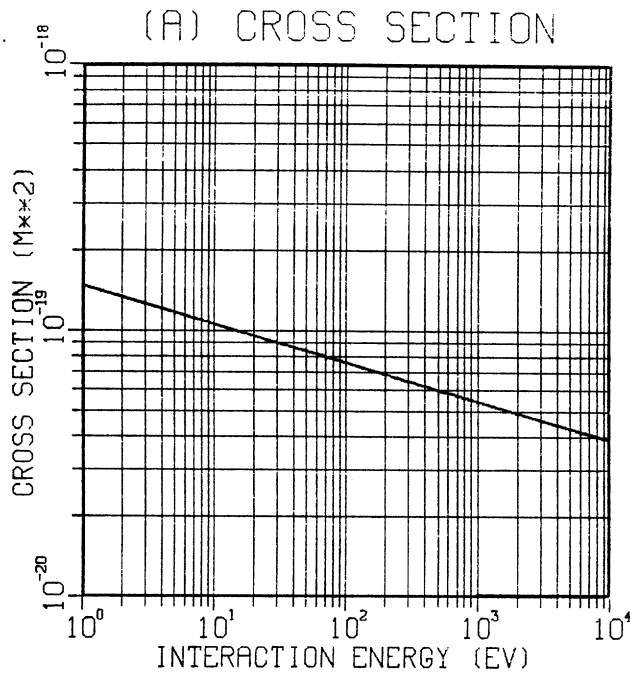

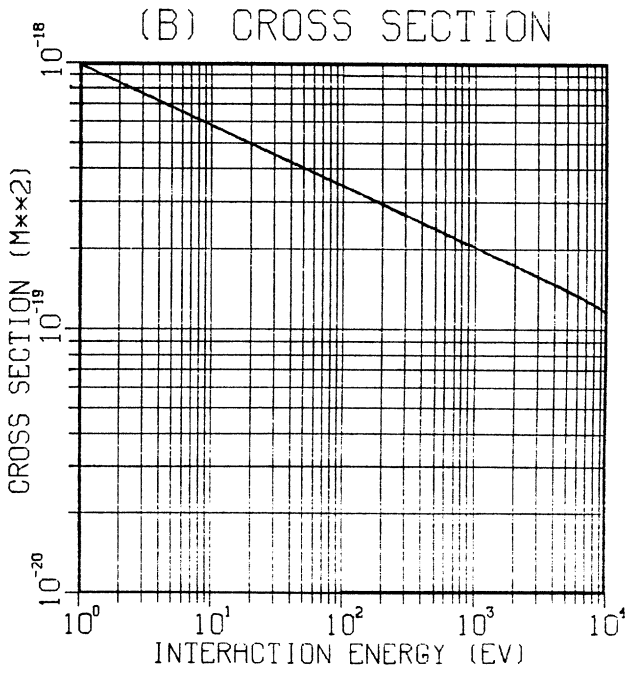

Figure 3.14: Interaction cross-sections σ for (H_2^+, H_2) and (H^+, H) charge exchange. Dashed line shows corresponding curve for the latter cross-section from Ref.[3.73] for comparison.

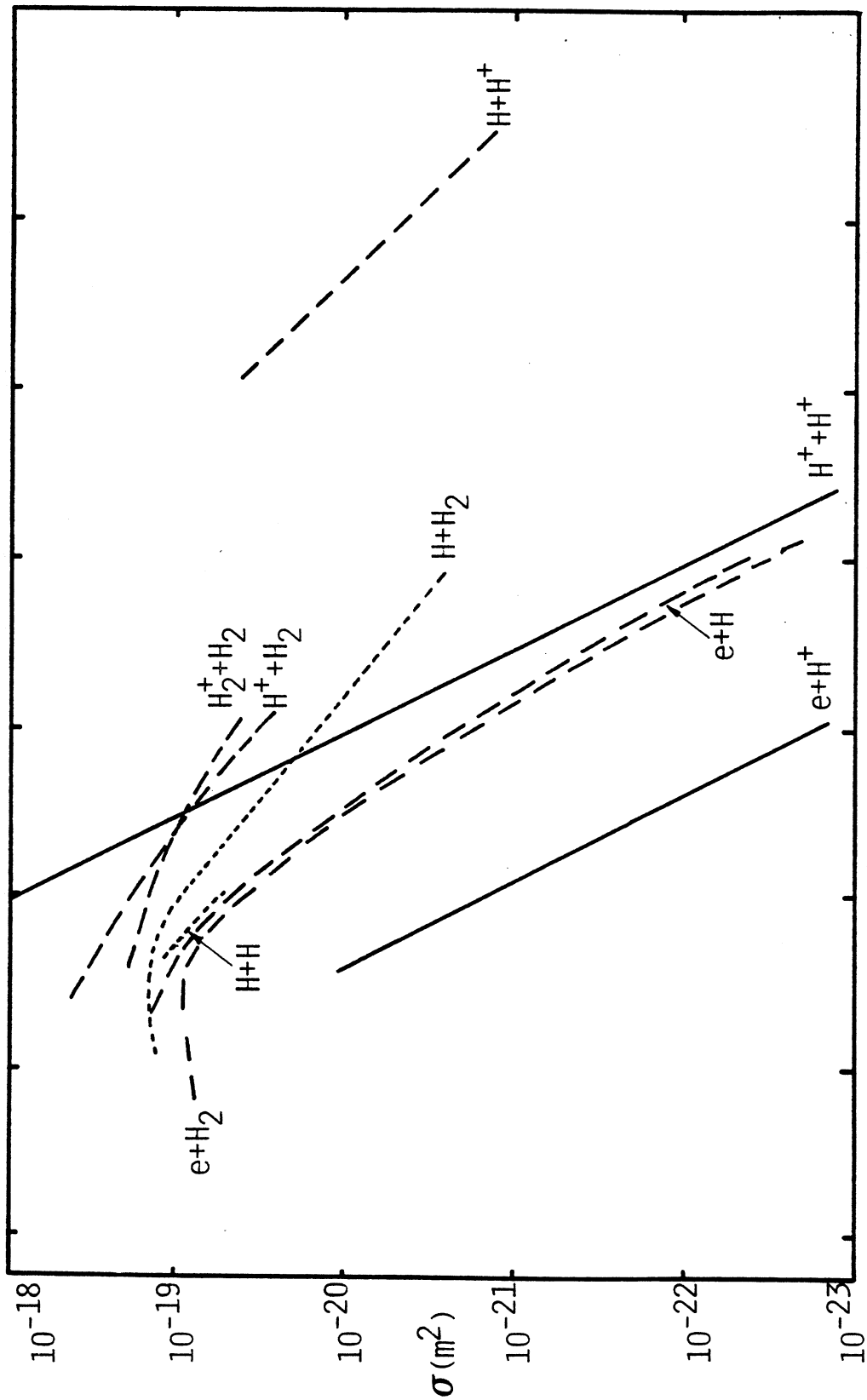

Figure 3.15: Elastic scattering cross-sections for energy transfer.

4.0 0-D Modelling of Plasma Edge Conditions

The first step in this analysis of plasma/neutral gas transport in divertors is to establish representative conditions in the exhaust region. In particular, it would be very useful to have a simple global model that could be used to estimate particle and energy flows, and ion and neutral temperatures and densities, in terms of reasonably known or controllable input parameters. Given such a model, we can determine which operating conditions are attainable (e.g. a cold, high density, radiating edge or a hot, collisionless edge), and which are desirable (e.g. low heat flux to target).

As outlined in Chapter 2, a variety of models have been developed to try to understand and predict edge conditions. However, few calculations present a global, self-consistent model that can provide edge parameters for a wide range of operating conditions and divertors. Heifetz et al [4.55] have a 2-D fluid model of the scrape-off and axisymmetric divertor/limiter region, but it is not particularly convenient for fast estimates, for collisionless edges, or for bundle diverted tokamaks. Harrison et al [4.53] have studied an INTOR poloidal divertor using analytic models similar to those presented here, but the method is not immediately generalizable. Furthermore, their results are parametrized in terms of divertor plasma temperature rather than a more physical "knob" such as gas fuelling rate.

In this chapter, a coupled 0-D model is developed to provide these estimates of edge conditions. Basically, mass and energy balances are made around the core, scrape-off layer and divertor. The particular transport and reaction rates are described by simple models in terms of region-averaged temperatures and densities, resulting in a set of non-linear algebraic equations. The equations are written in steady-state since it is expected that next generation machines will have sufficiently long pulses for the edge conditions to reach equilibrium.

In Section 4.1, the structure of the global model and the balance equations are described, while the specific transport models are given in Section 4.2. These transport models are each fairly simple and intuitive, but there are many of them so this section is further subdivided. The resulting global model is compared against experimental results in Section 4.3, and the uncertainties in both the data and the code results noted. Since the model seems modestly able to match experimental results, it is finally applied, in Section 4.4, to the analysis of edge conditions. The results include a consistent comparison of

the behavior of bundle divertors, poloidal divertors and pumped limiters for these next generation tokamak designs.

4.1 Description of Global Edge Model

The basic structure of the model is shown in Figure 4.1. The reactor (nominally a tokamak) is divided into three regions: the plasma core with average ion density $n_{c,i}$ and average temperature $T_{c,i}$; the scrape-off layer with ions ($n_{s,i}, T_{s,i}$) and neutrals ($n_{s,n}, T_{s,n}$); and the divertor/limiter region with ions ($n_{d,i}, T_{d,i}$) and neutrals ($n_{d,n}, T_{d,n}$). The input data can be classed into three sets: (1) plasma core conditions; (2) geometry; and (3) model parameters. For a given design, the core conditions and geometry should be known, while the parameters are estimated from other calculations and experimental results.

A full description of the variables used in this chapter is provided in Table 4.1. However, some notational rules were followed: $\dot{N}$ is particle flow (particles/s); Γ is particle flux (particles/m^2-s); n is density (particles/m^3); Q is energy flow (W); q is energy flux (W/m^2) and T/E are temperature/energy (eV or J). The first subscript denotes regions (e.g. c – core, s – scrape-off, d – divertor, t – target), and double first subscript denotes flow between regions (e.g. cs – core to scrape–off, dw – divertor to wall). The second subscript denotes species (e.g. i – ion/electron, n – neutral atomic hydrogen, α – alpha particles) or process (e.g. f – fuelling, r – radiation, cx – charge exchange, ei – electron impact ionization, er – electron recombination).

Mass and energy balances yield the following ten equations.

Core Plasma

Direct core fuelling, plus recycling and charge exchange neutrals from the edge counter the convective particle loss and consumption into helium ($f_{cs,cx}$ is the fraction of neutrals that charge exchange and leave the core, $f_{sc,cx}$ is the fraction of neutrals that charge exchange and enter the core from the scrape–off layer):

$$\dot{N}_{c,f} + (1 - f_{cs,cx})\dot{N}_{sc,n} + f_{sc,cx}\dot{N}_{s,cx} = \dot{N}_{cs,i} + 2\dot{N}_{c,\alpha} \tag{4.1}$$

Direct core heating plus the energy of the fuelling hydrogen balances the radiative and convective losses, and provides for the ionization (E_i) and thermalization of the fuel:

$$Q_{c,h} + Q_{c,\alpha} + \frac{3}{2}T_{s,n}\dot{N}_{sc,n} + \frac{3}{2}T_{s,i}f_{sc,cx}\dot{N}_{s,cx}$$

$$= Q_{c,r} + Q_{cs,i} + (1 - f_{cs,cx})\dot{N}_{sc,n}E_i + \frac{3}{2}T_{c,cx}f_{cs,cx}\dot{N}_{sc,n} + (\frac{3}{2}T_{c,f} - E_i)\dot{N}_{c,f} \qquad (4.2)$$

Scrape-off Layer Plasma

Hydrogen diffusing out of the core plus ionization maintain the plasma against losses to the divertors and walls:

$$\dot{N}_{cs,i} + \dot{N}_{s,ei} = \dot{N}_{sd,i} + \dot{N}_{sw,i} \qquad (4.3)$$

Convected energy from the core is transported or radiated to the divertors and walls, and thermalizes the cold ions formed from neutral gas interactions:

$$Q_{cs,i} = Q_{sd,i} + Q_{sw,i} + Q_{s,r} + (E_i - \frac{3}{2}T_{s,n})\dot{N}_{s,ei} + \frac{3}{2}(T_{s,i} - T_{s,n})\dot{N}_{s,cx} \qquad (4.4)$$

Scrape-off Layer Neutrals

Recycling from the divertor and the walls, plus direct fuelling, counter the losses by reactions in the edge itself or to the core (g_d is the number of divertor channels, R_w is the wall recycling coefficient, $f_{ds,cx}$ is the fraction of divertor charge-exchange neutrals that escape):

$$g_d\dot{N}_{ds,n} + f_{ds,cx}\dot{N}_{d,cx} + \dot{N}_{s,f} + R_w\dot{N}_{sw,i} + R_w(1 - f_{sc,cx})\dot{N}_{s,cx}$$

$$= \dot{N}_{s,cx} + (1 - R_w)\dot{N}_{sw,n} + \dot{N}_{sc,n}(1 - f_{cs,cx}R_w) + \dot{N}_{s,ei} \qquad (4.5)$$

Recycling neutrals from the divertor and wall supply energy, which is then lost by neutrals at the scrape-off layer neutral temperature hitting these walls:

$$g_dQ_{ds,n} + \frac{3}{2}T_{d,i}f_{ds,cx}\dot{N}_{d,cx} + \frac{3}{2}T_wR_w(\dot{N}_{sw,i} + (1 - f_{sc,cx})\dot{N}_{s,cx} + \dot{N}_{sw,n} + f_{cs,cx}\dot{N}_{sc,n}) + \frac{3}{2}T_w\dot{N}_{s,f}$$

$$= \frac{3}{2}T_{s,n}(\dot{N}_{s,cx} + \dot{N}_{sw,n} + \dot{N}_{s,ei} + \dot{N}_{sc,n}) \qquad (4.6)$$

Divertor Plasma

Plasma flowing in from the scrape-off layer, plus ionizations, supply plasma ions against recombination at the walls, the target or through electron interactions:

$$\frac{\dot{N}_{sd,i}}{g_d} + \dot{N}_{d,ei} = \dot{N}_{dw,i} + \dot{N}_{dt,i} + \dot{N}_{d,er} \qquad (4.7)$$

Power flowing in to each divertor from the scrape-off layer, plus energy carried with newly ionized neutrals, is lost by convection, conduction, radiation and charge exchange to the walls and target:

$$\frac{Q_{sd,i}}{g_d}+(\frac{3}{2}T_{d,n}-E_i)\dot{N}_{d,ei}+\frac{3}{2}T_{d,n}\dot{N}_{d,cx}=Q_{dw,i}+Q_{dt,i}+Q_{d,r}+\frac{3}{2}T_{d,i}\dot{N}_{d,cx}+\frac{3}{2}T_{d,i}\dot{N}_{d,cr} \tag{4.8}$$

Divertor Neutrals

Direct fuelling, recycling from walls and recombination maintain the neutral density against losses through the divertor throat, to the pumps, to the walls, and by ionization:

$$\frac{\dot{N}_{d,f}}{g_d}+R_w(\dot{N}_{dt,i}+\dot{N}_{dw,i})+\dot{N}_{d,er}=\dot{N}_{ds,n}+f_{d,p}\dot{N}_{d,p}+(1-R_w)(\dot{N}_{dt,n}+\dot{N}_{dw,n}+\dot{N}_{d,cx})+\dot{N}_{d,ei} \tag{4.9}$$

The energy of the fuel and recycling neutrals is lost by convection back to the scrape-off, to the pumps, to the walls, or in reactions:

$$\frac{3}{2}T_w\left[\frac{\dot{N}_{d,f}}{g_d}+R_w(\dot{N}_{dt,i}+\dot{N}_{dw,i}+\dot{N}_{dt,n}+\dot{N}_{d,cx}+\dot{N}_{dw,n})+(1-f_{d,p})\dot{N}_{d,p}\right]+\frac{3}{2}T_{d,i}\dot{N}_{d,er}$$

$$=Q_{ds,n}+\frac{3}{2}T_{d,n}\dot{N}_{d,p}+\frac{3}{2}T_{d,n}(\dot{N}_{d,ei}+\dot{N}_{d,cx}+\dot{N}_{dt,n}+\dot{N}_{dw,n}) \tag{4.10}$$

If all variables are expressed as external inputs or as functions of n and T in each region, then we can solve for the ten unknowns $n_{c,i}, T_{c,i}, n_{s,i}, T_{s,i}, n_{s,n}, T_{s,n}, n_{d,i}, T_{d,i}, n_{d,n}, T_{d,n}$. In practice, $n_{c,i}$ and $T_{c,i}$ are probably known for a particular design, so $\dot{N}_{c,f}$ and $Q_{c,h}$, the core fuelling rate and the external core heating rate, are chosen as unknowns. Since the models for mass and energy flow involve non-linear dependencies on n and T, the solution procedure is to write the equations as linear functions of the particle and energy fluxes Γ and q for each region ($\Gamma_{s,i}, q_{s,i}, \Gamma_{s,n}, q_{s,n}$ and so on), estimate the non-linear terms, and iterate. In particular:

(1) Estimate unknown n, T;

(2) Calculate non-linear terms using estimated n, T;

(3) Solve linear system for Γ and q;

(4) Determine n, T from Γ, q;

(5) Go to Step (2) and repeat until convergence.

Some care is needed in the iteration process since the high recycling conditions may cause large fluctuations in the non-linear terms from iteration to iteration. This is reduced by a combination of: (1) starting from a "known" low-recycling regime (artificially high pumping) and slowly reducing pumping until the final state is reached; and (2) underrelaxing sensitive variables such as $T_{s,i}$ and $T_{d,i}$.

4.2 Transport Models

In this section, the flow models used for each region are briefly described. These models relate the particle and energy flows $\dot{N}$ and Q to known variables and to the fluxes Γ and q, which in turn are described in terms of densities and temperatures n and T.

4.2.1 Core Plasma – Perpendicular Transport

Consider the plasma core cross-field particle and energy transport. Core plasma conditions are assumed to be known, for the device being considered, based on other calculations or experimental data. These parameters are then input to this model to provide the driving terms for the edge analysis. Radial profile effects are included since the input parameters are core-averaged or integrated quantities.

Particle and energy confinement times, τ_p and τ_E, are interpretted to be related to the particle transport (ion or electron) and convective/conductive energy transport (ion plus electron) from the core as

$$\dot{N}_{cs,i} = \frac{n_{c,i}V_c}{\tau_p} \tag{4.11}$$

$$Q_{cs,i} = \frac{3T_{c,i}n_{c,i}V_c}{\tau_E} \tag{4.12}$$

Other definitions of these confinement times are possible [4.54].

Radiation losses from the core due to impurities are expressed as a fraction of the input heating power, $f_{c,r}$,

$$Q_{c,r} = f_{c,r}(Q_{c,h} + Q_{c,\alpha}) \tag{4.13}$$

The alpha heating power $Q_{c,\alpha}$ is fixed by the core density and temperature, and is also an input. However, the remaining core external heating power, $Q_{c,h}$, is self-consistently

calculated as a solution to Eqn.(4.2). This refers to ohmic or RF power. The conversion of hydrogen into helium is a loss rate $2\dot{N}_{c,\alpha}$ where $\dot{N}_{c,\alpha}$ is the helium production rate,

$$\dot{N}_{c,\alpha} = \frac{Q_{c,\alpha}}{3.5MeV} \tag{4.14}$$

The helium ash is assumed to diffuse out with the hydrogen and flow into the divertor and pumps. Energy transfer associated with the helium is neglected since its detailed transport is not calculated and since $n_{He}/n_{c,i} \ll 1$. This is reasonable for all but DT machines such as TFTR–Upgrade where there will be appreciable fusion power but possibly poor confinement of the 3.5 MeV α particles.

Neutral particles can flow in from the scrape-off layer at a rate $\dot{N}_{sc,n}$, and are assumed to promptly equilibrate with the core conditions. A direct core fuelling rate $\dot{N}_{c,f}$ supplies neutrals into the core with temperature $T_{c,f}$, and may represent neutral beam heating or pellet fuelling.

Some fraction $f_{cs,cx}$ of the incoming neutrals will charge exchange and escape. It is assumed that about half of the resulting high-energy neutrals will be directed out and escape the core, while the remainder will be reionized and retained, so

$$f_{cs,cx} \approx 0.5 \frac{\langle \sigma v \rangle_{cx}}{\langle \sigma v \rangle_i + \langle \sigma v \rangle_{cx}} \tag{4.15}$$

The factor of 0.5 basically accounts for geometry effects. Since the reactions occur about a mean free path into the plasma, those neutrals which are directed outwards are likely to escape. Note also that the mean free path for the hot neutrals is longer by about the speed ratio, or $\sqrt{T_{c,cx}/T_{s,n}}$.

Since these charge exchange neutrals may be an appreciable power flow channel to the first wall, it is desirable to include profile effects to get the correct charge exchange energy. Many experimental profiles can be approximately described by

$$T_{c,i}(r) \simeq T_0 \left[1 - \left(\frac{r}{a_L} \right)^{c_1} \right]^{c_2}; \quad n_{c,i}(r) \simeq n_0 \left[1 - \left(\frac{r}{a_L} \right)^{c_1} \right]^{c_2} \tag{4.16}$$

where a_L is the machine limiter radius; T_0 and n_0 refer to center values; and c_i are constants. The profiles can range from peaked, almost triangular, profiles such as on DITE ($c_1 \sim 2, c_2 \sim 3$ [4.14]), to parabolic profiles such as on ALCATOR-A or ASDEX ($c_1 \sim 2, c_2 \sim 1$ [4.20,4.26]). Other profile shapes are also possible, such as $T_{c,i}(r) \approx$

$T_0 \exp(-c_1 r^2)$ (ALCATOR-A [4.20]). Furthermore, the c_i are not necessarily equal for temperature and density - $c_{2,T}/c_{2,n} \sim 2$ for ASDEX [4.26]. Here, average values of $c_1 \approx 2$ and $c_2 \approx 1$ are used with $T_0 = 1.5 T_{c,i}$ and $n_0 = 2 n_{c,i}$. The mean radius where the charge exchange reaction occurs is $r_{cx} \approx (a - \lambda_{cx}/4)$, where $\lambda_{cx} = \sqrt{8 T_{s,n}/\pi m_i}/n\langle\sigma v\rangle_{cx}$; n and $\langle\sigma v\rangle_{cx}$ are evaluated at r_{cx}; and the factor of 1/4 accounts for the random direction of the incoming neutrals.

4.2.2 Edge Plasma (Scrape-off and Divertor) - Parallel Transport

Ions and electrons are assumed to flow along field lines with $\Gamma = nv$, where $v = Mc$ is the bulk velocity, M is the Mach number of the parallel flow, and c is the local speed of sound, defined here as $c = \sqrt{2T/m_i}$. Other definitions of the speed of sound are possible, the most general being $c = \sqrt{(\gamma_e T_e + \gamma_i T_i)/m_i}$. The present choice corresponds to equal ion/electron temperatures and large parallel thermal conductivity - both reasonable for exhaust plasmas, but certainly providing approximate scaling for other cases.

In general, the flow Mach number (and thus the bulk velocity) along the field lines is determined by solving the total (ion plus electron) parallel momentum equation. This may be written, in steady state, as

$$\frac{1}{2} nm \frac{dv^2}{dz} + \frac{dp}{dz} + mv \frac{\dot{N}}{V_s} \simeq 0 \tag{4.17}$$

where the terms include the convective gradient (or ram pressure), the pressure gradient and momentum dilution from a volumetric particle source $\dot{N}/V_s$ with no net momentum; $V_s \simeq \delta_{s,i} A_s$ is the volume of the scrape-off plasma; $\delta_{s,i}$ is the scrape-off plasma thickness; A_s is the separatrix surface area; n is the ion density (which equals the electron density due to quasineutrality); m is the ion mass ($m_i \gg m_e$); and $p = 2nT$ is the total pressure. Electron-ion collisional friction and electric field effects cancel in the total momentum equation. However, this expression neglects neutral friction, viscosity, flow area changes and vorticity, which may be significant as discussed by Singer and Langer [4.42] who develop an ordering of the terms.

Combining Eqn.(4.17) with the continuity equation, $d\Gamma/dz = \dot{N}/V_s$, the equations become

$$\frac{1 - M^2}{M(1 + M^2)} \frac{dM}{dz} = \frac{1}{\Gamma} \frac{d\Gamma}{dz} + \frac{1}{2T} \frac{dT}{dz} \tag{4.18}$$

Integrating from z to $z = L$ [4.53],

$$\frac{M^2+1}{M}\frac{M_L}{M_L^2+1} = \frac{\Gamma_L}{\Gamma}\sqrt{\frac{T_L}{T}} \tag{4.19}$$

Harbour and Morgan [4.8] compared this equation with the results of a more complete 1–D numerical model and found reasonable agreement.

Since the flow starts off subsonic, the addition of mass causes an increase in velocity. In principle, the flow can become sonic at a divertor throat and then supersonic with the further addition of particles in the divertor or simply the expansion of the flow. This is most likely in a bundle divertor where a large field at the throat can cause the plasma flux bundle to compress then expand as in a converging/diverging nozzle.

The Mach number of the scrape–off flow has been measured in several experiments (normalized to the same expression for sound speed): 0.3 FM-1 [4.1]; 0.3 DIVA [4.2]; 0.5 - 1 T-12 [4.3]; 0.14 ASDEX [4.4]; and 0.15 DITE MK1 [4.5]. At the divertor/limiter target, however, an electrostatic sheath forms, with the ions flowing at the local speed of sound, $M \simeq 1$ ([4.46],PDX [4.7]).

In a reactor divertor, the actual pumping speed is likely to be much less than in present experiments where extensive gettering is used. Consequently there may be even higher recycling and correspondingly lower Mach number flow in the scrape–off [4.6], although the flow will still reach sonic speed at the target.

Thus the Mach number will range from zero at the field line symmetry point, to unity at the target sheath edge. It will likely be small in the scrape–off layer and accelerate up to sonic speeds near the target. Taking z to be in the scrape–off (i.e. $L_{s,i}/2$) and L to be the target (i.e. $L_{s,i} + L_{d,i}$), and assuming $M(0) = 0$, $M_{s,i}^2 \ll 1, M_{target} \simeq 1$, then

$$M_{s,i} \simeq \frac{1}{4}\frac{\Gamma_{sd,i}}{\Gamma_{dt,i}}\sqrt{\frac{T_{s,i}}{T_{d,i}}} \simeq \frac{1}{4}\frac{\dot{N}_{sd,i}}{g_d\dot{N}_{dt,i}}\sqrt{\frac{T_{s,i}}{T_{d,i}}} \tag{4.20a}$$

In the divertor, the Mach number is assumed to be between the scrape–off and target values.

$$M_{d,i} \approx 0.5(1. + M_{s,i}) \tag{4.20b}$$

The parallel particle fluxes are $\Gamma_{sd,i} = n_{s,i}M_{s,i}c_{s,i}$ and $\Gamma_{dt,i} = n_{d,i}M_{d,i}c_{d,i}$. The ion parallel flux out of the scrape-off layer and into the divertor/limiter is

$$\dot{N}_{sd,i} = g_d\Gamma_{sd,i}A_{di} \tag{4.21}$$

(where g_d is the number of divertor/limiter channels) and similarly, the ion parallel flux in the divertor and onto the target is, per divertor channel,

$$\dot{N}_{dt,i} = \Gamma_{dt,i} A_{ti} \tag{4.22}$$

where A_{di} and A_{ti} are the areas perpendicular to the flow.

The energy transported by the plasma ions and electrons is treated in somewhat more detail. A description of the full equations is given in Stacey [4.40]. Two-fluid equations in a relatively low collisionality (but still fluid) limit are described by Petravic et al [4.41] and a careful investigation of the ordering of the terms in a higher collisionality limit is given by Singer and Langer [4.42]. Here it is assumed that the important behavior can be described in steady-state for each species by

$$\nabla \cdot \left[(\frac{1}{2} mnv^2 + \frac{3}{2} nT + p)\underline{v} + \underline{w} \right] = U \tag{4.23}$$

and similarly for the electrons, where the terms on the LHS include directed energy, thermal energy, work and heat flux terms, and U is the net volumetric heat source for the particular species. Although viscosity may be important in the momentum equation, viscous heating is generally small and has been neglected.

This equation is then simplified further. Since parallel motion along field lines is much faster than perpendicular motion, only parallel heat transfer is calculated through Eqn.(4.23). Cross-field heat transfer is estimated separately by a semi-empirical model. The ion and electron equations are added to obtain a total parallel energy balance

$$\frac{d}{dz}\left[(5 + M^2) T\Gamma + w \right] = \frac{Q}{V_s} \tag{4.24}$$

where $v = Mc$; $p = nT$ (for each species); $m_e \ll m_i$; and Q is the net energy carried by parallel transport (i.e. energy convected and conducted in from core minus radiated energy, perpendicular transport, and cooling from neutral interactions), and assumed to be uniform throughout the edge plasma volume V_s.

In the scrape-off layer, it is assumed that the heat flux can be written as a conductive term, $w = -k(dT/dz)$ where $k = k_0 T^{2.5}$ is the classical plasma thermal conductivity, and that the particle source is uniform along z so $d\Gamma/dz = \dot{N}_{sd,i}/V_s$. Thus Eqn.(4.24) becomes a second order non-linear differential equation for $T(z)$. Since the intent here is

only to obtain an average plasma temperature consistent with the heat flux that must be removed in steady-state, the equation is even further simplified. In particular, an average temperature $T_{s,i}$ is used in the convective term, although the derivatives are retained in the conductive term because they are necessary to calculate conduction. Equation (4.24) then becomes, for the scrape-off,

$$\frac{d}{dz}\left(k_0 T^{2.5}\frac{dT}{dz}\right) - \frac{\eta T_{s,i}\dot{N}_{sd,i}}{V_s} + \frac{Q_{sd,i}}{V_s} = 0; \quad \left.\frac{dT}{dz}\right|_0 = 0 \tag{4.25}$$

where

$$k_0 = \frac{148\epsilon_0^2}{e^4 m_e^{0.5}\ln\Lambda}$$

and $N_{sd,i}$ or $Q_{sd,i}$ are the net parallel particle or energy source/sink rate into this steady-state scrape-off layer plasma; and $\eta_{s,i} \simeq 5$ (since $M_{s,i}^2 \ll 1$) is the convective heat transfer enhancement factor. This is easily solved for T, yielding

$$T_{s,i}^{3.5} = T_{d,i}^{3.5} + \frac{7L_{s,i}^2}{4k_0}\left(\frac{Q_{sd,i}}{V_s} - \frac{\eta_{s,i}T_{s,i}\dot{N}_{sd,i}}{V_s}\right) \tag{4.26a}$$

or

$$T_{s,i} = \frac{k_0 T_{d,i}^{3.5} + 1.7L_{s,i}^2 Q_{sd,i}/V_s}{k_0 T_{s,i}^{2.5} + 1.7L_{s,i}^2\eta_{s,i}\dot{N}_{sd,i}/V_s} \tag{4.26b}$$

where T is evaluated at $z = 0$. Equation(4.26b) can be solved iteratively for $T_{s,i}$.

In deriving Eqn.(4.26) from Eqn.(4.24), it was assumed that the parallel heat flux term w could be written in the form $w = -k(dT/dz)$ where k was the thermal conductivity. This is certainly reasonable in a collisional plasma, $\lambda/L \ll 1$, where λ is the collision mean free path and L is the characteristic parallel length. However it is quite possible for the edge plasma to be neither fully collisional nor collisionless, but somewhere between the extremes, $0 < \lambda/L < \infty$.

By definition, the heat flux vector is defined for monatomic particles as $\underline{w} = \frac{1}{2}m\int|\underline{u} - \underline{v}|^2\underline{u}f(\underline{u})d^3u$ where $\underline{v}$ is the bulk velocity [4.42]. That is, $\underline{w}$ represents heat transported by particles in the co-ordinate system where the bulk velocity is zero. The total heat transfer in the laboratory co-ordinates, of course, is related to this plus the heat convected by all particles moving at the bulk velocity. Thus w may be small but is not in general zero, even if the flow is collisionless or if the particles are all moving in one direction.

The classical derivation of thermal conductivity assumes collisional flow in a near-equilibrium situation, where a temperature difference dT exists between two points separated by a distance dz. In the collisional regime, $\lambda \ll dz$ so particles at each point are in equilibrium with the local temperature. Thus particles moving from the hotter region to the colder region will transfer more energy than the equivalent flux of particles flowing back, leading to a net energy flow from the hotter region of the form $w = -k(dT/dz)$. The thermal conductivity is easily derived in this case, or can be heuristically obtained by noting that the heat transfer is diffusive with step size λ and time $\tau = \lambda/c$ where c is the local particle speed or sound speed, so $k \approx n\lambda^2/\tau \approx nc\lambda$ [4.18]. As the mean free path λ gets comparable to the system dimension L, the collisions are not with particles λ apart, but with the system boundaries at a distance L. The particles flowing in each direction are in equilibrium with the boundaries a distance L apart, so $w \approx -k(\lambda_{effective}/\lambda)(T_L - T_0)/L$, where $\lambda_{effective} \approx (1/\lambda + 1/L)^{-1} = \lambda/(1 + \lambda/L)$ is the effective collisional step size.

As a further argument, though certainly not definitive, consider the results of more rigorous calculations of shear stress (or momentum transfer) in linear Couette flow with no net flow and assuming a two-stream Maxwellian velocity distribution, which show that viscosity μ scales as $1/(1 + 2\lambda/L)$ over all λ/L [4.18]. Since μ/k is constant in the collisional limit, a more correct accounting of the collisionality might be obtained by replacing k with $k/(1 + 2\lambda/L)$. In the scrape-off layer, $L = L_{s,i}$ and λ is the electron collisional mean free path λ_{ee} since electron parallel conductivity dominates.

Thus the heat flux w is correctly described for collisional plasmas, and is approximately described for collisionless plasmas by the use of an effective thermal conductivity. The approximation is expected to be reasonable when there is an appreciable flux of particles in each direction (reasonable if $M \ll 1$) and where the particle source in each direction is roughly Maxwellian (a reasonable assumption for edge plasmas). It should be noted that this effective thermal conductivity is not used to calculate a temperature distribution along the scrape-off (which would make no sense if $\lambda \gg L$) but rather to estimate the conduction-like heat flux between two regions of edge plasma at differing temperatures.

Classically, $\lambda_{ee} = 1/n_e\sigma$ where σ is the Coulomb collision cross-section for energy transfer (Eqn.3.9). It is worth mentioning "Langmuir's paradox" at this point, which refers to Langmuir's early observation that electrons (in a mercury discharge with $T_e \sim 10eV$)

were anomalously collisional. It was subsequently thought that electrons along a given magnetic field line had a strictly Maxwellian distribution function, even at very high energies. However the process that affected the electron distribution - apparently plasma sheath oscillations - did not hold at higher temperatures [4.19]. Here, the classical value for λ_{ee} is used.

In the divertor region, the plasma parallel flow contacts the material target and so the energy and particles must ultimately flow through the electric field that forms in a thin deBye sheath region in front of the target. In this sheath, the ion and electron densities and energies are not equal and the velocity space distributions are substantially non-Maxwellian. Rather than analyze this region in detail, it is treated as a special boundary condition to Eqn.(4.24). In particular, we take $q_{dt,i}$ proportional to $T_{d,i}\Gamma_{dt,i}$ and solve to obtain

$$T_{d,i} \simeq \frac{Q_{dt,i}}{\eta_{d,i}\dot{N}_{dt,i}} = \frac{Q_{dt,i}}{\eta_{d,i}\Gamma_{dt,i}A_{di}} \tag{4.27}$$

The heat flux $\eta_{d,i}\Gamma_{dt,i}T_{d,i}$ now includes a convective part, $(5+M^2)T_{d,i}\Gamma_{dt,i}$ where $M \simeq 1$ at the target, and the effect of the sheath, about $3T_{d,i}\Gamma_{dt,i}$ (depending on secondary electron emission). From more careful analysis, values for $\eta_{d,i}$ from 6 to 10 are expected [4.47,4.54] and are experimentally observed (4–10 DIVA [4.2], 8 ASDEX [4.4], 6–15 DITE MK1B [4.5]). DITE (and other machines) also observed values as high as 200 during operation with their MK1A bundle divertor, but this was attributed to superthermal electrons [4.5]. In this model, $\eta_{d,i} \simeq 10$ is used.

4.2.3 Edge Plasma (Scrape-off and Divertor) - Perpendicular Transport

The ion perpendicular transport across the field lines and into the walls is described by a cross-field diffusion coefficient. In some studies, it is described as $D_\perp \approx 1/n_e$, i.e. classical cross-field scaling (DITE MK1B [4.5]). In general, however, transport scaling at the edge is understood much less than transport scaling in the plasma core. For example, the theoretical picture is complicated by the observed strong fluctuations, plasma turbulence and reactions with edge neutrals. Experimentally, density and temperature fall off roughly exponentially (or slower) with characteristic scale lengths that are in rough agreement with $D_\perp \approx 0.1 - 1\, D_{Bohm}$ ([4.54],0.1 DIVA [4.2], 0.1 T-12 [4.3], 0.6 ASDEX [4.4], 3. PDX [4.7], 1. ALCATOR-C [4.9]). In this analysis, it is assumed that $D_\perp \simeq f_B D_{Bohm} = f_B T_e/16eB$, where $f_B \approx 1$ for particle diffusion. The scale lengths for energy are of the same order

as the density scale lengths [4.10], $(f_B)_{energy} \approx (f_B)_{density}$. With these assumptions, the density and temperature fall off with scale lengths

$$\delta_{s,i} = \sqrt{\frac{(f_B)_{density} D_{Bohm} L_{s,i}}{M_{s,i} c_{s,i}}}; \quad \delta_{s,T} = \sqrt{\frac{(f_B)_{energy} D_{Bohm} L_{s,i}}{M_{s,i} c_{s,i}}} \tag{4.28a}$$

Similar expressions are used to determine the additional spreading in the divertor region,

$$\delta_{d,i} = \sqrt{\delta_{s,i}^2 \frac{B_s}{B_d} + \frac{(f_B)_{density} D_{Bohm} L_{d,i}}{M_{d,i} c_{d,i}}}; \quad \delta_{d,T} = \sqrt{\delta_{s,T}^2 \frac{B_s}{B_d} + \frac{(f_B)_{energy} D_{Bohm} L_{d,i}}{M_{d,i} c_{d,i}}} \tag{4.28b}$$

These expressions assume parallel transit times given simply by $\tau_{||} \approx L/v_{||}$. There are two complicating factors here - mirror effects and neutral reactions. In the first case, the magnetic mirror at a bundle divertor throat (about 3 in DITE Mark 1) can reflect a reasonable fraction of the ions and so increase $\tau_{||}$. However, if the correct $v_{||}$ is used - $v_{||} = Mc$ where the Mach number accounts for mirroring effects - the expression is still correct. Furthermore, strong mirror microinstabilities are likely to help fill in the mirror loss cone such that the particle loss rate is somewhat independent of the mirror [4.44]. Secondly, since the ionization of the neutrals will tend to broaden the density profile [4.45], a better expression for the scale lengths $\delta_{s,i}$ or $\delta_{d,i}$ might be with an effective time $\tau \approx \tau_i \tau_{||}/(\tau_i + \tau_{||})$ where $\tau_i = 1/n_{neutral}\langle\sigma v\rangle_{ei}$. Here, this effect is indirectly included through f_B, the fraction of Bohm diffusion, since the value of f_B is based on experimentally measured $\delta_{s,i}$ in machines such as ASDEX where neutral ionization may be significant.

Given exponential particle and energy profiles, the perpendicular flux to the walls in diverted discharges is roughly the fraction of the profile that extends beyond the wall radius,

$$\dot{N}_{sw,i} = e^{-d_s/\delta_{s,i}}(\dot{N}_{sd,i} + \dot{N}_{sw,i}) = \frac{\dot{N}_{sd,i}}{e^{d_s/\delta_{s,i}} - 1} \tag{4.29a}$$

$$\dot{N}_{dw,i} = e^{-d_d/\delta_{d,i}}(\dot{N}_{dt,i} + \dot{N}_{dw,i}) = \frac{\dot{N}_{dt,i}}{e^{d_d/\delta_{d,i}} - 1} \tag{4.29b}$$

where $a + d_s$ is the limiter or wall radius, or d_s is the minimum distance between the separatrix and the first wall (or back-up limiter); and d_d is the minimum width of the divertor channel.

The energy flux to the walls, $Q_{sw,i}$ and $Q_{dw,i}$, is similarly the fraction of the flux extending beyond d, except that $\delta_{s,T}$ and $\delta_{d,T}$ are the characteristic temperature scrape-off lengths which are assumed to correspond more closely to the power profile.

In divertor or limiter discharges, the particle and energy fluxes to the first wall itself are usually sufficiently small that the exact values of the scale lengths are not critical. However in pumped limiter discharges, the bulk of the flow of particles and power strike the limiter front surface and leading edge - typically only 10% or so might actually pass behind into the limiter ducting (e.g. 8% ALCATOR-DCT [4.28]).

So for pumped limiters, $N_{sw,i}$ and $Q_{sw,i}$ have slightly different definitions from the divertor case. In particular, $N_{sd,i}$ (or $Q_{sd,i}$) is still the particle (or energy) flux into the limiter duct, but $N_{sw,i}$ (or $Q_{sw,i}$) is the particle (or energy) flux onto the limiter face and leading edge. Any diffusion flux to the first wall itself is neglected. All the preceding analysis is still correct. However $N_{sw,i}$ and $Q_{sw,i}$ are now the fraction of the flux that extends between $r = a$ and $r = a + d_{PL}$, where $a + d_{PL}$ is the outer radial distance of the pumped limiter leading edge from the plasma center,

$$\dot{N}_{sw,i} = (1 - e^{-d_{PL}/\delta_{s,i}})(\dot{N}_{sd,i} + \dot{N}_{sw,i}) = (e^{d_{PL}/\delta_{s,i}} - 1)\dot{N}_{sd,i} \qquad (4.30)$$

and similarly for $Q_{sw,i}$. Furthermore, $\dot{N}_{dw,i}$ and $Q_{dw,i}$ are not explicitly treated, but are included in the $N_{dt,i}$ and $Q_{dt,i}$ terms.

It should be noted that d_{PL} as used in Eqn.(4.30) is not always well-defined - in particular, for discrete flat limiters where different points on the leading edges are at different radii from the plasma core. This distinction can be significant because the particle and power crossing into the limiter slot is exponentially dependent on the minor radial position of the leading edge. This problem does not occur for toroidally continuous limiters or for poloidally shaped limiters.

In addition to particle and energy transport across field lines by convection and conduction, radiation losses may also be important in the edge regions. This is calculated ($Q_{s,r}$ and $Q_{d,r}$) using coronal equilibrium values for impurities and an enhanced ionization estimate for hydrogen as described in Section 3.3.

4.2.4 Edge Neutral Transport

It is expected that a large fraction of the ions and neutrals striking the walls or target will recycle as uncharged molecular hydrogen. Here it is assumed that all particles

recycle as H_2 at the wall temperature, which then promptly dissociate in the presence of the plasma electrons to form $2H$, each with a Franck-Condon dissociation energy of about 3 eV (from the reaction data of Section 3.1, H is more likely than H^+ by about a factor of 2.5 over 1 - 100 eV). The neutral density calculated in this model thus refers to the atomic hydrogen density. If the particles that recycle from the wall as hot neutrals are included, the average energy of the atoms is given by $E = (1 - R_N)E_d + R_N R_E E_0$, where R_N and R_E are the particle and energy reflection coefficients defined in Section 3.2.2, $E_d \approx 2 - 4$ eV is the dissociation energy and E_0 is the incident ion energy. Since $R_N R_E E_i \approx 1.5 - 2$ eV for $30 < E_i < 200$ eV, the assumption that $E \approx 3$ eV is still reasonable [4.43]. A more complete discussion of the surface and dissociation reactions is given in Chapter 3.

The neutrals are assumed to be fully randomized. Then the flux of neutrals crossing unit area in one direction is $\Gamma = n\bar{v}/4$ where $\bar{v} = \sqrt{8T/\pi m}$ is the average particle speed [4.39]. This is not quite correct since there will in general be net flows of neutrals (into the pumps, for example) which will perturb the velocity distribution from an isotropic Maxwellian. However, the neutrals will be sourced largely by diffusion off the walls with Maxwellian speeds and approximately isotropic directions (averaging over all the surfaces) and in the molecular conductance (collisionless) regime expected, will not be aware of a net flow in any particular direction.

The bulk neutrals are not a major pathway for energy transfer, so are only simply modelled here based on the convective heat flux, $q = \frac{3}{2}T\Gamma$ where $\frac{3}{2}T$ is the average energy per atom assuming H behaves like an ideal monatomic gas [4.39]. Thermal conduction should be small in the low pressure, molecular flow regimes expected. Heat carried off by charge-exchange neutrals can be a major heat sink, but for these the energy is certainly carried off convectively so the expression is still valid. Thus,

$$\Gamma_{d,n} = \frac{n_{d,n}}{4}\sqrt{\frac{8T_{d,n}}{\pi m}} \tag{4.31a}$$

$$\Gamma_{s,n} = \frac{n_{s,n}}{4}\sqrt{\frac{8T_{s,n}}{\pi m}} \tag{4.31b}$$

$$q_{d,n} = \frac{3}{2}T_{d,n}\Gamma_{d,n} \tag{4.32a}$$

$$q_{s,n} = \frac{3}{2} T_{s,n} \Gamma_{s,n} \tag{4.32b}$$

The neutral fluxes to the first wall, divertor wall and divertor target are simply

$$\dot{N}_{sw,n} = \Gamma_{s,n} A_{fw} \tag{4.33}$$

$$\dot{N}_{dw,n} = \Gamma_{d,n} A_{dw} \tag{4.34}$$

$$\dot{N}_{dt,n} = \Gamma_{d,n} A_{tn} \tag{4.35}$$

A more accurate expression is used for the important neutral flux to the pump ports - ionization within the plasma channel is accounted for. This effect might be approximated by $e^{\delta_{d,i}/\lambda_d}$, where λ_d is the net mean free path for ionization or charge-exchange in the divertor, $1/\lambda_d = 1/\lambda_{d,ei} + 1/\lambda_{d,cx}$. However, this assumes that the neutrals cross the full plasma channel thickness and results in very low escape probabilities for some cold, dense plasmas. In these cases, the escape probability is dominated by neutrals recycling from the target at the edge of the plasma channel, as illustrated by Harrison et al [4.53] for the INTOR poloidal divertor. Without repeating their more complex and geometry-specific analysis, the escape probability can be simply estimated by assuming recycling occurs uniformly over the target and finding the integrated average attenuation,

$$\dot{N}_{d,p} = \Gamma_{d,n} A_p \int_0^{\delta_{d,i}} \frac{1}{\delta_{d,i}} e^{-(\delta_{d,i}-x)/\lambda_d} dx = \Gamma_{d,n} A_p \frac{\lambda_d}{\delta_{d,i}} (1 - e^{-\delta_{d,i}/\lambda_d}) \tag{4.36}$$

The cold neutral flow rate across the separatrix into the plasma core is the random neutral flux across the separatrix, corrected for attenuation through the scrape-off plasma,

$$\dot{N}_{sc,n} = \Gamma_{s,n} A_s e^{-G_{sc,n}\delta_{s,i}/\lambda_s} \tag{4.37}$$

Some fraction $f_{sc,cx}$ of the scrape-off charge exchange neutrals also penetrate into the core and ionize, the rest are assumed to strike the wall. This probability is likely to be different from 50% partly because of the geometry and partly because core-directed neutrals have a larger chance of further charge exchanging or ionizing within the scrape-off layer. Here $f_{sc,cx} \approx 0.33$ is assumed.

In the scrape-off, the electron impact and charge exchange rates are

$$\dot{N}_{s,ei} = \Gamma_{s,n} A_s (1 - e^{-G_{sc,n}\delta_{s,i}/\lambda_s}) \frac{\lambda_{s,cx}}{\lambda_{s,cx} + \lambda_{s,ei}} \tag{4.38a}$$

$$\dot{N}_{s,cx} = \Gamma_{s,n} A_s (1 - e^{-G_{sc,n}\delta_{s,i}/\lambda_s}) \frac{\lambda_{s,ei}}{\lambda_{s,cx} + \lambda_{s,ei}} \tag{4.38b}$$

where A_s is the separatrix area; $\delta_{s,i}$ is the scrape-off density scale length (Eqn.4.28a); the mean free path ratios are the reaction fractions for ionization and charge exchange; λ_s is the net mean free path for ionization plus charge exchange in the scrape-off, $1/\lambda_s = 1/\lambda_{s,ei} + 1/\lambda_{s,cx}$; and the neutral geometry factor $G_{sc,n}$, accounts for the random neutral motion - i.e. the flow is not necessarily directly radially inward from the first wall.

The net neutral flux from the divertor region to the scrape-off region is the random neutral flux through the divertor throat in each direction, corrected for attenuation by interactions with the plasma - in particular, ionization and charge-exchange. In ionization, the resulting ion is promptly swept along with the plasma flow by Coulomb collisions and by the electrostatic field in the divertor. In charge-exchange, the resulting hot neutral is assumed to be confined to the divertor. Thus, in either reaction, the initial neutral is pulled back to the target and does not contribute to neutral flow out of the divertor.

$$\dot{N}_{ds,n} = \Gamma_{d,n} A_{dn} e^{-G_{ds,n} L_{d,n}/\lambda_d} - \Gamma_{s,n} A_{dn} e^{-\delta_{s,i}/\lambda_{s,ei}} \tag{4.39}$$

where $L_{d,n}$ is the direct length from the target to the divertor throat; $G_{ds,n}$ is a geometry factor accounting for the increased path length travelled by a neutral as it bounces from wall to wall; and $\lambda_{s,ei}$ is the mean free path for ionization in the scrape-off layer (charge exchange neutrals continue into the divertor so are not attenuated).

The choice of geometry factors $G_{sc,n}$ and $G_{ds,n}$ for the scrape-off and divertor is complex. If the particle flux is travelling straight through a plasma slab of thickness d and mean free path λ, the fraction expected to pass through is $\Gamma_{direct}/\Gamma_{initial} = \exp(-d/\lambda)$. However, if the particles are not all travelling straight through the plasma, or if it is not a slab, or if the mean free path varies, or if molecular dissociation is included, the actual fractional flux may be quite different. The geometry factors are a simple attempt to relate the actual flux to the direct flux from $\Gamma_{actual}/\Gamma_{initial} \approx \exp(-Gd/\lambda)$ where G can, ideally, be prescribed by some simple formula.

In order to evaluate the neutral particle geometry factors, particularly with the full reaction chemistry and geometry, a 3-D Monte Carlo neutral transport code (described in Chapter 6) was used. The scrape-off was modelled as an infinite slab of uniform plasma. Hydrogen molecules at wall temperature were launched with a cosine distribution in angle, and the particles were tracked through dissociation, charge exchange and ionization. A range of cases were considered, ranging from $0.02 < d < 0.04$ m, $3 \times 10^{16} < n < 3 \times 10^{20}/\mathrm{m}^3$, and $10 < T_e < 1000$ eV which spanned over $0.0024 < d/\lambda_H < 24$ and $0.017 < d/\lambda_{H_2} < 170$. It was found that the geometry factor for this configuration could be reasonably described as a simple function $G \approx 1 + 2(\lambda/d)^{0.544}$ over the range of interest $0.001 < d/\lambda_H < 100$ (see also the more detailed discussion in Chapter 6).

This infinite slab with uniform plasma is a reasonable model for the scrape-off where the curvature is usually larger than the particle mean free path, and where average values for density and temperature are used. It is not so clearly a model for more complicated geometries such as in the divertor. However, it is assumed here that the geometry factor is similar on the basis of d/λ_H. Thus $G_{sc,n} \approx 1 + 2(\lambda_s/\delta_{s,i})^{0.544}$ and $G_{ds,n} \approx 1 + 2(\lambda_d/L_{d,n})^{0.544}$ where $\lambda_s, \lambda_d, \delta_{s,i}$ and $L_{d,n}$ have been defined earlier. In the limit of large mean free paths, these expressions reduce to $G \approx 1$. This value is often assumed in simple estimates of scrape-off shielding efficiency [4.6].

In principle, not all of a neutral's trajectory will be in plasma. In some divertor geometries, there may be a clear path for neutrals to recycle back to the scrape-off without being attenuated through the incoming plasma. However, any direct paths back to the scrape-off are generally only a small fraction of the total neutral flow area, and the more likely paths involve bouncing between walls down channels that are largely filled with plasma. Since it is desirable to keep neutrals from backflowing into the main plasma chamber (to build up neutral pressure in the divertor and to prevent sputtered impurities from contaminating the core plasma), most divertors would naturally make the channels just large enough to hold the influx of plasma. Thus Eqn.(4.39), which does not allow for direct recycling paths for neutrals from divertor to scrape-off, is a reasonable model for reactor conditions.

In the divertor, the reaction rate expressions are similar to those in the scrape-off

$$\dot{N}_{d,ei} = \Gamma_{d,n}\overline{A_{dn}}(1 - e^{-G_{ds,n}L_{d,n}/\lambda_d})\frac{\lambda_{d,cx}}{\lambda_{d,cx} + \lambda_{d,ei}} \qquad (4.40a)$$

$$\dot{N}_{d,cx} = \Gamma_{d,n}\overline{A_{dn}}(1 - e^{-G_{ds,n}L_{d,n}/\lambda_d})\frac{\lambda_{d,ei}}{\lambda_{d,cx} + \lambda_{d,ei}} \tag{4.40b}$$

where $\overline{A_{dn}} = (A_{dn} + A_{tn})/2$. Furthermore, since one divertor target option may be a dense gas jet or gas target, electronic recombination is included

$$\dot{N}_{d,er} = \Gamma_{dt,i}\overline{A_{di}}(1 - e^{-L_{d,i}/\lambda_{d,er}}) \tag{4.41}$$

where $\overline{A_{di}} = (A_{di} + A_{ti})/2$.

Some fraction of the hot charge-exchange neutrals may escape the divertor region. This is estimated as

$$f_{ds,cx} \approx \frac{A_{dn}}{A_{dn} + A_{tn} + A_p + A_{dw}}(1 - M_{d,i})$$

where the area ratio estimates the solid angle of the divertor throat relative to all the surrounding surfaces, and the Mach number factor roughly accounts for the charge-exchange neutral's directionality. This expression neglects multiple reactions.

The mean free paths for the various reactions are simply given by

$$\lambda_{s,cx} = \frac{1}{n_{s,i}\langle\sigma v\rangle_{s,cx}}\sqrt{\frac{8T_{s,n}}{\pi m}};\ \lambda_{d,cx} = \frac{1}{n_{d,i}\langle\sigma v\rangle_{d,cx}}\sqrt{\frac{8T_{d,n}}{\pi m}} \tag{4.42a}$$

$$\lambda_{s,ei} = \frac{1}{n_{s,i}\langle\sigma v\rangle_{s,ei}}\sqrt{\frac{8T_{s,n}}{\pi m}};\ \lambda_{d,ei} = \frac{1}{n_{d,i}\langle\sigma v\rangle_{d,ei}}\sqrt{\frac{8T_{d,n}}{\pi m}} \tag{4.42b}$$

$$\lambda_{d,cr} = \frac{1}{n_{d,i}\langle\sigma v\rangle_{d,er}}M_{d,i}\sqrt{\frac{2T_{d,i}}{m_i}} \tag{4.42c}$$

Finally, consider the divertor pumping system. Possible mechanisms include passive systems such as cryopumps or gettered surfaces, and active devices such as turbomolecular or diffusion pumps. The pumping rate of divertor chambers is usually specified as a speed S in m^3/s for H_2. Practical values range from 10 m^3/s for a set of turbomolecular pumps to 10^3 m^3/s for a heavily gettered divertor chamber. Pumping speeds are related to the particle flow rate and density through $S = f\dot{N}/n$, where $\dot{N}$ is the rate of particles striking the pump area (e.g. surface area for a titanium getter, entrance aperture area

for a turbomolecular pump), n is the particle density just outside the pump, and f is the pumping or absorption probability. Typical condensation coefficients for cryopumps are around 0.5 - 0.8; initial sticking coefficients for H_2 or D_2 on titanium getter are 0.05 - 0.2; and the pumping fractions for H_2 or N_2 in turbomolecular pumps are around 0.02 - 0.4 [4.21].

In this edge model, hydrogen is assumed to recycle from surfaces largely as molecular hydrogen at 0.025 eV, but to then promptly dissociate into 3 eV atomic hydrogen in the plasma region. This atomic hydrogen is then explicitly treated in the model. However in the pumps, the bulk of the flow should be molecular hydrogen. Thus a relationship must be defined between the atomic hydrogen flux and the molecular pumping speed,

$$S = \frac{f_{d,p}\dot{N}_{d,p}}{n_{d,n}} = \frac{f_{d,p}\Gamma_{d,n}A_p}{n_{d,n}} \tag{4.43}$$

where $\dot{N}_{d,p} = \Gamma_{d,n}A_p$ is the atomic hydrogen flux to the pumps, $n_{d,n}$ is the atomic hydrogen density in the divertor, and $f_{d,p}$ is the effective pumping speed for the atomic hydrogen taking into account that it is actually pumped as cold molecules. The hydrogen gas pressure in the divertor, $p_d = n_{H_2}T_{H_2}$, can be estimated assuming the recycling particle flux from the divertor walls is as thermalized molecules,

$$n_{H_2} = \frac{R_w[\dot{N}_{dw,n} + \dot{N}_{dw,i} + (1 - f_{ds,cx})\dot{N}_{d,cx}] + (1 - f_{d,p})\dot{N}_{d,p}}{2(A_{dw} + A_p)\sqrt{T_{H_2}/\pi m_i}} \tag{4.44}$$

Converting the incident atom flux to a molecular flux, then $f_{d,p} \simeq f_{H_2}\sqrt{T_{H_2}/2T_{d,n}}$ where $T_{H_2} \simeq 0.025$ eV and $f_{H_2} \approx 0.01 - 0.8$ is the molecular pumping fraction.

4.3 Comparison with Experiments

The plasma edge is still a poorly diagnosed region, and there is much room for error in translating the few local (and sometimes indirect) measurements into specific edge parameters. For example, poloidal and toroidal symmetry are often assumed so local power measurements at a few points can be extrapolated over the entire vacuum chamber to obtain total power. Furthermore, not all energy loss channels are measured. Thus it is not surprising that energy balances are often incomplete by 10 - 50% (e.g. ASDEX [4.4]).

A second and related problem is in collecting a self-consistent set of measured edge parameters. The data that exists was often obtained over many shots with a range of conditions such as core density and temperature, edge safety factor, and heating power. Thus some judgement is necessary in putting together a set of consistent edge parameters. For example, there was little data on impurities in the edge plasma, other than that oxygen was usually observed. In the comparisons in this chapter, 0.5% oxygen was assumed as a representative impurity.

Finally, and of particular interest here, is the accuracy of the models used in this analysis. Since they are simple 0–D models, an exact quantitative agreement is not expected even if the above two problems were resolved.

This edge model was compared with several divertor experiments to check its validity. In particular, discharges in ASDEX, DITE, and PDX were evaluated. These are all large devices with reasonably diagnosed edge plasmas. The machines are illustrated in Figure 4.2 and major parameters are given in Table 4.2.

4.3.1 ASDEX

ASDEX is a double-null poloidally diverted tokamak [4.4,4.11–4.13]. Its basic structure is illustrated in Figure 4.2a and the major machine parameters (some inferred) for the discharges of interest here are given in Table 4.2. ASDEX can operate in several modes, including diverted (D) discharges and diverted–plus–pumped (DP) discharges. These shots use both divertor chambers and have the same basic plasma characteristics, the difference being that the divertor chamber is coated with titanium getter before each DP discharge so as to provide very high pumping speeds.

Experimental data for representative ASDEX D and DP discharges are shown in Table 4.3, as are measurements and calculated values inferred from the literature. Also shown in Table 4.3 are the edge model results for similar discharges. In addition to the machine parameters in Table 4.2 and the flow models described earlier, certain plasma parameters were fixed for the comparison, notably the main plasma conditions.

The actual D discharges did not reach equilibrium because of the low divertor pumping speed, so the divertor neutral density increased with time as the plasma flowed into and filled up the divertor chamber. Since the present model is steady–state, two D discharges were crudely simulated by: (1) assuming equilibrium was reached; and (2) enhancing

the pumping speed. In the low density shot, the 15 m^3/s from the eight turbomolecular pumps was assumed, thus giving long-term equilibrium values. This may explain the lower calculated particle flow rates relative to the experimental values. The higher density shot was simulated with an effective divertor chamber pumping speed of 200 m^3/s to approximately represent the short term "pumping" associated with filling the divertor chamber and the walls. The DP discharges were straightforward to simulate because the high (10^3 m^3/s) pumping quickly brought conditions to equilibrium.

Other difficulties in modelling ASDEX were in obtaining the correct particle and convective/conductive energy losses from the plasma core, as described by Eqns. (4.11) and (4.12). First, while volume-averaged particle and energy densities are assumed in this analysis, usually line-averaged or central values are given in the literature. Consequently, in a purely parabolic profile for example, the line-averaged density is 1.3 times larger than the volume-averaged density. Secondly, the electron and ion temperatures are often quite different in present experiments yet are assumed equal in this model. Thirdly, the exact values of the energy and particle confinement times are not well known nor are they necessarily defined the same way as used here. Thus, in determining the plasma characteristics used in the simulations, representative core ion density, temperature and confinement times were chosen, taking some profile effects into account and making sure that reasonable agreement was obtained with the experimental heating power.

With all the above qualifications, the overall agreement is reasonable - a dense, cold, diverted edge plasma was observed and is predicted by the 0-D model. The basic particle and energy flows are also consistent, within a factor of three for energy and a factor of ten in density. The simulation with 200 m^3/s effective pump speed yields a much better match with experimental densities.

4.3.2 DITE

DITE is a bundle diverted tokamak [4.5,4.14–4.17]. The basic structure of the divertor is illustrated in Figure 4.2b and the geometry is given in Table 4.2. It has tested three bundle divertors, designated Mark 1A, Mark 1B and Mark 2 respectively. The first two were identical solenoidal coil divertors, although the second one was used on an upgraded DITE tokamak. The third (and present) divertor is similar in style but much improved in the engineering.

Table 4.4 compares the model to DITE experimental results. Reasonable agreement is obtained in all cases, although $\eta_{d,i} \approx 200$ was used in Mark 1A, consistent with the experimentally measured heat transfer enhancement factor. This higher value was attributed to suprathermal electrons. DITE Mark 1B also could operate with titanium gettered first walls. Experimentally, this noticeably reduced impurities, but in this hydrogen edge model the effect was primarily to increase the gas fuelling rate.

4.3.3 PDX

PDX, like ASDEX, is a tokamak with a poloidal divertor [4.7]. The basic structure is shown in Figure 4.2c and described in Table 4.2. PDX has four poloidal divertor coils so can operate in several modes. The data used here are for the double-null inside D (standard Dee) configuration without neutral beam heating.

Table 4.5 compares experimental data to the 0–D model. The plasma temperatures are in good agreement, plasma densities and divertor neutral pressure agree within a factor of a few, and particle flow rates are within an order of magnitude. Most of the power is calculated as reaching the target, consistent with measurements.

4.4 Applications

From the comparisons in the previous section, the 0–D edge model seems capable of describing the edge conditions in current diverted tokamak experiments. The general agreement seems to be about a factor of two in power and temperature, and an order of magnitude in density and particle flux, not inconsistent with the experimental error in determining these edge parameters. However it is emphasized that this does not validate the details of the model, but does indicate consistency with present experiments.

In this section, the model is applied to future machines to estimate their edge characteristics and the effect of different edge control options such as poloidal divertor, bundle divertor and pumped limiter. In particular, a proposed near-term experiment ALCATOR–DCT and a longer-term reactor-relevant machine INTOR are examined.

Once the basic machine and core plasma conditions have been defined, the edge conditions are only functions of the divertor geometry, the mode of fuelling, and the divertor pumping system. In the following applications, reference bundle divertor, poloidal

divertor and pumped limiter geometries are defined for each machine and the resulting edge conditions investigated.

4.4.1 INTOR

INTOR, the International Tokamak Reactor, is a conceptual design that would include reactor-relevant plasmas and the associated technology. The design has progressed through several stages and has considered bundle divertors, pumped limiters and, in the current reference design, poloidal divertors. The main machine parameters are given in Table 4.6. INTOR is an ignited machine so DT fuelling and alpha particle heating are assumed.

In the most recent INTOR report, Phase-2A [4.27], various operating modes for poloidal divertors and pumped limiters were considered: (1) a low density, high temperature regime; (2) a medium density and temperature regime; and (3) a low temperature, high density regime. Under INTOR conditions, these regimes correspond, for example, to edge temperatures of 1300 eV, 150 eV and 30 eV and densities of $10^{18}/m^3$, $10^{19}/m^3$ and $10^{20}/m^3$, respectively.

The consequences of operating in any particular regime can be substantial. Under hot edge conditions, assuming a $3T_e$ drop through the sheath, hydrogen will strike the divertor target with energies of a few keV, and multiply charged impurities will strike with 10 keV energies. Since the sputtering probability peaks at around 1 keV (see Section 3.2.3), and since the same power is transmitted by fewer particles than at lower edge temperatures, sputtering can be reduced. However, high Z materials have self-sputtering coefficients larger than unity in the keV or larger energy range so such a hot edge would best be designed with low Z materials. Under cold edge conditions, particles strike the target with energies 30 - 300 eV which, if not actually below sputtering thresholds, at least cause limited direct or self-sputtering for any material. The intermediate edge, however, corresponds to particle incident energies of several hundred eV to a few keV, right at the maximum in the sputtering cross-section. This edge temperature would cause very high sputtering and require rapid replacement of eroding surfaces or balanced redeposition (where the sputtered material local redepositing rate counters the local sputtering rate).

Besides the direct effect on sputtering rates, the edge conditions affect other engineering considerations. Unipolar arcing can occur if the potential difference between a

wall and the plasma is several keV. Thus this might be limiting in the case of high edge temperatures with a $3T_e$ sheath potential drop. Also, hot, low density edges are likely to be collisionless. Under these circumstances, the plasma is not necessarily Maxwellian. Interactions with recycling neutrals can occur on fast time scales and the resulting distribution functions may alter the usually assumed monotonically decreasing presheath electric field [4.36]. This possibility, and some consequences, are considered in Chapter 5 using a 1-D kinetic transport model.

A further advantage of low temperature, high density edge conditions is that radiation and charge exchange are enhanced and can transfer power from the streaming plasma onto the divertor walls, rather than concentrating it on the target. The conditions in this cool edge have been considered in several studies [4.4,4.48–4.50], and the existence of localized regions with these properties has been experimentally confirmed [4.51,4.52].

Regardless of which regime is preferred, there is some question as to how each could be achieved, if at all. A gross simplification would argue that pellet fuelling causes hot edge conditions, gas puffing causes medium edges, and radiation cooling may be necessary for cold edges [4.27]. However, it is not clear that the hot or medium edge would be stable, since the high sputtering rate would sharply increase impurities and thus radiation cooling. This could quickly bring the edge down to the cold condition, but it is not certain whether the associated impurity concentrations would hurt the central plasma.

Poloidal Divertor

Calculated edge conditions for INTOR with a single–null poloidal divertor [4.27] are given in Table 4.7. In addition to the usual fixed geometry and core conditions, the cross–field diffusion was taken to be 0.25 D_{Bohm}, consistent with [4.53], which yields scrape–off thicknesses of about 5 cm.

For the gas puffing base case, the edge temperature is about 210 eV and the edge density is about $3 \times 10^{18}/m^3$. The enhanced recycling near the target increases the particle flux by a factor of 5 over that leaving the scrape–off, while most of the energy carried out of the core hits the targets at 5 MW/m^2 (average). The neutral pressure in the divertor is 0.03 Pa, and the hydrogen pumping rate is 10% of the hydrogen flux leaving the core. Assuming helium is pumped about as well as hydrogen, this provides adequate helium removal.

The sensitivity of these edge conditions to various parameters is illustrated in Figure 4.4. Under the gas puffing base case, the divertor and scrape–off layer are fairly transparent to neutrals. Thus it does not matter whether hydrogen was supplied as pellets, or as gas puffing in the divertor or scrape–off. Varying pump speed over 50 – 400 m^3/s did not change edge conditions or energy transfer, but did increase the fractional pumping rate from 5 – 15%. Thus the fractional burnup or helium concentration could be controlled without affecting edge parameters.

The edge is sensitive to uncertainties in the particle confinement time. If it is about a factor of 1.7 larger than assumed here (1.4 s), a hot (>1 keV) low density ($< 10^{18}/m^3$) edge forms. The transition is fairly abrupt at a flux of about $2 \times 10^{22}/s$ from the core (Ref.[4.27] estimated this transition at $3 \times 10^{22}/s$). On the other hand, the edge parameters are not strongly sensitive to varying the cross–field diffusion over 0.1 – 1 D_{Bohm}. As the scrape–off thickness increased, so did the particle and energy flux to the back–up limiters, resulting in a small density increase and a temperature drop from 250 to 160 eV.

The base gas puffing conditions are hotter and less dense than those predicted by Harrison et al [4.53], given for comparison in Table 4.7. Their largely analytic work estimated 25 – 100 eV temperatures and much higher recycling, but their calculations started by fixing the scrape–off plasma density to a value much higher ($5 \times 10^{19}/m^3$) than determined here. A higher density would be expected to bring about lower edge temperatures for the same power, and to cause increased recycling because of the shorter ionization mean free path.

The calculated conditions correspond to the medium temperature edge conditions described in the US FED/INTOR report [4.27]. Since these temperatures are expected to cause high sputtering, it is possible that the subsequent radiation cooling will bring conditions down to a low temperature, high density edge. However, sputtering and impurity transport are not included in the present model so this cannot be self–consistently calculated. If 4% iron impurity in the edge is assumed, the temperature drops to about 70 eV, with 35 MW radiated in the edge.

In the US FED/INTOR report, it is argued that the cool, high density edge is possible, even without radiation cooling, if the input particle flux was large enough. This is consistent with the present results if the ion confinement time is shorter than assumed here (see

Figure 4.3), thus increasing the particle flux. In general, though, they predict higher recycling, making the cold edge easier to achieve. This difference is likely due to the way the local geometry is modelled. In their analysis, only the divertor region near the pump is treated, and it is approximated as a 0.7 m duct, forming a fairly closed geometry. In the present model, the entire divertor region (both targets) is simulated since equal particle and energy fluxes strike each target so both contribute to controlling the edge conditions, and since the net pumping is small (about 24% of incident particles), only a small asymmetry exists. Consequently the geometry is more open and it is easier for neutrals to escape the divertor. The actual answer is probably between these two values.

Pumped Limiter

Edge conditions with a double-edged pumped limiter (Figure 4.3b) are given in Table 4.8. For the gas puffing reference case, a hot, low density edge is attained with about 1.2 keV temperatures and 3 - 6 $\times 10^{16}/m^3$ plasma densities. Almost all the power and particles hit the outer surface of the limiter - only 7 MW and $2.6 \times 10^{21}/s$ come into the limiter slot (5% and 10%, respectively, of the scrape-off flux). The neutral pressure is 0.002 Pa and only 1% of the particles leaving the core are actually pumped.

This high temperature regime is not expected to be stable, and indeed was strongly sensitive to several parameters as illustrated in Figure 4.5. If more particles reach into the limiter slot, then a cold, high recycling regime is reached. For example, if cross-field diffusion is larger than assumed (0.25 D_{Bohm}), or if the particle confinement is shorter than assumed (1.4 s). Alternately, the presence of impurities can cool the edge sufficiently for the cold, recycling regime to start. The latter occurred with 3% argon concentration in the edge, in good agreement with the 4% argon requirement estimated in Ref.[4.27].

Once sufficient reactions occur in the diverted region, a positive feedback occurs whereby more recycling neutrals are ionized, and return to the target, producing a higher ion density and so further increasing the reaction rate, and so on. Once started, this series of reactions pulls the local plasma down to cold and dense conditions, limited only by the escaping fraction of charge-exchanged neutrals and declining reaction rates at low temperatures.

Bundle Divertor

Bundle divertor designs have been extensively modified since the early circular coil

DITE designs. In particular, a cascade bundle divertor consisting of three staged T-coils has been shown to satisfy basic plasma and engineering constraints for an INTOR-class tokamak [4.29]. Calculated edge parameters with such a bundle divertor are given in Table 4.9. For the gas puffing base case, a cold and dense divertor plasma is readily achieved with about a 30 eV temperature and $4 \times 10^{19}/m^3$ density. The scrape-off region is at 110 eV and a comparable density. Much simpler estimates by Harrison et al [4.37] for edge conditions with a bundle divertor on a comparable tokamak are also given in Table 4.9. The particular divertor was a substantially different design with a large $q_D \approx 20$ and correspondingly long L_{si}, as well as a much larger diverted flux bundle (13 m^2). However, the overall results are comparable.

Although thick compared to poloidal divertor or pumped limiter edges, the low pumping speed and high charge exchange rate in the divertor allowed reasonably good recycling from the divertor, and consequently gas puffing in the edge at about $8 \times 10^{21} DT$ atoms/s is adequate. The sensitivity is illustrated in Figure 4.6.

The neutral gas pressure in the divertor is large - 5 Pa (0.05 torr), with a neutral density of 4.4×10^{20} atoms/m^3. The characteristics of the vacuum pumps used in TFTR are shown in Figure 4.7. Basically, the high speed turbomolecular pumps do not work well above 10^{-1} Pa (10^{-3} torr), and in fact just the backing pumps would seem appropriate for the expected divertor pressure. However, the speed of such pumps is about a factor of ten lower than the turbomolecular pumps, so the overall bundle divertor pump speed should be about an order of magnitude lower than that used for poloidal divertors or pumped limiters. In particular, 5 m^3/s was chosen for the reference case as being compatible with the high divertor pressure. The corresponding hydrogen pumping rate is 7.5×10^{21} atoms/s, or about 25% of the flux leaving the core. This value could easily be adjusted, depending on the helium behavior and desired burnup fraction.

Of the 124 MW generated in the plasma core, 37 MW are radiated, 23 MW reach the first wall and back-up limiter (because of the thick 0.15 m scrape-off layer), and the remaining 62 MW enter the divertor. There about 14 MW is lost by radiation and charge exchange to the side walls, while 44 MW reach the target. The resulting direct heat flux to the target will be difficult to cool, although the ion temperature is sufficiently low that sputtering should be no problem. The heat flux could be reduced below 10 MW/m^2 by

adding flux expansion coils, by using a gas jet target, or by seeding the edge with an impurity (e.g. $\geq$ 3% Fe). Although a high neutral pressure was reached in the divertor, this cool gas blanket was unable to redistribute enough of the plasma energy on its own, possibly because of the small divertor plasma volume.

Finally, note from the sensitivity runs in Figure 4.6 that the bundle divertor edge is well-behaved and only smoothly varying over a fairly wide range in parameters, unlike the pumped limiter or (to a lesser degree) the poloidal divertor edge. This would add confidence to a design with a bundle divertor controlled edge since many of the parameters (cross-field diffusion and particle confinement time) are not well-known.

4.4.2 ALCATOR-DCT

ALCATOR-DCT is a next-step experimental tokamak designed to investigate or demonstrate long pulse operation, RF current drive and heating, superconducting magnets, and high aspect ratio scaling [4.22, 4.23]. Early versions considered pumped limiters as the primary exhaust system. Subsequent designs considered bundle divertors [4.24] and a more recent version requires modifying the vacuum vessel in order to permit an internal poloidal divertor [4.25]. The main machine parameters are given in Table 4.6. ALCATOR-DCT is not an ignition experiment so is assumed to run with a hydrogen plasma. Furthermore, several classes of discharges are possible, ranging from high $n\tau$ to current drive experiments [4.22]. Only the high $n\tau$ core conditions are simulated here, with $1 \times 10^{20}/\mathrm{m}^3$ core-averaged density and 600 eV core-averaged temperature maintained by 1800 kW core heating power.

Bundle Divertor

An advanced divertor has been considered for ALCATOR-DCT with a preliminary design [4.24] plus improvements [4.30] to reduce coil currents and expand the diverted flux bundle. The basic design is illustrated in Figure 4.8, and representative edge conditions calculated for ohmic discharges are given in Table 4.10.

Figure 4.11 shows the effect of varying the fuelling location and rate with fixed 5 m^3/s pump speed. The minimum fuelling required is 6×10^{21} protons/s (marked A on Figure 4.11) of core fuelling - either with neutral beams or pellets. This corresponds to, for example, twenty 2 mm diameter H_2 pellets injected per second. Larger pellets (3 mm or bigger diameter) would add more than 100% each to the particle content of

the core plasma. From pellet injection experiments on machines like ISX and ASDEX [4.31,4.38], this would be expected to degrade confinement. Note, however, that the present analysis does not require large pellet velocities but rather just enough for the hydrogen to penetrate inside the separatrix. Simple estimates suggest 10 - 100 m/s are adequate for perpendicular injection. These speeds are well within current capabilities, although the repetition rate, while in the range of reactor-relevant rates, is an extrapolation of current state-of-the-art [4.31,4.32,4.38]. Of course it may be that pellet fuelling direct to the plasma core is the desired fuelling mode, in which case high velocity pellets are required for any divertor configuration.

As gas is puffed in at the edge, the required pellet fuelling decreases until gas puffing becomes the sole fuelling mechanism at 13×10^{21} protons/s (marked B on Figure 4.11). This is larger than the pellet fuelling value because roughly half of the gas is ionized and swept away into the divertor. Beyond this value, any additional "fuelling" must be in the divertor itself since further fuel to the core or scrape-off region will force the core into a cooler, denser equilibrium than of interest here. Gas puffing in the divertor is possible because the gas does not escape back into the main chamber - that is, the bundle divertor provides excellent screening against recycling hydrogen.

Although a wide range of fuelling rates (and other parameters) were considered, the plasma temperatures (Figure 4.11a) remained fairly constant. The scrape-off temperature initially dropped because of the cold neutrals added to this region, and then was largely unaffected by the addition of further gas to the divertor because of the good divertor isolation. The divertor plasma temperature slowly dropped with the dilution of the divertor energy among the increasing number of particles.

The distribution of the input power (1.8 MW) is shown in Figure 4.11b. Increasing the fuelling rate increased the divertor density and the reaction rate, and resulted in a substantial shift of power from the target to the walls. The H_2 pressure in back of the divertor (Figure 4.11c) rose to a substantial 16 Pa (0.2 torr).

The scrape-off plasma density initially increased as gas puffed neutrals were added, then dropped somewhat as further neutrals were added to the divertor. The latter effect is probably due to the general increase in calculated bulk flow velocity as particles are added, an effect that is initially compensated in the scrape-off by gas puffing.

The effect of changing pumping speed is shown in Figure 4.12 for pure gas puffing. Not surprisingly, the divertor gas pressure rises substantially as the pumping speed decreases and the increased neutral density transfers power from the target to the wall. Other quantities were largely unchanged. Also shown are the results of varying the cross-field diffusion coefficient from simply D_{Bohm}. The effect is not large.

Poloidal Divertor

Two poloidal divertor options have been considered for ALCATOR-DCT - a single-null external poloidal divertor and a single-null internal poloidal divertor. The classic engineering trade-offs in this choice are, respectively, superconducting versus normal coils, unlinked versus linked coil sets, high current versus low current, and small versus large TF coils. Experiments so far have opted for low power internal poloidal divertors (PDX, ASDEX), but the strong emphasis on reliability and maintainability usually gives the edge to external divertors for power reactors (FED/INTOR [4.27]). In fact, one of the prime purposes of the proposed ASDEX-Upgrade experiment is to test a reactor-relevant external poloidal divertor [4.27]. A representative machine configuration for the external coil option on ALCATOR-DCT is shown in Figure 4.9.

The expected edge conditions with gas fuelling and an ohmic discharge are given in Table 4.10. Since the scrape-off and divertor are fairly transparent to neutrals, it does not matter exactly where the fuel is supplied. For the same reasons, conditions do not change much if the pump speed is changed by a factor of ten - only the required fuelling rate changes proportionally. This poloidal divertor is also not sensitive to the cross-field diffusion coefficient (Figure 4.13).

Pumped Limiter

Two pumped limiter options for ALCATOR-DCT have also been examined in some detail - a set of 12 poloidally flat discrete limiters (6 top, 6 bottom near pump ports) [4.33], and a flat toroidal limiter with one leading edge [4.28]. The major trade-offs in the actual design choice are the increased access in the discrete design versus the larger surface area of the belt design. The latter configuration is analyzed here as a representative pumped limiter design, and is illustrated in Figure 4.10.

The effectiveness of pumped limiters is dependent on the collection fraction, the fraction of ions flowing in the scrape-off layer that travel into the limiter slot, $e^{-d_{PL}/\delta_{s,i}}$.

This fraction in turn is a function of the position of the limiter leading edge, and the perpendicular scale length in the scrape-off. The results with $D_\perp = 0.5 D_{Bohm}$ but varying leading edge are shown in Figure 4.14. As the collection fraction increases, the limiter changes from a medium temperature edge limiter discharge to a cold edge with appreciable neutral pressure inside the limiter. In fact, the neutral pressure starts to rise faster than linearly with the incoming flux, consistent with experimental observations on PDX and MACROTOR [4.34,4.35] and indicating plasma plugging of the limiter slot. The power behind the limiter increases linearly with the collection fraction, although an increasing percentage is lost to the limiter slot side walls by radiation, charge exchange and convection.

These results show that the larger the collection fraction, the colder the edge. However, the collection efficiency is varied by shifting the position of the leading edge, and 30% collection efficiency implies that the 2 cm thick leading edge (allowing space for coolant) is sitting right on the separatrix at the position of maximum heat flux. A more reasonable position would be to move the leading edge about 16 cm outwards. This would decrease the leading edge heat flux by 90%, but also reduces the collection efficiency to around 2%. The edge conditions for this case are given in Table 4.8. For comparison, the pumped limiter design by Brooks et al [4.28] placed the leading edge at about 16 cm out with an 8% collection fraction in a 1.88 cm thick density scrape–off layer. They also anticipated a 150 eV edge temperature, although their analysis was for an RF heated discharge rather than the high $n\tau$ ohmic discharge evaluated here.

As with the poloidal divertor, the pumped limiter edge conditions are unchanged as pump speed changes by a factor of two. However, conditions are definitely dependent on the cross–field diffusion coefficient. This is because changing $D_\perp$ changes the perpendicular scale length, and so the collected fraction, which changes all the edge conditions (Figure 4.14). Since $D_\perp$ is not entirely predictable, any pumped limiter design for DCT should either be movable, or very forgiving!

4.5 Summary

In this chapter, a coupled steady state 0–D model of tokamak edge conditions is developed, compared with experimental results on ASDEX, DITE and PDX, and applied to ALCATOR–DCT and INTOR. The model, for all its simplification of the many complicated (and often poorly understood) phenomena, generally reproduced experimental results and expected trends at least qualitatively. Thus the model seems suitable for use in larger system codes which wish to incorporate basic plasma physics models. Indeed, the results of this section, illustrating the interactions between plasma and neutrals that control the edge conditions, imply that a model of at least this complexity should be included in any system or plasma code for a long–pulse, diverted machine.

Possible INTOR edge conditions varied over the full range from hot, low density to cold, high recycling regimes. Assuming 1.4 s average core particle confinement time, 0.25 D_{Bohm} edge cross–field diffusion coefficient and a small impurity concentration (0.5% oxygen), the single–null poloidal divertor produced a 100 eV edge, the pumped limiter a 1 keV edge, and the bundle divertor resulted in a cold 30 eV divertor plasma.

The pumped limiter and (to a lesser extent) the poloidal divertor, were sensitive to variations in cross–field diffusion rate, core particle confinement and impurities, which could make edge conditions much hotter or colder even for fairly small changes from the reference parameters. This sensitivity gives these exhaust systems flexibility in producing desired edge conditions. For example, the addition of 3% argon to the plasma edge would cool the pumped limiter edge down to 30 eV. On the other hand, the transitions between regimes are fairly abrupt. The bundle divertor, with its small volume, long plasma channel and small returning path to neutrals, is naturally in the cold, high recycling regime so is not strongly sensitive to these important but uncertain parameters.

The neutral H_2 pressure in the divertors ranged from 0.1 – 0.6 Pa for the poloidal divertor and pumped limiter, and 1. – 20. Pa with the bundle divertor. The former are compatible with turbomolecular pumps and 200 m^3/s pump speeds should provide adequate helium removal if helium behaves roughly like hydrogen in the divertor. The high bundle divertor pressure, however, means that the turbomolecular pumps can be bypassed and mechanical backing pumps (Roots blowers, for example) applied directly. Given the high neutral pressure and the lower speeds of these pumps, the exhaust system

requirements are more like 5 m^3/s, again with adequate helium removal.

The power to the divertor targets was 5 MW/m^2 for the poloidal divertor, 1 MW/m^2 for the pumped limiter, and 40 MW/m^2 for the bundle divertor. For comparison (see Table 1.1), nuclear reactor fuel pins operate at 1 - 3 MW/m^2. The poloidal divertor heat flux is appreciable but reasonable. The pumped limiter heat flux is also acceptable, and the limiter front surface and leading edge heat flux were estimated to be comparable (2.4 and 1.0 MW/m^2) [4.27]. The bundle divertor heat flux is quite large since the divertor design yields a tall, thin flux bundle at the target location so the resulting surface area is small. Even the high neutral gas pressure is unable to dissipate more than 20% of the hot, focussed plasma energy. Thus a complete bundle divertor design would also have to include, for example, flux expander coils to take the diverted flux and spread it over a much larger area. Alternately, supersonic gas jets on other novel target designs are necessary. Another feature of the bundle divertor is the thick scrape–off, resulting in appreciable diffusion of energy to the first wall or back–up limiters.

In ALCATOR–DCT, all options yielded reasonable edge conditions and hydrogen pumping ability. The basic results were similar to INTOR. The pumped limiter had the hottest edge at around 110 eV. This could cause appreciable sputtering. Both magnetic divertors had sufficiently cold edges that sputtering should be no problem. The bundle divertor showed a very high gas pressure in the divertor of about 5 Pa, leading to a cold dense gas blanket that spread almost half of the divertor power onto the walls rather than the target, reducing the target power to a high but tolerable 8 MW/m^2. It would be interesting to extend these results to test the effect of varying geometry.

Finally, there are several areas for improvements in the global edge model. The first improvement would be in the modelling of various geometry or profile sensitive effects. At present $G_{sc,n}$ and $G_{ds,n}$, the important geometry factors in the scrape–off and divertor, are only estimated and a better scaling law is desirable. For example, the present model basically treats the scrape–off as a uniform slab of thickness $\delta_{s,i}$ with density $n_{s,i}$ and temperature $T_{s,i}$. In fact, the profiles are exponential and extend beyond $\delta_{s,i}$. These factors could change the appropriate value for $G_{sc,n}$. And $G_{ds,n}$ is important because it directly relates to plasma plugging of the divertor and the achievable divertor gas pressures. There may be significant differences between different divertor geometries other than

those presently described by the effective direct length for neutrals. The escape fractions $f_{ds,cx}$, $f_{sc,cx}$ and $f_{cs,cx}$ could also be better calculated, most likely with the direct inclusion of multiple reactions.

Secondly, the numerical algorithm might be improved over the iteration process used in the present code because of the important nonlinear interaction terms in the equations. Indeed, at present the code cannot solve for some cold edge conditions, (although it can tell if they occur) precisely because the nonlinear terms are large and almost exactly cancel each other. Under these circumstances, the algorithm would probably be more effective if the reaction rates were used as the iteration variables so that the non-linear terms were directly included, and the other quantities calculated in terms of these variables.

4.6 References

[4.1] H.Hsuan, M.Okabayashi and S.Ejima, "Measurements of plasma flow velocity into the divertor of the FM-1 spherator by using ion acoustic wave propagation", Nucl. Fus., 15, 1975, 191.

[4.2] DIVA Group, "Divertor experiments in DIVA", Nucl. Fus., 18(12), 1978, 1619.

[4.3] A.Bortnikov et al, "T-12 divertor experiment", p.687, Proc. 8th Inter. Conf. on Plasma Phys. and Contr. Nucl. Fus. Res., Brussels, 1980.

[4.4] ASDEX Team, "Divertor experiments in ASDEX", IPP III/73, Max-Planck-Institut fur Plasmaphysik, October 1981.

[4.5] S.K.Erents et al, "Experimental results from the DITE bundle divertor", p.697, Proc. of 8th Inter. Conf. on Plasma Phys. and Contr. Nucl. Fus. Res., Brussels, 1980.

[4.6] P.J.Harbour, "Divertor problems", in "Plasma physics for thermonuclear fusion reactors", (G.Casini, ed.), Harwood Academic Publishers, England, 1981, 255.

[4.7] D.Meade et al, "PDX experimental results", p.665, Proc. 8th Inter. Conf. on Plasma Phys. and Contr. Nucl. Fus. Res., Brussels, 1980.

[4.8] P.Harbour and J.Morgan, "Models and codes for the plasma edge region", Culham Laboratories, UKAEA, CLM-R234, 1982.

[4.9] A.Hayzen, D.Overskei and J.Moreno, "Probe measurements of the boundary plasma in Alcator C", PFC/JA-81-10, MIT PFC, April 1981.

[4.10]S.Zweben and R.Taylor, "Edge-plasma properties of the UCLA tokamaks", Nucl. Fus., 23,(4), April 1983, 513.

[4.11]M.Keilhacher et al, "Impurity control experiments in the ASDEX divertor tokamak", Proc. of 8th Inter. Conf. on Plasma Phys. and Contr. Nucl. Fus. Res., Brussels, 1980, p. 351, Vol. II.

[4.12]E.R.Muller, K.Behringer and H.Niedermeyer, "Total radiation losses and energy balance for ohmically heated divertor discharges in ASDEX", IPP III/74, Max-Planck-Institut fur Plasmaphysik, December 1981.

[4.13]F.Wagner, "Investigation of limiter recycling in the divertor tokamak ASDEX", IPP III/171, Max-Planck-Institut fur Plasmaphysik, August 1981.

[4.14]P.E.Stott et al, "A review of work on plasma-wall interaction and divertor experiments on DITE", CLM-P473, Culham Laboratories, October 1976.

[4.15]D.Goodall, "Energy flux and surface temperature measurements at surfaces in the DITE tokamak", CLM-P472, Culham Laboratories, October 1976.

[4.16]J.W.M.Paul et al, "Review of results from DITE tokamak", CLM-P502, Culham Laboratories, October 1977.

[4.17]K.B.Axon et al, "Results from the DITE experiment", Paper IAEA-CN-41/R-3, 9th Inter. Conf. on Plasma Phys. and Cont. Nucl. Fus. Res., Baltimore USA, September 1982.

[4.18]W.Vincenti and C.Kruger,Jr., "Introduction to physical gas dynamics", J.Wiley & Sons Inc., New York, 1967.

[4.19]R.Drake, "Control of plasma/wall interactions in tandem mirrors", Nucl. Tech. /Fusion, 3(3), May 1983, 405.

[4.20]R.Petrasso et al, "X-ray imaging studies of Alcator-A radiation and internal disruptions", Nucl. Fus., 21(7) 1981, p.881.

[4.21]G.L.Weissler and R.W.Carlson, "Vacuum physics and technology", Academic Press, New York, 1979.

[4.22]J.H.Schultz and D.B.Montgomery, "HESTER – A hot electron superconducting tokamak experimental reactor", PFC/RR-82-24, M.I.T. Plasma Fusion Center, April 1983.

[4.23]J.H.Schultz and D.B.Montgomery, "Design of the Alcator DCT tokamak at M.I.T.", PFC/JA-83-15 , M.I.T. Plasma Fusion Center, May 1983.

[4.24]T.F.Yang, A.S.Wan and P.J.Gierszewski, "A preliminary bundle divertor design for Alcator DCT", PFC/RR-83-9, M.I.T. Plasma Fusion Center, April 1983.

[4.25]J.H.Schultz, private communication, May 1983.

[4.26]O.Kluber and H.Murmann, "Energy confinement in the tokamak devices PULSATOR and ASDEX", IPP III/72, Max-Planck-Institut fur Plasmaphysik, April 1982.

[4.27]"U.S. FED - INTOR, U.S. contributions to the INTOR Phase 2A Workshop, critical issues", Vol. I, USA FED - INTOR/82-1, October 1982.

[4.28]J.N.Brooks et al, "Pumped limiter study for ALCATOR DCT", Argonne National Laboratory, unpublished report, 1983.

[4.29]T.F.Yang, "Optimization and Monte Carlo modelling of bundle divertors", PFC/JA-82-32, submitted to Nucl. Fus., June 1983.

[4.30]T.F.Yang, private communication, June 1983.

[4.31]C.Ardelfinger et al, "Pellet injections for JET", IPP 1/193, Max-Planck-Institut fur Plasmaphysik, September 1981.

[4.32]S.Milara and C.Foster, "Review of pellet fuelling", Jrnl. of Fusion Energy, 1(1), 1981.

[4.33]B.Lipshultz, private communication, May 1983.

[4.34]R.Jacobsen, "Preliminary particle scoop limiter measurements in PDX", PPPL-1825, Princeton University, August 1981.

[4.35]S.Talmadge and R.Tayor, "Pumped limiter experiments on MACROTOR", paper 9S9, 23rd Annual Meeting of Div. Plasma Phys., Amer. Phys. Soc., New York, October 1981 (Bull. Am. Phys. Soc., 26(7), September 1981).

[4.36]A.Bailey and G.Emmert, "A theoretical model for hot plasma flowing to a wall with recycling", UWFDM-473, University of Wisconsin - Madison, May 1982.

[4.37]M.Harrison et al, "Bundle divertor considerations for reactor-like tokamaks", p.587, Vol. 2, 8th Inter. Conf. on Plasma Phys. and Contr. Nucl. Fus. Res., Brussels, 1980.

[4.38]C.Chang, L.Jorgensen, P.Nielson, L.Lengyel, "The feasibility of pellet re-fuelling of a fusion reactor", Nucl. Fus., 20(7), 1980, 859.

[4.39]F.Reif, "Fundamentals of statistical and thermal physics", McGraw-Hill Book Co., New York, 1965.

[4.40]W.Stacey, Jr., "Fusion plasma analysis", John Wiley & Sons, New York, 1981.

[4.41]M.Petravic et al, "A cool, high density regime for poloidal divertors", PPPL-1824,

Princeton University, August 1981.

[4.42]C.E.Singer and W.D.Langer, "Axisymmetric tokamak scrape–off transport", PPPL–1824, Princeton University, August 1982.

[4.43]A.V.Nedospasov and M.Z.Tokar, "Divertors with strong recycling in the layer near the wall", Nucl. Fus., 21(4), 1981, 465.

[4.44]A.T.Mense and G.A.Emmert, "Mirror microinstabilities in divertors", Nucl. Fus., 15, 703 (1975).

[4.45]G.Becker and C.E.Singer, "Simulation of plasma transport in the scrape–off region of ASDEX", IPP III 175, Max–Planck–Institut fur Plasmaphysik, November 1981.

[4.46]D.Bohm, "Minimum ionic kinetic energy for a stable sheath", in A.Guthrie and R.K.Wakerling (eds.), "The characteristics of electrical discharges in magnetic fields", McGraw–Hill Co., New York, 1949.

[4.47]J.N.Brooks, "Kinetic solution of the sheath region in a fusion reactor", ANL/FPP/TM–124, Argonne National Laboratory, December 1979.

[4.48]Y.Igitkhanov et al, Nucl. Fus., 18(3), 415 (I978).

[4.49]A.Kutky, "Effect of radiating impurities and Bohm transport on a cool plasma-mantle", Physica Scripta, 26(1), 27 (I982).

[4.50]W.Tendler and R.S.Chhabra, "Transport of neutrals in a multicomponent cool plasma mantle", Phys. Fluids, 25(11), 2101 (1982).

[4.51]F.Alladio et al, "Regime of enhanced particle recycling in high density tokamak discharges in the Frascati torus", Phys. Lett. A, 90(8), 405 (1982).

[4.52]Various papers in "Symposium on energy removal and particle control in toroidal fusion devices", Princeton, July 1983 (to be published in Jrnl. of Nucl. Mat.).

[4.53]M.F.A.Harrison, P.J.Harbour and E.S.Hotston, "Plasma characteristics and gas transport in the single-null poloidal divertor of INTOR", Nucl. Tech./Fusion, 3, 432 (1983).

[4.54]J.Hugill, "Transport in tokamaks – a review of experiment", Nucl. Fus., 23(1), 1983, p.331.

[4.55]D.Heifetz et al, "Monte–Carlo model of neutral particle transport in diverted plasmas", PPPL–1843, Princeton University (Jrnl. Comp. Phys., 46(2), 1982, 309).

[4.56]"Tokamak Fusion Test Reactor final design report", PPPL–1475, Princeton University, August 1978.

Table 4.1: List of variables

a	Minor radius [m];
A_{di}	Divertor throat projected area perpendicular to ion flow [m^2];
A_{dn}	Divertor throat area [m^2];
A_{dw}	Divertor wall area [m^2];
A_{fw}	First wall area [m^2];
A_p	Pump port area [m^2];
A_s	Separatrix surface area [m^2];
A_{tn}	Divertor target surface area [m^2];
A_{ti}	Divertor target projected area perpendicular to ion flow [m^2];
B	Magnetic field [Tesla];
c	Speed of sound [m/s];
D	Diffusion coefficient [m^2/s];
d_d	Width of divertor channel [m];
d_{PL}	Distance of pumped limiter leading edge from separatrix [m];
d_s	Width of scrape-off layer [m];
E_i	Ionization energy [J];
f_B	Fraction of Bohm diffusion;
$f_{cs,cx}$	Fraction of neutrals in core that charge-exchange and escape (to scrape–off);
$f_{ds,cx}$	Fraction of charge exchange neutrals in divertor that escape (to scrape–off);
$f_{d,p}$	Fraction of neutral atoms entering pump ports that are pumped;
$f_{sc,cx}$	Fraction of charge exchange neutrals in scrape–off that escape (to core);
g_d	Number of divertor channels
$G_{ds,n}$	Geometry factor for neutrals recycling from the divertor;
$G_{sc,n}$	Geometry factor for neutrals recycling from the scrape-off;
$L_{d,i}$	Length of divertor chamber for ions [m];
$L_{d,n}$	Effective direct length of divertor chamber for neutrals [m];
$L_{s,i}$	Length of scrape-off layer for ions [m];
$M_{d,i}$	Plasma bulk flow Mach number in divertor;
$M_{s,i}$	Plasma bulk flow Mach number in scrape–off;
$n_{c,i}$	Core hydrogen ion density [atoms/m^3];
$n_{d,i}$	Divertor hydrogen ion density [atoms/m^3];
$n_{d,n}$	Divertor atomic hydrogen (neutral) density [atoms/m^3];
$n_{s,i}$	Scrape-off hydrogen ion density [atoms/m^3];
$n_{s,n}$	Scrape-off atomic hydrogen (neutral) density [atoms/m^3];
$\dot{N}_{c,\alpha}$	Helium production rate [atoms/s];
$\dot{N}_{c,f}$	Neutral core fuelling rate [atoms/s];
$\dot{N}_{cs,i}$	Ion flow rate from core [atoms/s];

Table 4.1: List of variables (continued)

$\dot{N}_{d,cx}$	Divertor charge-exchange rate [atoms/s];
$\dot{N}_{d,ei}$	Divertor electron impact ionization rate [atoms/s];
$\dot{N}_{d,er}$	Divertor recombination rate [atoms/s];
$\dot{N}_{d,f}$	Neutral flow rate into gas boundary at target plate [atoms/s];
$\dot{N}_{ds,n}$	Net neutral flow rate from divertor back to scrape-off [atoms/s];
$\dot{N}_{dt,i}$	Ion flow rate from divertor/limiter [atoms/s];
$\dot{N}_{dt,n}$	Neutral flow rate to target [atoms/s];
$\dot{N}_{dw,i}$	Ion flow rate to divertor walls [atoms/s];
$\dot{N}_{dw,n}$	Neutral flow rate to divertor walls [atoms/s];
$\dot{N}_{p}$	Neutral flow rate to pump ports [atoms/s];
$\dot{N}_{s,cx}$	Scrape-off layer charge exchange rate [atoms/s];
$\dot{N}_{s,ei}$	Scrape-off layer electron impact ionization rate [atoms/s];
$\dot{N}_{s,f}$	Neutral gas fuelling rate to scrape-off [atoms/s];
$\dot{N}_{sc,n}$	Neutral flow rate from scrape-off into the plasma core [atoms/s];
$\dot{N}_{sd,i}$	Ion flow rate from scrape-off [atoms/s];
$\dot{N}_{sw,i}$	Ion flow rate to first wall/limiter [atoms/s];
$\dot{N}_{sw,n}$	Neutral flow rate to first wall [atoms/s];
p	Pressure [N/m^2];
q	Heat flux [W/m^2];
q_a	Safety factor at plasma edge;
Q_c	Power convected and conducted from core to scrape-off [W];
$Q_{c,a}$	Core alpha heating rate [W];
$Q_{c,h}$	Core external heating rate [W];
$Q_{c,r}$	Core radiation rate [W];
$Q_{d,r}$	Divertor radiation rate [W];
$Q_{dt,i}$	Power flow from divertor ions to target [W];
$Q_{s,r}$	Scrape-off layer radiation rate [W];
$Q_{sd,i}$	Power flow from scrape-off ions to divertor ions [W];
R	Major radius [m];
R_E	Fraction of particle energy striking wall that recycles promptly;
R_N	Fraction of particles striking wall that recycle promptly;
R_w	Fraction of particles striking walls or target that are recycled;

Table 4.1: List of variables (continued)

$T_{c,cx}$	Temperature of charge-exchange neutrals from core [J];
$T_{c,f}$	Core fuelling neutral temperature [J];
$T_{c,i}$	Core plasma temperature [J];
$T_{d,i}$	Divertor plasma temperature [J];
$T_{d,n}$	Divertor neutral temperature [J];
$T_{s,i}$	Scrape-off plasma temperature [J];
$T_{s,n}$	Scrape-off neutral temperature [J];
T_w	Temperature of neutrals from walls and target [J];
V_c	Volume of core plasma [m^3];
$\delta_{d,i}$	Density decay length in divertor plasma [m];
$\delta_{s,i}$	Density decay length in scrape-off layer plasma [m];
ϵ_0	Permittivity of free space, 8.854×10^{-12} C-V/m;
Γ	Particle flux [particles/m^2-s];
η	Convective heat transfer factor;
λ	Mean free path [m];
μ	Viscosity [kg-m/s^2];
σ	Reaction cross-section [m^2];

Subscripts

c	core;
s	scrape–off;
d	divertor;
w	wall;
t	target;
p	pump.;
cs	core to scrape-off;
sc	scrape-off to core;
ds	divertor to scrape-off;
sd	scrape-off to divertor;
i	ion/electrons;
n	neutrals (atomic hydrogen);
α	alpha particles;
cx	charge exchange;
ei	electron impact ionization;
er	electron impact recombination;
f	fuelling;
r	radiation;

Table 4.2: Machine parameters for ASDEX, DITE and PDX

	ASDEX D/DP	DITE Mk1A/Mk1B/Mk2	PDX
R (m)	1.65	1.17	1.38
a (m)	0.40	0.18/0.18/0.21	0.38
V_c (m^3)	5.21	0.75/0.75/1.0	4.36
q_a	4.4/2.2	3/3/2	3
B (Tesla)	2.8	1.0/1/2	2
A_{di} (m^2)	0.033/0.066	0.015	0.063
A_{dn} (m^2)	0.6	0.023	0.69
A_{dw} (m^2)	2	0.04	4.0
A_{fw} (m^2)	31	14	47
A_p (m^2)	13	0.4	15
A_s (m^2)	26	8.3/8.3/9.7	21
A_{ti} (m^2)	0.033/0.066	0.013	0.06
A_{tn} (m^2)	0.6	0.013	0.69
d_s (m)	0.04	0.08/0.08/0.05	0.15
d_d (m)	0.06	0.13	0.2
$L_{s,i}$ (m)	11.4/5.7	26	6.5
$L_{d,n}$ (m)	0.35	0.35	0.33
$L_{d,i}$ (m)	9.7/4.8	0.35	8.1
g_d	4	2	4

Table 4.3: ASDEX edge conditions

	D discharge		DP discharge	
	Experiment	0-D Model	Experiment	0-D Model
*$T_{c,i}$ (eV)	200–500	300	200–500	300
*$n_{c,i}$ (1/m^3)	$2.1/4.5 \times 10^{19}$	$2.1/4.5 \times 10^{19}$	2.8×10^{19}	2.8×10^{19}
$Q_{c,h}$ (kW)	290/540	320/600	450	400
*$(Q_{c,r} + Q_{c,cx})/Q_{c,h}$	~0.3/0.2	0.3/0.2	~0.12	0.11
$T_{c,cx}$ (eV)	–	90/70	–	80
*$\dot{N}_{c,f}$	0	0	0	0
*τ_E (ms)	40–70	70	40–70	60
*τ_p (ms)	35	35	35	35
*Species	H	H	H	H
$T_{s,i}$ (eV)	20–80	15/14	–	20
$n_{s,i}$ (1/m^3)	–	$2.6/3.1 \times 10^{18}$	–	3.1×10^{18}
$\dot{N}_{sd,i}$ (1/s)	–	$3.1/6.9 \times 10^{21}$	–	4.5×10^{21}
$\dot{N}_{s,f}$ (1/s)	$2.3/6 \times 10^{21}$	$0.1/3.1 \times 10^{21}$	2×10^{21}	3.8×10^{21}
*$\delta_{s,i}$ (cm)	2.3	2.6/2.4	–	2.5
$n_{s,n}$ (1/m^3)	–	$3.8/8.4 \times 10^{16}$	–	5.5×10^{16}
$M_{s,i}$	0.14	0.16/0.15	–	0.18
$T_{d,i}$ (eV)	5–10	10	10	16
$n_{d,i}$ (1/m^3)	2×10^{19}/–	$1.7/2.2 \times 10^{18}$	–	1.6×10^{18}
$T_{d,n}$ (eV)	–	3	–	3
$n_{d,n}$ (1/m^3)	$2/6 \times 10^{19}$	$0.2/0.4 \times 10^{19}$	–	1.0×10^{18}
$\dot{N}_{dt,i}$ (1/s)	1.7×10^{22}	$0.6/1.3 \times 10^{22}$	–	6.9×10^{21}
*S_p (m^3/s)	15	15/200	1000	1000
$(Q_{d,r} + Q_{d,cx})/Q_{c,h}$	~0.3/0.5	0.2/0.2	0.3	0.2
$Q_{dt,i}/Q_{c,h}$	~0.2/0.15	0.3/0.4	0.4	0.5
$p_{d,n}$ (Pa)	0.01/0.03	0.01/0.03	–	0.008

*0–D model value fixed

Table 4.4: DITE edge conditions

	Mark 1A		Mark 1B		Mark 2	
	Experiment	0-D Model	Experiment	0-D Model	Experiment	0-D Model
*$T_{c,i}$ (eV)	250	250	300	300	500	500
*$n_{c,i}$ (1/m^3)	6×10^{18}	6×10^{18}	6×10^{18}	6×10^{18}	2×10^{19}	2×10^{19}
$Q_{c,h}$ (kW)	-	50	80-100	90	< 1000	560
*$(Q_{c,r} + Q_{c,cx})/Q_{c,h}$	~0.3	0.2	~0.4	0.4	~0.4	0.4
$T_{c,cx}$ (eV)	> 100	170	~100	190	-	230
*$\dot{N}_{c,f}$ (1/s)	0	0	0	0	0	0
*τ_E (ms)	14	14	14	12	14	14
*τ_p (ms)	14	14	14	14	14	14
*Species	H	H	D	D	-	H
$T_{s,i}$ (eV)	< 70	25	30	51	50-100	75
$n_{s,i}$ (1/m^3)	5×10^{18}	2.2×10^{17}	-	1.0×10^{18}	-	2.2×10^{18}
$\dot{N}_{sd,i}$ (1/s)	10^{20}	3.3×10^{20}	1×10^{20}	4.2×10^{20}	-	1.8×10^{21}
$\dot{N}_{s,f}$ (1/s)	-	2.2×10^{20}	7×10^{20}	3.8×10^{20}	$\sim 10^{21}$	1.8×10^{21}
*$\delta_{s,i}$ (cm)	-	3.5	3	3.4	-	3.1
$n_{s,n}$ (1/m^3)	$\sim 10^{15}$	1.0×10^{16}	-	1.9×10^{16}	-	5.9×10^{16}
$M_{s,i}$	-	0.71	0.15	0.21	-	0.23
$T_{d,i}$ (eV)	-	3	28	50	-	73
$n_{d,i}$ (1/m^3)	-	5.8×10^{17}	5×10^{17}	4.7×10^{17}	-	1.5×10^{18}
$T_{d,n}$ (eV)	-	3	-	3	-	3
$n_{d,n}$ (1/m^3)	-	1.1×10^{18}	-	2.0×10^{18}	-	2.7×10^{18}
$\dot{N}_{dt,i}$ (1/s)	-	3.2×10^{20}	6×10^{19}	5.2×10^{20}	-	2.0×10^{21}
*S_p (m^3/s)	50	50	50	50	200	200
$(Q_{d,r} + Q_{d,cx})/Q_{c,h}$	-	0.02	-	0.04	-	0.02
$Q_{dt,i}/Q_{c,h}$	~0.5	0.7	0.1-0.2	0.5	~0.3	0.4
$p_{d,n}$ (Pa)	-	0.009	-	0.02	-	0.02

*0-D model value fixed

Table 4.5: PDX edge conditions

	Experiment	0-D Model
*$T_{c,i}$ (eV)	400	350
*$n_{c,i}$ (1/m^3)	2.5×10^{19}	2.5×10^{19}
$Q_{c,h}$ (kW)	300	360
*$(Q_{c,r} + Q_{c,cx})/Q_{c,h}$	0.3	0.3
$T_{c,cx}$ (eV)	-	120
*$\dot{N}_{c,f}$ (1/s)	0	0
*τ_E (ms)	20–80	70
*τ_p (ms)	-	40
*Species	H	H
$T_{s,i}$ (eV)	10–15	18
$n_{s,i}$ (1/m^3)	$4 - 15 \times 10^{18}$	1.8×10^{18}
$\dot{N}_{sd,i}$ (1/s)	2×10^{22}	3.5×10^{21}
$\dot{N}_{s,f}$ (1/s)	5×10^{21}	7.6×10^{20}
*$\delta_{s,i}$ (cm)	~5	3.8
$n_{s,n}$ (1/m^3)	-	4.3×10^{16}
$M_{s,i}$	-	0.13
$T_{d,i}$ (eV)	10–15	16
$n_{d,i}$ (1/m^3)	$2 - 7 \times 10^{18}$	9.2×10^{17}
$T_{d,n}$ (eV)	-	3
$n_{d,n}$ (1/m^3)	-	1.0×10^{18}
$\dot{N}_{dt,i}$ (1/s)	-	7.0×10^{21}
*S_p (m^3/s)	200	200
$(Q_{d,r} + Q_{d,cx})/Q_{c,h}$	-	0.15
$Q_{dt,i}/Q_{c,h}$	~0.7	0.5
$p_{d,n}$ (Pa)	0.001–0.01	0.007

*0-D model value fixed

Table 4.6: Machine parameters for ALCATOR-DCT and INTOR

	ALCATOR-DCT BD/PD/PL+	INTOR BD/PD/PL+
R(m)	2	5.3
a(m)	0.4	1.6
V_c(m^3)	6.32	260
q_a	2.1	2.1/3
B(Tesla)	7	5.5
A_{di} (m^2)	0.0135/0.24/0.005	0.3/1.9/0.33
A_{dn} (m^2)	0.015/3.8/0.052	0.7/50/3.3
A_{dw} (m^2)	1.4/6/0.16	10/100/46
A_{fw}(m^2)	41	380
A_p (m^2)	0.85/0.72/0.045	2.2/7.5/3.3
A_s(m^2)	31.6	335
A_{ti} (m^2)	0.035/0.25/0.005	0.4/1.9/0.33
A_{tn} (m^2)	0.05/2.5/0.05	0.6/13/3.3
d_s (m)	0.06/0.1/0.06	0.20/0.15/0.18
d_d (m)	0.06/0.3/0.1	0.5/1.7/0.1
$L_{s,i}$ (m)	37.7/13/13	196/35/49
$L_{d,n}$ (m)	0.8/0.2/0.3	2.5/1/0.7
$L_{d,i}$ (m)	0.8/2.1/3.1	2.5/7/7
g_d	2/1/24	2/1/2

+ BD-Bundle divertor; PD-Poloidal divertor; PL-Pumped limiter.

Table 4.7: Edge conditions for INTOR with single-null poloidal divertor

		Gas Puffing	Plus 4% Fe	Harrison et al [4.53]
*	$T_{c,i}$ (eV)	10^4	10^4	-
*	$n_{c,i}$ (1/m^3)	1.4×10^{20}	1.4×10^{20}	-
*	$Q_{c,\alpha}$ (MW)	124	124	124
	$Q_{c,h}$ (MW)	3.5	1.3	-
	$Q_{c,r}$ (MW)	38	38	49*
	$Q_{c,cx}$ (MW)	2.8	0.7	-
	$T_{c,cx}$ (eV)	1200	1000	-
	$\dot{N}_{c,f}$ (1/s)	0	0	-
*	τ_E (s)	1.4	1.4	-
*	τ_p (s)	2.0	2.0	-
*	Species	DT	DT	DT
	$T_{s,i}$ (eV)	210.	70.	66.-92.
	$n_{s,i}$ (1/m^3)	3.2×10^{18}	1.1×10^{19}	5×10^{19}*
	$\dot{N}_{sd,i}$ (1/s)	4.0×10^{22}	7.0×10^{22}	-
	$\dot{N}_{s,f}$ (1/s)	3.6×10^{21}	6.0×10^{21}	-
*	$\delta_{s,n}$ (cm)	5.6	4.6	5.2
	$n_{s,n}$ (1/m^3)	1.3×10^{16}	3.4×10^{16}	-
	$M_{s,i}$	0.05	0.04	~0.01
	$T_{d,i}$ (eV)	200	61	25-66
	$n_{d,i}$ (1/m^3)	1.6×10^{18}	6.2×10^{18}	9.0×10^{19}
	$T_{d.n}$ (eV)	50	3	-
	$n_{d,n}$ (1/m^3)	3.5×10^{18}	6.3×10^{18}	1.0×10^{19}
	$\dot{N}_{dt,i}$ (1/s)	2.0×10^{23}	4.2×10^{23}	2.6×10^{24}
	$Q_{d,r}$ (MW)	0.7	8	6.4
	$Q_{d,cx}$ (MW)	13	6	2.8
	$Q_{dt,i}$ (MW)	64	41	66
*	S_p (m^3/s)	200	200	100
	$p_{d,n}$(Pa)	0.03	0.05	-
	q_{fw} (MW/m^2)	0.13	0.2	0.13
	q_{dw} (MW/m^2)	0.14	0.12	0.1
	q_{ln} (MW/m^2)	5.0	3.3	5.0

*Fixed parameters

Table 4.8: Edge conditions for INTOR with toroidal pumped limiter

		Gas Puffing	Plus 3% argon
*	$T_{c,i}$ (eV)	10^4	10^4
*	$n_{c,i}$ (1/m^3)	1.4×10^{20}	1.4×10^{20}
*	$Q_{c,\alpha}$ (MW)	124	124
	$Q_{c,h}$ (MW)	5.7	0.8
	$Q_{c,r}$ (MW)	39	37
	$Q_{c,cx}$ (MW)	5	0.3
	$T_{c,cx}$ (eV)	1200	1100
	$\dot{N}_{c,f}$ (1/s)	0	0
*	τ_E (s)	1.4	1.4
*	τ_p (s)	2.0	2.0
*	Species	DT	DT
	$T_{s,i}$ (eV)	1230	66
	$n_{s,i}$ (1/m^3)	5.7×10^{16}	6.7×10^{18}
	$\dot{N}_{sd,i}$ (1/s)	2.6×10^{21}	1.1×10^{22}
	$\dot{N}_{s,f}$ (1/s)	6.6×10^{20}	7.4×10^{21}
*	$\delta_{s,n}$ (cm)	5	6.2
	$n_{s,n}$ (1/m^3)	3.2×10^{16}	7.8×10^{16}
	$M_{s,i}$	0.22	0.03
	$T_{d,i}$ (eV)	1200	57
	$n_{d,i}$ (1/m^3)	2.4×10^{16}	3.8×10^{18}
	$T_{d,n}$ (eV)	4	3
	$n_{d,n}$ (1/m^3)	2.7×10^{17}	8.8×10^{18}
	$\dot{N}_{dt,i}$ (1/s)	2.9×10^{21}	8.5×10^{22}
	$Q_{d,r}$ (MW)	0.003	0.3
	$Q_{d,cx}$ (MW)	1	1.9
	$Q_{dt,i}$ (MW)	5.6	7.8
*	S_p (m^3/s)	200	200
	$p_{d,n}$(Pa)	0.002	0.07
	q_{fw} (MW/m^2)	0.3	0.3
	q_{dw} (MW/m^2)	0.02	0.05
	q_{ln} (MW/m^2)	0.8	1.2

*Fixed parameters

Table 4.9: Edge conditions for INTOR with bundle divertor

		Gas Puffing	Harrison et al [4.37]
*	$T_{c,i}$ (eV)	10^4	-
*	$n_{c,i}$ (1/m^3)	1.4×10^{20}	-
*	$Q_{c,\alpha}$ (MW)	124	126
	$Q_{c,h}$ (MW)	0	0
	$Q_{c,r}$ (MW)	37	26
	$Q_{c,cx}$ (MW)	0	-
	$T_{c,cx}$ (eV)	-	-
	$\dot{N}_{c,f}$ (1/s)	0	$3. \times 10^{22}$
*	τ_E (s)	1.4	-
*	τ_p (s)	2.0	1
*	Species	DT	DT
	$T_{s,i}$ (eV)	110	350
	$n_{s,i}$ (1/m^3)	3.1×10^{19}	10^{19}
	$\dot{N}_{sd,i}$ (1/s)	5.0×10^{22}	$3. \times 10^{22}$
	$\dot{N}_{s,f}$ (1/s)	7.9×10^{21}	0
*	$\delta_{s,n}$ (cm)	15	10
	$n_{s,n}$ (1/m^3)	5.3×10^{16}	-
	$M_{s,i}$	0.03	0.2
	$T_{d,i}$ (eV)	34	30
	$n_{d,i}$ (1/m^3	3.8×10^{19}	-
	$T_{d,n}$ (eV)	3	-
	$n_{d,n}$ (1/m^3)	4.4×10^{20}	$3. \times 10^{20}$
	$\dot{N}_{dt,i}$ (1/s)	8.1×10^{23}	-
	$Q_{d,r}$ (MW)	1.7	-
	$Q_{d,cx}$ (MW)	12	-
	$Q_{dt,i}$ (MW)	44	-
*	S_p (m^3/s)	5	100
	$p_{d,n}$(Pa)	3	-
	q_{fw} (MW/m^2)	0.1	-
	q_{dw} (MW/m^2)	0.8	-
	q_{tn} (MW/m^2)	40$^+$	3.8

*Fixed parameters $^+$No flux expansion coil

Table 4.10: Representative edge conditions for ALCATOR-DCT

	Bundle divertor	Poloidal divertor	Pumped limiter
*$T_{c,i}$ (eV)	600	600	600
*$n_{c,i}$ (1/m^3)	1×10^{20}	1×10^{20}	1×10^{20}
$Q_{c,h}$ (kW)	1790	1850	1860
*$Q_{c,r}$ (kW)	180	150	130
$Q_{c,cx}$ (kW)	5	57	70
$Q_{dw,i}$ (kW)	104	4	1610
$T_{c,cx}$ (eV)	110	110	110
$\dot{N}_{c,f}$ (1/s)	0	0	0
*τ (ms)	110	110	110
*Species	H	H	H
$T_{s,i}$ (eV)	50	42	120
$n_{s,i}$ (1/m^3)	3.0×10^{19}	3.7×10^{18}	4.5×10^{16}
$\dot{N}_{sd,i}$ (1/s)	1.3×10^{22}	7.8×10^{21}	1.4×10^{20}
$\dot{N}_{s,f}$ (1/s)	1.3×10^{22}	1.2×10^{20}	3.2×10^{18}
$\delta_{s,i}$ (m)	0.023	0.017	0.016
$n_{s,n}$ (1/m^3)	1.2×10^{17}	3.5×10^{16}	4.3×10^{16}
$M_{s,i}$	0.17	0.097	0.17
$T_{d,i}$ (eV)	11	39	105
$n_{d,i}$ (1/m^3)	4.1×10^{19}	1.8×10^{18}	2.0×10^{16}
$T_{d,n}$ (ev)	3	3	3
$n_{d,n}$ (1/m^3)	7.5×10^{20}	2.0×10^{18}	7.9×10^{16}
$\dot{N}_{dt,i}$ (1/s)	4.3×10^{22}	2.1×10^{22}	2.0×10^{20}
$Q_{d,r}$ (kW)	90	40	0.2
$Q_{d,cx}$ (kW)	360	190	2.6
$Q_{dt,i}$ (kW)	730	1310	33
*S_p (m^3/s)	5	10	10
$p_{d,n}$(Pa)	5	0.02	0.0006
q_{fw} (MW/m^2)	0.01	0.006	0.005
q_{dw} (MW/m^2)	0.3	0.03	0.0007
q_{ln} (MW/m^2)	8$^+$	0.5	0.03

*Fixed parameters $^+$ No expansion coil

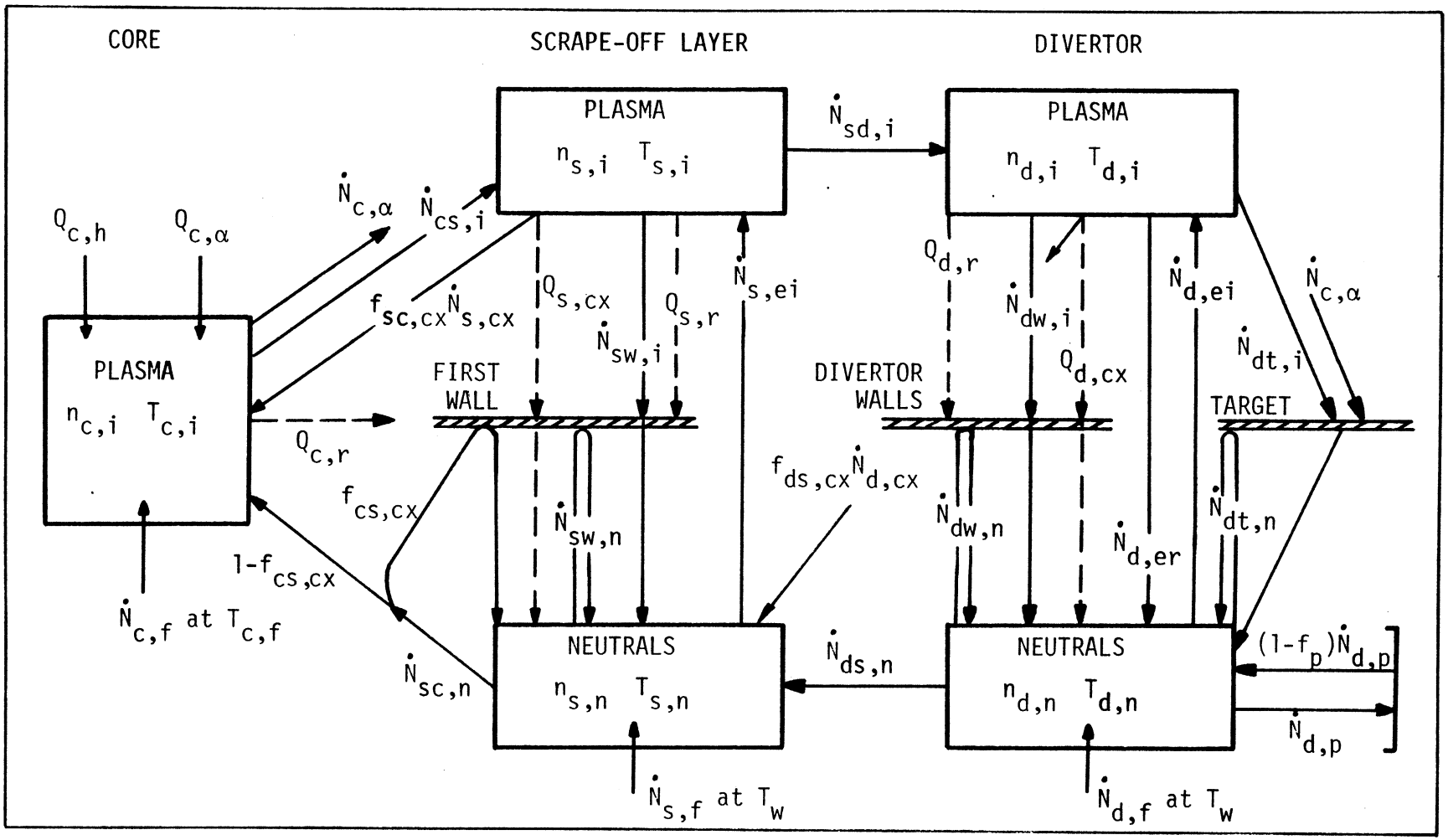

Figure 4.1: Particle and energy flows in 0-D edge model. Solid lines indicate particle plus energy transfer, dashed lines indicate energy transfer alone. The variables are described in Table 4.1.

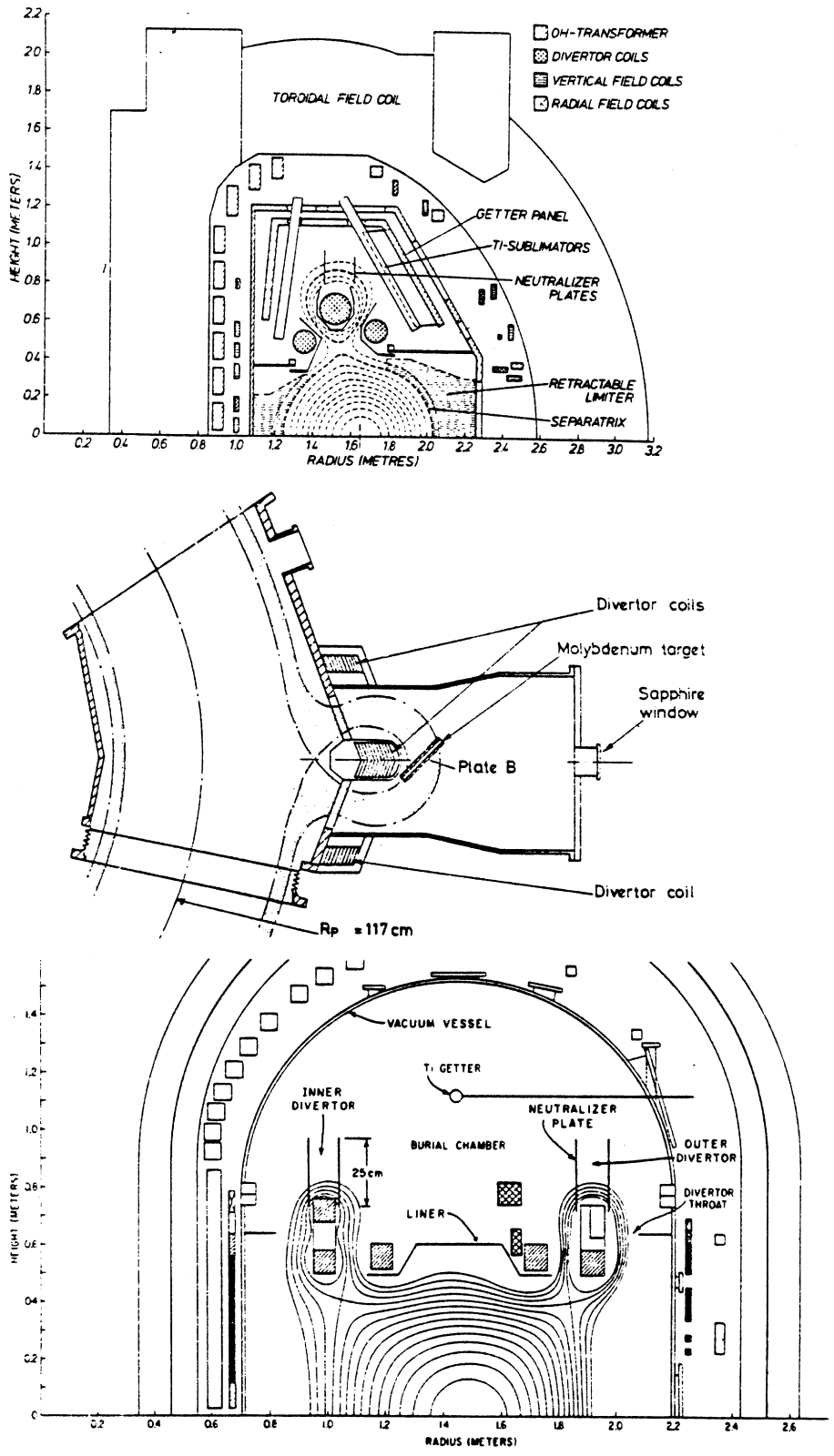

Figure 4.2: Divertor configurations for ASDEX, DITE and PDX.

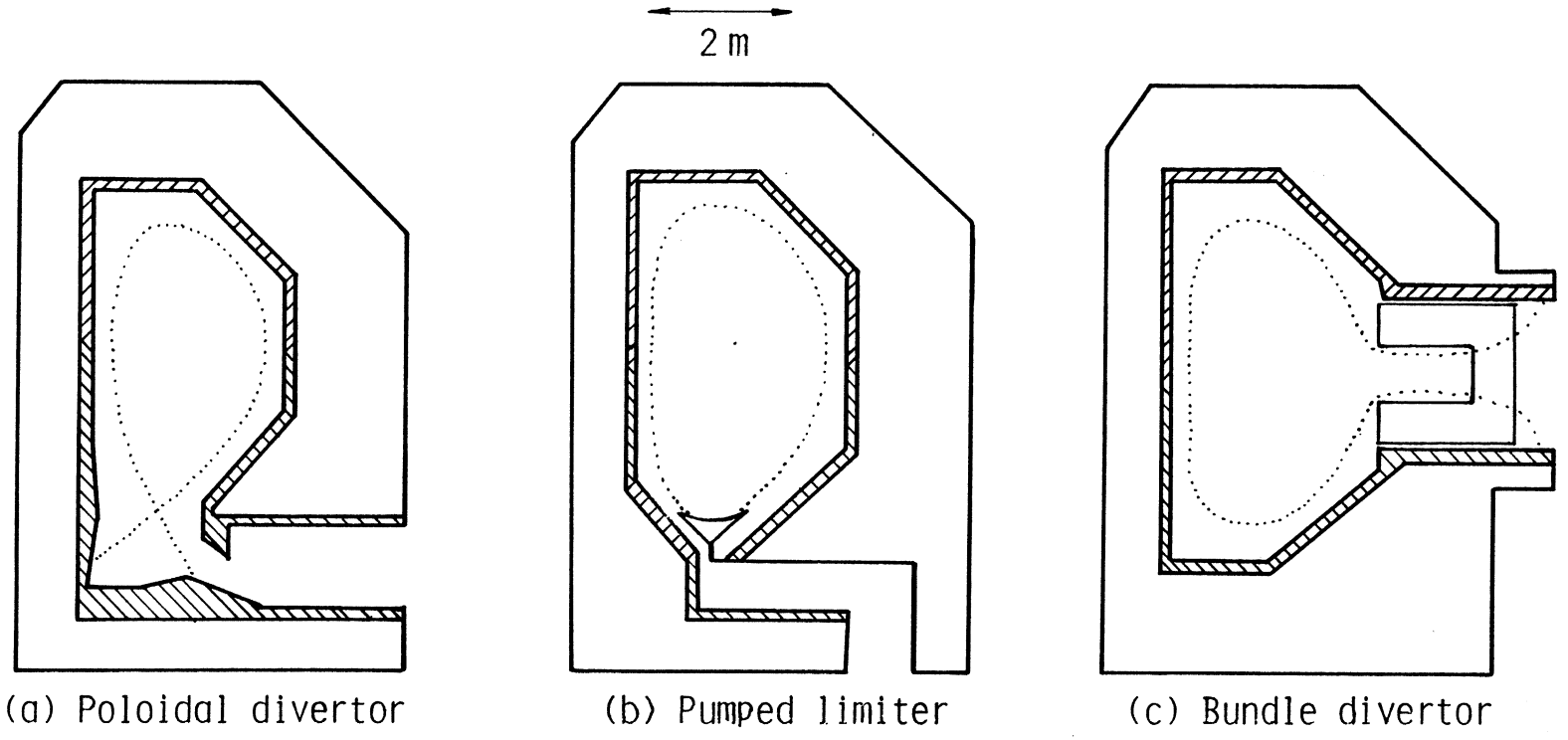

Figure 4.3: Poloidal cross-section of INTOR illustrating exhaust system options.

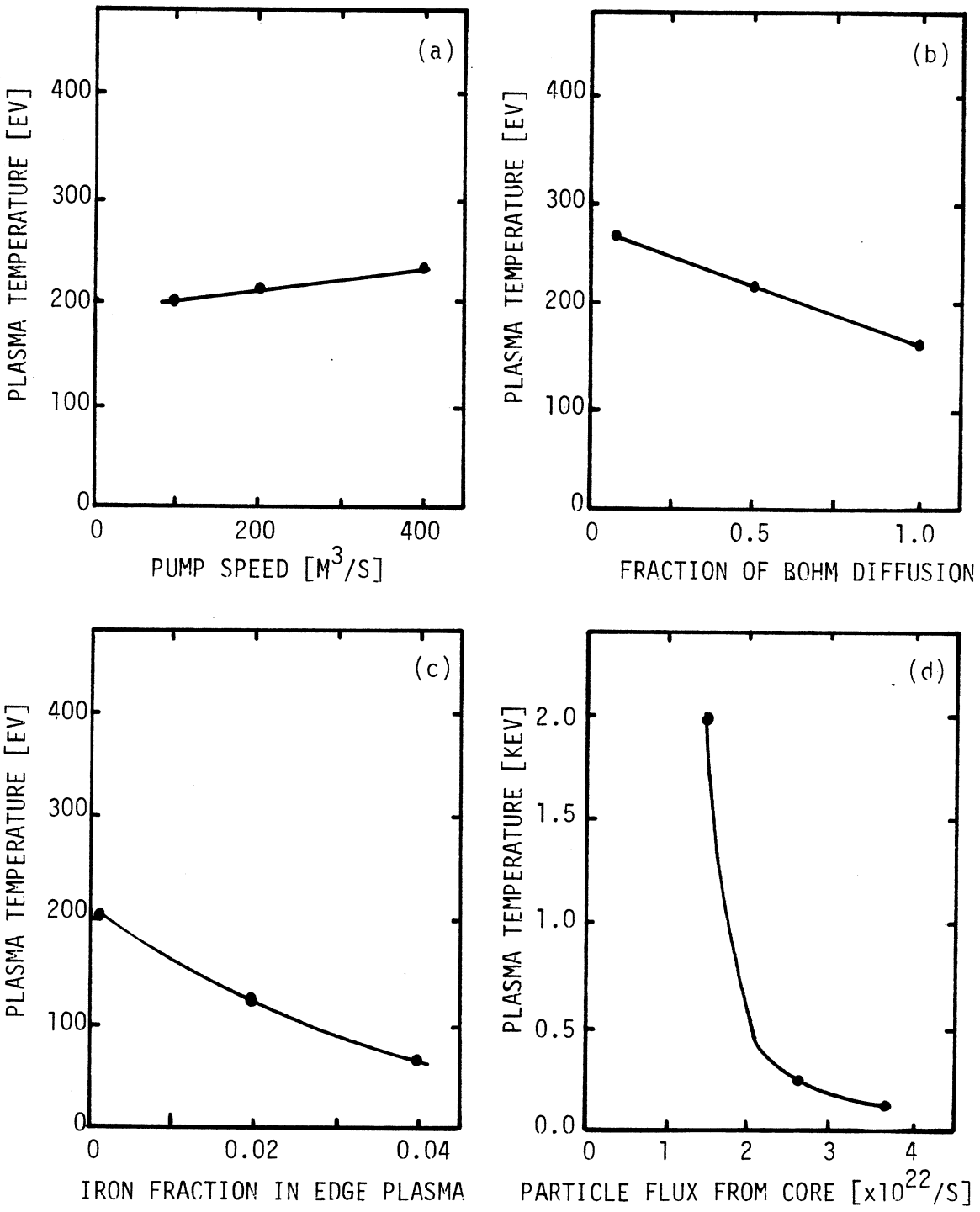

Figure 4.4: Sensitivity of INTOR single-null poloidal divertor edge temperatures to: (a) pump speed; (b) cross-field diffusion coefficient; (c) impurity content; and (d) plasma core particle confinement.

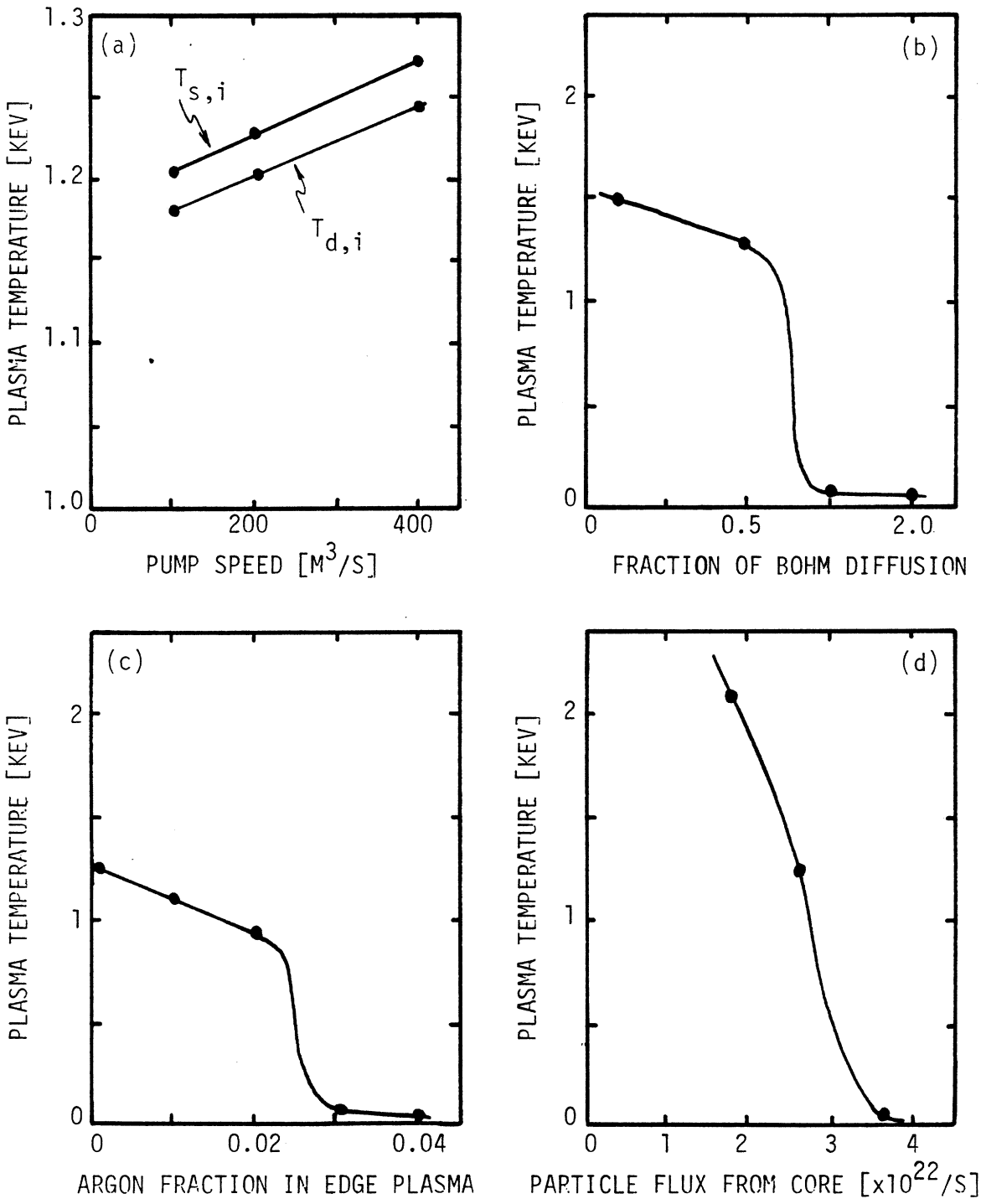

Figure 4.5: Sensitivity of INTOR pumped limiter edge temperatures to: (a) pump speed; (b) cross-field diffusion coefficient; (c) impurity content; and (d) plasma core particle confinement.

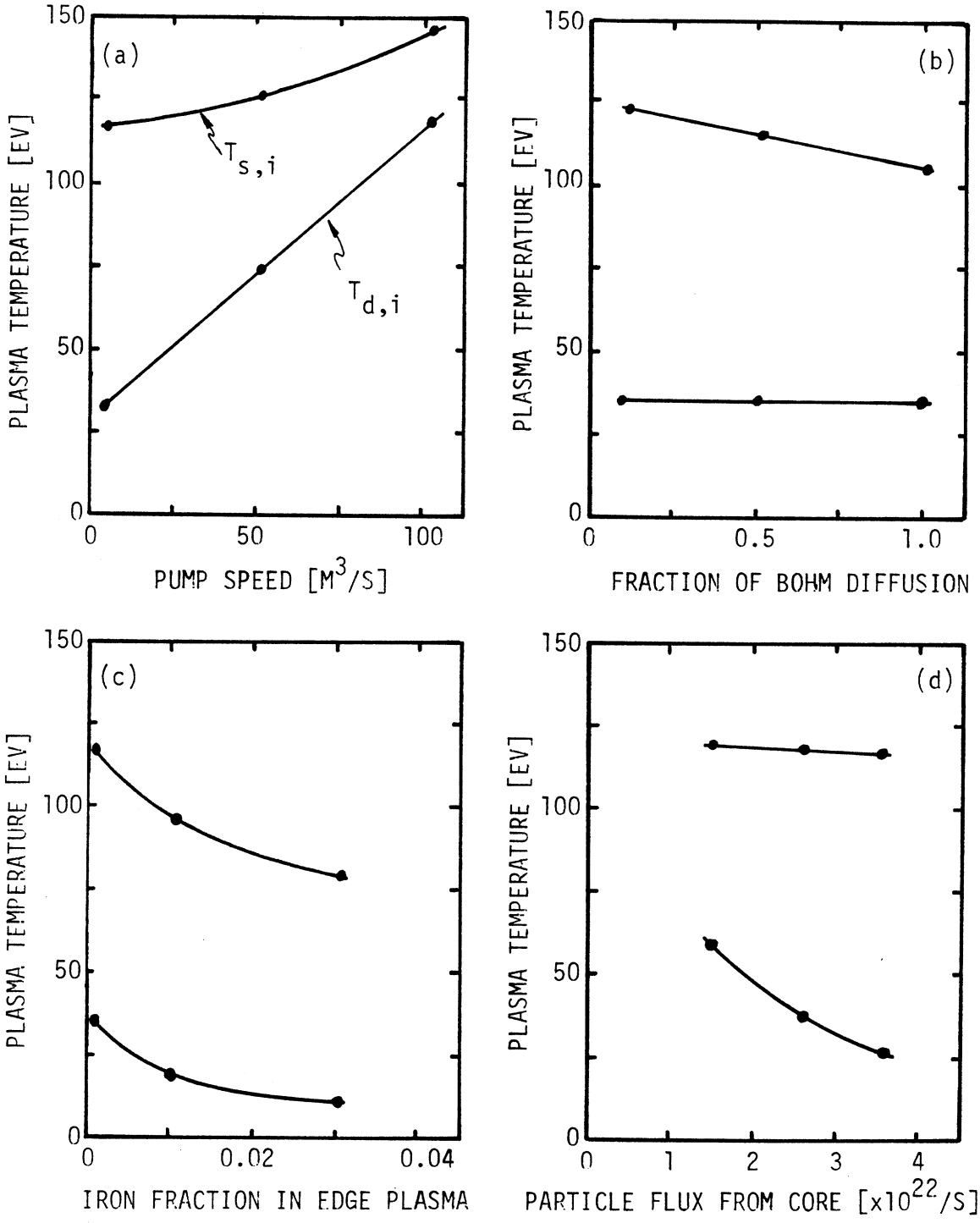

Figure 4.6: Sensitivity of INTOR bundle divertor edge temperatures to: (a) pump speed; (b) cross-field diffusion coefficient; (c) impurity content; and (d) plasma core particle confinement.

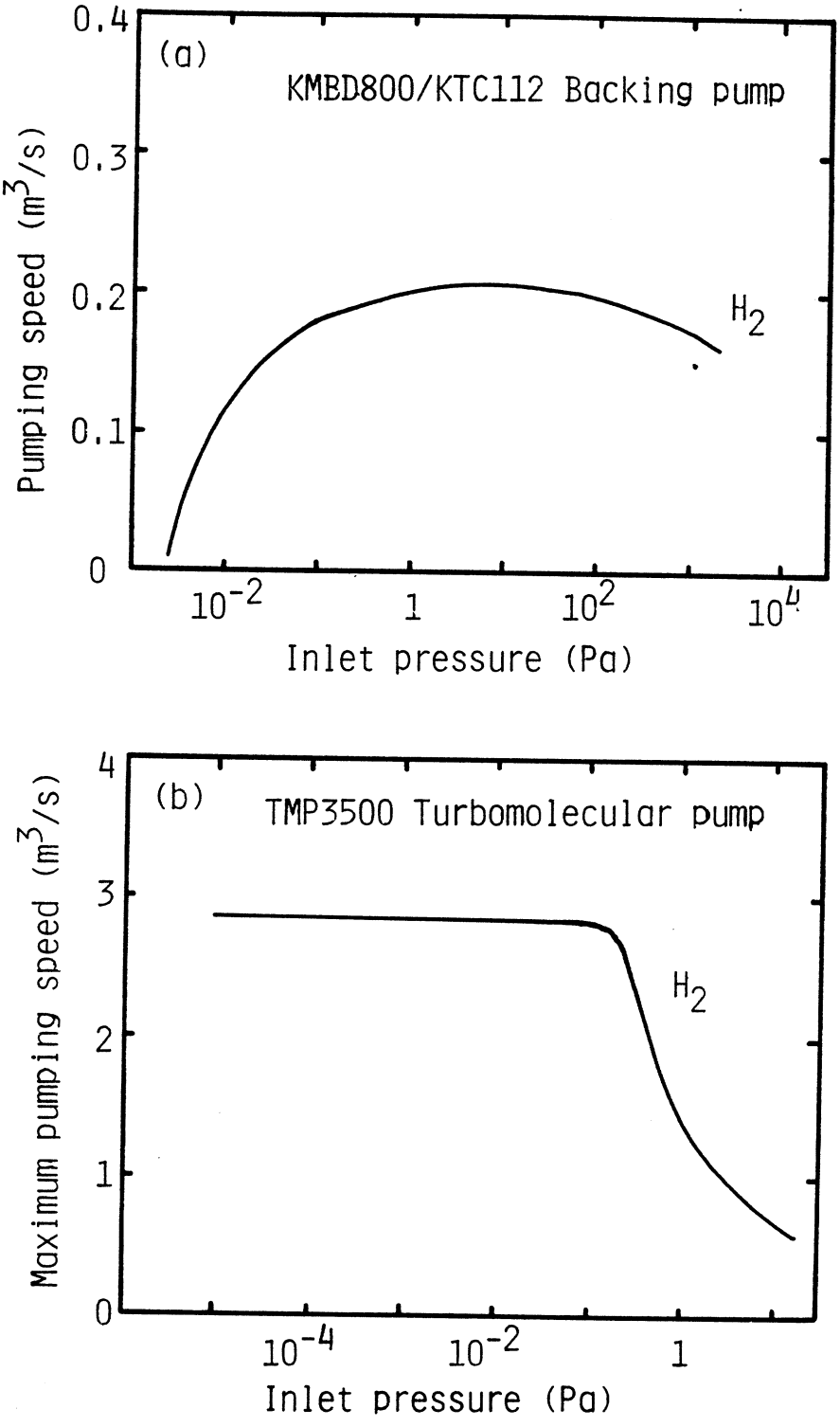

Figure 4.7: Performance curves for the TFTR KMBD800/KTC112 Backing Pump and the TMP3500 High-Vacuum Turbomolecular Pump [4.56].

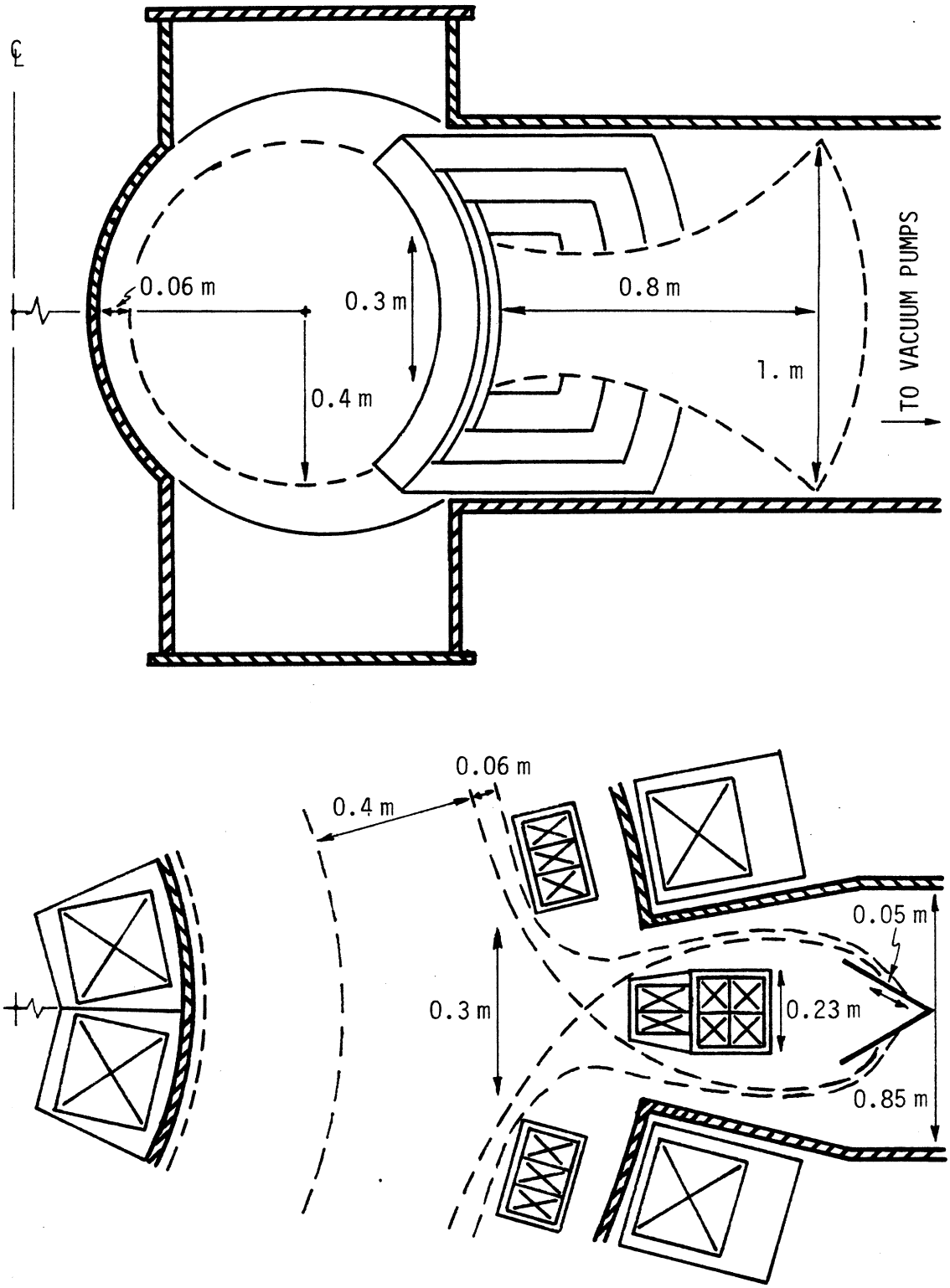

Figure 4.8: Vertical (top) and horizontal (bottom) cross-sections through ALCATOR-DCT showing location of plasma, cascade bundle divertor and access ports.

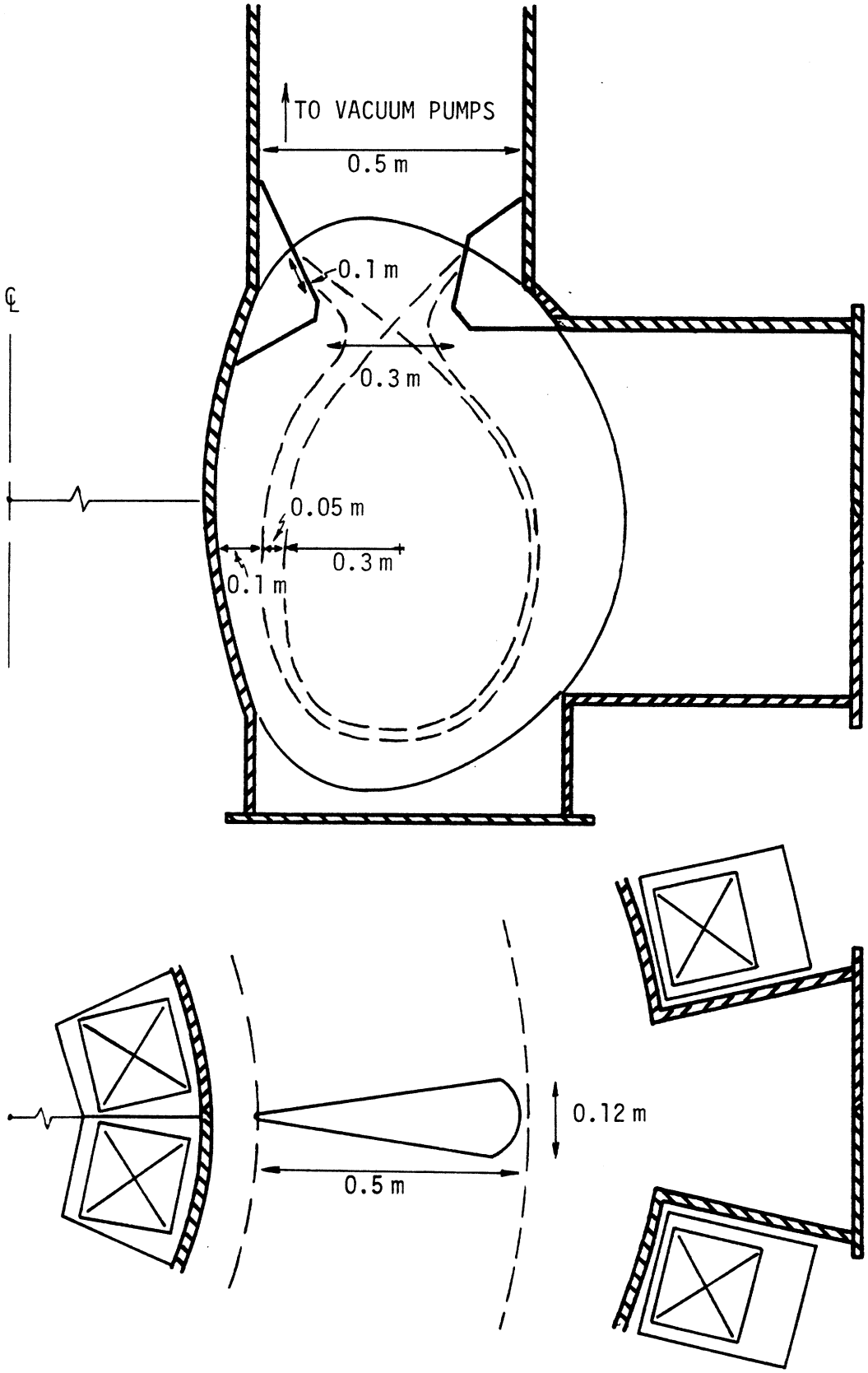

Figure 4.9: Vertical (top) and horizontal (bottom) cross-sections through ALCATOR-DCT showing location of plasma, single-null external coil poloidal divertor and access ports.

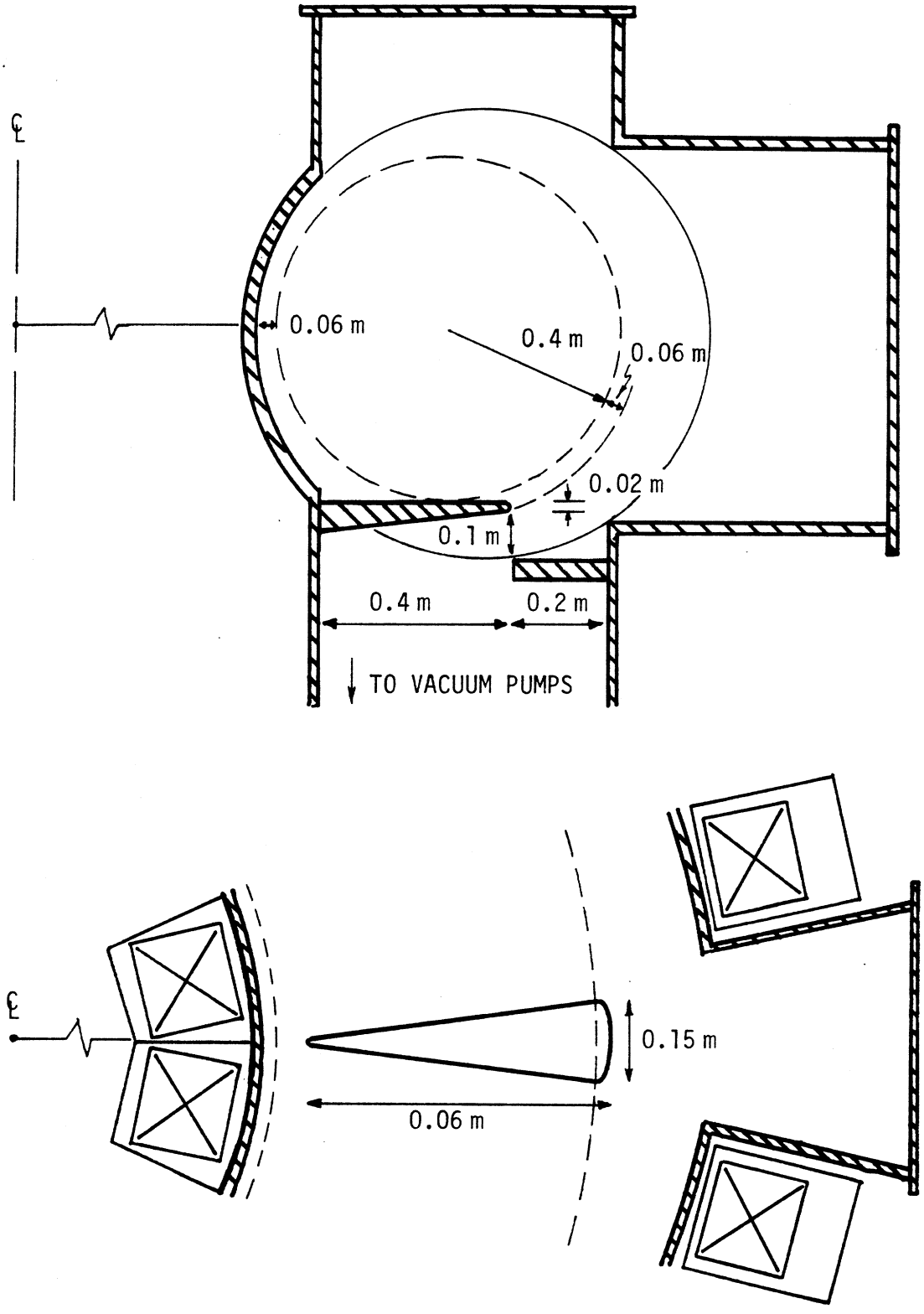

Figure 4.10: Vertical (top) and horizontal (bottom) cross-sections through ALCATOR-DCT showing location of plasma, flat toroidal pumped limiter and access ports.

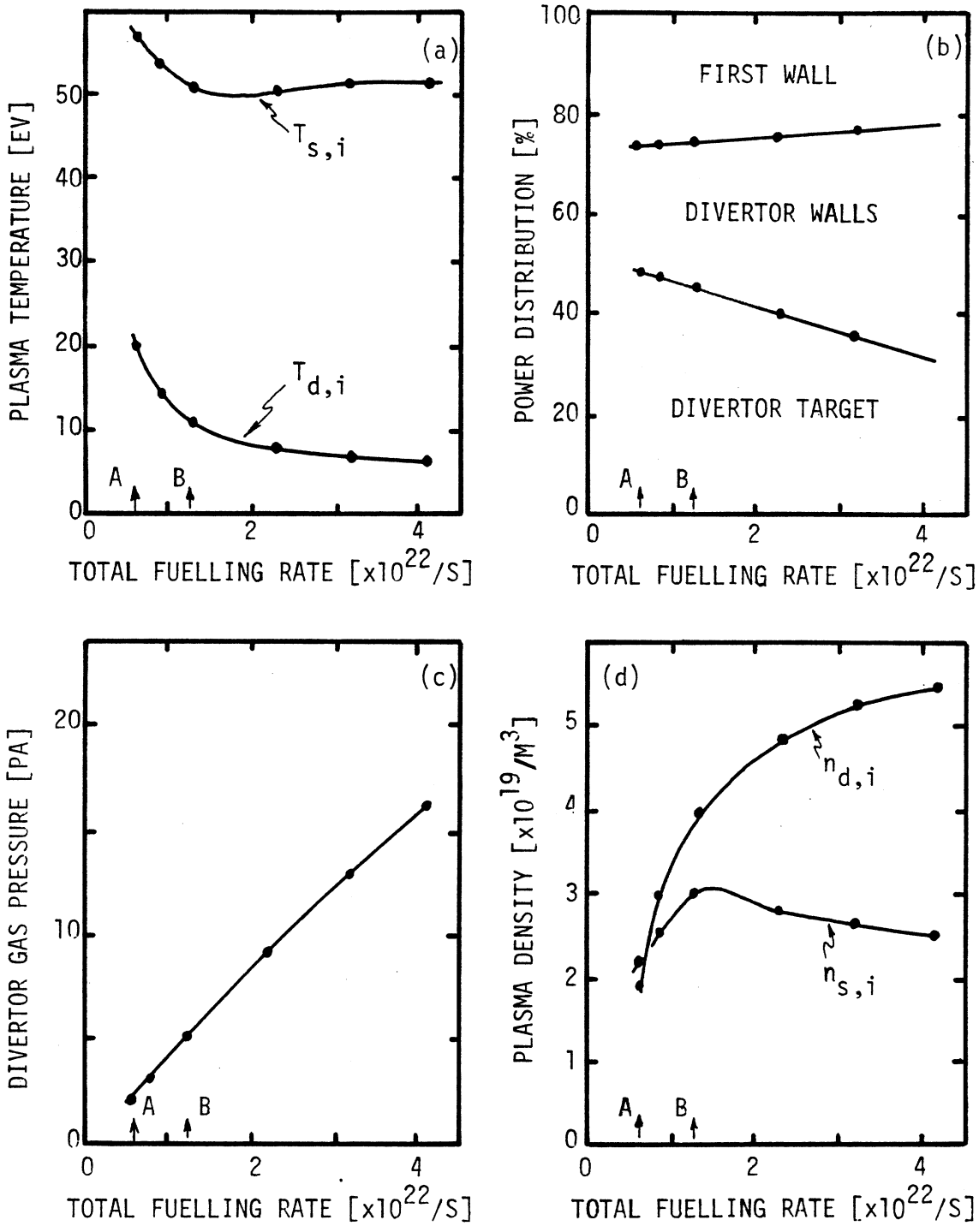

Figure 4.11: Variation of edge conditions in ALCATOR-DCT with bundle divertor, as the total fuelling rate is increased. Point A corresponds to direct core fuelling, point B to only gas puffing in the scrape-off layer. Beyond this point, any additional hydrogen must be added in the divertor itself.

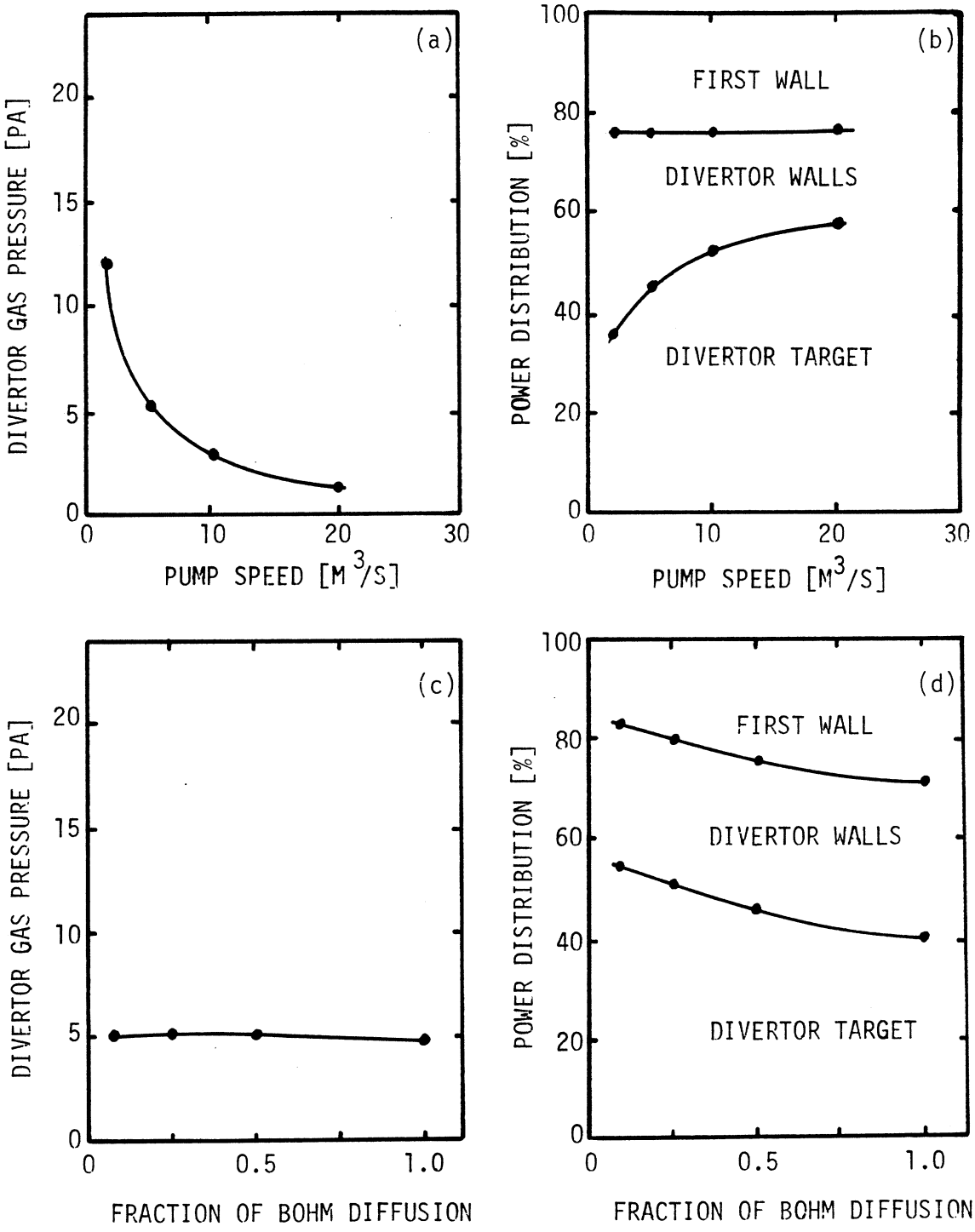

Figure 4.12: Sensitivity of edge conditions in ALCATOR-DCT with bundle divertor to pump speed and cross-field diffusion coefficient. Fuelling is solely by gas puffing.

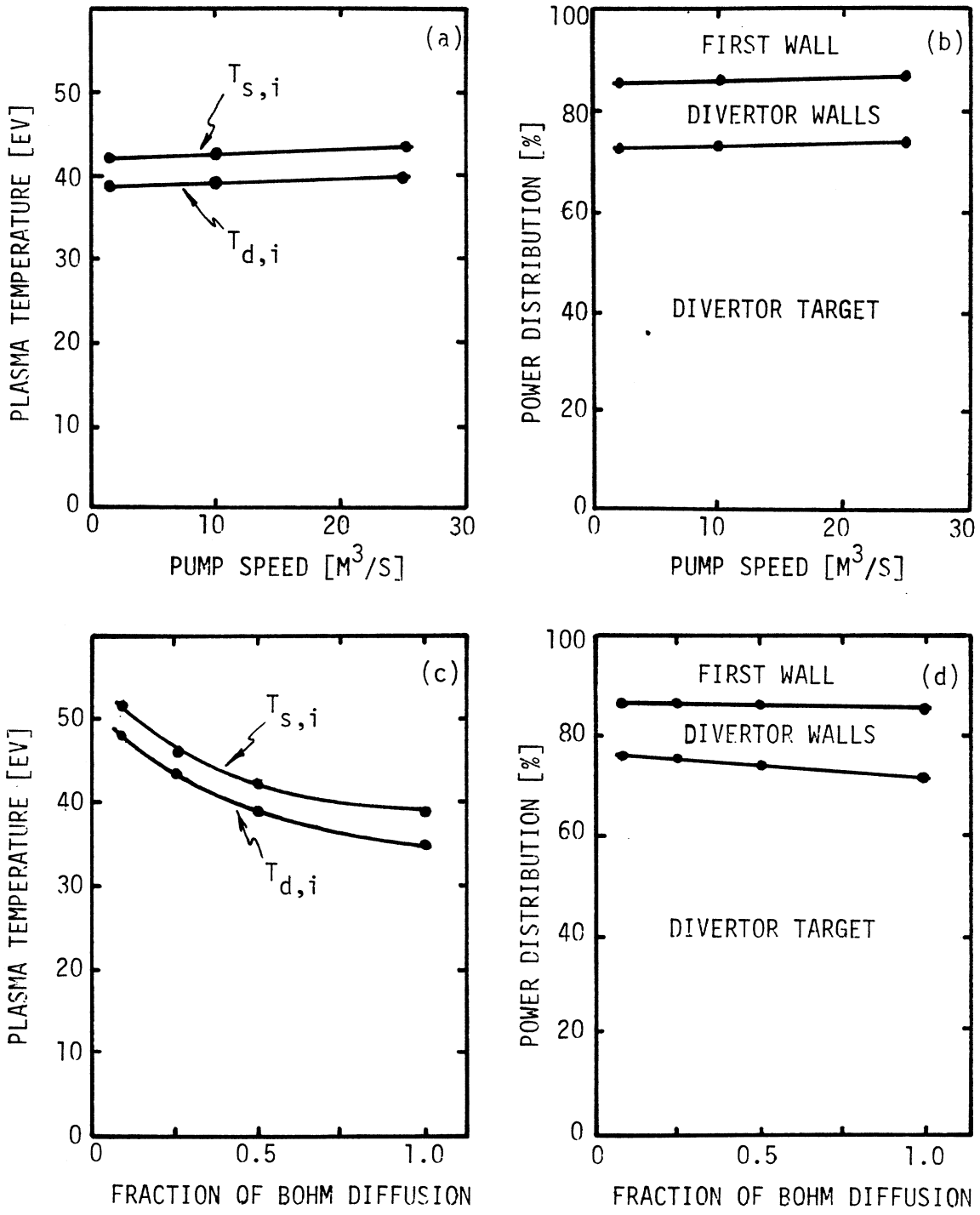

Figure 4.13: Sensitivity of edge conditions in ALCATOR-DCT with single-null poloidal divertor to pump speed and cross-field diffusion coefficient.

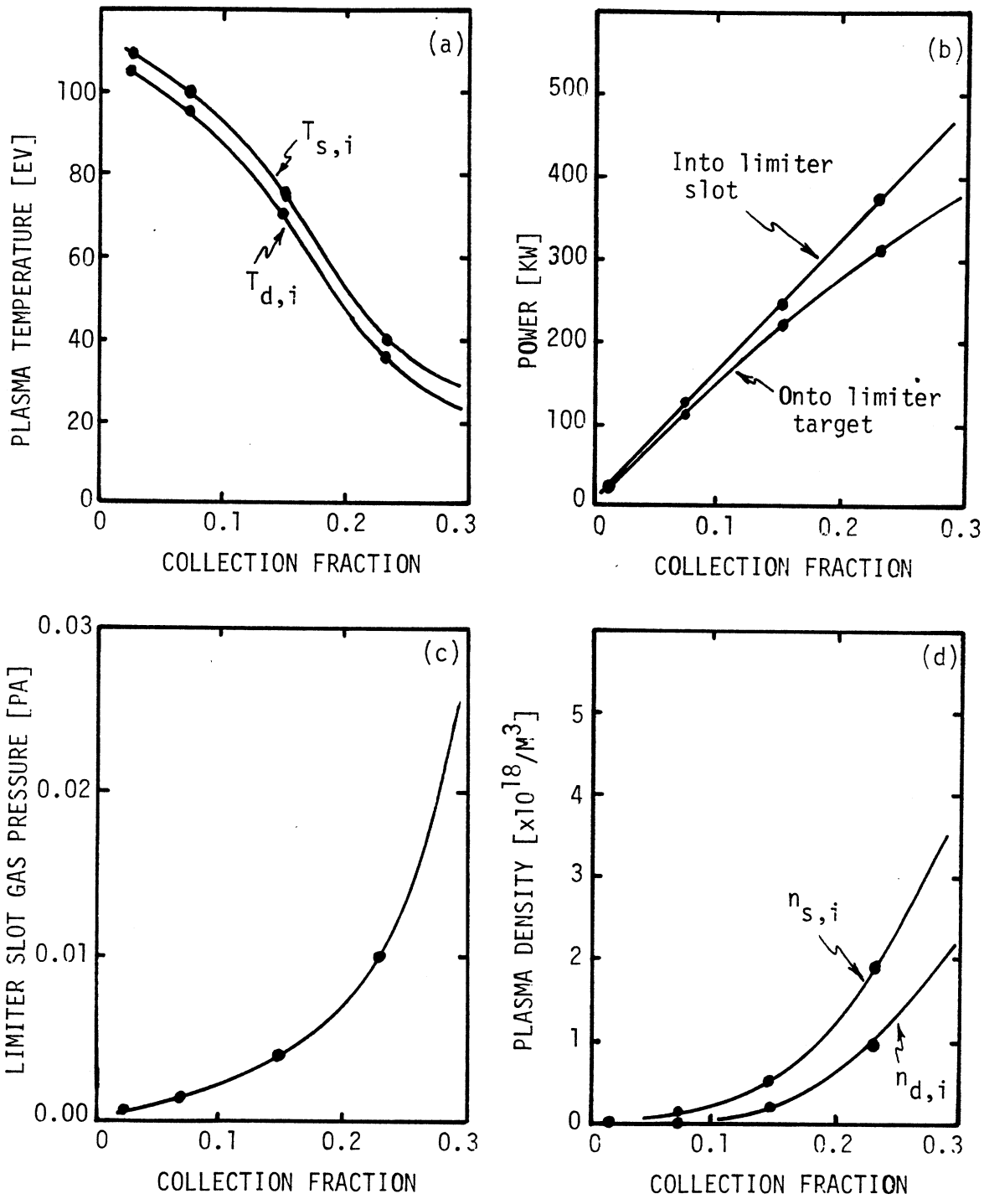

Figure 4.14: Sensitivity of edge conditions in ALCATOR-DCT as pumped limiter slot is opened to collect more of the scrape-off particle flux.

5.0 1-D Kinetic Transport Model of Collisionless Divertor

It is commonly assumed that the edge plasma is sufficiently collisional that the ions and electrons are Maxwellian with temperatures T_i and T_e and bulk flow velocities $\underline{v_i}$ and $\underline{v_e}$. This allows a fluid treatment for the plasma flow with the usual mass, momentum and energy equations, discussed in some detail by Singer and Langer [5.1] and Post et al [5.2], for example. However, the edge plasma is not necessarily collisional, and even if the scrape-off layer itself is, it is quite possible for the plasma flow in a divertor to be effectively collisionless - that is, the self-collision time may be longer than the divertor transit time. This might not seem to matter if the incoming flow is already Maxwellian anyway (say from collisional flow in the scrape-off layer), but there are processes that can change the velocity distribution faster than the transit time. These include magnetic mirror effects, neutral gas interactions, and presheath electric fields. On the other hand, since the divertor plasma is colder than the scrape–off plasma because of neutral interactions, the divertor may be more collisional than the scrape–off.

Table 5.2 summarizes the range of collisionality λ/L calculated from the cases analyzed in Chapter 4. From these results it can be seen that present experiments are roughly in the transition region between the two limits. For the proposed larger machines, pumped limiters may occur with collisionless boundaries while bundle divertors will likely operate with collisional boundaries. Poloidal divertors may be able to operate in either extreme (as far as plasma performance is concerned). Consequently, there is a need to be able to analyze collisionless exhaust plasmas to explore this mode of operation.

In the global model described in Chapter 4, it was assumed that $T_i \sim T_e$ and that the plasma flow could be adequately described as simple bulk flow at some Mach number. Neutral/plasma interactions were treated within the bounds of a 0–D model, but magnetic mirroring and presheath electric field structure were not included except possibly through the flow Mach number. The effects of collisionality, while not explicitly in the particle transport equations, were estimated in the energy transport relations.

However, more detailed analytical treatments of collisionless plasmas have been made. Early analyses such as Hinton and Hazeltine [5.11] and El-Nadi [5.12] calculated the parallel edge transport under simplified poloidal divertor or toroidal limiter conditions. Typically, the ion velocity distribution at the separatrix was determined, and the radial 1-D

drift kinetic equation then approximately solved in the scrape–off layer assuming collisional electrons, weakly collisional ions and a perfectly absorbing target. The resulting scrape–off parallel loss terms could be used in radial transport calculations.

Becker [5.20] computed steady–state ion guiding–center distributions near the separatrix by solving the drift–kinetic equation with Coulomb ion–ion and electron–ion collisions, and ionization and charge exchange reactions with neutrals. He found that the reactions could distort the ion distribution from Maxwellian much faster than Coulomb collisions could relax it, even for fairly low neutral densities. For example, at $T_i \sim T_e \sim 50$ eV, a neutral density of only 0.1% of the ion distribution would produce a 10% deviation in $f(v_{||} = 0)$. He postulated that such distortions might cause microinstabilities in boundary plasmas, and noted that for $T_i \sim T_e > 50$ eV and $n_{neutral}/n_{ion} > 10^{-3}$, a fluid description of ions with classical collision coefficients would be inaccurate.

Nicolai and Mense [5.3,5.13] considered the effects of magnetic mirroring and electrostatic potentials on 1–D parallel particle transport in bundle divertors, calculating the appropriate fluxes through the loss cone at the divertor throat. However, various instabilities were assumed to cause rapid relaxation beyond this point to Maxwellian distributions. Furthermore, neutral interactions were neglected or assumed to be weak.

Emmert et al [5.4,5.5,5.6] analyzed collisionless 1–D parallel flow in bundle divertors assuming Maxwellian distributions in the scrape–off, and included mirroring, electric fields and neutrals. The resulting non–Maxwellian distributions were not assumed to thermalize by instabilities or self–collisions during the divertor transit time. Their results indicated a substantial drop (2 – 4 T_e) in electrostatic potential simply due to the magnetic field variation alone. However when neutrals were added, this potential drop was reduced and, in fact, could become a potential peak ($< 0.3\ T_e$) with sufficiently high recycling.

Thus, the interaction of neutral gas can have an appreciable effect in the high recycling scenarios currently favored for achieving low edge temperatures, yet have been only simply modelled in these analytic studies. To more fully characterize the interactions between the plasma particles, the neutral gas and the self-consistent electric field that forms under collisionless conditions, a numerical kinetic treatment of the transport was developed and is described in this chapter.

5.1 Derivation of Transport Equations

The most general solution starts with the Boltzmann equation for each species

$$\frac{df}{dt} = \frac{\partial f}{\partial t} + \underline{v} \cdot \nabla f + \frac{\underline{F}}{m} \cdot \frac{\partial f}{\partial \underline{v}} = \left(\frac{\partial f}{\partial t}\right)_c \tag{5.1}$$

The problem is simplified based on the 1-D nature of magnetic divertors or pumped limiters where the primary plasma and energy flow is along the magnetic field and onto a neutralizing plate. Here we assume the plasma is moving perpendicular to the target, as would be expected in bundle divertors or possibly local pumped limiters. The plasma usually only grazes the target in poloidal divertors or toroidal pumped limiters, so these cases must be considered in terms of an effective velocity normal to the target. Neutral particle motion is also described in terms of an effective or projected velocity parallel to the plasma flow into the target. For cases where 3-D neutral behavior is important to the particle and energy transport, a 3-D Monte Carlo neutral transport code was developed and is described in the next chapter.

For this 1-D geometry, it is more convenient to use the drift-kinetic equation. This is obtained (following Ref.[5.7]) by replacing the usual distribution function $f(t, \underline{x}, \underline{v})$ with the guiding center distribution function $f(t, x, W, \mu, \underline{v}_d)$, where

$$W = \frac{1}{2}m(v_{\parallel}^2 + v_{\perp}^2) + q\phi = W_k + q\phi$$

is the particle energy,

$$\mu = \frac{mv_{\perp}^2}{2B}$$

is the adiabatic invariant, ϕ is an electrostatic potential, and $\underline{v}_d$ is a drift velocity (neither parallel motion nor gyromotion). Then

$$\frac{df}{dt} = \frac{\partial f}{\partial t} + \frac{d\underline{x}}{dt} \cdot \nabla f + \frac{dW}{dt}\frac{\partial f}{\partial W} + \frac{d\mu}{dt}\frac{\partial f}{\partial \mu} + \frac{d\underline{v}_d}{dt} \cdot \nabla_{v_d} f = \left(\frac{\partial f}{\partial t}\right)_c \tag{5.2}$$

Now, $d\mu/dt = 0$, treating μ as a constant of the motion for the plasma particles, and either neglecting $v_{\perp}$ for neutral particles or assuming it is unaffected by collisions. Also, $dW/dt = dW_k/dt + qd\phi/dt$. Averaging Eqn.(5.2) over a gyroperiod, note that the only affected term is dW_k/dt which becomes the average rate of change of kinetic energy over

a gyroperiod. To evaluate this, dot $\underline{v}$ into the equation of motion $m d\underline{v}/dt = q(\underline{E} + \underline{v} \times \underline{B})$ to obtain

$$q\underline{v} \cdot \underline{E} = m\underline{v} \cdot \frac{d\underline{v}}{dt} = \frac{d}{dt}\left(\frac{1}{2} m\underline{v} \cdot \underline{v}\right) = \frac{dW_k}{dt} \tag{5.3}$$

The gyroperiod average of Eqn.(5.3) is

$$\left\langle \frac{dW_k}{dt} \right\rangle = -\frac{q\Omega}{2\pi} \oint_\Omega \underline{E} \cdot d\underline{l} + q(\underline{v}_{\|} + \underline{v}_d) \cdot \underline{E}$$

$$= -\frac{q\Omega}{2\pi} \int_\Omega \nabla \times \underline{E} \cdot d\underline{s} + q(\underline{v}_{\|} + \underline{v}_d) \cdot \underline{E}$$

$$= \frac{q\Omega}{2\pi} \int_\Omega \frac{\partial \underline{B}}{\partial t} \cdot d\underline{s} + q(\underline{v}_{\|} + \underline{v}_d) \cdot \underline{E}$$

$$\simeq \mu \frac{\partial \underline{B}}{\partial t} + q(\underline{v}_{\|} + \underline{v}_d) \cdot \underline{E} \tag{5.4}$$

Substituting back into Eqn.(5.2),

$$\frac{\partial f}{\partial t} + v_{\|} \frac{\partial f}{\partial x} + \left[\mu \frac{\partial B}{\partial t} + q(\underline{v}_{\|} + \underline{v}_d) \cdot \underline{E} + q \frac{d\phi}{dt}\right] \frac{\partial f}{\partial W} + \frac{d\underline{v}_d}{dt} \nabla_v f = \left(\frac{\partial f}{\partial t}\right)_c \tag{5.5}$$

In steady-state, $\partial/\partial t = 0$. Also, $B = B(x)$ and $\phi = \phi(x)$, so for these quantities, $d/dt = v_{\|} \partial/\partial x$. Neglecting any drift motions, $\underline{v}_d = 0$. Then Eqn.(5.5) becomes

$$v_{\|} \frac{\partial f}{\partial x} + \left[-q v_{\|} \frac{\partial \phi}{\partial x} + q v_{\|} \frac{\partial \phi}{\partial x}\right] \frac{\partial f}{\partial W} = \left(\frac{\partial f}{\partial t}\right)_c \tag{5.6}$$

Finally, Eqn.(5.6) becomes the trajectory equation

$$v_{\|} \frac{\partial f}{\partial x} = \left(\frac{\partial f}{\partial t}\right)_c \tag{5.7}$$

where it should be noted that, since $f = f(x, W, \mu)$, $v_{\|} = v_{\|}(x, W, \mu)$ is defined along a line of constant energy W, for constant B or small μ.

This is the fundamental equation used in subsequent analysis. Note that the original (coupled) partial differential equation in f has been reduced to a set of first-order ordinary differential equations coupled by the collision term. The general procedure is to solve

the set of five coupled trajectory equations for e, H, H^+, H_2 and H_2^+ including the interactions discussed in Section 3.1.1.

The collision operator can be expanded in several ways. The important charged/neutral reactions involve little energy or momentum transfer. Self-collisions among neutral particles can be neglected at low densities. Ion self-collision time, nominally by multiple small-angle scattering through the electric field, will be neglected compared to the transit time for the ions in the duct. Thus, for neutrals and ions, assuming $v_{\|} \gg v_{\perp}$,

$$\left(\frac{\partial f_i}{\partial t}\right)_c = \sum_j f_i(v_i, x) \int_{v_j} |v_i - v_j| \; \sigma_{ij}(|v_i - v_j|) \; f_j(v_j, x) \; dv_j \tag{5.8}$$

It is also assumed that the electrons can be described by a Maxwellian distribution,

$$f_e(x, v_{\|}, v_{\perp}) = A \exp\left(-\frac{1}{2}\frac{m_e(v_{\|}^2 + v_{\perp}^2)}{T_e} + \frac{e\phi(x)}{T_e}\right) \tag{5.9}$$

Integrating over velocity space and defining $\phi(0) = 0$,

$$n_e(x) = n_e(0) \exp(e\phi(x)/T_e) \tag{5.10}$$

This is the usual Boltzmann relation for isothermal electrons. This expression is a reasonable approximation in two regimes: collisional divertor electrons, but with sufficiently high thermal conductivity that T_e is constant; or collisionless divertor electrons sourced as a Maxwellian distribution at T_e from a collisional scrape = off layer, with essentially no interactions in the divertor other than with any electric field present. A consequence of this expression is the inability to directly determine electron heat transfer.

Finally, Maxwell's relations, which define the electromagnetic field relations,

$$\nabla \cdot \underline{B} = 0; \quad \nabla \times \underline{B} = \frac{\underline{J}}{\mu}; \quad \nabla \times \underline{E} = -\frac{\partial \underline{B}}{\partial t}; \quad \nabla \cdot \underline{E} = -\nabla^2 \phi = (n_i - n_e)\frac{e}{\epsilon_o} \tag{5.11}$$

For constant and uniform magnetic field, $\nabla \cdot \underline{B} = 0$ automatically and $\nabla \times \underline{B} = 0 = \underline{J}$ so there is no net current flow in the duct - i.e. ambipolar flow. Furthermore, $\nabla \times \underline{E} = 0$ since $\partial B/\partial t = 0$, consistent with simple parallel fields of the form $\underline{E} = E_{\|}(x)\hat{\underline{x}}$. These electrostatic fields are needed to maintain ambipolar flow. Finally, Eqn.(5.11d) is eliminated by assuming quasi-neutrality, $n_i \simeq n_e$.

5.2 Conditions of Applicability of Kinetic Transport Model

The approximations made in deriving the above set of equations imply an ordering of the fundamental time scales governing the behaviour. Thus, for example, the ion Boltzmann equation without any Fokker-Planck operator assumes that ion-ion collisions are slow compared to atomic reactions and the divertor transit time. In general,

$$\tau_{reactions} \quad or \quad \tau_{transit} \quad \ll \quad \tau_{ii} \quad or \quad \tau_{00} \tag{5.12}$$

$$\begin{bmatrix} atomic \\ reactions \end{bmatrix} \approx \begin{bmatrix} divertor \\ transit \end{bmatrix} \ll \begin{bmatrix} ion \\ thermalization \end{bmatrix} \approx \begin{bmatrix} neutral \\ thermalization \end{bmatrix}$$

These times can be evaluated as [5.7,5.8],

$$\tau_{ee} \simeq \frac{6(6\pi m_e)^{1/2}\epsilon_0^2(3T_e)^{3/2}}{n_e e^4 \ln\Lambda} = 4.94 \times 10^{10}\frac{[T_e(eV)]^{3/2}}{n_e(1/m^3)} \ (s) \tag{5.13a}$$

$$\tau_{reactions} \simeq \frac{1}{n_{reactant}\langle\sigma v\rangle_{reaction}} \tag{5.13b}$$

$$\tau_{i,transit} \simeq \frac{L}{v_i} \simeq L\left(\frac{m_i}{2T_i}\right)^{1/2} \simeq 7.22 \times 10^{-5}L(m)\left[\frac{A}{T_i(eV)}\right]^{1/2} \ (s) \tag{5.13c}$$

$$\tau_{ii} \simeq \frac{6(6\pi m_i)^{1/2}\epsilon_0^2(3T_i)^{3/2}}{n_i e^4 \ln\Lambda} \simeq 2.12 \times 10^{12}[A]^{1/2}\frac{[T_i(eV)]^{3/2}}{n_i(1/m^3)} \ (s) \tag{5.13d}$$

$$\tau_{00} \simeq \frac{1}{\sqrt{2}n_0\langle\sigma v\rangle_{00}} \simeq \frac{0.78 \times 10^{16}}{n_0(1/m^3)}\left[\frac{A}{T_0(eV)}\right]^{1/2} \ (s) \tag{5.13e}$$

where A is the atomic mass, and $\sigma_{00} \simeq 10^{-20}$ m^2 is the atomic size. Also, the ion cyclotron period is $\tau_{c,ion} = m_i/eB = 3 \times 10^{-8}/B(T)$ s.

Figure 5.1 shows these time scales as a function of temperature for plausible divertor conditions. The ordering outlined in Eqn.(5.11) is best satisfied over 80 eV under the given conditions. Below 100 eV, it would be desirable to add self-collisions to the ions. For other densities, the appropriate temperature range will vary.

5.3 Solution Procedure

Numerical solutions were obtained for the situation where there is an electrostatic potential peak by starting at the peak and solving the trajectory or characteristic equation, Eqn.(5.7), outwards. Some discussion is also given to procedures for obtaining a more general solution, with or without the potential peak.

5.3.1 Solution with Potential Peak

The numerical solution was obtained by an explicit marching algorithm that starts at the peak ($x = 0$) and integrates out towards the divertor throat, iterating on the potential at each step to obtain local quasineutrality. Initial conditions at the peak are taken to be Maxwellian outgoing (towards throat) ions and neutrals at the wall temperature, and Maxwellian incoming ions (towards target) at the scrape-off temperature (see Figure 5.2).

Starting the integration at the peak itself is particularly convenient for the characteristic equations solved since all particle trajectories turn at or before this point, or pass unhindered to the target. Representative trajectories in the (x, v_x) phase space are shown in Figure 5.2c. Of course, this assumes that a peak exists. This is not necessarily the case and the results show, among other things, conditions for the existence of a peak.

The general numerical procedure is as follows:

1) establish initial distributions for incoming and outgoing ions and neutrals at $x = 0$, the potential peak, on a set of velocity trajectories;

2) estimate the next value of the potential based on an initial guess or quadratic extrapolation

from previous values;

3) integrate the ion and neutral trajectory equations out one step (using Simpson's rule) including ion/neutral collisions as given by Eqn.(5.7);
4) compute new velocities along each trajectory based on the last velocities and the change in electrostatic potential;
5) integrate over the trajectories to determine the ion and neutral density;
6) calculate electron density from the Boltzmann relation, Eqn.(5.10);
7) if the ion and electron densities are not equal, adjust the potential guess and repeat steps (2) - (6) until adequate quasineutrality is obtained.

A variable grid spacing was used so that the step size could be made smaller if necessary in order to get convergence in Step (7). Normally step size was chosen such that the fractional changes in each step were expected to be less than some value (e.g. 0.01) based on the rate of change in the previous step.

A simple differencing scheme is used in the algorithm. Average values of the distribution function $\overline{f_k}(x^n, v_i^n)$ are maintained between velocities v_i^n and v_{i+1}^n and axial duct position x^n for species k. Each $f_k^n(v_i^n) \equiv \overline{f_k}(x^n, v_i^n)$ is defined over a half of the 1-D velocity space - either $-\infty < v_i < 0$ for particles entering the duct towards the target (defined as the minus axial direction), or $0 < v_i < \infty$ for particles travelling away from the target towards the duct throat.

Initially, all f_k^n are defined at x^n with the same initial velocity trajectories v_i (where $n = 0$ and $x^0 = 0$ at the potential peak). The change in f_k^n over step $\Delta x^n = x^{n+1} - x^n$ due to collisions is computed on the basis of f_k^n by Eqn.(5.7). The collided particle distribution function velocities are then "accelerated" across the estimated potential drop $\Delta\phi^n = \phi^{n+1} - \phi^n$, such that $\frac{1}{2}m_k(v_i^{n+1})^2 = \frac{1}{2}m_k(v_i^n)^2 + q_k\Delta\phi^n$. If the potential increases, some trajectories may turn around and can no longer be followed. Since it is assumed that $x^0 = 0$ is the peak, the potential must drop, and a new velocity trajectory is created. The initial value of $f_k^{n+1}(0)$ on this trajectory is that of the incoming flux of species k that turns around at potential $\phi^{n+1}(x^{n+1})$, and any other sources of zero velocity particles at x^{n+1}. If the incoming flux is assumed to be Maxwellian at T_i, and if it is not strongly affected by the reactions, then the turning value is $f_k^{n+1}(0) = f_k^0(0)\exp(\phi^{n+1}/T_i)$.

At this point, there are several distributions $f_k^{n+1}(v_{ik}^{n+1})$, where the velocities v_{ik}^{n+1}

are species k dependent because of mass and charge differences. One possibility is to linearly interpolate all distributions onto a uniform set of velocities, such as the velocity trajectories for H^+ ions. This choice makes collisional particle transfers simple because the energy groups are identical. If the neutrals are interpolated onto H^+ trajectories, then it also keeps the fine meshing consistent among the species - e.g. it avoids a highly structured H^+ distribution with closely-spaced velocity trajectories reacting and transferring particles to a crudely-spaced set of H trajectories in the same energy range. The numerical error in this approach is only in the interpolation of the trajectories since all quantities are conserved in collisions.

A second possibility is to just follow trajectories from some initially specified set, without doing any adjustment. This avoids interpolating on each step, but complicates the particle transfers due to collisions since there is no correct way to transfer particles between species (such as H to H^+) if the energy groups are different. One might simply transfer the reacted particles from the original species energy group (i) to the nearest energy group (h) in the reactant species, say that which contains the average velocity. This only approximately conserves all quantities, with the accuracy improving as the energy group size decreases. One quantity can be explicitly conserved by adjusting the contribution to the new energy group to be

$$\left[\Delta f_h^{n+1}(v_h^{n+1})\right]_{reactant} = \Delta f_k^{n+1}(v_{ik}^{n+1})\frac{(v_i^c - v_{i+1}^c)}{(v_h^c - v_{h+1}^c)} \tag{5.14}$$

where $c = 1$ conserves particle density, $c = 2$ conserves particle flux and so on. If particles were transferred from the original to more than one new group, more quantities could be conserved. However, in the interests of computer time, only one quantity (typically density) is explicitly conserved.

While both these methods were tried, the latter approach was preferred. This is because only a small fraction of all the particles react on any given step, so the numerical error in the collision process calculations is only on a small fraction of the total flux. In the first scheme, however, collisions are treated exactly but there is a small numerical error in the total flux on each step because of the interpolation of the distributions onto the new trajectories. For the same local numerical error (governed by the energy group and spatial grid sizes), the total error was larger because it affected all the particles and not just the reacting fraction.

5.3.2 General Solution

The previous section focussed on solutions obtained assuming the existence of an electrostatic potential peak. This yielded a natural starting point for the solution of the characteristic equations. In this section, some attention is also given to the more general problem of finding the solution for an arbitrary (but physical) profile. This would have the advantage of allowing the full range of collisionless solutions to be found (including those with an expanding magnetic field), to better understand the conditions that led to a potential peak, and to eliminate the approximations inherent in taking some uncertain location, with estimated distributions, as the starting point for the calculations. This general problem turned out to be much more difficult and no satisfactory solutions were found in the course of this work. However, the approaches that were tried and their problems are summarized here to serve as background information for future work.

Consider the "known" information. A plasma is entering the divertor with velocity distribution characteristic of the scrape–off and the divertor throat. For example, a Maxwellian H^+ plasma with bulk velocity v and temperature T_i could be assumed if the scrape–off is sufficiently collisional. The flux leaving the divertor at the throat depends on the details of the reactions and electric field structure so is not known. At the other end of the diverted field lines is the target. Here, the incident flux is the entering flux adjusted by reactions and the electric field, and is also not known. However, given an incident flux, the recycling flux is simply a specified function of the surface chemistry. The problem then is to solve the transport equations between the two ends, each with incompletely specified conditions at each boundary.

The first issue in setting up a general algorithm is how to treat that unknown half of the velocity space on each iteration. For example, the distribution at the boundary could be guessed and the full distribution integrated along (as in the procedure described in Section 5.3.1) until the other end was reached. This approach requires a full solution over all velocity space, even though half of the distribution is not being solved with the correct boundary condition. A second choice would be to integrate the known half distributions in from the known boundary condition, with fixed distributions in the unknown half from the previous pass. Then store the new half solution and integrate out the previously fixed half-distributions from the newly estimated boundary condition directly obtained from the

last step. This seems more reasonable, but requires considerable storage. A third choice is to follow this last prescription, but simply store the distribution moments - density, bulk velocity and average energy. The detailed distributions are only needed for exact calculations of distribution dependent charge exchange. However, very reasonable results should still be obtained. This latter choice was used for the iterative scheme.

The second issue relates to the treatment of the electrostatic potential. Ideally, this could be solved for through Poisson's equation, Eqn(5.11d). In practice, this is almost never done since, while the plasma will be almost charge neutral, even a small difference due to numerical error will give rise to very large electric fields. For example, an error of only $10^{12}/m^3$ in a $10^{20}/m^3$ plasma (a relative error of 10^{-8}) would imply 20 kV electric fields over 1 m distances! The basic approach, as in the previous section, was to solve for the potential by iterating an estimate until charge neutrality was obtained.

The final approach, then, was to obtain the numerical solution to the general problem with an explicit marching algorithm that iterates between the boundary conditions at the target and the main plasma (or divertor throat). The ion, neutral and electron transport equations are solved out from the target for outgoing particles and then in from the main plasma for incoming particles. From the new charge densities (either on each step or over the entire region), a new potential profile is estimated and the process repeated until quasi-neutrality is obtained.

While the overall procedure seemed reasonable and still fairly flexible at this level of detail, no satisfactory complete algorithms were found. The crux of the problem was apparently in determining how to iterate on the potential. That is, given an initial guess for the potential $\phi(x)$ and the resulting local charge density $q(x) = e[n_i(x) - n_e(x)]$ under this assumed potential, how should $\phi(x)$ be adjusted such that $q(x) \equiv 0$ (except in the sheath, of course, where Poisson's equation should be solved). Several approaches were tried. They can be classed into three groups: local adjustment of $\phi(x)$ on each step; global adjustment of $\phi(x)$ separate from $f(x, v)$ integration; and parametric optimization of $\phi(x)$. The specific algorithms are outlined in Table 5.3, along with some remarks on the difficulties encountered.

The local adjustment of $\phi(x)$ through the modified secant rule was quite successful in the solutions starting at the peak (described in Section 5.3.1), but was not satisfactory here

because it required knowing which fluxes (incoming or outgoing) were more important - something which is not generally known until the solution is obtained. To see this, consider the two extremes of high recycling and zero recycling from the target. In the former, the incoming ion flux is only slightly perturbed by the field while the cold outgoing ions are very strongly influenced, so ϕ should be adjusted on an outward integration from the target where the correct boundary conditions are known for these cold ions. In the latter extreme, there is no point adjusting on the outward integration, but rather it must be based on the incoming stream of ions from the scrape-off boundary condition. In between these extremes, it is not clear how to do the adjusting.

The global adjustment procedure tried to separate the $\phi(x)$ iteration from the $f(x,v)$ integration in order to incorporate the global influence of ϕ into the iteration mechanism. Assuming a fixed $\phi^0(x)$, the trajectory equations can easily be integrated to yield $q(x) = e[n_i(x) - n_e(x)]$. In order to get $q(x) \equiv 0$, adjust $\phi^0(x)$ by $\Delta\phi(x)$ which is obtained from

$$q[\phi^{new}(x)] \simeq q[\phi^0(x)] + \frac{\partial q}{\partial \phi}\Delta\phi(x) \equiv 0 \tag{5.15}$$

where $\partial q/\partial\phi$ is estimated and $\phi^{new} = \phi^0 + \Delta\phi$. Since changing the potential at any point can change $q(x)$ everywhere, the procedure involves inverting a full $N \times N$ matrix (N is the number of spatial points) and is sensitive to errors in estimating $\partial q/\partial\phi$. More importantly, this approach assumes that the initial guess ϕ^0 is sufficiently close to the correct value that a small linear perturbation can yield the answer - otherwise higher order terms are needed in the expansion of $q(\phi^0 + \Delta\phi)$ and the equations are no longer linear and directly solvable for $\Delta\phi$. However, such an accurate initial guess for $\phi(x)$ is not usually possible.

The third procedure constructed a simple model for the potential that had three adjustable parameters, $\phi_{target}, \phi_{peak}$ and x_{peak}, and fixed $\phi_{throat}(x_{throat}) = 0$. Using a simple linear fit between the points $(0, \phi_{target})$, (x_{peak}, ϕ_{peak}), and $(x_{throat}, 0)$, all physical solutions for $\phi(x)$ could be crudely modelled. Then, $\int q^2(x)dx$ or some other measure of global non-neutrality could be calculated as a function of the adjustable parameters. Various optimizing routines could then be applied to find the parameters that minimized this global non-neutrality. It was hoped that this method could transform a very crude initial guess for $\phi(x)$ into a much better guess that procedures such as the linear perturbation scheme

could then converge with. Indeed, random search in parameter space with periodic volume shrinkage around the local minimum was a very robust, fairly fast algorithm that could obtain improvements in $\int q^2(x)dx$ by factors of ten. However, it seemed that the simple 3-parameter model was too simple and yielded only broad, wide-ranging minima. Better localization would require more parameters, which rapidly required unreasonable amounts of computer time with this algorithm.

In summary, several algorithms were tried in an effort to obtain a general solution to the 1-D kinetic transport relations in the presence of neutral/ion collisions, rather than one that assumed the existence of a potential peak and started calculations from that point. No satisfactory algorithms were found in the course of this work.

5.4 Results

For a fully absorbing target, the plasma flows in from the scrape-off and is neutralized and absorbed at the target. Since the electrons travel faster (at comparable temperatures), they escape first and charge the target plate negatively with respect to the plasma. The electric field that forms is confined largely to a thin deBye sheath just in front of the target. However, a presheath extends farther into the plasma and serves to accelerate the ions up to sonic flow, at which point appreciable charge separation occurs and the "sheath" forms. Under these circumstances, the potential drops monotonically from the throat to the target.

Now consider the neutral atomic hydrogen recycling from the target. Ionization and charge exchange will replace the cold H^0 with cold H^+ ions. For equal fluxes of ions and neutrals (i.e. complete recycling from target), the cold H^+ density would become larger than the hot incoming H^+ density by the velocity ratio, thus increasing the positive charge density within about a mean free path of the target. This increases the local electrostatic potential and may form a peak if the cold ion density is large enough.

The effect of this peak is to accelerate the cold ions away from the target and so limit the buildup of positive charge. It also attracts more electrons to this point, as is needed to maintain local quasineutrality. From the Boltzmann relation for the electrons, it can also be seen that an increase in electron density implies a locally increased potential.

This is the physical picture behind the formation of a potential peak. To investigate the characteristics of this peak, the trajectory equation, Eqn.(5.7), was solved using the numerical methods outlined in Section 5.3.1.

5.4.1 Atomic Hydrogen and Charge Exchange Model

If wall recycling occurs mostly as atomic hydrogen, then the H and H^+ temperature will be on the order of 0.025 - 0.1 eV depending on the target surface temperature. If wall recycling occurs mostly as molecular hydrogen, then there will be a outward flux of H_2 and H_2^+ at 0.025 - 0.1 eV, plus an outward flux of H and H^+ at about 3 eV, the dissociation energy. The actual recycling temperature T_w is not critical since in either case it is much smaller than the incoming plasma temperature and so the cold ion behavior is expected to be dominated by the electrostatic potential.

Various reactions and species are possible. However, to characterize the solutions, only a very simple model is needed. Here, all the molecular reactions are neglected and it is assumed that the wall recycles primarily H. Furthermore, the important reactions are those that form cold H^+ - that is, electron impact ionization and resonant charge exchange. Since the latter is usually much larger (see Section 3.1.1), only charge exchange was initially included.

Finally, the potential peak must occur some distance from the target - it must be at least outside the deBye sheath, and furthermore must occur far enough out for there to be an appreciable density of cold ions, probably within an ionization or charge exchange mean free path from the target. However, the position is not initially known but would have to come out of the analysis. Consequently it is not possible to specify the densities of H and H^+ at the peak itself based on known target and pump characteristics. Rather the total outward flux is specified as some recycling fraction R (by mass) of the incoming ion flux to the target. Thus a fully absorbing plate would have $R = 0$, while a reflecting plate would have $R = 1$. Here, R is specified at the potential peak where the numerical algorithm starts, so is slightly different from R at the target. Then the ratio of H^+/H within this recycling fraction is treated as an adjustable parameter and a family of solutions obtained. It is actually more useful to treat the free parameter as $P = n_{cold\ H+}/n_{hot\ H+}$, evaluated at the peak, since this ratio directly drives the solutions.

Once the parameters T_i, T_e, T_w, P, R and a density or flux are specified, the calculation

can begin. The results show the evolution of the potential densities and the distributions away from the peak as illustrated in Figures 5.3 - 5.5 for a case with $T_i = T_e = 2$ keV, $T_w = 0.05$ eV, $R = 1.26, P = 18.$ and $n_H(peak) = 8 \times 10^{20}/\text{m}^3$, and Figure 5.6 for $R = 1.1, P = 20$ and $n_H(peak) = 4 \times 10^{19}/\text{m}^3$.

The potential profile (Figure 5.3) peak is about 12% of the electron temperature and occurs over several mean free paths for H charge exchange. Beyond this point, most of the initial cold H has reacted so there is no longer any cold ion source. In the direction towards the plate, the profile simply drops off rapidly. This is consistent with the large and increasing H density (and thus cold H^+ source) towards the plate. Of course, at some point the conditions for the formation of the sheath would be reached, quasineutrality could no longer be assumed, and Poisson's equation would have to be solved until the plate was reached. This would then pin down the location of the peak. Such a matching to a sheath solution was not done here. Consequently the curve on the target side of the peak is only illustrative of the potential profile in this region.

Figure 5.4 shows the density profiles along the divertor. The cold thermal H rapidly drops off because of charge–exchange. Hot H and H^+ from charge exchange also form because of the reactions. Since the initial conditions at the potential peak assumed no hot H, this density drops to zero here. In reality, the curve would be smooth through $x = 0$ because of the formation of hot outgoing H between the target and the peak. Since the only reaction in these calculations was charge exchange, the H/H^+ ratio levels off towards the throat as the potential flattens out and equilibrium is reached in the charge transfer process. Finally, the hot incoming H^+ is almost unaffected by the whole process (the peak is only 12% of T_i), except that the rapid drop in potential towards the target is reflected in a corresponding drop in the H^+ density as the ions are accelerated inwards.

Figure 5.5 shows the normalized ion distributions at the divertor throat. The incoming distribution is a simple Maxwellian as specified for the boundary condition. The outgoing distribution, however, rises to a sharp peak and cutoff. This cutoff energy corresponds to the potential drop between peak and throat. The almost singular nature at this point arises from the high cold ion density at the potential peak which is accelerated outwards by the potential. The width of this peak in the distribution function is approximately the temperature of the cold ions, T_w.

Figures 5.3 - 5.6 are representative of the solutions found over a wide range in input parameters. Although the magnitude of densities and potentials might change, the same qualitative behavior with a potential peak was observed. However, it was also found that no sensible solution could be found under certain conditions. A sample potential profile from such a case is shown in Figure 5.7. Here the potential simply drops from the peak outwards and does not level off as would be expected in any physical solution. The range of solutions can be plotted on (R, P) coordinates as shown in Figure 5.8. For any given recycling ratio, no solution exists for P smaller than some value.

The nature of this solution limit boundary can be understood as follows. As the boundary is approached from large $P = n_{cold\ ions}/n_{hot\ ions}$, the electrostatic potential drop from target to throat, $\Delta\phi$, increases until finally $\Delta\phi$ becomes effectively infinite (Figure 5.9). Physically, the potential drop is required to sweep the cold particles formed at the target away in the steady-state solution. The smaller the cold ion population (i.e. the smaller P is at a given R), the smaller the initial electric field gradient and the larger the cold neutral population, so the harder it is to prevent an accumulation at the plate. This sets the minimum value of P. As R increases, the number of cold particles at the plate increases for a given incoming flux, so the larger the minimum value of P must be.

To understand the functional dependence of the solution limit, consider a very simple model for the behavior near the peak. Flat distributions of hot and cold H^+ are assumed, each extending out to characteristic velocities $v_h = \sqrt{2T_h/m}$ and $v_c = \sqrt{2T_c/m}$ with densities n_{h0} and n_{c0}, respectively, at the peak. At some distance x away from the peak, towards the throat, the potential will have fallen to $-\phi(x)$ (from $\phi(0) = 0$), where it is assumed that $T_c \ll \phi \ll T_h, T_c$. The hot H^+ distribution will be essentially unchanged since $T_h \gg \phi$, although it will have increased by a small amount representing those "hot" ions (more correctly, incoming ions) which were turned by the potential between here and the peak, $2n_{h0}\sqrt{\phi/T_h}$ (these turned ions must be accounted for in both directions). The initial cold H^+ flux has been accelerated so the density at x is smaller by a factor of $\sqrt{T_c/\phi}$. There is an additional ion component from charge transfer to cold neutrals, $2\sigma v_i n_{h0} n_{n0} x/v_\phi$, where the neutral density at $x = 0$ is n_{n0} and their mean speed is $v_\phi/2 \simeq \sqrt{\phi/2m}$. Finally, the Boltzmann relation for the electrons is $n_e = n_{e0}e^{-\phi/T_e} \simeq n_{e0}(1 - \phi/T_e)$. From quasineutrality, $n_{e0} = n_{h0} + n_{c0}$ and, at x,

$$n_{h0}\left(1+2\sqrt{\frac{\phi}{T_h}}\right)+n_{c0}\sqrt{\frac{T_c}{\phi}}+2\sigma n_{n0}xn_{h0}\sqrt{\frac{T_h}{\phi}}=(n_{h0}+n_{c0})(1-\frac{\phi}{T_e}) \qquad (5.16)$$

Neglecting terms of order ϕ/T_e or $\sqrt{T_e/\phi}$ with respect to $\sqrt{\phi/T_h}$, this simplifies to

$$\phi+\sigma n_{n0}xT_h-\frac{P}{2}\sqrt{T_h\phi}=0 \qquad (5.17)$$

where $P\equiv n_{c0}/n_{h0}$. This requires $P>4\sqrt{\sigma n_{n0}x}$ in order for a solution to exist. Now $\sigma n_{n0}x$ is just the "optical thickness" of the neutrals to the incoming plasma, and is more correctly defined as $\int_0^x \sigma n_n(s)ds$. Thus we obtain the requirement

$$P=\frac{n_{c0}}{n_{h0}}>4\left[\int_0^\infty \sigma n_n(s)ds\right]^{1/2} \qquad (5.18)$$

where the integration has been extrapolated to infinity since P ought to satisfy this criterion independent of x, and since n_n is rapidly attenuated to zero.

If σ is constant, then $n_n(x)$ is approximately exponential and this integral becomes $n_{n0}v_c/n_{h0}v_h$ or $R-P\sqrt{T_c/T_h}$. The resulting line is also shown on Figure 5.7 where $\int \sigma n_n dx \simeq R$ for the conditions studied here. It can be seen that this line qualitatively matches the numerical solution boundary, and is consistent with the picture that the minimum cold ion density at the peak is set by the necessity of forming sufficient electric field to drive these plus subsequent cold ions away.

One consequence of Eqn.(5.18) is that the solution limit is not strongly affected by the plasma temperature since the dominant cross-section, charge exchange, is fairly constant, dropping by only a factor of 10 over four decades in energy, 1 eV - 10 keV.

In a specific application, it is necessary to pin down P and R to determine if a peaked potential solution exists. The recycling fraction R is a simple function of the target surface properties, but P cannot be related to the usually known boundary conditions on the basis of the present analysis - a more general solution is required that solves between correct target and divertor throat boundary conditions. However, the present results show that a peaked potential can exist, and indicate some characteristics of such a solution.

5.4.2 Molecular Hydrogen Model

Since hydrogen is most likely to recycle from the target as molecules, the model was expanded to include molecular hydrogen, and the ionization, charge exchange and

dissociation reactions described in Section 3.1.1. Deuterium was used as the hydrogen isotope. Again, the procedure was to solve out from the assumed potential peak to the divertor throat, starting at the peak with Maxwellian incoming D^+ and Maxwellian outgoing D_2 and D_2^+. The results were very similar to those obtained with only atomic hydrogen and charge exchange.

In Figure 5.10, the evolution of the distribution functions away from the peak is illustrated for the artificial case of no molecular dissociation - only D_2 ionization and dissociation. This brings out several features that are not otherwise clearly seen. At the peak, all distributions are assumed to be Maxwellian, although with large differences in temperatures. Away from the peak, the reactions convert cold D_2 into cold D_2^+ which is accelerated out by the self-consistently developing electric field. This pushes out the D_2^+ distribution, with a sharp peak corresponding to the D_2^+ density at the peak itself. Further away, the cold D_2 has been sharply reduced although a hotter D_2 tail is produced by charge exchange between remaining cold D_2 and hot, accelerated D_2^+. Far enough away, all the D_2 has been ionized. The incident D^+, meanwhile, is unaffected by any reactions here, and the only effect is the reflection of slower D^+ by the electric field. The reflected velocity forms a sharp boundary at $v = \sqrt{2\phi/m_i}$, and is larger than the D_2^+ peak by the square root of the mass ratio.

When the full reactions are included, the distributions are complicated by the dissociation of D_2 (Figure 5.11). Neutral D makes a brief appearance before it too is ionized. Also, the D^+ and D_2^+ distributions are smoothed out considerably from their behavior when treated individually (see Figures 5.5 and 5.10). The basic behavior of the solutions is not qualitatively different from the earlier atomic hydrogen models. However, there is a definite change in length scales, as seen by comparing the potential profile in Figure 5.11 with that in Figure 5.3. The cold (0.025 eV) D_2 has a high ionization cross-section so rapidly ionizes and causes a sharp initial drop in the potential. Then the dissociated D and D^+ (3 eV) react over longer distances.

5.4.3 Comparison with Other Models

McKenty [5.10,5.15] considered the molecular and atomic reactions (dissociation, ionization and charge exchange) discussed in Section 3.1.1, and integrated between the target and divertor throat. A similar numerical approach was used, assuming the existence

of the peak and solving the trajectory equations away in both directions with iteration to match the divertor throat boundary conditions. Poisson's equation was used near the wall when the electric field gradient became large. The results (and numerical behavior) were very similar to those presented here. Figure 5.12 shows the potential and density profiles between peak and throat, and the distribution functions at $x = 0.1$ m, for 100 eV plasma temperatures. When R and P were varied, the potential was found to rise to as much as 0.3 T_e before turning over and falling sharply through the deBye sheath.

Bailey and Emmert [5.6,5.14] considered the problem analytically, and also came up with a requirement for the existence of a solution. Their model was based on atomic hydrogen, a truncated Maxwellian ion distribution, and neglected the thermal energy of the cold ions. They calculated the potential rise as a function of T_i/T_e and found it to vary from 0.056 at $T_i/T_e = 10$, to 0.22 at $T_i/T_e = 1$, to 0.33 at $T_i/T_e = 0.1$.

Sizonenko and Shergin [5.16] have also apparently considered this situation, although only their abstract has been obtained.

Figure 5.11 compares the solution limits obtained from these various models. Exact agreement is not expected since the curves are all calculated under different assumptions and temperatures. Nonetheless, the overall behavior seems fairly insensitive to these details.

5.4.4 Stability

Finally, we briefly touch on the question of the stability of the highly non-thermal distribution functions as shown in Figures 5.5, 5.6, 5.10 and 5.11. Consider the simplest class of such instabilities - those associated with electrostatic waves. Since the present situation involves non-thermal ion and thermal electron distributions, we expect the instability to be excited by the ion distribution but stabilized by Landau damping on the electrons. Estimating the instability growth rate γ from the usual expressions for ion and electron Landau damping derived from the linearized Vlasov equation [5.21,5.22],

$$\gamma \simeq \gamma_i + \gamma_e = \frac{\pi}{2}\frac{\omega\omega_{pi}^2}{k^2}\frac{\partial \hat{f}_i}{\partial v}\bigg|_{\omega/k} + \frac{\pi}{2}\omega\frac{\omega_{pe}^2}{k^2}\frac{\partial \hat{f}_e}{\partial v}\bigg|_{\omega/k} \tag{5.19}$$

where ω/k is the phase velocity of the waves with the largest growth rate, $\omega \simeq \omega_{pe}$ if finite ion temperature effects are neglected ($k^2\lambda_{deBye}^2 \ll 1$), $\hat{f}_i$ and $\hat{f}_e$ are the normalized distribution functions, and ω_p is the plasma frequency, $\omega_p = \sqrt{ne^2/\epsilon_0 m}$. The maximum

growth rate occurs at the wave phase velocity $v_\omega = \omega/k$ where $\partial \hat{f}_i/\partial v$ is largest positive compared with $\partial \hat{f}_e/\partial v$, which is always negative and stabilizing for a thermal distribution.

In the present class of distributions, $\hat{f}_i$ is sharply peaked at $v = \sqrt{2\phi/m_i}$ where $\phi \ll T_c$, and the worst growth rate occurs near here. As an example, this expression is evaluated for the case illustrated in Figure 5.11 at x = 1 m, where $T_e = T_i = 1$ keV and $n = 3.8 \times 10^{19}/\text{m}^3$. Taking ϕ = 73 eV and evaluating γ at $v_\omega = \sqrt{2\phi/m_i}$, we obtain $\gamma \approx 10^{11}$/s!

While this indicates instability, the growth rate value must <u>not</u> be interpretted literally since Eqn.(5.23) assumes the deviation from the thermal distribution is only a "gentle bump", not a sharp peak. An exact check on stability to electrostatic waves is provided by the Penrose criterion [5.22] which applies to any double-humped distributions $F(v)$,

$$\int_{-\infty}^{\infty} \frac{F(v_0) - F(v)}{(v - v_0)^2} dv < 0 \quad \text{for instability} \tag{5.20}$$

where $F(v) = f_e(v) + (m_e/m_i) f_i(v)$, and the minimum is at v_0. For the same example as above, the Penrose integral is less than zero so the distribution is indeed unstable. This criterion, however, does not give the growth rate. Interestingly, no signs of instabilities were observed other than possibly at the solution boundary discussed previously.

Other instabilities are also possible. In a real divertor, the perpendicular velocity space distribution must also be considered. Velocity space anisotropies would give rise to loss-cone instabilities. Then there are electromagnetic waves such as drift waves, which would be excited by the density gradients along the field lines and cause low-level turbulence.

The detailed susceptibility of collisionless plasma distributions to instabilities is beyond the scope of the study. This discussion simply points out the need for more careful treatment. If instabilities arise, we could expect the potential peak to be reduced but not necessarily eliminated since it is the "hot"/"cold" ion nature of the ion distribution that causes the peak. Enhanced turbulence might even be useful since it could efficiently spread the plasma energy over the walls rather than just onto the target, a possibility that may exist even in collisional plasmas because of the curvature of the field lines [5.23].

5.5 Applications

In the previous sections, it was shown that it is possible for a potential peak to occur in a divertor duct under collisionless flow conditions. The magnitude of the peak relative to the main plasma is a function of several parameters, notably R, P and T_e/T_i, but several calculations all independently suggest that it is no more than 0.3 T_e in plausible divertor conditions ($R \simeq 1, T_e/T_i \approx 1$). The next question, then, is what are the consequences of such a potential profile - i.e. one rising up to about 0.3 T_e from the main plasma potential, then dropping by about 3 T_e through the usual deBye sheath to the target.

In general, such a potential profile reflects some fraction of the incoming scrape–off layer ion flux back to the main plasma. For a Maxwellian incoming distribution, a 0.3 T_e peak would reflect at most $1 - e^{-0.3}$ or 26% of the incoming hydrogen. For example, with $T_i = T_e = 1$ keV, $R = 1, P = 3.84$ and $n_{D_2}(peak) = 1.63 \times 10^{20}$ /m^3 (see Figure 5.11), the potential drop is 0.08 T_e, the incoming D^+ flux dropped 7% from throat to peak, and the convected ion power dropped 4%. A more interesting question is the effect, if any, on parallel thermal conduction through electrons, usually the dominant heat flow mechanism. Since the present model assumed Maxwellian electrons at constant T_e, and thus infinite conductivity, the power flow through electrons could not be calculated.

Impurities, though, are more sensitive to small electric fields because of their charge state. As with hydrogen, the potential peak would reflect incoming impurities and reduce the divertor's impurity shielding efficiency. In addition, it would either accelerate divertor–generated impurities back out into the main plasma or confine them to near the target, depending on which side of the peak they became ionized. Since the peak is calculated to occur close to the target, such a potential peak seems more likely to hurt than help.

The quantitative effect on impurities is outside the scope of this study, although it has been briefly addressed in Ref.[5.19] where it was estimated that hydrogen ion drag could counter the adverse effect of the potential peak on impurities. This calculation, however, neglected the drag of the outflowing cold ions and it assumed that the time scale for Coulomb friction was fast compared with the impurity divertor transit time, which is not necessarily compatible with the collisionless conditions assumed for the potential peak to form in the first place.

As a parting thought, it may be possible to adjust the location of the peak by the

placing of pumps and gas sources along the divertor so as to maximize the confining aspect of this peak, but this was not investigated here.

5.6 Summary

In this chapter, some particular consequences of collisionless plasma exhaust in a divertor were explored. In particular, 1-D models with H, H^+, H_2 and charge exchange or ionization and molecular dissociation reaction were used to identify and characterize a family of solutions where the electrostatic potential profile rose to a peak of as much as 0.3 T_e before falling through the deBye sheath at the target. This potential peak results when cold ions formed by reactions with cold recycling neutrals build up in density near the target, creating an electric field that accelerates the cold ions away from the plate and limits their density buildup. Such an effect could not be observed in a a single-temperature fluid model, since it formed, in this analysis, as a result of co-existence of cold and hot ions.

Conditions under which such a potential profile could form were studied numerically, and the resulting limits agreed with various other calculations ranging from a very simple physical model, to a similar but more accurate code, to a more detailed analytic study. Although no studies have specifically looked for such a potential profile, some experiments on the Wisconsin Octupole [5.17,5.18] were indicative of complex electric field structure.

The consequences of a potential peak were not studied in detail here. However, such a small peak ($< 0.3T_e$) is unlikely to have a drastic effect on hydrogen flow, but may be an appreciable factor for impurities. Incoming impurities may be reflected by the peak, and divertor-generated impurities might be accelerated back towards the main plasma [5.19]. Sputtering in the presence of a peak was studied by McKenty [5.15] who found that H_2^+ sputtering was comparable to the usually considered H^+ sputtering for iron and $T_e > 80$ eV. However, it is likely that this latter effect is a consequence of the sheath, not the potential peak.

A general inadequacy in the various models is that they assume that a peak exists, and then seek to investigate the existence and behavior of such a solution. It would be desirable to have a solution for the full range of possible collisionless behaviors ranging from simple monotonic drops to the target to the more complicated peaked

profiles observed here. Some effort was devoted to adopting the simple solution scheme used here to this general problem, but with no success. It may be that the method of characteristics approach is not the best choice for a more general problem where it is not initially clear how the characteristic trajectories behave – e.g. if they turn around or not. An alternate approach might be to solve the 2-D phase space problem using a finite difference algorithm.

However, more useful next steps in the development of this model would be to add a better electron model such as solve the electron fluid equations, and to add ion–ion self–collisions. The electron model would allow full calculations of heat transfer, while the addition of self–collisions would extend the range of applicability of the model to the colder, more collisional edge regimes usually preferred for limiting target erosion.

5.7 References

[5.1] C.E.Singer and W.D.Langer, "Axisymmetric tokamak scrape-off transport", PPPL-1920, Princeton University, August 1982.

[5.2] D.E.Post, J.Heifetz and M.Petravic, "Models for poloidal divertors", PPPL-1913, Princeton University, July 1982.

[5.3] A.Nicolai, "Numerical simulation of the transport processes in the scrape–off region and the burial chamber of a bundle divertor", Jrnl. Nucl. Mater., 93 & 94(1980)231.

[5.4] G.Emmert, "Modelling of bundle divertors", UWFDM–343, University of Wisconsin–Madison, January 1980.

[5.5] G.Emmert and A.Bailey, "Modelling of bundle divertors –II", UWFDM–365, University of Wisconsin–Madison, July 1980.

[5.6] A.Bailey and G.Emmert, "A theoretical model for hot plasma flowing to a wall with recycling", UWFDM–473, University of Wisconsin–Madison, May 1982.

[5.7] W.M.Stacey, "Fusion plasma analysis", Wiley and Sons (New York), 1981.

[5.8] G.Weissler and R.Carlson (eds.), "Vacuum physics and technology", Academic Press, New York, 1979.

[5.9] P.Gierszewski,R.L.Morse and T.F.Yang, "Ion-neutral transport in 1–D divertor channel with potential peak", Bull. Am. Phys., 26(7), September 1981, 1058.

[5.10]P.Gierszewski, P.McKenty, J.McCullen and R.Morse, "Structure of wall plasmas near divertor neutralizer plates or limiters", Phys. Rev. Lett., 49(9), August 1982, 650.

[5.11]F.L.Hinton and R.D. Hazeltine, Phys. Fluids 17, 2236 (1974).

[5.12]A.El-Nadi, "Effect of scrape-off on tokamak radial transport", Phys. Fluids, 22(8), 1570, (1979).

[5.13]A.Nicolai and A.T.Mense, "Computer modelling of the bundle divertor, Part 1: Basic equations", ORNL/TM-6852, May 1979.

[5.14]J.D.Callen et al, "Plasma transport and impurity behavior in the edge and divertor regions of a tokamak", paper IAEA-CN-38/Y-3, 8th Inter. Conf. on Plasma Phys. and Cont. Nucl. Fus. Research, Brussels, July 1980.

[5.15]P.McKenty, "Numerical simulation of wall plasmas near divertor neutralizer plates or limiters", Ph.D. thesis, Nucl. Eng., University of Arizona, 1983.

[5.16]V.L. Sizonenko and G.G.Shergin, "Plasma layer in a near-wall gas pillow", Fizika Plazmy, 7(6), 1981, 1258.

[5.17]C.Strawitch and G.Emmert, "Non-ambipolar transport in a magnetic divertor", University of Wisconsin, DOE-ET/53051-3, February 1980.

[5.18]C.Strawitch, "Plasma transport in a simulated magnetic divertor configuration", University of Wisconsin, DOE-ET/53051-20, March 1981.

[5.19]J.A. Schmidt et al, "Impurity control physics", Ch. VI, vs. FED-INTOR/82-1, Critical Issues, Vol. 1, October 1982.

[5.20]G.Becker, "Non-Maxwellian ion distributions in the ionization zone of the tokamak boundary", IPP III/69, Max-Planck-Institut fur Plasmaphysik, Garching, May 1981.

[5.21]F.V.Chen, "Introduction to plasma physics", Plenum Press, New York, 1974.

[5.22]N.A.Krall and A.W.Trivelpiece, "Principles of plasma physics", McGraw-Hill, New York, 1973.

[5.23]T.F.Yang and J.D.Callen, "Stability of the plasma in a bundle divertor", Nucl. Fus., 20(9), 1177 (1980).

Table 5.1: List of variables

A	Atomic mass;
B	Magnetic field strength [T];
E	Electric field [V/m];
$f(v)$	Distribution function [s/m^4];
$\hat{f}(v)$	Normalized distribution function;
k	Wave number [1/m];
m	Mass [kg];
n	Density [1/m^3];
P	Ratio of cold ion to hot ion densities at peak;
q	Electric charge;
R	Ratio of outward mass flux to inward mass flux at peak;
T	Temperature [J];
v	Velocity [m/s];
W	Particle energy [J];
x	Axial distance [m];
ϵ_0	Permittivity of free space, 8.854×10^{-12} C/V-m;
γ	Instability growth rate [1/s];
μ	Adiabatic invariant [J/T];
ϕ	Electrostatic potential [eV];
σ	Reaction cross-section [m^2];
τ	Characteristic time [s];
ω	Wave frequency [1/s];
$\ln \Lambda$	Coulomb logarithm;

Table 5.2: Collisionality of plasma exhaust on various machines computed from 0-D edge model

	Scrape-off temperature T_{si}(eV)	Divertor temperature T_{di}(eV)	Scrape-off collisionality λ_{ii}/L_{si}	Divertor collisionality λ_{ii}/L_{di}
ASDEX poloidal divertor				
D discharge	15	10	0.1	0.1
DP discharge	20	16	0.1	0.2
DITE bundle divertor				
Mark 1A	25	3	1	1
Mark 1B	50	50	1	200
Mark 11	70	70	1	200
PDX poloidal divertor	18	16	0.4	0.5
ALCATOR-DCT				
Bundle divertor	50	11	0.03	0.08
Poloidal divertor	40	40	0.5	4
Pumped limiter	110	110	200	2000
INTOR				
Bundle divertor	110	30	0.03	0.2
Poloidal divertor	130	130	1	10
	82	75	0.2	2
Pumped limiter	1260	1230	$>$ 5000	$>$ 5000
	50	30	0.07	0.2

Table 5.3: Electrostatic potential convergence algorithms
(how to adjust $\phi(x)$ such that $q(x)/e = n_i(x) - n_e(x) \equiv 0$.)

Method	Difficulties
1. Adjust $\phi(x)$ locally, i.e. on each step, for local quasineutrality.	
•With approximate $q(\phi)$ model based on Boltzmann electrons and conservation of ion flux	•Model was too crude
•By modified secant rule •Plus periodically returning back to boundary and repeating	•Must start solution at the dominant boundary, which is not initially known
2. Adjust $\phi(x)$ globally, separately from the $f(x,v)$ integration.	
•Estimate $\Delta\phi(x)$ based on the Boltzmann electrons only	•Must include ions or will obtain pathological solutions
•Estimate $\frac{\partial q}{\partial \phi}(x)$ by observing effect of small changes in $\phi(x)$ - point or step changes; invert matrix and solve for $\Delta\phi(x)$	•Assumes initial guess is close enough that linear perturbation will give answer; sensitive to noise in derivatives; derivative matrix is full and large
3. Parametrize $\phi(x)$ in terms of $\phi_{wall}, \phi_{peak}, x_{peak}$ and optimize	
•NAG library routine - nonlinear optimizer with constraints	•Too much noise in derivatives; routine sensitive to small numerical fluctuations in local density
•Random search in parameter space with volume shrinkage •Optimize by hand	•Parametric model too crude - only broad minima found; more parameters would require too much computer time

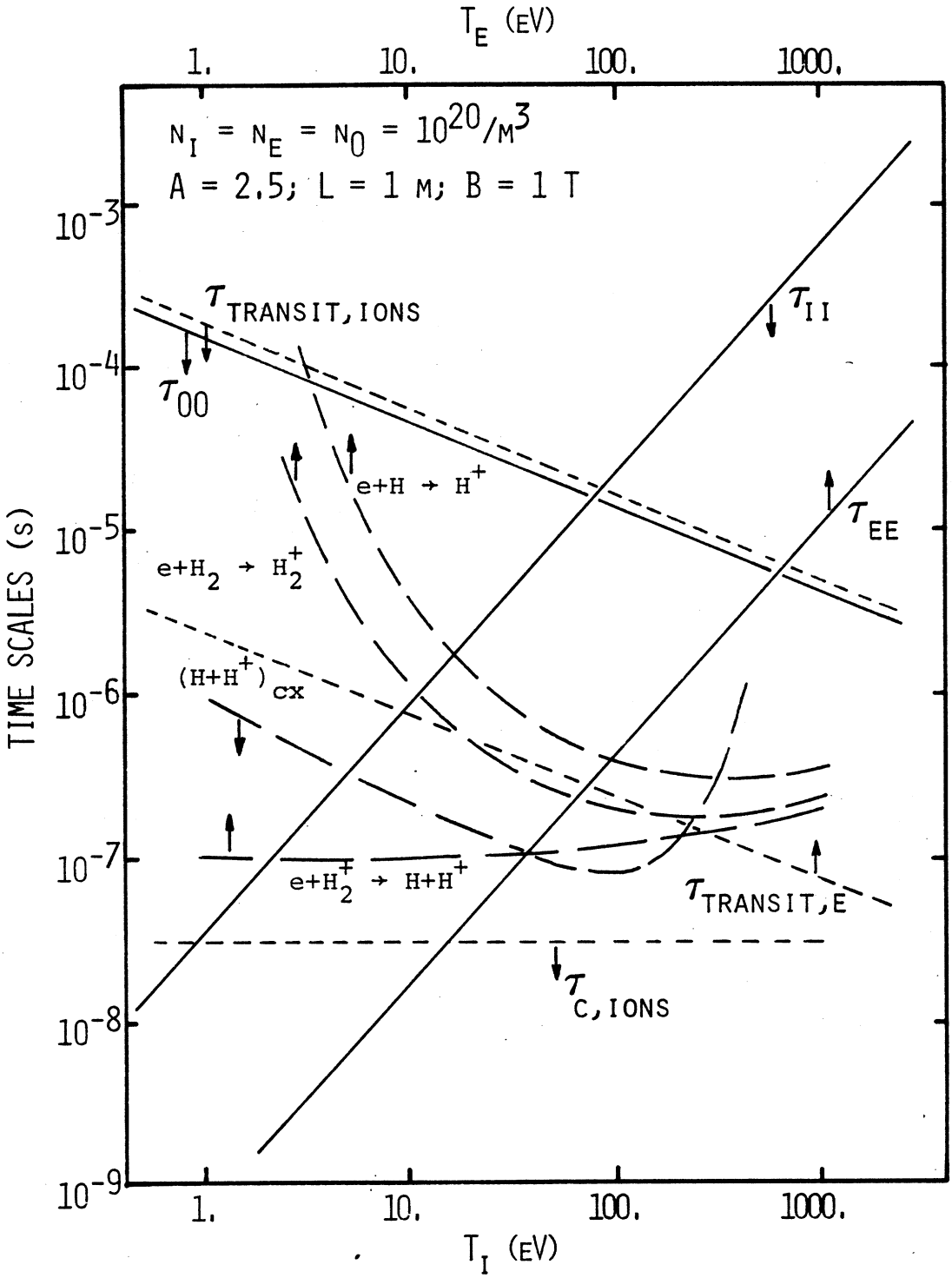

Figure 5.1: Time scales for various processes.

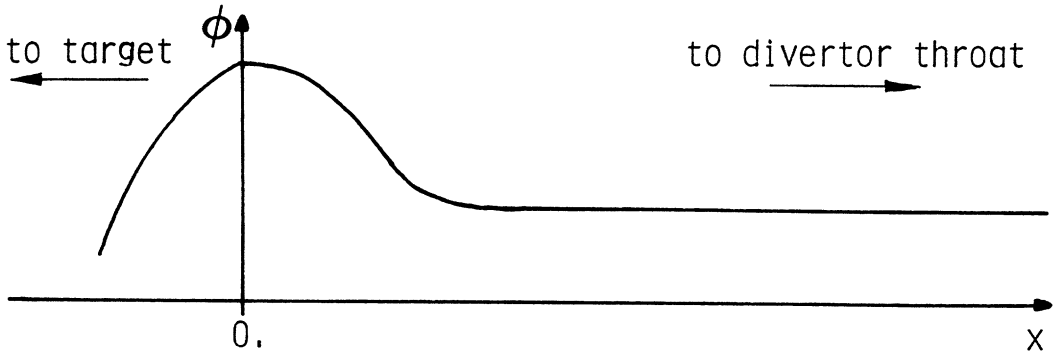

(a) Electrostatic potential profile along magnetic field lines.

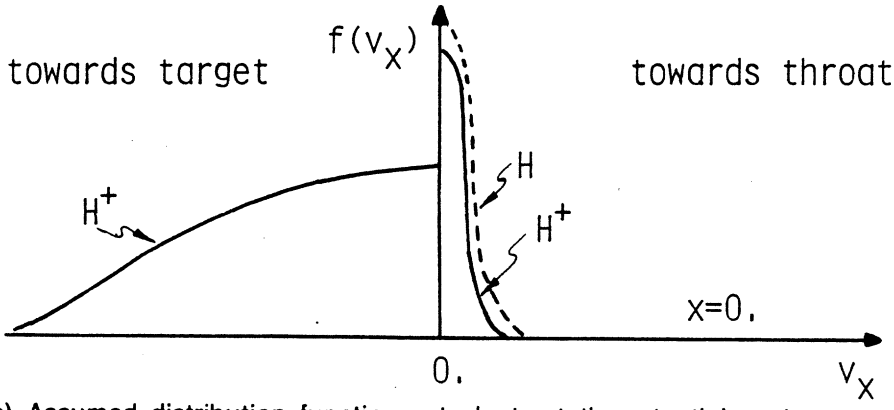

(b) Assumed distribution functions at electrostatic potential peak.

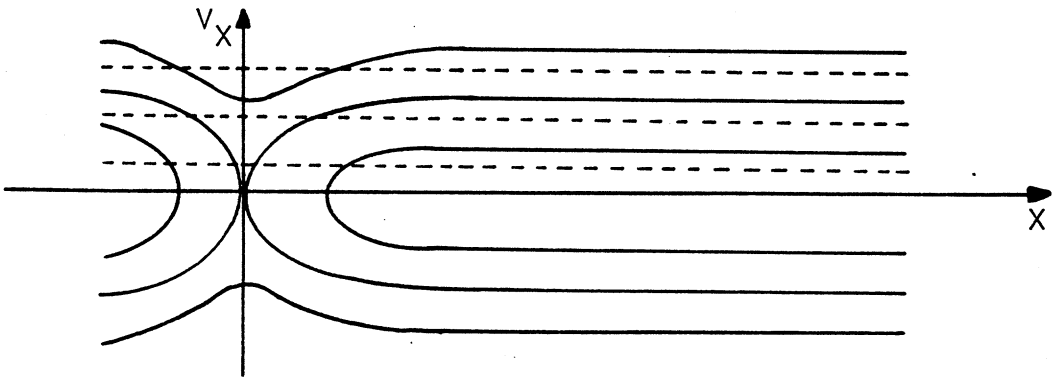

(c) Phase-space trajectories for ions (——) and neutrals (---).

Figure 5.2: Geometry and characteristics of numerical solution.

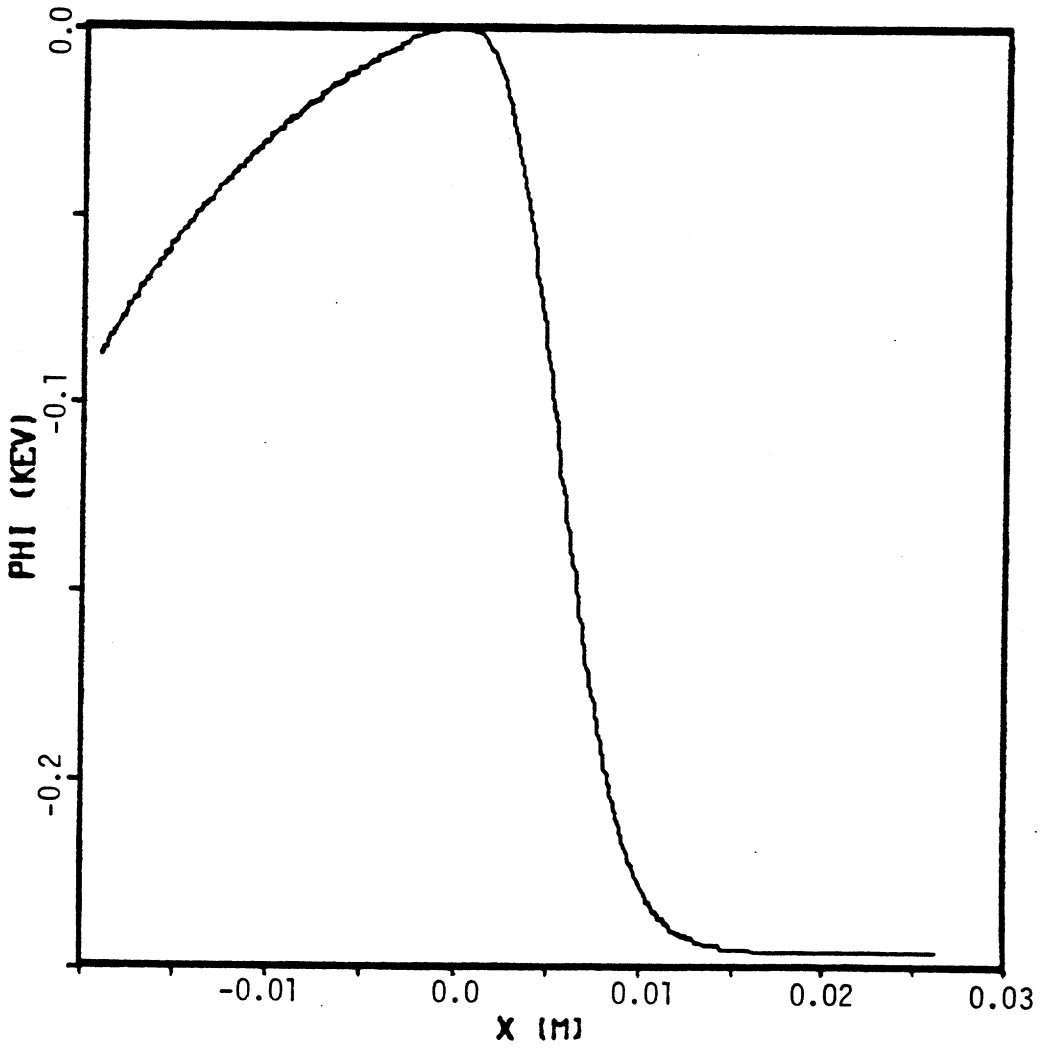

Figure 5.3: Electrostatic potential profile along the divertor for $T_e = T_i = 2$ keV, $T_w = 0.05$ eV, $R = 1.26, P = 18.$ and n_H(peak) = $8.0 \times 10^{20}/\text{m}^3$. The throat is at $x = 1$ m, the target at some small negative x.

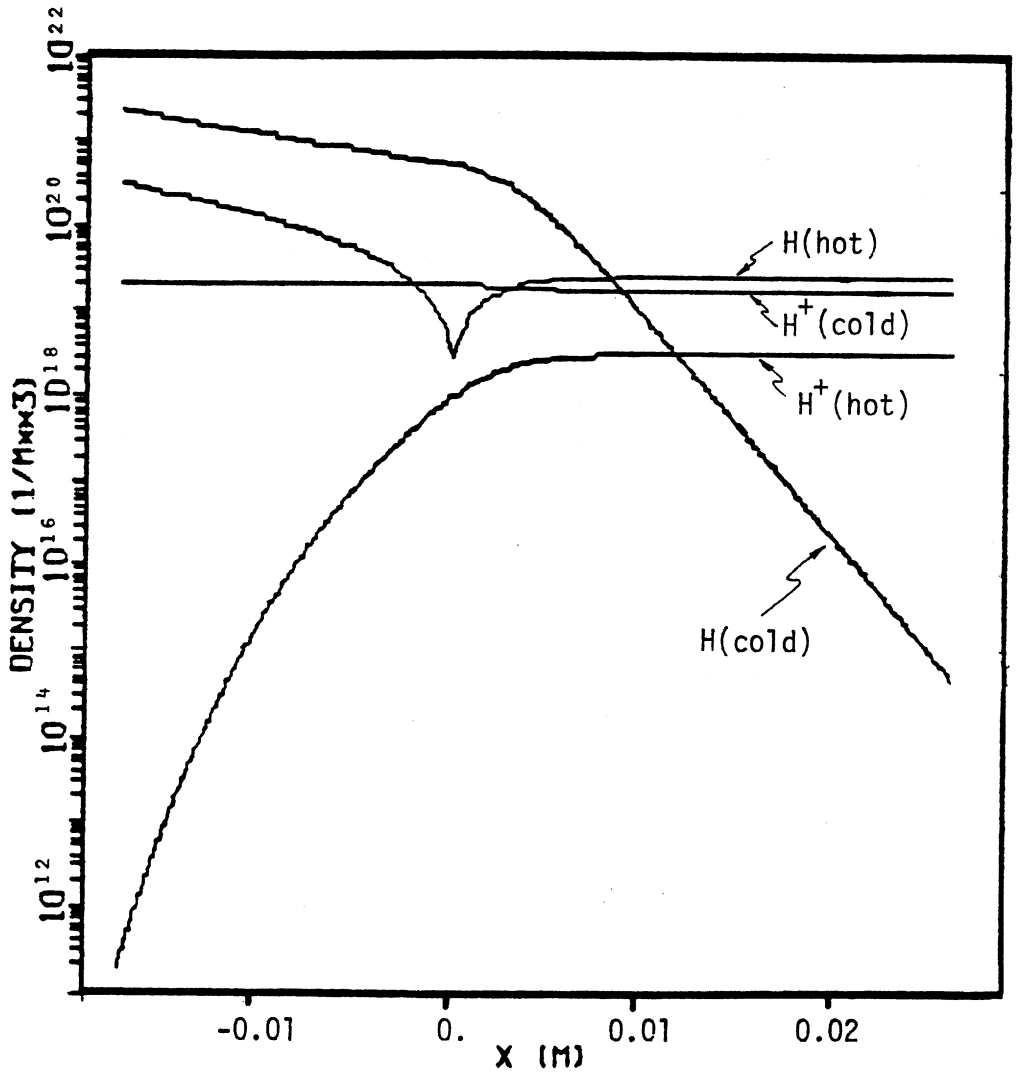

Figure 5.4: Density profiles along divertor for the same conditions as Figure 5.3.

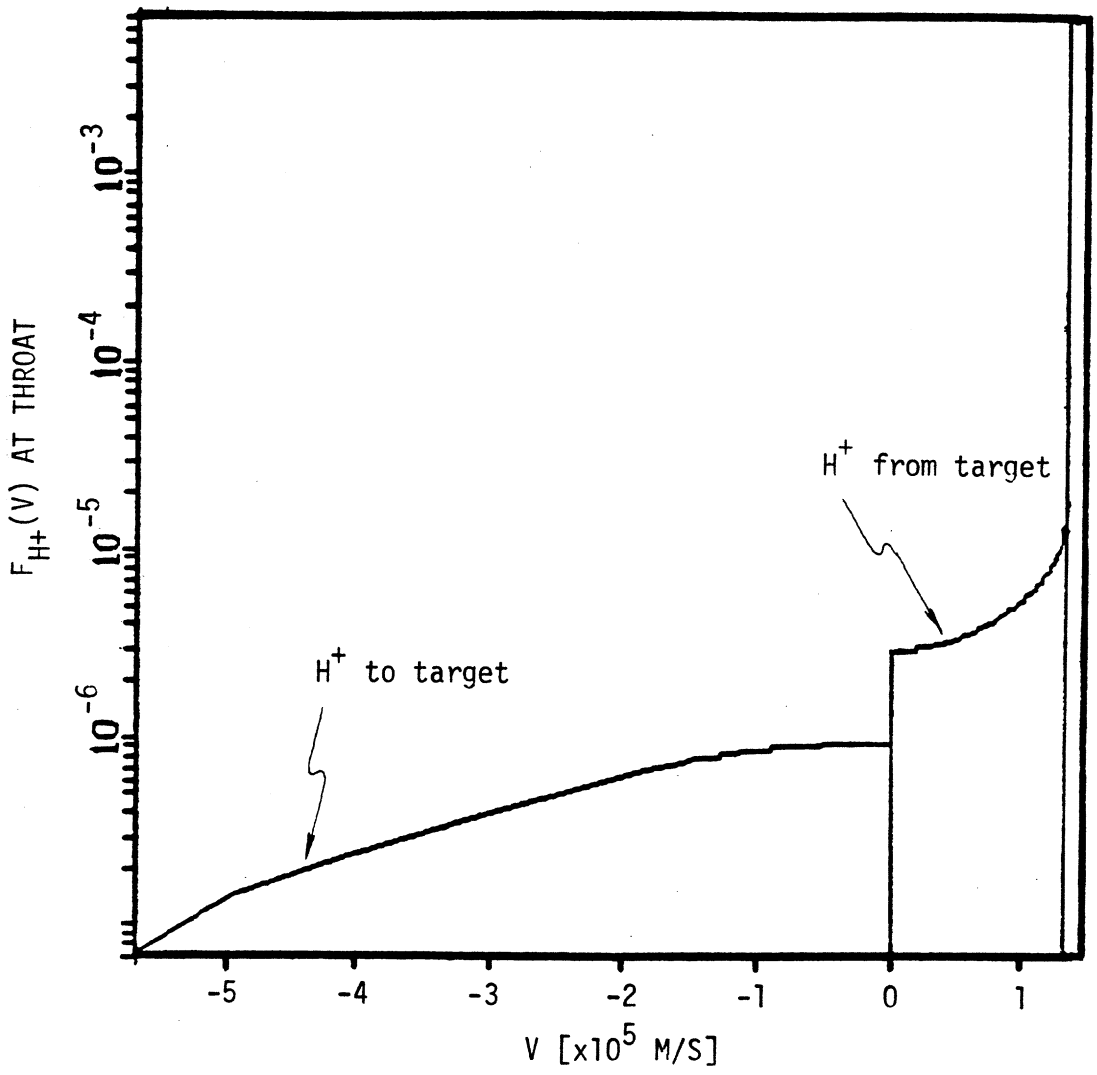

Figure 5.5: Normalized distribution function for H^+, $\hat{f}_i(v)$ at the divertor throat for the same conditions as Figure 5.3.

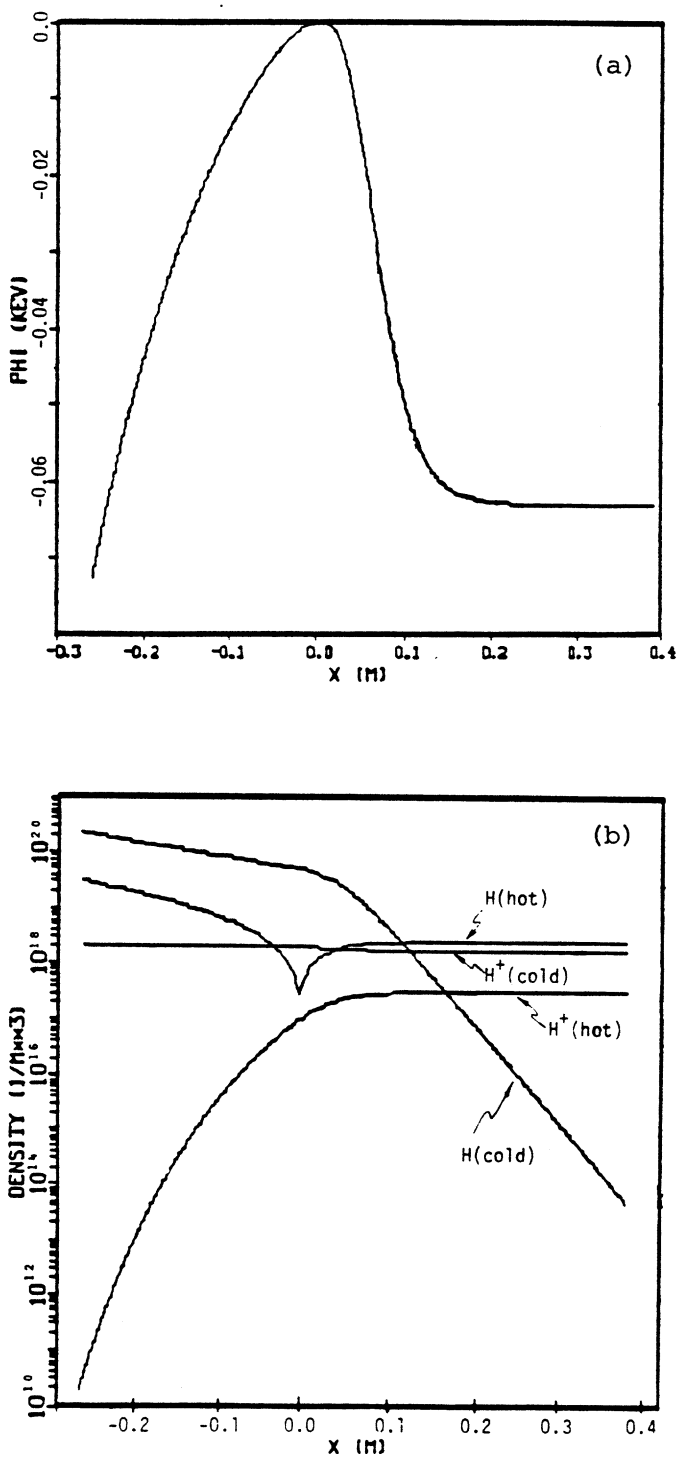

Figure 5.6: Electrostatic potential and density profiles for $T_i = T_e = 2$ keV, $T_w = 0.05$ eV, $R = 1.13, P = 20$ and $n_H(peak) = 5.0 \times 10^{19}/\mathrm{m}^3$.

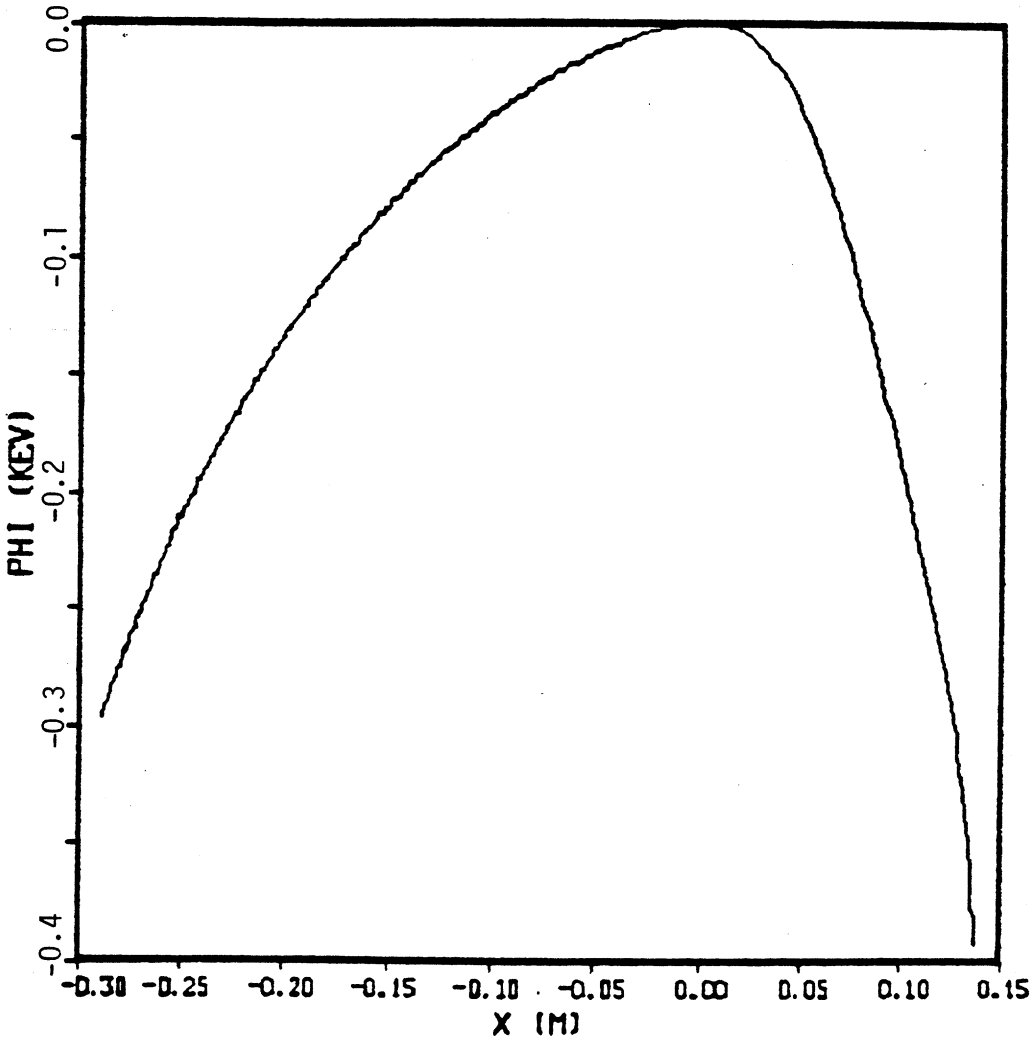

Figure 5.7: Illustrative unphysical potential profile obtained with small P. Here, $T_i = T_e = 2$ keV, $T_w = 0.05$ eV, $R = 1.0, P = 10.$ and $n_{ij}(peak) = 4.0 \times 10^{19}/\mathrm{m}^3$.

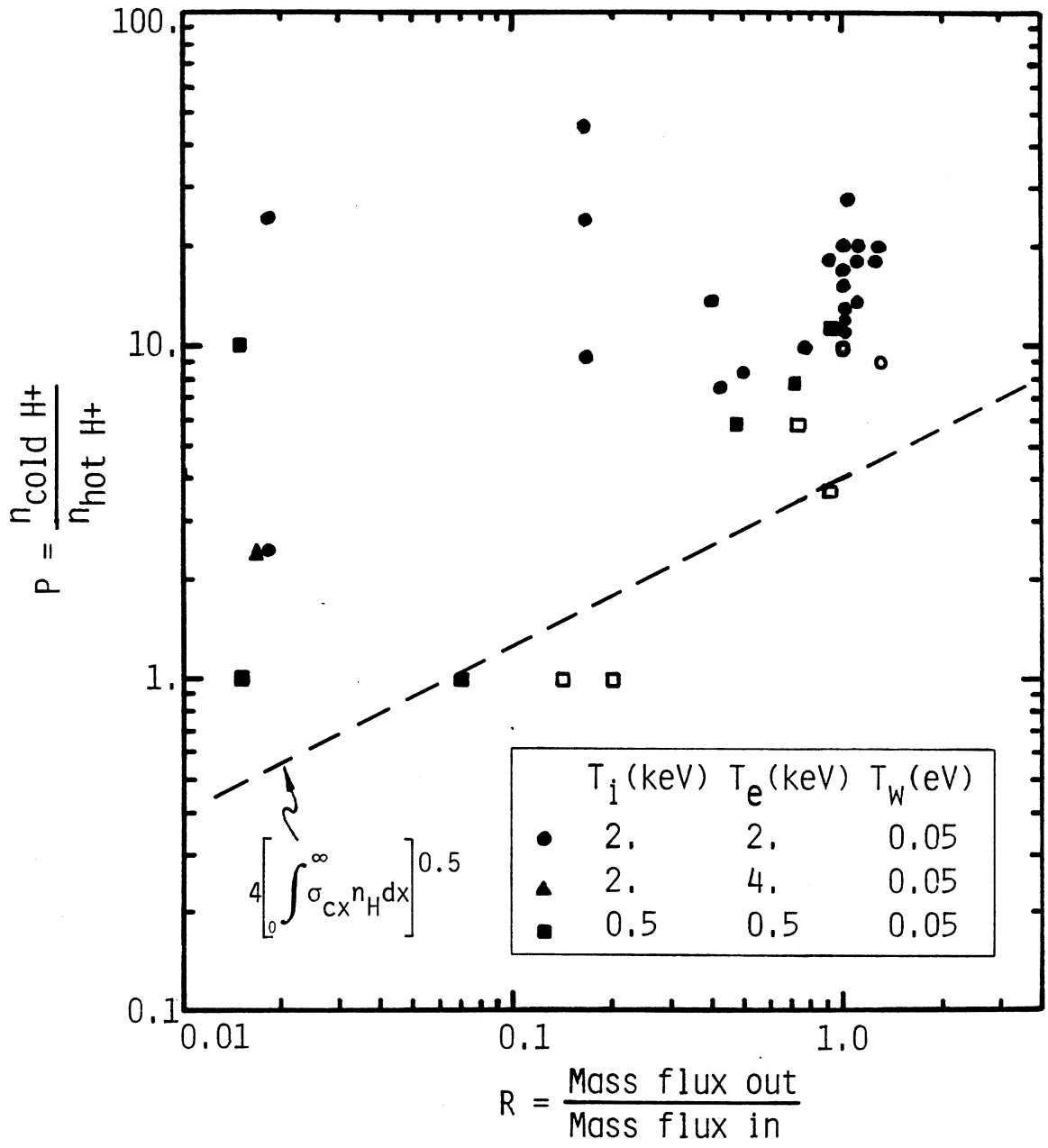

Figure 5.8: Location of solutions on (R, P) coordinates for atomic deuterium and $\sigma_{cx} = 5.0 \times 10^{-19}$ m^2, where R is the recycling ratio from the target and P is the ratio of cold outgoing ions to hot incoming ions at the potential peak. Open symbols indicate no physical solution possible with potential peak.

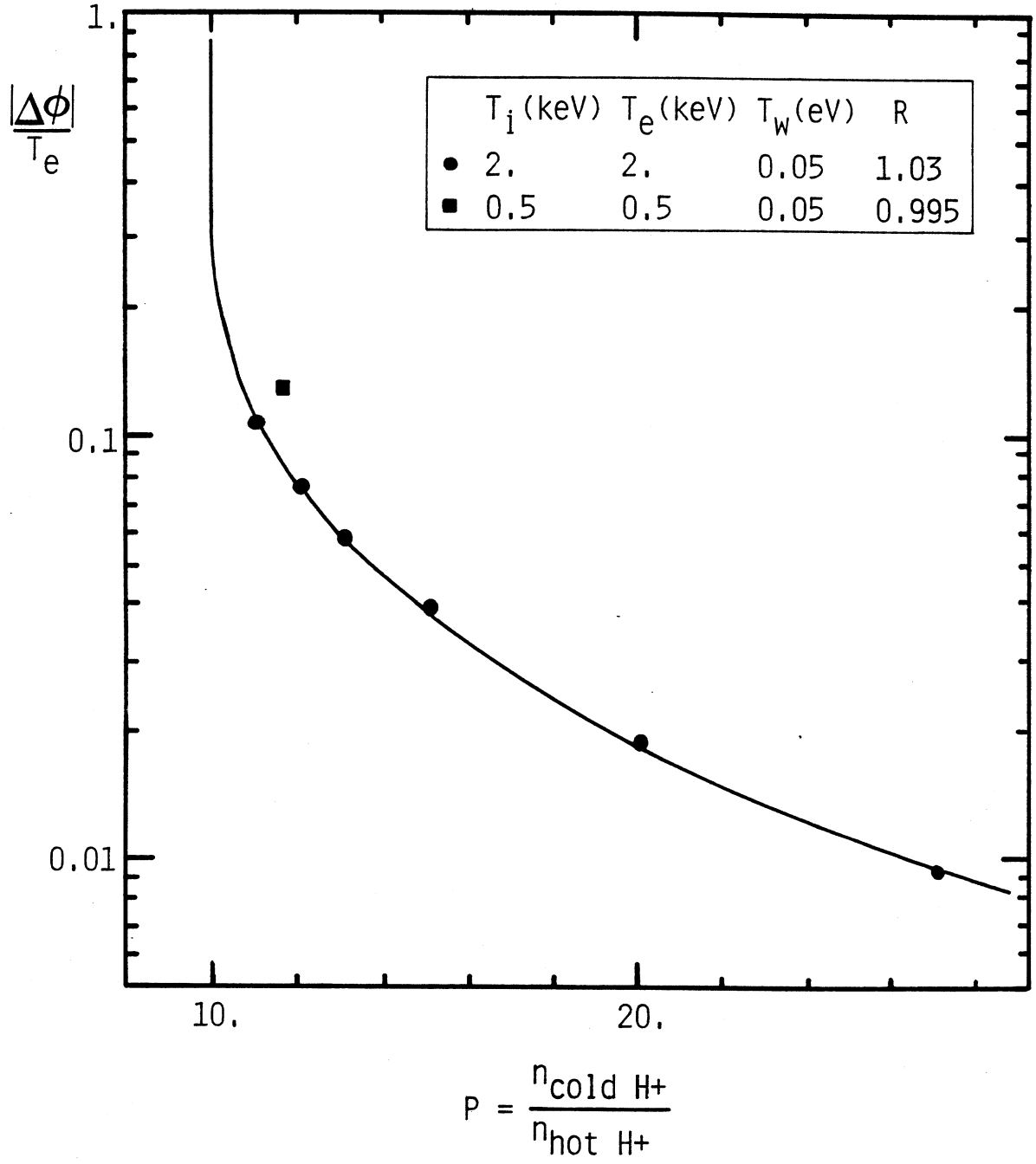

Figure 5.9: Maximum potential drop from peak to divertor throat as a function of P at fixed R for atomic deuterium and $\sigma_{cx} = 5.0 \times 10^{-19}$ m^2.

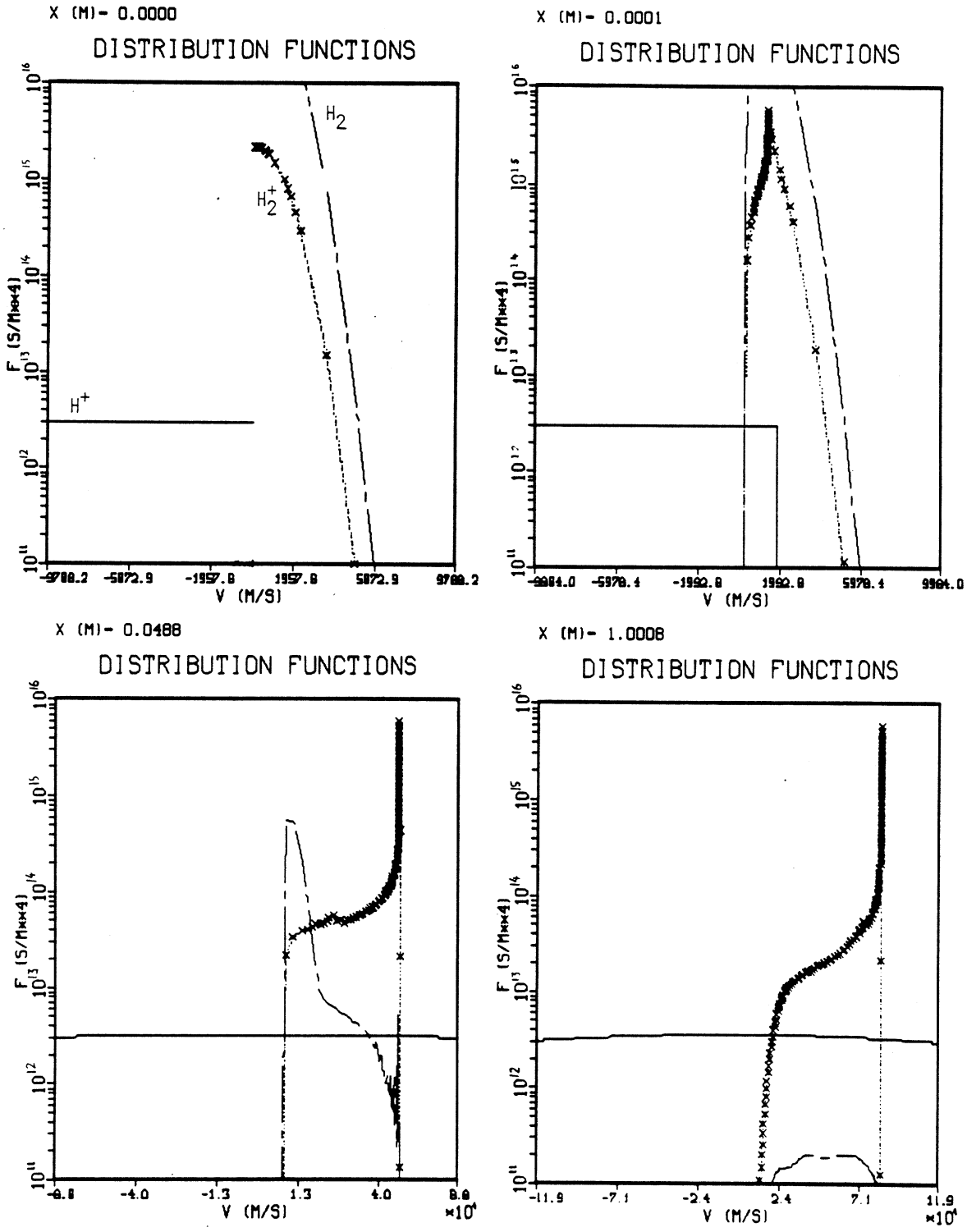

Figure 5.10: Evolution of distribution functions between peak ($x = 0$ m) and throat ($x = 1$ m) for molecular deuterium recycling from the target and with dissociation artificially suppressed. For this case, $T_i = T_e = 1$ keV, $T_w = 0.05$ eV, $P = 3.76, R = 1.0, n_{D_2}(peak) = 1.6 \times 10^{20}/\text{m}^3$ and the potential drop was 140 eV.

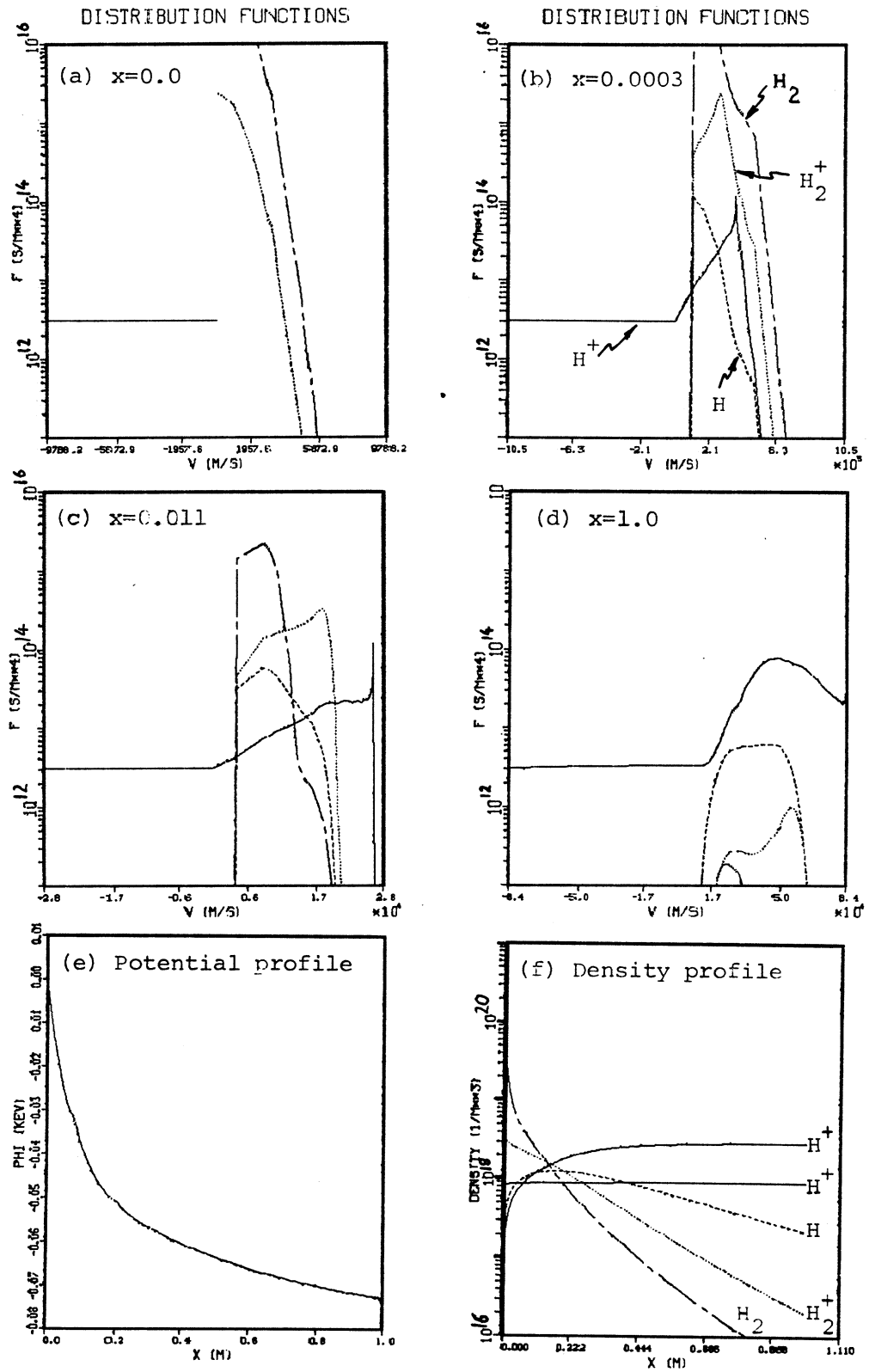

Figure 5.11: Distribution functions (a) - (d), potential (e) and density (f) profiles along divertor for full molecular reactions and $T_i = T_e = 1$ keV, $T_w = 0.05$ eV, $R = 1.0, P = 3.84$ and $n_{D_2}(peak) = 1.63 \times 10^{20}/\mathrm{m}^3$.

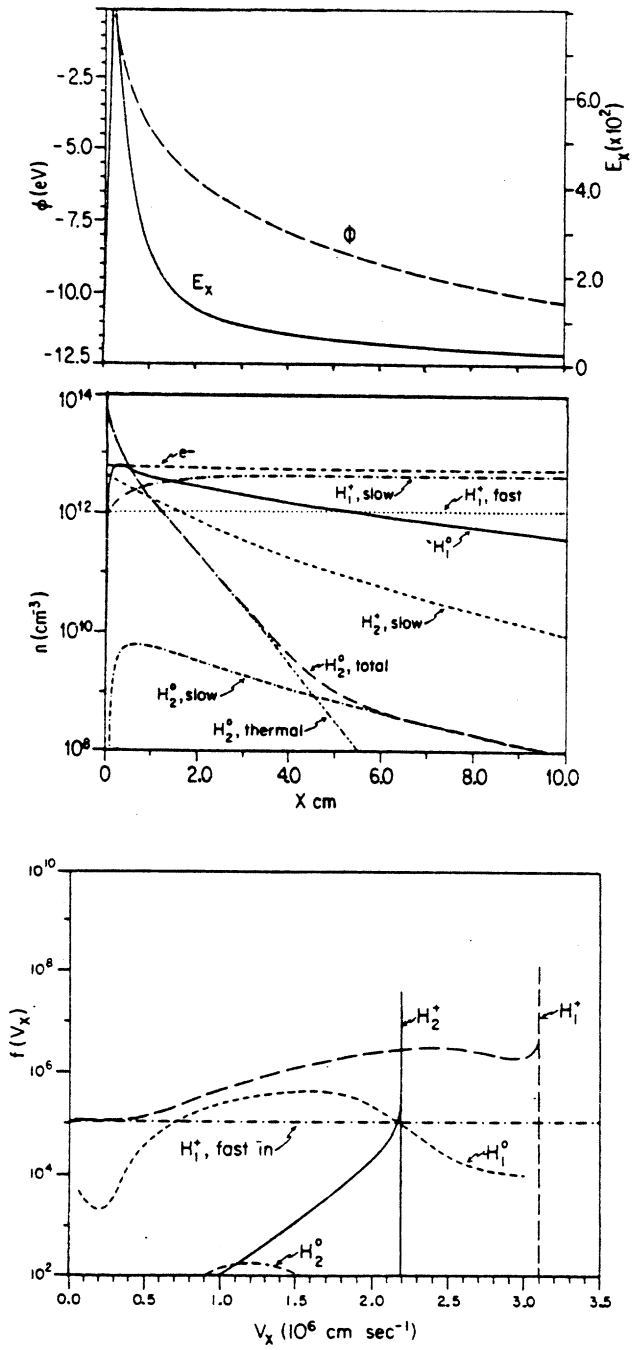

Figure 5.12: Density and potential profiles and throat distributions for $R = 1, T_i = T_e =$ 100 eV, including molecular hydrogen [5.10,5.15].

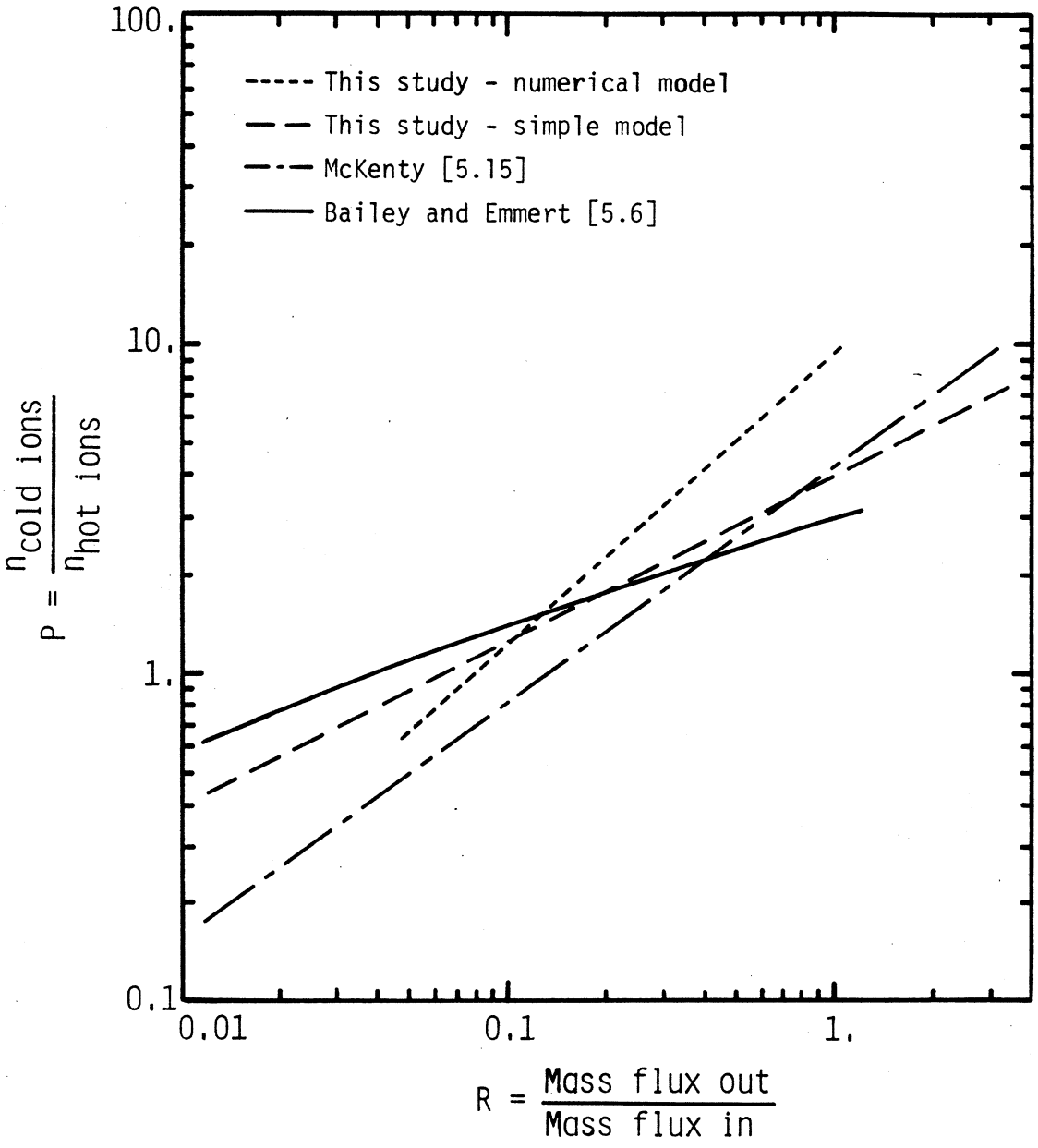

Figure 5.13: Comparison of solution boundary as calculated by various models.

6.0 3-D Monte Carlo Modelling of Neutral Gas Transport

Many analyses simplify the plasma transport problem to 1-D, possibly with approximate corrections for perpendicular diffusion. Neutral particles, however, travel in a fully 3-D manner. In particular, bundle divertors, with varying cross-sectional area and bent flow channels, take advantage of a convoluted geometry to help confine the neutrals and impurities near the target plate and vacuum pumps. However, while it may be necessary to include the full 3-D geometry in transport calculations, the numerical algorithms required can become correspondingly complicated.

Of the techniques available, the Monte Carlo method of statistical trials is particularly attractive when fast, large computers are available. This is especially true here since the movement of a particle through a region is a random process - the more common fluid approximation simply relies on there being enough particles involved that statistical variations can be neglected and the aggregate flow described adequately in terms of average properties. The Monte Carlo method itself is described in Refs. [6.1,6.2].

In this chapter, a basic steady-state 3-D Monte Carlo model for neutral particle transport is described. Similar but 2-D Monte Carlo codes have been developed by Seki et al [6.6] and Heifetz et al [6.7], and have been applied primarily to poloidal divertors and toroidal pumped limiters.

The basic model is applied as follows:

(1) Specify the geometry;

(2) Specify the physics occurring at each volume element;

(3) Launch a particle from an emitting surface and follow its trajectory through the volume, including reactions, until it (or its reaction product) is absorbed;

(4) Repeat step (3) for enough particles to accumulate good statistics.

6.1 Geometry

An arbitrary 3-D volume is described by dividing a rectangular volume into many smaller volume elements, obtained by slicing it along planes perpendicular to the axes (Figure 6.1). Since each volume element is itself rectangular, sloping or curved surfaces must

be approximated as a series of small blocks. Using such a simple geometry considerably eases computational requirements.

Each volume element is defined as either solid or vacuum. Furthermore, solid elements may have different surface characteristics - they may be absorbing, emitting, diffusely reflecting and/or specularly reflecting, and vacuum elements may contain neutrals and/or plasma. The present model emphasizes 3-D neutral transport, so the plasma is not self-consistently calculated but must be prescribed from separate calculations. The background neutrals, however, are accumulated in the course of the calculations, so can be self-consistent if the scattering reactions are included.

6.2 Surface Reactions

The interaction of particles with a solid surface was summarized in Section 3.2. Briefly, there are three classes of reactions considered here: absorption, diffuse reflection and specular reflection. The extent to which any of these happen is a function of surface conditions, and the type and energy of the incoming particles.

6.2.1 Absorption

If the incoming particle can penetrate deeply enough into the surface, it may become physically stuck. Alternately, it might chemically react with the material - not necessarily by covalent bands, but perhaps by a Van der Waals surface attraction. Both these mechanisms saturate eventually, and should not be an appreciable particle sink under long-pulse conditions. More usefully, an absorbing volume element effectively represents the inlet to an active device such as a turbomolecular pump. Then the absorption probability is simply the probability that the particle will pass through the inlet ducting and be pumped. This absorbed fraction f_a is related to the pumping speed S by

$$f_a = \frac{S}{\bar{v}A/4} \tag{6.1}$$

where $\bar{v}$ is the average particle speed, A is the inlet aperture size, and free molecular flow is assumed.

6.2.2 Diffuse Reflection

For solid surfaces, particles that are initially absorbed may subsequently diffuse back to the surface and evaporate off, or be knocked off by other incoming particles. Incoming

particles themselves may not stay on the surface long enough to react with it, but simply bounce off. The extent of these latter processes is generally described in terms of momentum and thermal accommodation coefficient.

In the limit of full accommodation, the particle is diffusely reflected. It is emitted with a Maxwellian speed distribution characteristic of the surface temperature,

$$f_M(v) = 4\pi\left(\frac{m}{2\pi T}\right)^{3/2} v^2 e^{-v^2/v_{th}^2}; \quad \int_0^\infty f_M(v)dv = 1 \tag{6.2}$$

where $v_{th} = \sqrt{2\,T/m}$, and T is the surface temperature. The direction of the emitted particle usually follows the Lambertian cosine law, where the probability of a particle entering an elementary solid angle Ω is proportional to the cosine of the angle with respect to the surface normal at that point θ [6.3],

$$p(\Omega) = \frac{\cos\theta}{2\pi}; \quad \int_0^{4\pi} p(\Omega)d\Omega = 1\,. \tag{6.3}$$

In the Monte Carlo method, a way of generating emitted particles with the correct characteristics is required – in particular, the correct speed and angular distribution for diffuse reflection. Most computers have intrinsic functions that supply a random number ξ uniformly distributed over (0,1). This must then be transformed to the desired random number x with distribution $p(x)$ over x_{min} to x_{max}. In general, the transformation is

$$\xi = \int_{x_{min}}^{x} p(s)ds; \quad \text{where} \int_{x_{min}}^{x_{max}} p(s)ds = 1\,. \tag{6.4}$$

Consider the particle speed first. For the distribution given by Eqn. (6.2), the transformation cannot be performed analytically. Note that for the slightly different distribution

$$f(v) = \frac{m}{T} v e^{-v^2/v_{th}^2}; \int_0^\infty f(v)dv = 1 \tag{6.5}$$

the transformation yields

$$v = v_{th}\sqrt{-\ln(\xi)} \tag{6.6}$$

This resulting distribution is shown in Figure 6.2a, compared with the desired speed distribution (Eqn. 6.2), for molecular hydrogen and a surface temperature of 300 K. It can be seen that Eqn.(6.6) is not a bad approximation – it has almost the same probable speed and high energy tail, it is just too small at low energies. Another approximation

which uses two uniform random numbers ξ_1 and ξ_2 is

$$v = v_{th}\sqrt{-\ln(\xi_1\xi_2)} \tag{6.7}$$

This is shown in Figure 6.2b, and is also not a bad approximation. Both these transformations are fast, which is a significant advantage in Monte Carlo codes (it is sometimes said that it is better to be fast than accurate). However, an accurate distribution can be generated as follows. Consider $v = \sqrt{v_x^2 + v_y^2 + v_z^2}$, where the velocity components are 1-D Maxwellians with

$$f(v) = \left(\frac{m}{2\pi T}\right)^{0.5} e^{-v^2/v_{th}^2}; \quad \int_{-\infty}^{\infty} f(v)dv = 1 \tag{6.8}$$

Again, this expression cannot be analytically transformed according to Eqn.(6.4). However, Eqn.(6.8) is simply a Gaussian distribution with mean $\bar{v} = 0$ and variance $\sigma_v^2 = T/m$. There are several ways to generate normal Gaussian distributions from uniform random numbers, ξ_i. The simplest follows from the Central Limit Theorem of statistics which states that if the ξ_i are independent random numbers with mean $\bar{\xi}$ and variance σ_ξ^2, then $\eta = \sum_{i=1}^{n} \xi_i$ is normally distributed with mean $n\bar{\xi}$ and variance $n\sigma_\xi^2$. In practice, n approximately 4 to 8 is adequate, where the resulting distribution is primarily valid for $|v - v_{th}| \leq nv_{th}/2$. This leads to a simple, accurate prescription for generating a Maxwellian speed v from $f_M(v)$:

$$v = v_{th}\sqrt{\frac{3}{2}\sum_{j=1}^{3}\left(\sum_{i=1}^{4}\xi_i - 2\right)^2} \tag{6.9}$$

where we note that for ξ_i uniform over (0,1), $\bar{\xi} = 1/2$ and $\sigma_\xi^2 = 1/12$, and that the transformation between normal distributions is $(v - \bar{v})/\sigma_v = (\eta - \bar{\eta})/\sigma_\eta$. The result of this transformation, which takes about 50 μs on a Cray-1s, is shown in Figure 6.2c.

The second part of the Monte Carlo treatment of diffusely reflected particles is the angular distribution, which satisfies the cosine law, Eqn.(6.3). Here two angles, θ (from the surface normal) and ϕ (azimuthally around the surface normal), must be chosen such that a cosine law distribution is generated. Define $p(\Omega) = p(\theta)p(\phi)$ where $\int_0^{\pi/2} p(\theta)\sin\theta d\theta = 1$ and $\int_0^{2\pi} p(\phi)d\phi = 1$. Thus $\int_0^{4\pi} p(\Omega)d\Omega = 1$, where $d\Omega = \sin\theta d\theta d\phi$. Using Eqn.(6.4), pick

two uniform random numbers ξ_1, ξ_2, and set

$$\xi_1 = \int_0^{\phi} p(\phi)d\phi = \frac{\phi}{2\pi} \quad \text{so} \quad \phi = 2\pi\xi_1 \tag{6.10a}$$

and

$$\xi_2 = \int_0^{\theta} p(\theta)\sin\theta d\theta = \frac{1-\cos 2\theta}{2} \quad \text{so} \quad \theta = \sin^{-1}\sqrt{\xi_2} \tag{6.10b}$$

The θ dependence is illustrated in polar plot form in Figure 6.2d.

6.2.3 Specular Reflection

In the opposite limit of no accommodation, the particle is reflected with only the direction of one velocity component reversed. That is, for a particle with velocity $\underline{v} = (v_x, v_y, v_z)$ hitting a surface in the y-z plane, the reflected particle has velocity $\underline{v} = (-v_x, v_y, v_z)$. According to the data of Section 3.2.2, it holds for some fraction of incident particles. This specular reflection can also be applied along symmetry planes to reduce the size of the problem.

For real surfaces, there is always some accommodation. If the surface does not permanently absorb the incident particle, the probability for prompt reflection is $R_N(E_i, \theta)$, given approximately by Eqn.(3.12c), where E_i is the incident energy and θ is the angle from the surface normal. Otherwise the particle is trapped in the surface until, in steady-state, it thermally desorbs as an uncharged particle at the wall temperature and a cosine law angular distribution as described in Section 6.2.2.

The prompt reflected particles emerge with an energy distribution which may be taken from Eqn.(3.13). According to Eqn.(6.4), this energy distribution can be obtained from uniform random numbers ξ by (see Figure 6.3)

$$E = E_p\left[\left(1+\frac{E_i^2}{E_p^2}\right)^{\xi} - 1\right]^{0.5} \tag{6.11}$$

The angular distribution of the reflected particles varies from cosine-law at normal incidence, to pure specular reflection at $\theta = 90°$. Here, the probability of cosine-law emergence is roughly estimated as

$$p_{cosine-law} \approx (1 - \frac{\theta}{90°}) \tag{6.12}$$

6.3 Particle Reactions

Reactions are treated on a volume element basis. As the particle traverses a given volume element, the various reaction probabilities per particle per traversal are compùted based on the local neutral gas and plasma properties. If the test particle reacts (according to a random number), then the location of the reaction is determined and the "new" or reacted test particle is started from this position. If there is no reaction, the test particle is moved to the volume element boundary and the process repeated for the crossing of the next volume element.

6.3.1 No Reaction

It is possible that no reaction at all occurs. This is determined first based on the test particle k trajectory length d_{kj} in the volume element j, and on the local total mean free path $\lambda_j = [1/\lambda_{j,ei} + 1/\lambda_{j,cx} + ...]^{-1}$ where ei denotes electron impact ionization, cx denotes charge exchange, and so on for all the possible reactions. This probability of no reaction is

$$p_{j,nr} = \exp\left(\frac{-d_{kj}}{\lambda_j}\right) \tag{6.13}$$

and the corresponding probability of some reaction is $(1 - p_{j,nr})$. In a given volume, a uniform random number ξ is determined, and no reaction occurs if $\xi < p_{j,nr}$.

If a reaction occurs, the distance d_r can be calculated from Eqn.(6.4),

$$\xi = \int_0^{d_r} e^{-x/\lambda_j} \frac{dx}{\lambda_j}$$

which yields

$$d_r = -\lambda_j \ln \xi \tag{6.14}$$

where d_r is the distance, and ξ is a uniform random number on (0,1) so that $1 - \xi$ and ξ are equivalent. This yields an exponentially distributed range of distances with mean free path λ_j. Note that since it has already been determined that a reaction occurs, Eqn.(6.14) must be reapplied until $d_r \leq d_{kj}$.

6.3.2 Ionization

The probability of electron impact ionization, $H + e \rightarrow H^+ + 2e$, in volume element j is

$$p_{j,ei} = (1 - p_{j,nr}) \frac{\lambda_j}{\lambda_{j,ei}} \tag{6.15}$$

where $(\lambda_j/\lambda_{j,ei})$ is the probability of ionization given that some reaction occurs in the element. The ionization mean free path is $\lambda_{j,ei} = v_{kj}/n_{j,e}\langle\sigma v\rangle_{j,ei}$ where v_{kj} is the local test particle velocity; $n_{j,e}$ the local electron density; and $\langle\sigma v\rangle_{j,ei}$ is the reaction rate computed from Eqn.(3.5f).

At present, the code does not track ionized particles. Thus if an ionization occurs, the location is noted and the tracking algorithm is stopped for that particular test particle.

6.3.3 Charge Exchange

The probability of charge exchange, $H + H^+ \rightarrow H^+ + H$, in volume element j is

$$p_{j,cx} = (1 - p_{j,nr})\frac{\lambda_j}{\lambda_{j,cx}} \tag{6.16}$$

where $(\lambda_j/\lambda_{j,cx})$ is the probability of charge exchange given that a reaction occurs, and $\lambda_{j,cx} = v_{kj}/n_{j,i}\langle\sigma v\rangle_{j,cx}$, where the reaction rate is estimated by $\langle\sigma v\rangle_{j,cx} \approx \sigma_{j,cx}v_{j,i}$, $v_{j,i}$ is the local ion thermal velocity, $n_{j,i}$ is the local ion density, and $\sigma_{j,cx}$ is obtained from Eqn.(3.1h). The charge–exchange neutral is subsequently tracked.

The characteristics of this charge–exchange neutral are estimated based on the average properties of the local plasma – temperature and bulk flow velocity. The plasma is flowing along magnetic field lines with temperature T_j, local Mach number M_j, and magnetic field vector $\underline{B}_j$, all of which must be externally specified from a separate solution to the plasma flow (such as described in Chapters 4 or 5). The new neutral is described by velocity components parallel and perpendicular to $\underline{B}_j$. The parallel velocity is obtained from a shifted 1–D Maxwellian at T_j using the same procedures as those leading to Eqn.(6.9). The perpendicular component is presently estimated assuming the perpendicular energy is 1–D Maxwellian at T_j. A random gyroangle then specifies the final direction.

6.3.4 Molecular Dissociation

Much of the hydrogen recycling from the walls will be in molecular form. A variety of dissociation, charge exchange and ionization reactions are possible as illustrated in Figures 3.1–3.4. However, the most important reactions over 1 eV – 1 keV are likely to be reactions (1)–(5) discussed in Section 3.1.1, basically electron impact ionization and electron impact dissociation:

1) $e + H_2 \rightarrow H_2^+ + 2e$

2) $e + H_2 \rightarrow 2H + e$

3) $e + H_2 \rightarrow H + H^+ + 2e$

4) $e + H_2^+ \rightarrow H + H^+ + e$

5) $e + H_2^+ \rightarrow 2H$

The most likely reaction over much of the energy range is $e + H_2 \rightarrow H_2^+ + 2e$. Since H_2^+ has a large dissociation cross-section, dissociation is assumed to promptly follow this ionization. The probability of molecular dissociation in volume element j is

$$p_{j,md} = (1 - p_{j,nr})\frac{\lambda_j}{\lambda_{j,md}} \tag{6.17}$$

where $(\lambda_j/\lambda_{j,md})$ is the probability of molecular dissociation given that a reaction occurs, and $\lambda_{j,md} = v_{kj}/n_{j,e}\langle\sigma v\rangle_{j,md}$ where $\langle\sigma v\rangle_{j,md}$ is the dissociation rate and v_{kj} is the molecular velocity.

The dissociation rate is $\langle\sigma v\rangle_{j,md} = \langle\sigma v\rangle_{j,1} + \langle\sigma v\rangle_{j,2} + \langle\sigma v\rangle_{j,3}$ where the number subscript refers to the reaction number above. The fraction that appears as charged atomic hydrogen is

$$f_{charged} = \frac{1}{2\langle\sigma v\rangle_{j,md}}\left[\langle\sigma v\rangle_{j,3} + \langle\sigma v\rangle_{j,1}\frac{\langle\sigma v\rangle_{j,4}}{\langle\sigma v\rangle_{j,4} + \langle\sigma v\rangle_{j,5}}\right] \tag{6.18}$$

with the remainder (1 - $f_{charged}$) forming neutral atomic hydrogen.

6.3.5 Elastic Scattering

If the neutral particle density is large enough, neutral/neutral scattering reactions may be important. This is not expected to matter in the cases of immediate interest, so these reactions are not presently modelled. Nonetheless, the basic prescription is given here since they would be a useful addition.

The basic procedure is to compute the elastic scattering reaction probability $p_{j,es}$ based on the mean free path $\lambda_{j,es}$ as for the other reactions. Some data on scattering cross-sections are given in Section 3.1.3. The only "trick" is to supply the background neutral density and temperature as needed for $\lambda_{j,es} = v_{kj}/n_{j,n}\langle\sigma v\rangle_{j,es}$. Since the present model accumulates an increasingly more accurate estimate for $n_{j,n}$ and $T_{j,n}$ with each particle tracked, all the necessary information is already available. The final step is to determine the new direction and velocity of the scattered neutral, as well as the counter-reaction effect on the local background neutrals. These could be estimated, for example, from hard sphere collision kinematics.

6.4 Parameter Estimation and Variance Reduction

The trajectories of several thousand particles through the geometry is only an indirectly interesting result. The goal is to provide reliable estimates of useful quantities such as the returning flux of neutrals from the divertor, the density profile of particles in the volume, or the charge exchange energy loss to the walls. These must all be inferred for particle fluxes of order $10^{20} - 10^{22}/\mathrm{m}^2$-s based on the calculated trajectories of $10^3 - 10^6$ random particles.

As part of the tracking algorithm, the program computes the distance d_{kj} a particle k travels in a given volume element j as it passes through it. Since the particle speed v_{kj} is also known, the time spent in the particular volume is $t_{kj} = d_{kj}/v_{kj}$. Thus the average distance (or mean free path) a particle travels before being absorbed or ionized is

$$\overline{d} = \frac{1}{N_p} \sum_{k=1}^{N_p} \sum_{j=1}^{N_v} d_{kj} w_k \tag{6.19}$$

where N_p is the number of particles launched; N_v is the number of volume elements; and w_k is the particle weight.

A more useful parameter is the neutral density in a given volume element. This is proportional to the time spent in the volume, and is given by

$$\overline{n_j} = \frac{1}{N_p} \sum_{k=1}^{N_p} n_{kj} = \frac{S}{V_j N_p} \sum_{k=1}^{N_p} t_{kj} w_k \tag{6.20}$$

where S is the actual source rate (particles/s) and V_j is the volume of the element.

This scoring procedure is generally referred to as a path-length estimator. Other approaches such as the pseudo-collision algorithm used by Heifetz et al [6.7] are also possible. The path-length estimator is the simplest conceptually, and thus easy to implement. It may require extensive geometric calculations since the path length in each volume element must be computed. The pseudo-collision approach bypasses step-by-step geometric calculations, in exchange for some pre– and post–processing of the data, a slightly more complicated collision algorithm and a step size based on the minimum mean free path. In this code, because of the straightforward Cartesian geometry, the simpler path-length estimator is used.

In practice, the density is not computed only after all the particles have been tracked as implied by Eqn.(6.20), but rather is maintained as a best-estimate based on all the particles followed up to the current point in the calculations. Thus, the best-estimate after N_p particles, $\overline{n}_j^{N_p}$, is given by Eqn.(6.20), and the new estimate after following an additional particle $k = N_p + 1$ which spends time t_{kj} in volume element j, is

$$\overline{n}_j^{N_p+1} = \overline{n}_j^{N_p} \frac{N_p}{N_p+1} + \frac{S}{V_j(N_p+1)}(t_{kj} w_k) \tag{6.21}$$

Any time a reaction occurs, the type and location of the reaction can be recorded. Thus the number of particles that are absorbed on a pump inlet volume element $N_{pump,j}$ give the fractional pumping efficiency at that location, $N_{pump,j}/N_{pump,total}$. Similarly, the energy difference between the incoming and reflected particle will tell how much energy was transported to the walls.

The Monte Carlo approach does not calculate the exact answer, but rather provides an estimate. It is desirable to know the error or variance in this estimate, and to try to reduce this variance. In general, from N estimates of some quantity x, we obtain $x_k, k = 1, N$. Consistent and unbiased estimates of the mean and variance of x are:

$$\overline{x} = \frac{1}{N}\sum_{k=1}^{N} x_k; \quad \sigma_x^2 = \frac{1}{N-1}\left[\sum_{k=1}^{N} x_k^2 - N\overline{x}^2\right] \tag{6.22}$$

In essence, the kth particle tracked by the Monte Carlo algorithm yields some quantity, say n_{kj}, a density estimate for volume j, and the average over all the particles N_p gives an estimate $\overline{n}_j$. It would also be possible to calculate n_{kj}^2 and thus determine σ_n^2 from Eqn.(6.22). In practical implementations, this requires considerably more memory for the code if the variance is to be calculated for many quantities. It is also not immediately clear how to compute n_{kj}^2 if the test particle makes multiple passes through the volume element with differing weights because of other reactions.

The simplest way to estimate the error or variance is to simply repeat the Monte Carlo calculation (with entirely different random numbers). Then, from the Central Limit Theorem of statistics, the estimates $\overline{n}_j$ from all the calculations will tend towards a normal distribution with the correct mean value. The advantage of this approach to determining error is that it is very simple to implement and is entirely independent of the particular

algorithms used. Its disadvantage is the required computer time. In the Monte Carlo results presented here, three approaches were used to keep the statistical error small without requiring inordinate computer time: tracking a reasonable number of particles ($N_p \approx 10^4 - 10^5$) in each calculation; repeating the calculation to obtain an estimate of the error; and the use of variance reduction procedures.

An important part of an efficient Monte Carlo program is variance reduction, i.e. algorithms that will yield a good estimate of desired quantities with smaller error for the same amount of computation. A number of techniques including splitting, Russian roulette, the exponential transform and antithetic variates, are discussed in Refs.[6.1,6.2]. Basically, more weight is placed on the regions of interest. For example, one can stop following a particle when it enters an uninteresting region, or double the particle when it enters an important region. If the particle weights are adjusted appropriately, the final estimates for the parameters of interest are still correct but the uncertainty is smaller.

In the present program, splitting and Russian roulette are used. In particular, if a particle could undergo certain reactions (e.g. ionization, gettering), it may be split into two particles, one with weight $(1-p)w_o$ which does not react and one with weight pw_o that does react, where w_o is the incident particle's weight and p is the reaction probability. However, if a particle's weight becomes so low that it is unlikely to contribute much to the desired estimates (yet would require the same tracking computational effort as a fully weighted particle), Russian roulette is applied. Here, the particle is "killed" with probability p, or continued with weight w_o/p.

Particles are initially launched with a weight proportional to the source strength but normalized to an average of unity over all the sources. For example, in a double-null poloidal divertor the outer target plates typically get 80% of the particle and energy flux, with the inner plates getting the remainder. In simulating the recycling neutrals, particles are launched and tracked from each plate in turn, but the outer plate particles would have an initial weight of 1.6 while the inner plate particles would start with 0.4.

6.5 Applications

6.5.1 Conductance Calculations

For low pressures and Maxwellian distributions, the throughput of a vacuum system Q (molecules/s or torr-liter/s) is related to the pressure difference between the ends of the system by

$$Q = C(P_2 - P_1) \tag{6.23}$$

where C is the conductance between points 1 and 2. At low pressures, or the free-molecular flow regime, C is independent of absolute pressure and dependent only on geometry. At high pressures, the conductance is larger and increases with pressure. Experimental and theoretical results are available for the conductance of various geometries under free molecular flow conditions [6.3,6.4,6.5]. Here the code is compared against reference calculations for four geometries: straight rectangular duct; straight cylindrical duct; cylindrical elbow; and cone.

First note that it is convenient to compare conductances in terms of a simple aperture (or opening) conductance and a probability of passage (the Clausing factor),

$$C_{12} = C_A P_{12} = \frac{1}{4}\bar{v}A_1 P_{12} \tag{6.24}$$

where $C_A = vA_1/4$, is the conductance of an aperture of area A_1 (the volume of Maxwellian gas per unit time passing from one side of the aperture to the other) and P_{12} is the probability that a molecule incident on area 1 of the duct will be transmitted through to side 2. Also, since conductances are independent of direction,

$$A_1 P_{12} = A_2 P_{21}\,. \tag{6.25}$$

In testing the program, approximately 10,000 particles were launched from one side of the duct and followed until they either returned to the original side or reached the other end of the duct, and the corresponding transmission probability calculated as the fraction that made it across the duct. These results are compared with values from Ref. [6.4] in Figures 6.4 and 6.5.

In Figure 6.4a and b, excellent agreement is shown for a range of length/diameter ratios for square straight, rectangular straight, cylindrical straight and cylindrical bent

ducts. The good agreement with circular cross-section ducts is particularly noteworthy since only rectangular volume elements are currently allowed in the program. This good agreement was obtained simply by using square duct cross-sections with equal area to that of the corresponding circular cross-section duct.

In Figure 6.5, the code is compared with published results for 20° circular cones. Here the agreement was generally poor because of the limitations of the rectangular geometry - the conical ducts were simulated with a few stepped square ducts. Clearly the agreement improved as the number of steps (N) increased. If the limiting conductance is assumed to be the first stepped square duct, then the expected P_{12} (shown in Figure 6.5a for $N = 4$) is in rough agreement with the calculated values. This is consistent with the limited geometry being at fault here, rather than the code itself. Furthermore, it suggests that the model will reasonably simulate cones if $L/N \ll R_1$ when this entrance duct effect becomes small. Figure 6.5b also shows some corresponding results for the reverse probability.

A further complication of the rectangular geometry limitation is that the angular distribution of emitted particles is not the same as if the surfaces are sloped, especially for specular or cosine–law surfaces. This error is reduced for uniform emission, if the neutral density is large so that self–collisions quickly randomize the velocities, if the neutrals interact with a strong plasma that changes their velocity (e.g. through dissociation), or if there are multiple reflecting surfaces with neutrals travelling in many directions and thus averaging out the differences.

The conclusion from these tests is that the model can successfully calculate conductances for geometries it can simulate with rectangular blocks. Other shapes (e.g. cylindrical ducts) may also be treated, but some will require very small elements if the sloped surfaces are an important part of the geometry and even so, the directionality of particle reflections may not be exactly simulated.

6.5.2 PDX Particle Scoop Simulation

A simple plasma edge particle scoop limiter was tested on PDX to verify the concept of plasma plugging and limiter pumping [6.11]. The device (cross–section shown in Figure 6.6) consisted of a 2 x 6.3 cm^2 duct oriented parallel to the edge magnetic field, with a neutralizing plate and gas plenum at the far end. A pressure probe in the plenum

recorded the steady-state gas pressure for different edge conditions. Figure 6.6 shows the results for deuterium plasmas with 10–20 eV edge temperatures and $10^{18} - 10^{19}/m^3$ edge electron densities. The plenum pressure was seen to increase faster than linearly with electron density, illustrating plasma plugging of the duct throat.

The experiment was simulated with this Monte Carlo code using the device geometry as shown in Figure 6.6, except that the angled source plate was replaced with three steps (because of the rectangular geometry restriction in the present code). The duct was filled with a 15 eV, uniform density plasma flowing at 0.3 times the local sound speed. The walls were assumed to be iron at 0.03 eV. Hydrogen molecules were uniformly launched from the neutralizer plate with a wall temperature distribution, and allowed to react in the particle scoop until they escaped back into the main plasma or were completely ionized.

The computed densities were then scaled to yield the neutral gas pressure in the plenum based on the steady-state particle flux to the neutralizer plate. This flux was estimated from the plasma edge conditions $\dot{N} = nMcA$ plus the recycling flux formed from the ionization and trapping of outflowing neutral hydrogen, $\dot{N}/f_{esc}$, where $\dot{N}$ is plasma input flow, n is edge ion density, M is flow Mach number, c is the plasma sound speed, and f_{esc} is the fraction of neutrals leaving the neutralizer plates that escape back into the plasma edge plus ionized neutrals that flow back into the main plasma. Calculating this fraction in general requires solving the plasma flow equations self-consistently with the neutral transport, including any electric fields that may form. The present model only performs neutral transport calculations so this fraction cannot be determined. Here it was assumed that roughly two-thirds of the ion flow along the duct itself was towards the target (assuming $M \simeq 0.3$), while virtually all the hydrogen ionized in front of the target was swept back in.

The results are shown in Figure 6.6. The theoretical plenum gas pressure increases linearly with edge electron density, in good agreement with Monte Carlo neutral transport calculations by Heifetz et al [6.7,6.11]. The experimental results are similar, but show a much faster rise with density - pressure increased roughly as the square of the edge electron density. This effect, a consequence of "plasma plugging", has been observed in other experiments [6.12]. That is, as the edge density (and thus incoming plasma flux) increases, the recycling neutrals have a greater probability of ionizing in the duct. This

enhances the plasma density near the target, which further increases the local ionization rate, and so on. This local increase in ionization rate was not modelled here (the code cannot self–consistently calculate plasma flow), so the PDX experiment could not be exactly simulated.

Thus the program agreed with other neutral transport calculations and was able to track the correct answer for this situation to the extent possible without also self–consistently treating the plasma transport.

6.5.3 Geometry Factor Calculations

A neutral particle emitted from a divertor target plate or first wall has some chance of penetrating the adjacent plasma and reaching the core. Such recycling can simplify fuelling, but it also raises the possibility of easy access to the core for edge–generated impurities. If this recycling is small, very high neutral pressures can be maintained in divertor chambers or limiter shadows, which would ease pumping requirements and lead to a cold, dense edge plasma. The consequences of this recycling have been investigated experimentally and theoretically, and the importance is illustrated in Chapter 4.

The degree of attenuation is difficult to solve analytically because of the complex reactions and geometry that must be included in the calculation. In Chapter 4, it was assumed that the effect could be described by simple attenuation

$$\frac{\Gamma}{\Gamma_0} \approx e^{-Gd/\lambda} \tag{6.26}$$

where Γ is the neutral particle flux; λ is the neutral mean free path; d is the direct path length from, say, divertor target to divertor throat or from first wall to separatrix; and G is a geometry factor that accounts for everything else, but in particular recognizes that neutrals do not simply travel directly from target to throat, or from first wall radially inward to the plasma core.

Similar forms for the attenuation factor have been proposed. In particular, Igitkhanov et al[6.8] studied the conductance of a cylindrical duct with a radially parabolic plasma profile and correlated the results by

$$\frac{\Gamma}{\Gamma_0} \approx \frac{e^{-d/\lambda_{eff}}}{1 + 0.4d/a + 0.2d/\lambda_{eff}} \tag{6.27}$$

where d is the duct length; a the duct radius; and λ_{eff} is an effective mean free path incorporating wall collisions. In the limit of no plasma, λ_{eff} becomes large and Eqn.(6.27)

reverts to the usual expression for vacuum conductance of a duct [6.4]. However, this latter vacuum conductance expression is obtained assuming both ends of the duct are perfectly absorbing. This may not be relevant to a reactor divertor chamber with only a small steady-state pumping speed, in which case $\Gamma/\Gamma_0 \approx 1$ in the zero plasma limit.

Scrape–off Geometry Factor

In a tokamak, the scrape–off conditions are typically in the range $0.01 < d/\lambda < 100$, so in principle span the full range from low to high core shielding from edge recycling hydrogen and impurities. Simple estimates of scrape-off layer shielding efficiency typically assume $G \approx 1$ [e.g. 6.10]. Reality, as usual, is more complicated.

If the scrape–off plasma is modelled as an infinite, uniform slab of thickness d and reaction mean free path λ, then the attenuation is

$$\frac{\Gamma}{\Gamma_0} \equiv e^{-Gd/\lambda} = \int_0^{2\pi} e^{-d/\lambda \cos\theta} p(\Omega) d\Omega \qquad (6.28)$$

where $p(\Omega)$ is the probability of neutrals travelling in the direction of the solid angle Ω into the plasma slab, and θ is the angle from the normal to the plasma. Results for uniform emission, $p(\Omega) = 1/2\pi$, are presented in Figure 6.7 based on Romberg integration of Eqn.(6.28). For cosine–law behavior, $p(\Omega) = \cos\theta/\pi$, similar calculations show that G varies only between 1 and 2. With uniform emission, G is large for small d/λ because of the presence of grazing particles which travel large distances parallel to the plasma slab surface before reacting or escaping. This G would level off in practice because of the finite curvature of the scrape–off. With both models, the detailed emission profiles become insignificant as d/λ becomes large, and G approaches unity.

If Eqn.(6.28) is evaluated with a thermal velocity distribution and λ based on the cross–section at the average velocity $\bar{v} = \sqrt{8T/\pi m}$, the results are slightly different because of the $d/\lambda \sim 1/v$ dependence in the exponential – $\langle 1/v \rangle = 4\bar{v}/\pi$.

However, in order to more accurately evaluate the neutral particle geometry factors, particularly with the full reaction chemistry, the 3–D Monte Carlo neutral transport code was used. The scrape–off was modelled as an infinite slab of uniform plasma. Hydrogen molecules at wall temperatures were launched with a cosine distribution in angle, and the particles were tracked through dissociation, charge exchange and ionization. Charge exchange neutrals were assumed to flow along the slab. A range of cases were considered,

ranging from $0.02 < d < 0.04$ m, $3 \times 10^{16} < n_{H+} < 3 \times 10^{20}/\text{m}^3$, and $10 < T_e < 1000$ eV which spanned over $0.0024 < d/\lambda_H < 24$ and $0.017 < d/\lambda_{H_2} < 170$. The behavior of the particles is shown in Figure 6.7 and the corresponding geometry factor G_{sc} in Figure 6.8. The short mean free path and isotropic dissociation of H_2 cause G_{sc} to rise quickly. On the basis of these calculations, a reasonable estimate is

$$G_{sc} \approx 1 + 2(\lambda_H/d)^{0.544} \tag{6.29}$$

Divertor Geometry Factor

It is much more difficult to construct a simple generic divertor geometry model. However, to a first approximation, the critical factor is still the "optical thickness" of the plasma to a random flux of neutrals and Eqn.(6.29) is still useful, where d is the direct path length from divertor target to divertor throat. Evaluating specific divertor geometries – ASDEX and DITE – yields the points shown on Figure 6.8, which are in reasonable agreement with this assumption.

6.5.4 DITE Mark 1 Bundle Divertor

The 3-D Monte Carlo model was applied to analyzing neutral gas behavior in several existing or planned machines. Plasma properties were inferred from experimental data or calculated through the global model discussed in Chapter 4. The results refine the simple model's neutral gas calculations to better determine the divertor gas pressure, divertor recycling and divertor pumping speed effects.

In the DITE Mark 1 bundle divertor (Figure 4.2a), a small bundle of magnetic flux lines were pulled about 0.25 m outside the main separatrix (0.2 m from the plasma axis) into a target. Titanium gettering in the divertor provided hydrogen pumping. This divertor was modelled with the geometry (at midplane) shown in Figure 6.9a, $10^{18}D^+/\text{m}^3$ and 30 eV plasma, 2.5×10^{20} deuterons/s striking each side of the target and with a wall recycling coefficient of 0.9 to simulate pumping. The calculated midplane neutral density profiles are shown in Figure 6.9c and d.

The results show that an average neutral atom recycling from the target has an 5% chance of reaching the main chamber, 29% of being pumped, and 66% of being ionized. The D_2 back pressure in the divertor is 0.01 Pa (1×10^{-4} torr) with a 1.5×10^{20} atoms/s pumping rate (about 50 m^3/s based on D_2 density). The D density in front of the target

is $3.8 \times 10^{18} D/m^3$. These compare with the $5. \times 10^{17} D/m^3$, 0.02 Pa calculated in Chapter 4, with 50 m^3/s pumping.

Thus even in this divertor with a large D mean free path (0.35 m) and the relatively open geometry, only 5% of the ions striking the target returned to the main vacuum chamber as neutrals. This is a direct consequence of geometric effects which sharply increase the neutral particles' effective path length back to the main chamber. Here, an average neutral travels 0.5 m before reacting or escaping. A further 30% could return as part of the bulk ion flow, assuming about half of the ionized hydrogen flows back along the magnetic field lines towards the target.

6.5.5 ASDEX Poloidal Divertor

ASDEX has a double-null poloidal divertor (Figure 4.2a) where the plasma is pulled through two narrow channels to targets about 0.5 m from the null points (0.4 m minor radius). The large divertor chamber may be titanium coated for hydrogen pumping. The divertor plasma was modelled, based on the ASDEX calculations in Chapter 4 (Table 4.3), with $3 \times 10^{18}/m^3$ ion density, 10 eV at the target increasing to 17 eV near the null point, and a total flux of $7 \times 10^{21}/s$ H^+ striking the targets and recycling. Up/down symmetry, but in/out asymmetry of 20/80, in terms of particles and energy flows to the targets was assumed based on experimental results. The simulated geometry and the calculated atomic and molecular neutral densities are shown in Figure 6.10.

The results show large peaks in H density near the targets because of the locally high recycling, and a more uniform H_2 density throughout the rest of the divertor chamber. An average neutral recycling from the target has only a 0.8% chance of returning to the main chamber, 81% of ionizing, and 19% of being pumped (based on 0.96 wall recycling coefficient due to gettering). The H_2 pressure in the divertor is 0.003 Pa (3×10^{-5} torr) with a 1.3×10^{21} atoms/s pumping rate (about 940 m^3/s based on H_2). The H density near the targets is about $8 \times 10^{17}/m^3$. These values compare with the $1.6 \times 10^{18} H/m^3$ and 0.008 Pa estimated in Chapter 4, with 1000 m^3/s or 3.8×10^{21} atoms/s pump speed.

In contrast to the open nature of the DITE divertor, ASDEX had longer, narrower channels back to the plasma. This, plus the colder and denser plasma, appreciably reduced the fraction of neutrals escaping the divertor chamber. Experimentally, the consequent high recycling constrains the plasma edge temperature and results in a substantial loss

of energy to the divertor walls through radiation and charge exchange.

These results were obtained with 30,000 particles tracked. When an additional 30,000 protons were followed, the results generally changed by less than 5%. Also, with the present Cartesian geometry, the divertor chamber was simulated as a long slab in the toroidal direction. Changing the extent in this "toroidal" direction from 3 m (the machine diameter) to 1000 m had little effect on the results, provided the source strength was similarly scaled. This is not surprising since the neutrals interact with plasma and with the divertor chamber walls on much shorter length scales than the toroidal radius of curvature. This supports the analyses of the INTOR poloidal divertor and pumped limiter obtained with the 2-D neutral transport code DEGAS [4.27].

6.5.6 ALCATOR-DCT Bundle Divertor

An advanced bundle divertor has been designed for the proposed near-term tokamak ALCATOR-DCT. A flux bundle is pulled out through narrow channels onto a target some 0.8 m from the null point (machine minor radius is 0.4 m). Without expansion coils, the flux expands poloidally from 0.3 m to about 1 m and strikes a tall, thin area of the target (Figure 4.8). Expansion coils would pull the flux further away from the main plasma, and spread the diverted plasma over a larger target surface area.

The modelled divertor geometry at mid-plane is shown in Figure 6.11a. At higher and lower horizontal cross-sections, the geometry was modified to match the expanding flux bundle and coil geometry as illustrated in Figure 4.3. Plasma parameters were estimated based on the calculations in Chapter 4. Of particular interest was the case summarized in Table 4.10, with substantial H_2 pressure and charge exchange energy transfer to the walls. This was modelled here with a $3 - 5 \times 10^{19}/m^3$, 50-7 eV plasma flowing at Mach 0.2-0.6. A large pump duct at the outside of the divertor pumped particles with a 0.5% probability. Neutrals recycled from the targets at 5×10^{22} atoms/s. The calculated neutral density profiles at mid-plane are shown in Figure 6.11c and d.

An average neutral has about a 0.01% chance of escaping the divertor, 2% of being pumped, and 98% of being ionized. The calculated densities are about $4 \times 10^{19} H/m^3$ directly in front of the target, and about 1 Pa (0.01 torr) H_2 pressure with a pump speed of 6 m^3/s. These compare with the $7.5 \times 10^{20} H/m^3$ and 5 Pa H_2 pressure estimated in Chapter 4 with 5 m^3/s pump speed.

Since the plasma temperature is cold, sputtering is not a problem. Charge exchange processes extract 390 kW from the divertor plasma, while ionization and dissociation take another 150 kW (the 0-D model predicts 360 kW and 77 kW, respectively). Most of the charge exchange energy (~200 kW) is transferred to the divertor walls near the vacuum pump entrance. For this and neutron streaming reasons, the pumps should not be in close line-of-sight proximity to the target. Of the remaining power, 120 kW hits the target. The narrow divertor entrance channels receive less than about 1 kW/m^2 of charge exchange heat flux, with most of this from the cold dense plasma in front of the target.

These results were obtained with the divertor channel baffled against neutral backflow to the main chamber. Since only a comparatively small area could be baffled (0.07 m^2), this did not make much difference to the divertor neutral behaviour. The calculations took 6 minutes on a CRAY, with 50,000 particles followed. The results were reproducible to about 5%.

6.6 Summary

In this chapter, a 3-D Monte Carlo neutral model is presented. The code is used to estimate the geometry factors used in the global edge model of Chapter 4. The code was also used to illustrate some details of neutral behavior in divertor designs. Particular emphasis was placed on bundle divertors because of the limited transport analysis presented in the literature.

Particular results illustrated the ability of divertors to confine neutrals to the divertor chamber itself. The resulting pressures can be quite large - about 1 Pa in an advanced bundle divertor for ALCATOR-DCT, for example. Comparing these results with the estimates made in Chapter 4, the densities agree within the factor of ten expected, although the 3-D neutral profiles clearly show that this H density peaks very close to the target.

The primary limitations of the Monte Carlo model are the non-self-consistent plasma model and the rectangular geometry approximation. The Cartesian geometry considerably reduces computational requirements because it is easy to determine volume element boundaries, but requires simulating curved or angled surfaces as a series of stepped blocks. Circumstances where the curvature of the surface is dominant are only poorly treated, although agreement may improve if many small steps are used. This limitation

could be removed by allowing special volume elements with internal structure. (If most of the volume could be constructed as rectangular blocks, much of the time saving would be retained.) Alternately, the particular geometry could be abandoned in favor of a more general geometry such as that in the vacuum analysis code MV1A [6.9] or the plasma/neutral code DEGAS [6.7]. However, this geometry restriction is not believed to be a serious handicap in modelling divertors and many other devices because the effect of surface reflections is quickly lost in the presence of a plasma, high neutral densities, or complicated geometries with random, multiply-reflected fluxes of neutrals.

The desirability of self-consistently calculating plasma parameters is clear. Unfortunately, this requires a sophisticated numerical algorithm of its own for a complete description of the physics, although simple models might be constructed for each plasma volume element, similar in spirit to the coupled 0-D model of Chapter 4.

The next step in development of this particular code is to couple it with an improved plasma model, and possibly to include impurities.

6.7 References

[6.1] L.Carter and E.Cashwell, "Particle-transport simulation with the Monte Carlo method", TID-26607, ERDA, 1975.

[6.2] J.Spanier and E.M.Gelbarch, "Monte Carlo principles and neutron transport problems", Addison-Wesley Publ. Co., Reading, Mass. 1969.

[6.3] L.Levenson, N.Milleran and D.Davis, "Optimization of molecular flow conductance", 7th National Symposium on Vacuum Technology (1960) Transactions, p. 372,Pergamon Press, New York 1961.

[6.4] G.Weissler and R.Carlson (eds.), "Vacuum physics and technology", Vol. 14, Methods of Experimental Physics, Academic Press, New York 1979.

[6.5] C.Fan and S.Robertson, "Monte Carlo solution of mass, momentum and energy transfer for free molecule and near-free molecule flow through circular tubes", Proc, 6th Int. Symp. on Rarefied Gas Dynamics, (1968), Vol.I., p.655, Academic Press, New York, 1969.

[6.6] Y.Seki et al, "Numerical calculations of helium ash enrichment and exhaust by a simple divertor", Nucl. Fus., 20,(10), 1980, 1213.

[6.7] D.Heifetz et al, "A Monte Carlo model of neutral particle transport in diverted plasmas", PPPL-1843, Princeton University (Jrnl. Comp. Phys., 46(2), 1982, 309).

[6.8] Y.Igitkhanov et al, "Plasma effect on the gas conductance of a divertor channel", paper G-8, Tenth Eur. Conf. on Cont. Fus. and Plasma Phys., Moscow, 1981.

[6.9] M.R.Peterson, "MV1A - general description", LLNL, January 1981.

[6.10]P.J.Harbour, "Divertor problems", in "Plasma physics for thermonuclear fusion reactors", (G.Casini, ed.), Harwood Academic Publishers, England, 1981, 255.

[6.11]R.Jacobsen, "Preliminary particle scoop limiter measurements in PDX", PPPL-1825, Princeton University, August 1981.

[6.12]S.Talmadge and R.Taylor, "Pumped limiter experiments on MACROTOR", Paper 9S9, 23rd Annual Meeting of the Division of Plasma Physics/American Physical Society, New York, October 1981 (Bull. Am. Phys. Soc., 26(7), 1971, 1057).

Table 6.1: List of variables

A	Area [m^2];
d	Distance [m];
e	Electron charge, 1.60×10^{-19} C;
E	Energy [J];
$f(v)$	Distribution function [s/m^4];
$f_M(v)$	Maxwellian distribution function [s/m^4];
G	Geometry factor;
m	Mass [kg];
n	Density [$1/m^3$];
N_p	Number of particles tracked;
p	Probability;
S	Source strength [particles/s];
S_{pump}	Pump speed [m^3/s];
t_{kj}	Time particle k spends in volume element j [s];
T	Temperature [J];
v	Velocity [m/s];
v_{th}	Thermal velocity [m/s];
V	Volume [m^3];
w	Particle weight;
Γ	Particle flux [$1/m^2$-s];
λ	Mean free path [m];
θ	Angle from surface normal;
σ	Reaction cross-section [m^2];
ϕ	Angle around surface normal;
ξ	Uniform random number on (0,1);
Ω	Solid angle [steradians];

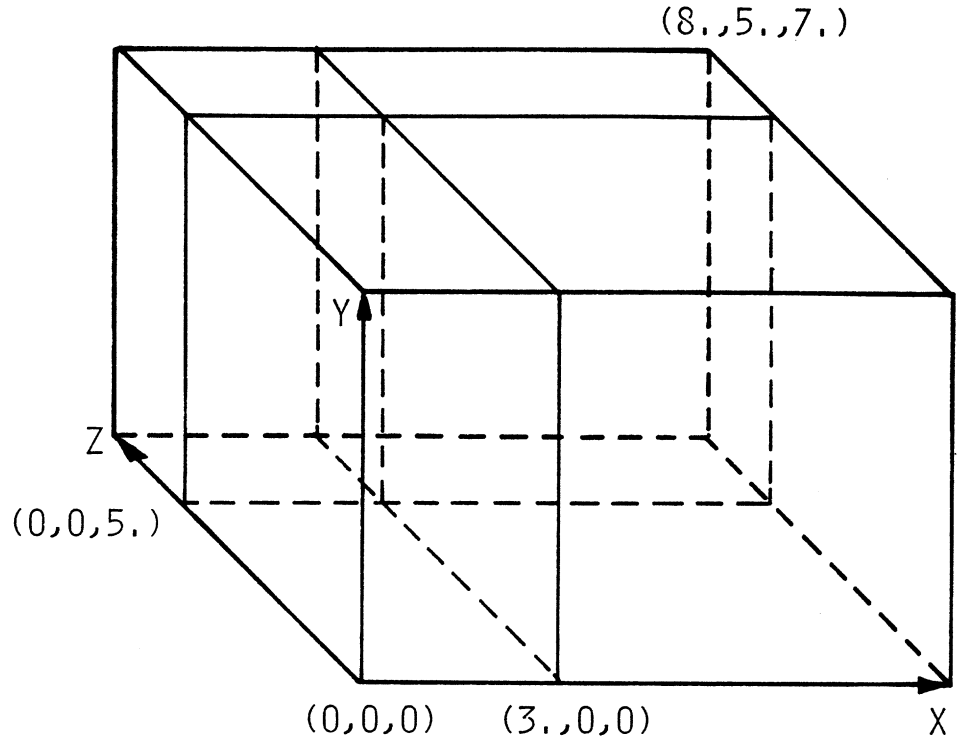

Figure 6.1: Representative geometry for Monte Carlo code calculations illustrating coordinate system. Here an 8 x 5 x 7 box has been divided into four volume elements by a yz-cut at $x = 3$, and an xy-cut at $z = 5$.

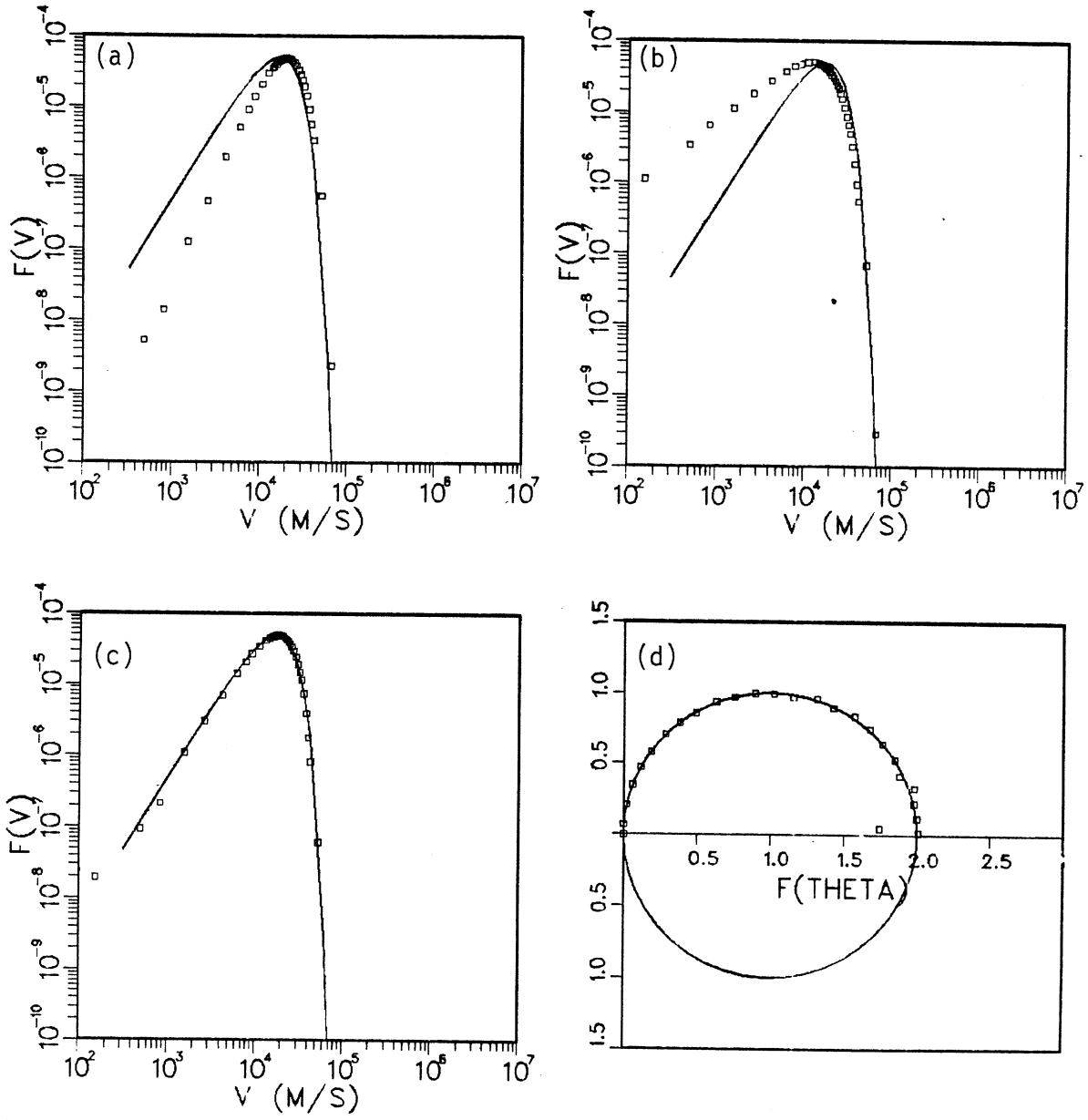

Figure 6.2: Random number generators for a 3-D Maxwellian speed distribution and a cosine law angular distribution. Solid line indicates the desired curve for 3 eV D, open symbols shows that generated from uniform random numbers ξ by: (a) $v = v_{th}\sqrt{-\ln(\xi)}$; (b) $v = v_{th}\sqrt{-\ln(\xi_1, \xi_2)}$; (c) $v = v_{th}\sqrt{\frac{3}{2}\sum_{j=1}^{3}(\sum_{i=1}^{4}\xi_i - 2)^2}$; and (d) Polar plot of angle from surface normal, $\theta = \sin^{-1}\sqrt{\xi}$

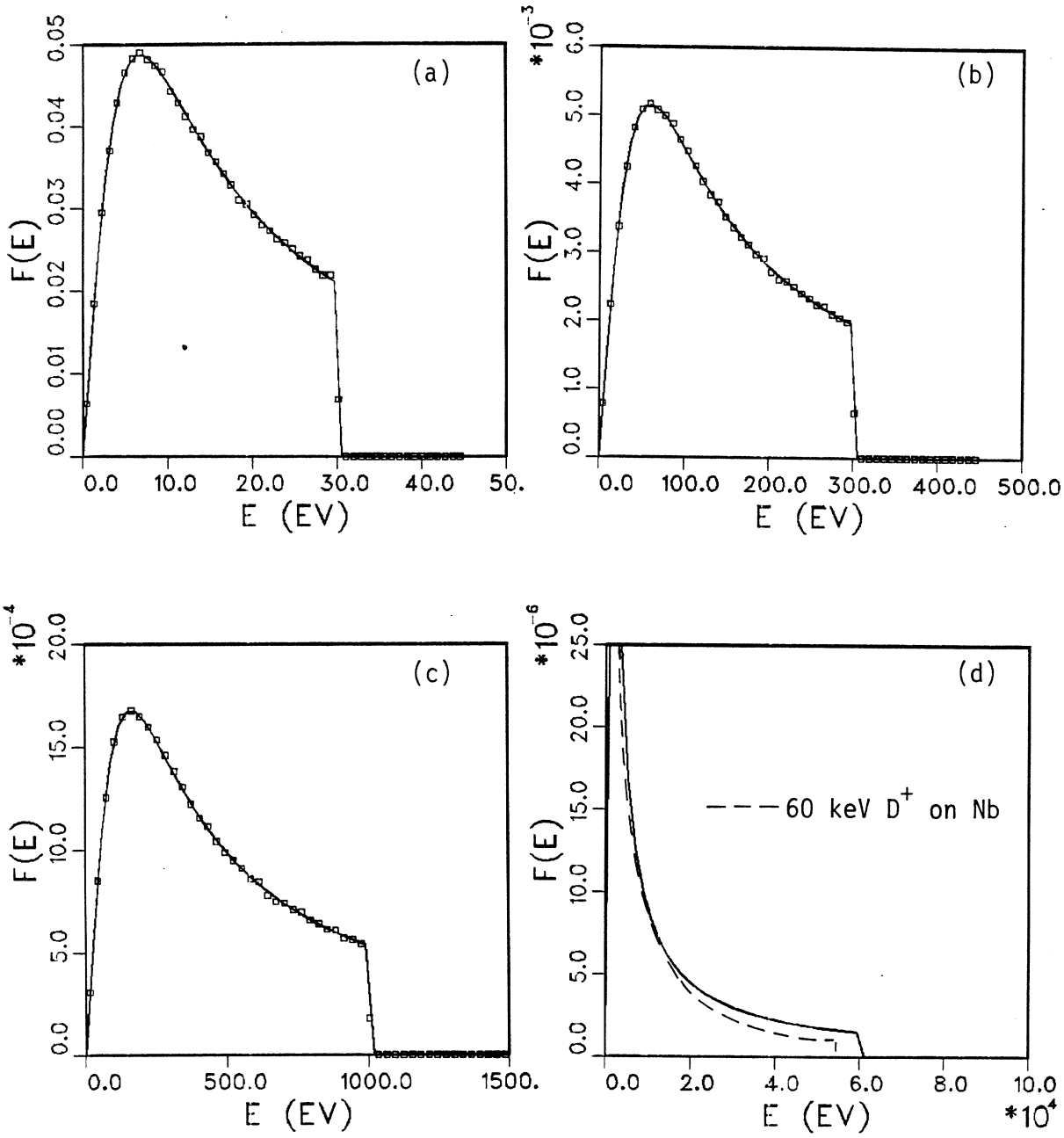

Figure 6.3: Energy distributions for reflected particles for different incident energies. The incident angle was 60°. The open symbols show the distribution generated from transformed random numbers. Experimental results for D^+ on niobium are shown in Figure 6.3d.

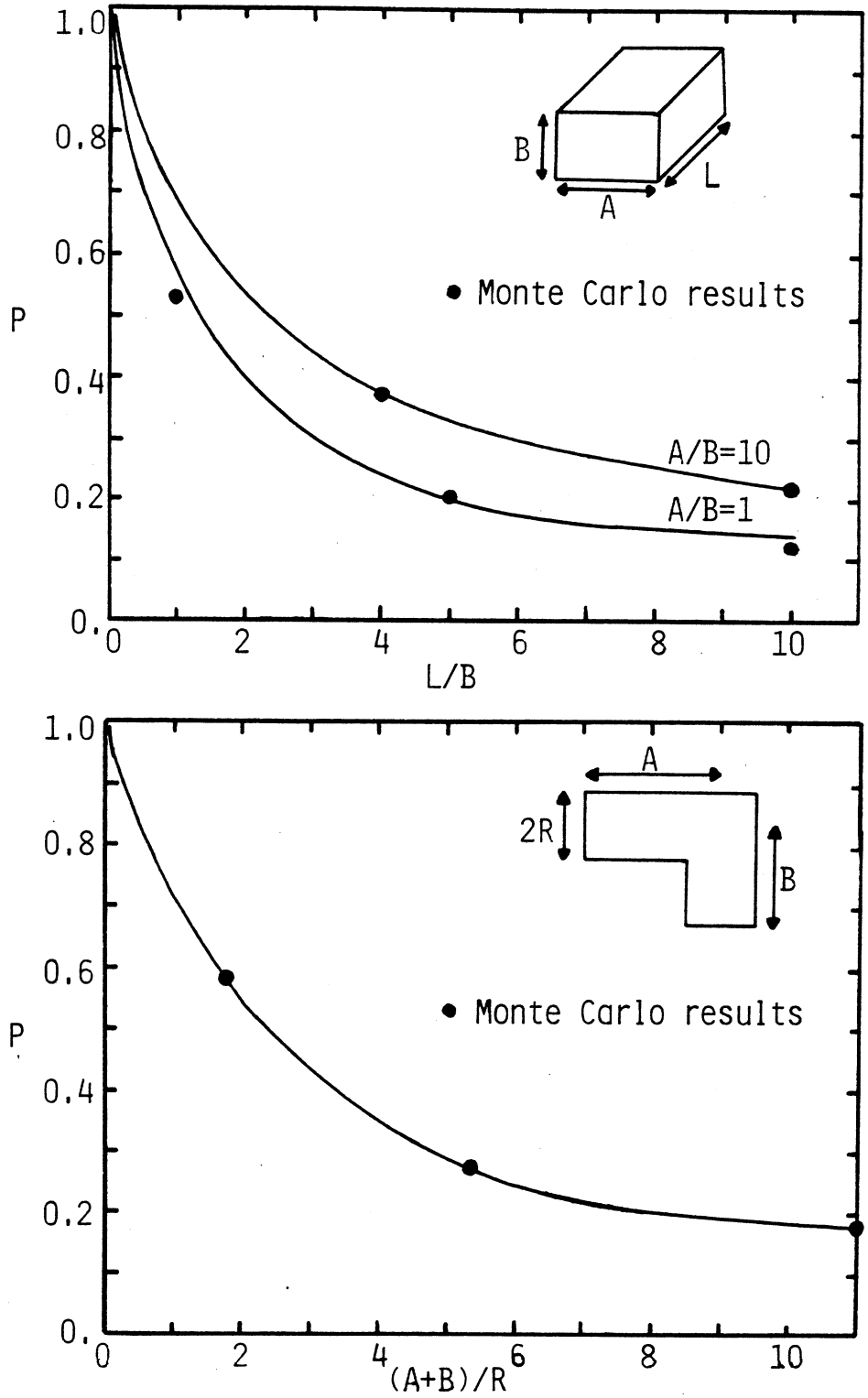

Figure 6.4: Comparison of Monte Carlo calculations (10^4 particles) with published transmission probability curves for: (a) square or circular (equal area) straight ducts; and (b) cylindrical bent ducts.

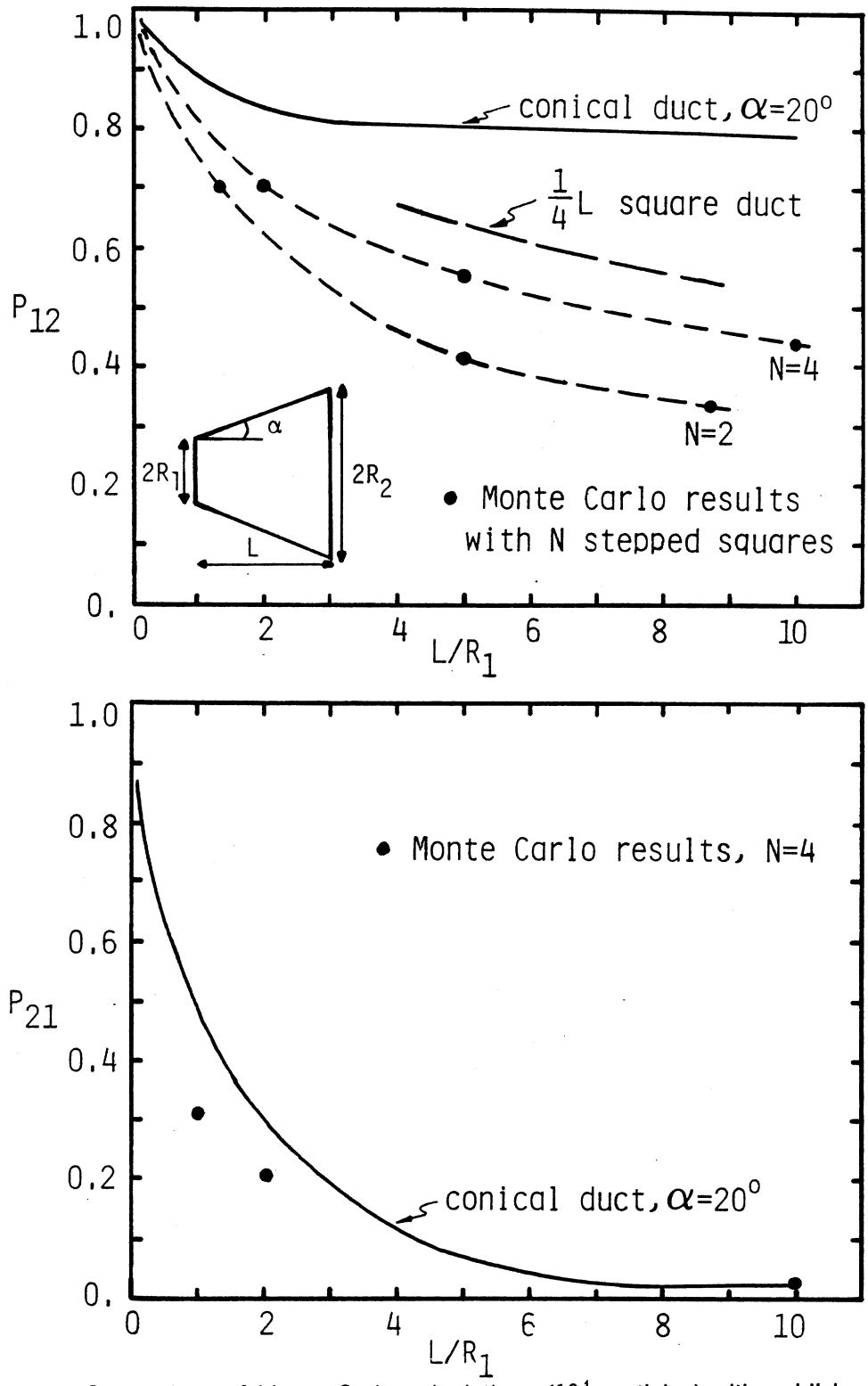

Figure 6.5: Comparison of Monte Carlo calculations (10^4 particles) with published transmission probability curves for a conical duct modelled as a set of N expanding boxes: (a) particles launched at small end; and (b) particles launched at large end.

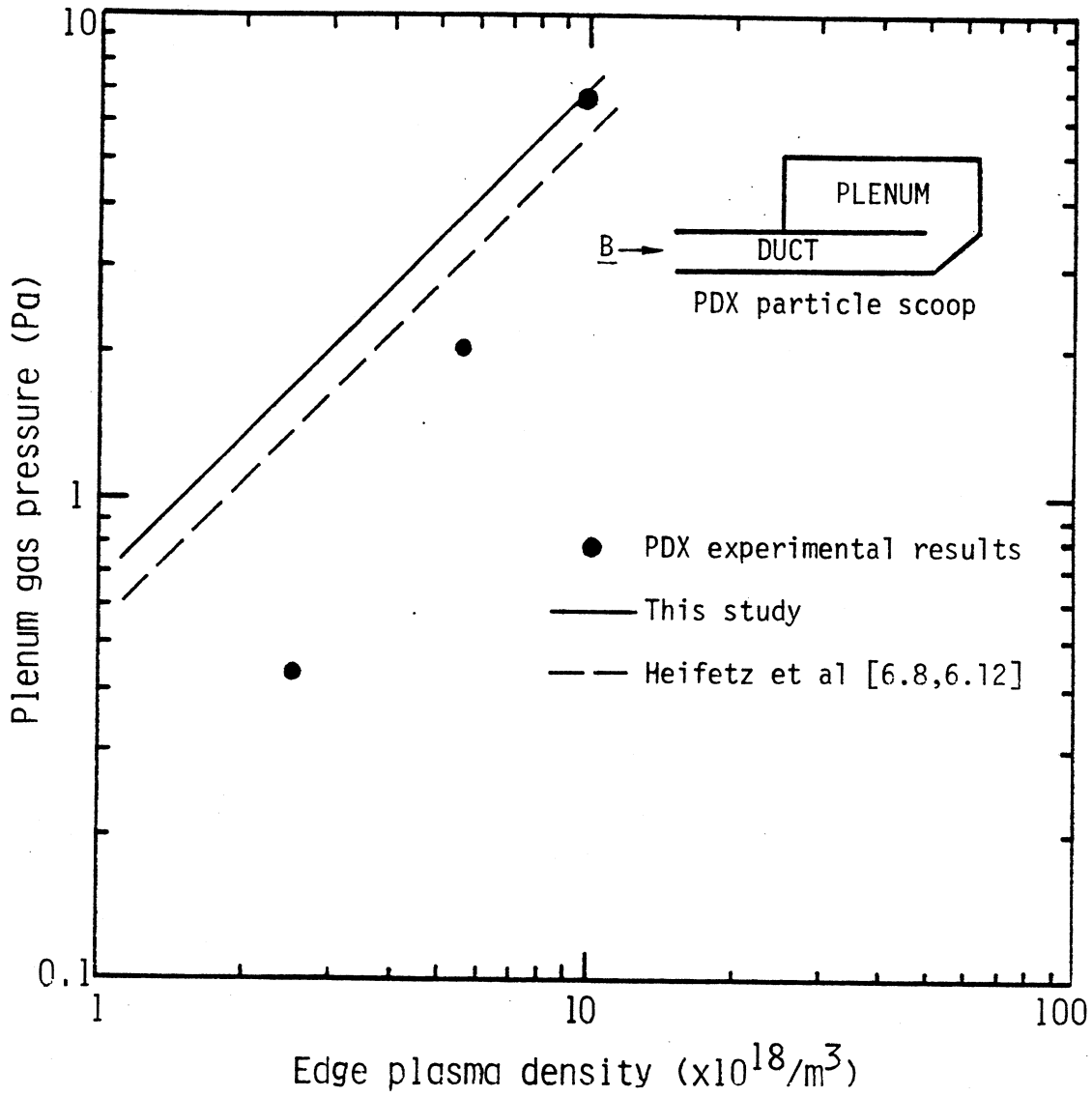

Figure 6.6: Variation in PDX particle scoop plenum gas pressure with plasma edge density, and comparison with Monte Carlo neutral transport calculations.

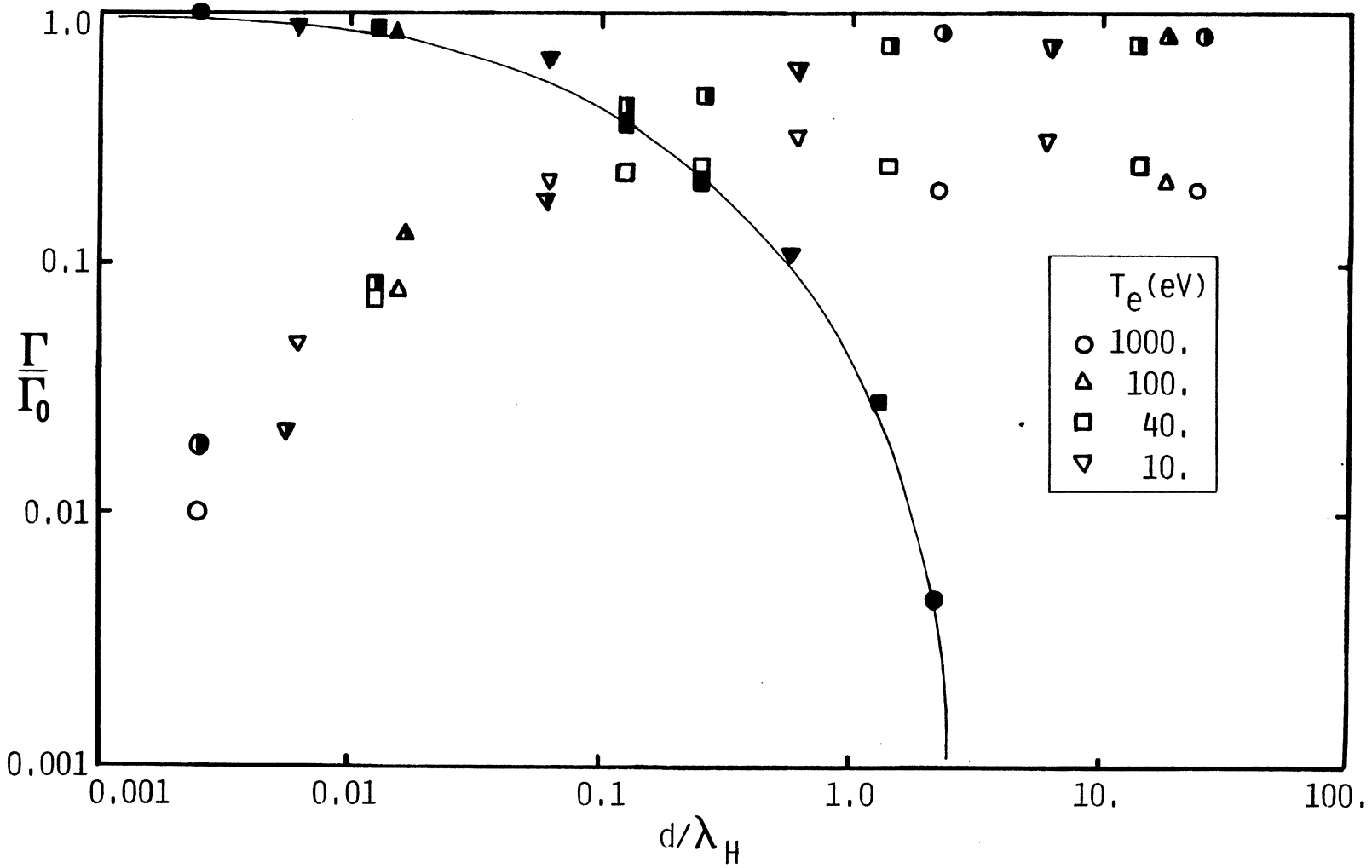

Figure 6.7: Fraction of particles crossing plasma (solid symbols), ionizing (partially-filled symbols), or returning to wall (hollow symbols), for an infinite slab of uniform plasma.

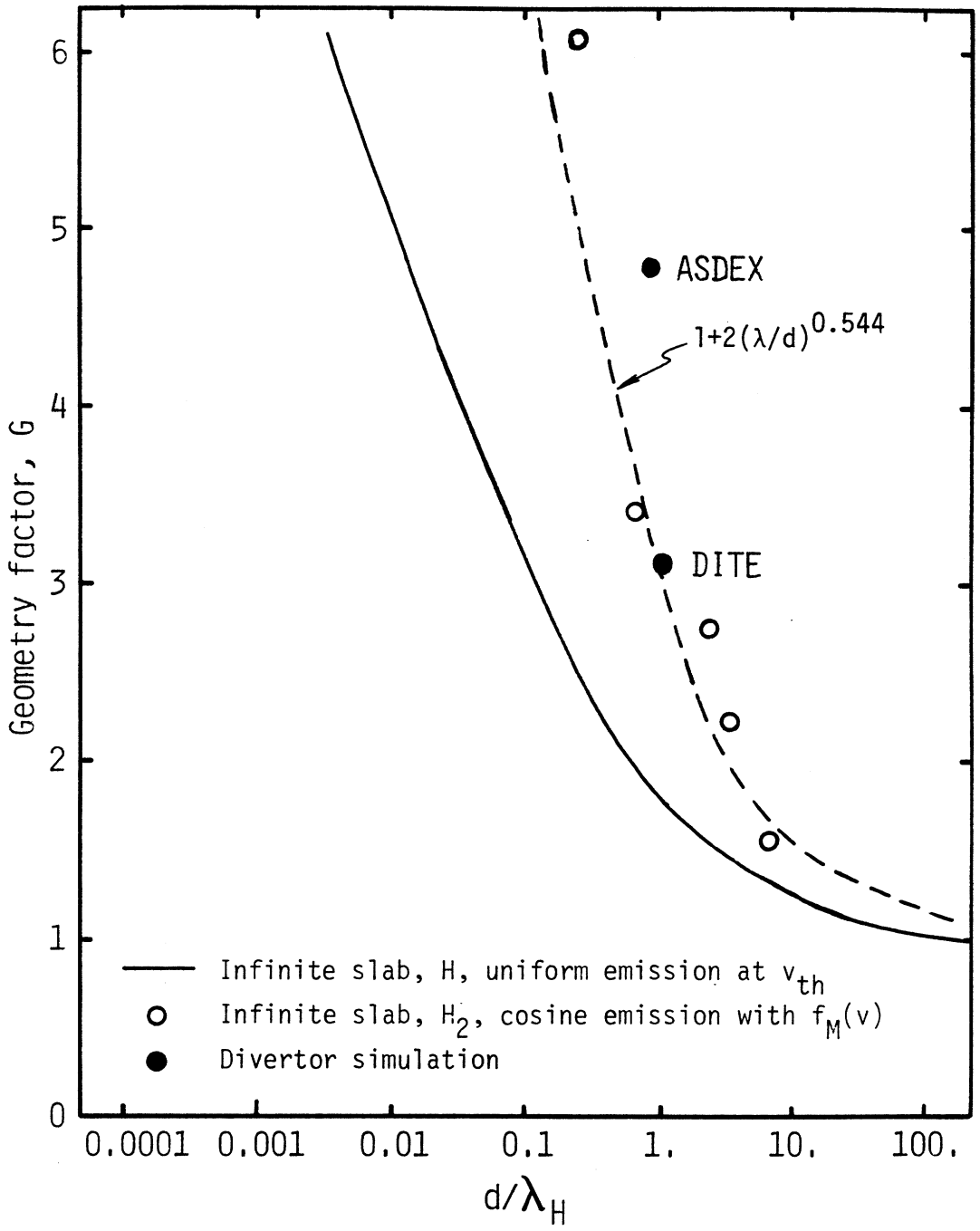

Figure 6.8: Geometry factor as a function of the ratio of plasma thickness d to atomic hydrogen mean free path λ_H.

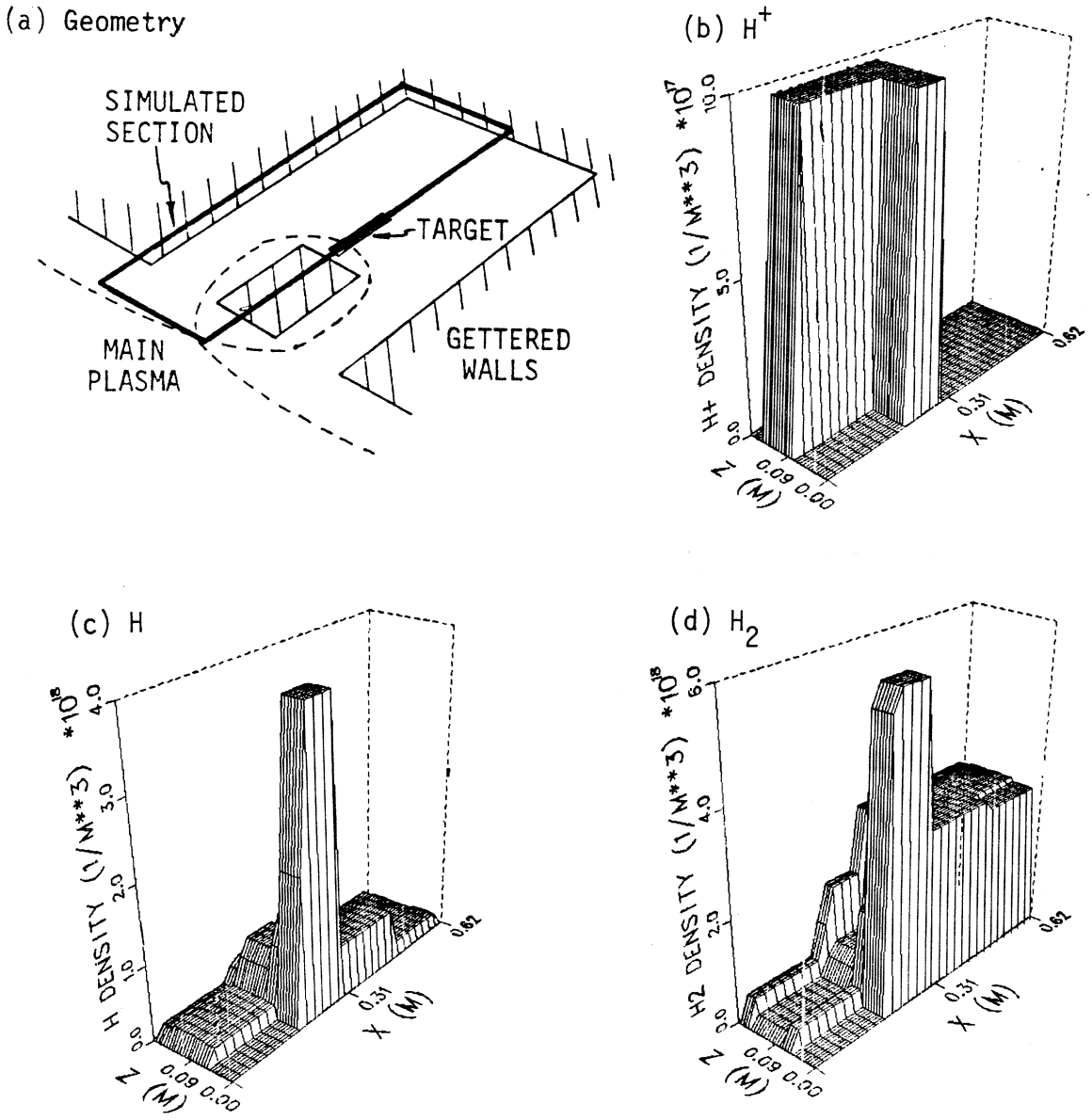

Figure 6.9: Neutral density profiles (at mid-plane) in DITE Mark 1B bundle divertor; only half of the divertor is shown: (a) geometry; (b) H^+ density profile; (c) H density profile; and (d) H_2 density profile.

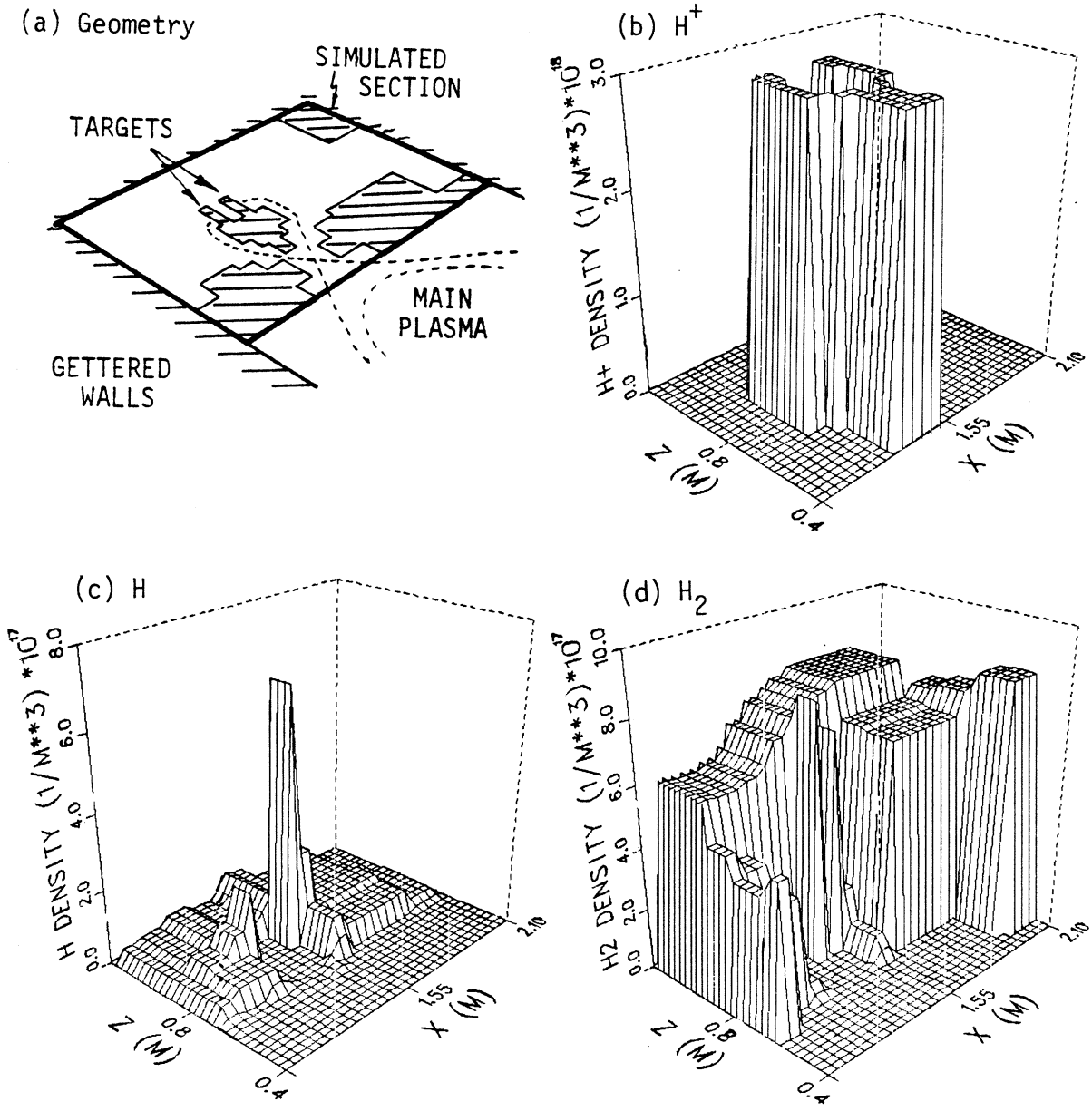

Figure 6.10: Neutral density profiles (poloidal plane) in upper poloidal divertor chamber of ASDEX: (a) geometry; (b) H^+ density profile; (c) H density profile; and (d) H_2 density profile.

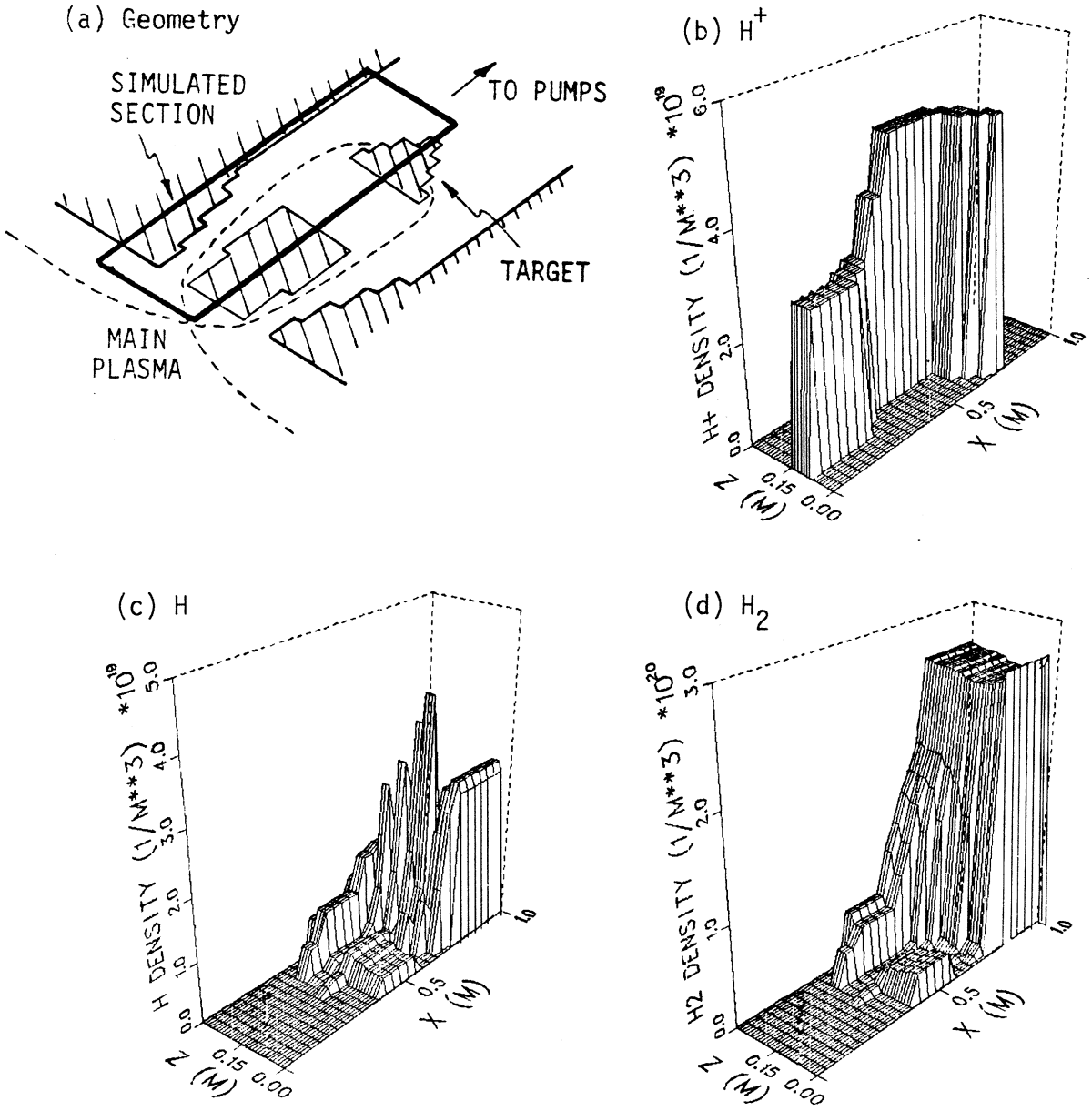

Figure 6.11: Neutral density profiles (at mid-plane) for ALCATOR-DCT bundle divertor; only half of the divertor is shown: (a) geometry; (b) H^+ density profile; (c) H density profile; and (d) H_2 density profile.

7.0 Summary and Recommendations

Plasma exhaust and edge modelling has received much attention in the past few years. As a consequence, edge condition for new machines can now be evaluated with much more certainty using a variety of computational models. Nonetheless, the field is far from closed. In this thesis, several relatively unexplored issues in hydrogen transport in divertors and limiters were studied.

7.1 Summary

There are many complex and often poorly quantified processes occurring in the plasma edge. Chapter 3 provides an updated review of our understanding of these reactions, determines the dominant physics, and establishes a reasonably complete set of correlations suitable for numerical analysis of the plasma/edge region.

There now seem to be a range of "options" for controlling edge conditions. It would be useful to have a relatively fast and accurate means of exploring these options so as to allow a consistent comparison of the choices for any particular machine. Thus, given engineering constraints on surface area and pumping ducts say, what are the best possible target conditions? What happens if a pumped limiter is used rather than a poloidal divertor? There are no models available to reasonably and easily explore all the major options - most are specific to particular conditions.

In Chapter 4, a steady-state global edge model is developed to address this need. This is a 0-D lumped parameter model of the plasma core, scrape-off region and divertor that relates particle and energy flows through simple physical models. The resulting set of coupled transcendental equations is solved by partial linearization (in terms of the choice of implicit and explicit variables) and iteration with relaxation of critical parameters. In the development of the overall model, several choices for the transport models were considered. The present set is believed to adequately describe hydrogen and energy transport in almost all the interesting options. In fact, the equations probably represent the minimum set of relations that should be used in any global edge model. A measure of the model's strength is the modest but reasonable agreement with a variety of experimental results, and with other analyses of reactor-class machines. The general agreement is

within a factor of three for temperature and power, and within a factor of ten for density and particle flow.

A further advantage of this model, besides its generality, is that it is constructed in terms of physical "knobs". That is, the input parameters are real engineering variables such as geometry, pump speed, and fuelling rate and locations. This is in contrast to other models where the knobs are, for example, the degree of recycling in front of the target, or the plasma temperature in front of the target. Of course, the model incorporates reasonable physical models such as Bohm-like cross-field diffusion, so the effect of different models can easily be tested if a better relation is developed or to simply explore the sensitivity of the results to particular assumptions.

This model was applied to evaluating edge conditions in two proposed tokamaks, ALCATOR-DCT and INTOR. Both are relatively large, long-pulse machines that will require reliable, and possibly reactor-relevant, exhaust systems. Bundle divertors, poloidal divertors and pumped limiters have all been considered and reasonable edge conditions were identified. There is no simple way to rank the exhaust systems, but particular points can be compared from the reference cases considered.

In general, the pumped limiter leads to the hottest edge, (1.2 keV INTOR, 110 eV ALCATOR-DCT), then the poloidal divertor (130 eV, 40 eV), and the bundle divertor has the coldest edge (30 eV, 7 eV in the divertor). However, the pumped limiter and, to a lesser degree, the poloidal divertor are sensitive to uncertainties in cross-field diffusion rates, core particle confinement and impurity concentrations. Small variations from the reference conditions could cause sharp changes in edge conditions. This leads to some flexibility, but also uncertainty, in designing with such exhaust systems. The bundle divertor naturally produces a cold, dense divertor plasma and is not sensitive to these parameters. Since the neutral gas pressure in a bundle divertor chamber on INTOR or ALCATOR-DCT can easily reach 1 Pa, only mechanical pumps are needed to exhaust the hydrogen. This should simplify the design, reduce costs, and improve reliability. Finally, the divertor target heat fluxes are expected to be reasonable in all cases, although flux expansion coils are necessary for an INTOR bundle divertor.

In Chapter 5, the case of collisionless edge plasmas was considered, since present divertor experiments are either close to the collisional/collisionless boundary (ASDEX) or

are collisionless (DITE) in the divertor itself, and since collisionless conditions are possible in reactor-relevant plasmas. For example, under certain low density, high temperature conditions ($T_e \sim 1000$ eV) the energy of particles striking the divertor target would be at least a few keV and thus beyond the peak in sputtering cross-sections, and since fewer particles would hit the surface for a given energy flux, target erosion would be even lower. It is not entirely clear that such a regime is attainable (it may be unstable because of impurity radiation) or desirable (self-sputtering and unipolar arcing limits), but it is a possible regime and certainly not adequately addressed in present fluid models. A further motivation is that plasma-neutral gas reactions and electrostatic sheath effects may appreciably distort the ion distributions from Maxwellian even at low temperatures – say, 50 eV or so.

A 2-D (x, v_x) plasma model was developed to study collisionless flow along a uniform magnetic field into a neutralizing target. The model included H, H^+ and H_2, and charge exchange, ionization and dissociation reactions. It was found that the production of cold ions from the various reactions led to a distorted distribution and the formation of a peak in the electrostatic potential profile. The numerical model solved the drift-kinetic equation in characteristic form, starting at the peak and integrating out towards the divertor throat. The characteristics of the resulting peaked potential profile were identified as a function of initial conditions. The results are in good agreement with recent calculations by other researchers. In particular the potential peak was at most 0.3 T_e for $T_i/T_e \sim 1$ and complete recycling from the target. This did not strongly influence net hydrogen particle flow towards the target. The effect on energy transfer was not calculated since the electrons were assumed to follow the Boltzmann relation – effectively assuming high collisionality and very large parallel thermal conductivity. The effect on impurities was also not calculated, although the peak may be a significant factor in containing or reflecting multiply charged impurity ions.

Finally, in Chapter 6, a 3-D Monte Carlo neutral model was developed to improve the evaluation of neutral recycling in complex divertor configurations where geometry is an important factor. Of particular interest is the evaluation of neutral transport in bundle divertors which partially rely on their convoluted internal structure to limit recycling and so improve target heat transfer and pumping conditions. In fact, bundle divertor neutral

transport has scarcely been treated at all until now.

The model tracks single particles through Cartesian geometries, accumulating a better estimate of local steady-state neutral densities and energies with each particle followed. A full set of the important plasma/neutral reactions and surface reactions are included. Densities and energies are calculated based on a path-length estimator, and some simply variance reduction techniques are applied (splitting and Russian roulette) to reduce the computational time. The Cartesian geometry restriction substantially simplifies the tracking algorithm, although it does place limits on the shapes that can be modelled. This is not believed to be a serious limitation since the cases of interest usually involve plasma/neutral or neutral/neutral reactions that rapidly remove any surface directionality effects, or because the complex, reflective geometries naturally produce random, fairly isotropic neutral fluxes. Another important feature of the model is the potential ability to perform self-collisions because the density estimate is continuously updated, although the self-scattering reactions are not yet included.

Since the present emphasis is on neutral transport (these are most affected by the geometry) and since a full self-consistent plasma model would itself require a sophisticated numerical model, at present only a simple externally specified plasma model is used where the density, temperature, flow Mach number and magnetic field vector are supplied in the same volume elements as used for the neutrals. The results illustrate the low probability of neutral recycling back to the main chamber, even in relatively simple, open divertor geometries. For bundle divertors in particular, high back pressures in the divertor chamber are easily attained. This enhanced neutral density makes pumping easier, and spreads the heat load over a much larger surface because of line radiation and charge exchange.

7.2 Recommendations

The primary areas for improvement or application of the models are described below.

Global Edge Model

1. Improve treatment of geometry effects in divertor – in particular, the geometry factor $G_{d,n}$ could be correlated for a larger range of conditions and better limits estimated for neutral particle escape in "open" geometries such as the INTOR poloidal divertor.

2. Explore the effect of changing geometry within a particular type of divertor. For example, can baffles or a smaller channel help the formation of cold, high density regimes in poloidal divertors or pumped limiters?
3. Improve the ability of the numerical model to handle very cold divertor conditions ($T_e \lesssim 5$ eV) possibly by changing the variables from particle and energy fluxes to the more critical reaction rates as the temperature becomes cold; this would extend the model towards treating gas blanket divertor concepts.

Collisionless Plasma Model

1. Improve modelling of electrons, possibly by the use of a fluid model; this would allow evaluation of the important electron energy transport term and better pin down the actual potential profile, rather than the family of solutions presently obtained.
2. Add ion self-collisions to extend the range of usefulness of the model to the more likely case of relatively cold plasmas ($T_e \sim 50$ eV).
3. Improve the numerical scheme so as not to depend on the assumption of a peaked potential profile.

Monte Carlo Neutral Transport Model

1. Improve the plasma model; a simple coupled lumped parameter model along the lines of that used in the global edge model would be relatively easy to implement and yet allow some self-consistency and feedback between the plasma and the neutrals.
2. Include neutral self-scattering reactions to handle high neutral densities such as would occur in gas target schemes.
3. Speed up the evaluation of reaction cross-sections, possibly by use of fast table lookup with a guess, since this subroutine currently consumes the most time.
4. Vectorize or otherwise optimize the code to improve speed.
4. Allow more general geometry; hopefully without sacrificing much speed. Although not described in this thesis, an annular version has already been developed that improves and simplifies the treatment of toroidal machines and cylindrical ducts.